

ANDREA PELLONI

ON THE COMPUTATION OF QCD CORRECTIONS
AND HIGGS OBSERVABLES

DISS. ETH NO. 27114

ON THE COMPUTATION OF QCD CORRECTIONS
AND HIGGS OBSERVABLES

A dissertation submitted to attain the degree of

DOCTOR OF SCIENCES of ETH ZÜRICH
(Dr. sc. ETH Zürich)

presented by

ANDREA PELLONI

Dipl., Eidgenössisches Polytechnikum

born on 20 July 1990

citizen of Switzerland

accepted on the recommendation of

Prof. Dr. C. Anastasiou, examiner

Prof. Dr. M. Grazzini, co-examiner

2020

Andrea Pelloni: *On the computation of QCD corrections
and Higgs observables*, © 2020

DOI: ???/ethz-a-

ABSTRACT

The thesis is divided into two parts: one focused on the analytic computation of high-order corrections to the Higgs-boson cross-section and the other concerning a numerical approach to the computation of amplitudes.

In the first part, we present the calculations that led to the Higgs boson rapidity distribution through next-to-next-to-next-to-leading order in the limit of an infinite top mass. In particular, we use finite fields and differential equations to obtain the partonic coefficient functions as an expansion around the production energy for the Higgs boson for the gluon fusion channel. We compute six orders of the threshold expansion with an error due to the truncation of the series estimated to less than 1% for rapidities within $|Y| < 2$. The error due to missing higher-order correction in the perturbative expansion is reduced to $^{+0.9\%}_{-3.4\%}$ in the range of rapidity $|Y| < 3$, estimated by varying the common scale $\mu = \frac{m_H}{2}$ by a factor of two around its central value.

In the second part, we discuss the numerical integration of amplitudes and integrals by means of the Loop-Tree Duality, where the energies of the loop momenta are integrated using the residue theorem and the remaining degrees of freedom are then integrated using Monte-Carlo techniques. To accommodate for the causal prescription of Feynman propagators in the presence of threshold singularities, we provide a general deformation of the integration variables that also matches the conditions arising from analytic continuation. This implementation is applied to a diverse range of finite integrals with a varying number of external legs and loops. We also treat the computation of divergent integrals and amplitudes at one-loop showing how to remove their IR singularities with the aid of counterterms that are compatible with the Loop-Tree Duality derivation. In particular, we present their application to the family of amplitudes $q\bar{q} \rightarrow n\gamma$ at next-to-leading order in QCD for an arbitrary number of photons in the final state and integrate for the case of two and three photons. At last, we show how the numerical instabilities that arise from the original derivation of the Loop-Tree Duality are handled by removing all the spurious poles that appear after the analytic integration of each loop momentum energy.

SOMMARIO

Questa tesi è divisa in due parti: la prima tratta il calcolo in forma analitica di correzioni ad alto ordine perturbativo in QCD per la sezione d'urto del bosone di Higgs, la seconda è focalizzata su un approccio numerico per il calcolo di ampiezze ed integrali.

Nella prima parte, presentiamo i calcoli che hanno portato ad ottenere la distribuzione di rapidità del bosone di Higgs al terzo ordine perturbativo nella teoria effettiva dove il quark top è da considerarsi con massa infinita. Nello specifico, mostriamo l'implementazione di campi finiti ed equazioni differenziali al fine di ottenere tale risultato. La distribuzione in rapidità è stata calcolata per il canale di produzione dove il bosone di Higgs è il risultato dalla fusione di due gluoni nello stato iniziale, ed ottenuta tramite un'espansione intorno all'energia di produzione del bosone. Presentiamo il risultato includendo i primi sei termini in questa espansione e stimiamo l'errore dovuto all'interruzione della serie a meno del 1% per rapidità $|Y| < 2$. L'incertezza per la distribuzione in rapidità, stimata variando la scala intorno al suo valore centrale $\mu = \frac{m_h}{2}$ per un fattore due, è ridotta a $^{+0.9\%}_{-3.4\%}$ per un valore di rapidità $|Y| < 3$.

Nella seconda parte, discutiamo l'integrazione numerica di ampiezze ed integrali usando la Loop-Tree Duality, dove le energie dei momenti di loop sono integrate usando il teorema del residuo, mentre l'integrazione delle componenti spaziali è ottenuta tramite metodi di Monte-Carlo. Presentiamo un metodo generale per deformare lo spazio di integrazione così da soddisfare la prescrizione causale dei propagatori di Feynman e le condizioni che emergono per la continuazione analitica. Appliciamo questa tecnica ad un ampio spettro di integrali finiti con un numero variabile di gambe esterne e loop. Inoltre consideriamo integrali ed ampiezze a 1-loop con divergenze infrarosse e mostriamo come regolarizzarli in una maniera che sia compatibile con la derivazione della Loop-Tree Duality. In particolare, presentiamo la regolarizzazione locale delle divergenze nel caso della famiglia di ampiezze $q\bar{q} \rightarrow n\gamma$ al primo ordine perturbativo in QCD per un numero arbitrario di fotoni nello stato finale. L'integrazione numerica è presentata nel caso di due e tre fotoni. Infine mostriamo come trattare le instabilità numeriche che affliggono l'espressione originale della Loop-Tree Duality tramite la rimozione di tutte quelle divergenze spurie che compaiono dopo ogni integrazione analitica delle energie dei momenti di loop.

DECLARATION

I declare that I have not previously submitted any material presented in this dissertation for any other degree at this or other university.

The research presented in this thesis has been carried out in collaboration with Z. Capatti, F. Dulat, B. Mistlberger, V. Hirschi, D. Kermanschah, and B. Ruijl. Aspects of this dissertation have been published in the following publications

- F. Dulat, S. Lionetti, B. Mistlberger, A. Pelloni, C. Specchia, Higgs-differential cross section at NNLO in dimensional regularisation. *JHEP* **07**, 017, arXiv: 1704.08220 [hep-ph] (2017)
- F. Dulat, B. Mistlberger, A. Pelloni, Differential Higgs production at N^3 LO beyond threshold. *JHEP* **01**, 145, arXiv: 1710.03016 [hep-ph] (2018)
- F. Dulat, B. Mistlberger, A. Pelloni, Precision predictions at N^3 LO for the Higgs boson rapidity distribution at the LHC. *Phys. Rev.* **D99**, 034004, arXiv: 1810.09462 [hep-ph] (2019)
- Z. Capatti, V. Hirschi, D. Kermanschah, A. Pelloni, B. Ruijl, Numerical Loop-Tree Duality: contour deformation and subtraction. *JHEP* **04**, 096, arXiv: 1912.09291 [hep-ph] (2020)
- Z. Capatti, V. Hirschi, D. Kermanschah, A. Pelloni, B. Ruijl, Manifestly Causal Loop-Tree Duality. arXiv: 2009.05509 [hep-ph] (Sept. 2020)
- Z. Capatti, V. Hirschi, A. Pelloni, B. Ruijl, Local Unitarity: a representation of differential cross-sections that is locally free of infrared singularities at any order. arXiv: 2010.01068 [hep-ph] (Oct. 2020)

ACKNOWLEDGEMENTS

"[...] I said young man, you can make real your dreams but you've got to know this one thing, no man does it all by himself [...]"

- Village People, YMCA

During my studies, I had the opportunity to interact with many people and greatly benefit from their knowledge. It is because of their willingness to share their experience and collaborate that I was able to reach the results shown here.

One of the first persons that I should thank is Babis Anastasiou. He has always shown great enthusiasm for all the projects I was involved in and believed in me maybe more than myself. He was also very helpful in keeping me focused on what was truly relevant for the computations by giving me his insight into the bigger picture.

During the beginnings of my PhD, I started working together with Bernhard Mistlberger, who thought me to always look for different ways to approach a problem, no matter how hard, and to dive into it with full commitment. Together with Falko Dulat, they showed generous support for a student which was moving his first steps in computing cross-sections and were ready to share with me all their knowledge.

A special thank goes to Caterina Specchia and Simone Lionetti for their warm welcome in the group. They were the first persons with whom I shared the office, and I will always remember with a smile the conversations we had. For sure, it wasn't easy for them to keep up with my endless interruptions with questions about the various projects.

Babis was the first one to push me into investigating ways to compute scalar integrals numerically. What came out of those first attempts is what is presented in the second half of this thesis. The whole project on direct integration would have never been possible if not for the dynamic collaboration with Zeno Capatti, Valentin Hirschi, Dario Kermanschah and Ben Ruijl. The great thing was that we all have different ideas on how to approach the Loop-Tree Duality method, and this has resulted in extremely interesting discussions on the direction we wanted the project to take. I'm looking forward to seeing what the future holds for us.

I'm also grateful to Rayan Haindl for the discussions we had about the removal of local singularities when I was working on the implementation of the numerical integration for amplitudes.

One thing that I particularly enjoyed was begin a TA and having to prepare and show exercises to the students. I found especially fun being the TA for QCD first under Achilleas Lazopoulos and then Vittorio Del Duca, since it allowed me to discuss with them all sorts of exciting aspects of QCD while undergoing the preparation of the exercises.

Last but not least, I want to thank Armin Schweitzer. I really enjoyed our exchanges during and after work. I always knew that I could knock on his door every time I felt like discussing any more or less relevant topic.

CONTENTS

I HIGGS DIFFERENTIAL

1	HIGGS DIFFERENTIAL CROSS SECTIONS	7
1.1	Kinematics	7
1.2	Phase Space	11
1.3	Gluon Fusion	13
1.4	Setup of the Calculation	17
1.4.1	Partonic coefficient function	17
1.4.2	Higgs differential phase space	19
1.5	Regularization of Coefficient Functions	21
1.6	Master Integrals	22
1.6.1	Integration by parts (IBP) identities	24
1.6.2	Lorenz invariance identities	26
1.7	Cutkosky's rule	26
1.8	NNLO Master Integrals	28
1.8.1	Double-real master integrals	29
1.8.2	Real-virtual master integrals	31
1.8.3	Expansion in the dimensional regulator	32
1.9	Numerical results for the Higgs diphoton signal	33
1.10	Conclusion	37
2	THRESHOLD EXPANSION	39
2.1	Rational Function Reconstruction	39
2.1.1	Finite Field	40
2.1.2	Rational Function Reconstruction	42
2.1.3	Chinese Remainder Theorem	46
2.1.4	Rational Reconstruction Theorem	48
2.2	Soft Expansion of Master Integrals	51
2.2.1	Differential Equation	51
2.2.2	One-loop non-planar box expansion	52
2.3	Threshold expansions for Higgs-differential cross-sections	60
2.3.1	Triple-Real threshold expansion	61
2.3.2	Double-Real-Virtual threshold expansion	63

2.4	Validating the Threshold Expansion for differential Observables at NNLO	64
2.5	Approximated N^3 LO Cross Section	69
2.5.1	Exact Scale Variation at N^3 LO	69
2.5.2	Numerical Results for approximate differential Distributions at N^3 LO . .	71
2.6	Conclusion	72
3	RAPIDITY DISTRIBUTION	75
3.1	Threshold Expansion	76
3.2	Exploiting the Divergence Structure	77
3.3	Matching to the Inclusive Cross Section	80
3.4	Phenomenological Results	81
3.5	Stability	83
3.6	Conclusion	85
II	DIRECT INTEGRATION	
4	LOOP-TREE DUALITY	89
4.1	Loop-Tree Duality	90
4.2	Contour Deformation	93
4.2.1	Construction at one loop	96
4.3	Subtraction	104
4.3.1	Regularizing Divergent scalar integrals	104
4.3.2	One-loop amplitudes	109
4.3.3	Divergent one-loop four- and five-point scalar integrals	115
4.3.4	One-loop amplitude for $q\bar{q} \rightarrow \gamma_1\gamma_2$ and $q\bar{q} \rightarrow \gamma_1\gamma_2\gamma_3$	119
4.4	Conclusion	122
5	MANIFESTLY CAUSAL LTD	125
5.1	Algebraic cancellation of spurious singularities	126
5.1.1	Generic case	127
5.1.2	Degenerate case	130
5.1.3	Manifest cancellations for polynomial numerators	131
5.2	Manifestly Causal LTD	133
5.2.1	Multi-loop derivation	134
5.2.2	Loop-by-loop iteration	135
5.2.3	Comparison of the cLTD and LTD representations	139
5.2.4	Numerical stability	140
5.3	Examples	141
5.3.1	One-loop photon self-energy	143
5.3.2	Box topology	145

5.3.3 Sunrise topology	147
5.4 Conclusion	149
III OUTLOOK	
6 CONCLUSION	153
IV APPENDIX	
A FEYNMAN RULES	159
B DIFFERENTIAL EQUATIONS	165
C LTD TABLES AND PROPAGATOR DEFINITIONS	169
D RECURSIVE CANCELLATION OF SPURIOUS SINGULARITIES	181
V REFERENCES	
BIBLIOGRAPHY	187

NOTATION

ABBREVIATIONS AND SYMBOLS

<i>cLTD</i>	manifestly causal LTD
<i>CRT</i>	Chinese remainder theorem
<i>RRT</i>	rational reconstruction theorem
<i>LHC</i>	Large Hadron Collider
<i>LTD</i>	Loop-Tree Duality
\overline{MS}	modified minimal subtraction
<i>LO</i>	Leading order
<i>NLO</i>	next-to-leading order
<i>NNLO</i>	next-to-next-to-leading order
<i>N³LO</i>	next-to-next-to-next-to-leading order
<i>PCF</i>	Parton coefficient function
<i>PDF</i>	Parton distribution function
<i>pQCD</i>	perturbative Quantum Chromodynamics
<i>QCD</i>	Quantum Chromodynamics
<i>QFT</i>	Quantum Field Theory
σ	Hadronic cross section
$\hat{\sigma}$	Partonic cross section
<i>SM</i>	Standard Model
<i>SSB</i>	spontaneous symmetry-breaking
<i>VBF</i>	Vector Boson Fusion

INTRODUCTION

Since the discovery of the first subatomic particle, the electron [7], there has been an enormous evolution in the understanding of ordinary matter. We now know that the electron represents only one of the six flavours of leptons, as presented in the context of the Standard Model of particle physics (SM). The other subatomic particles are organized into quarks which are subject to the strong interaction, and bosons that mediate the different forces of nature. The driving force behind the organization of the interactions between subatomic particles into a theory like the SM has been a tight collaboration between experimentalists and theoreticians. One notable example is the electro-weak interaction, with the massive weak bosons W and Z discovered at CERN by the UA1 and UA2 experiments in 1983 [8, 9], a mass that can be explained by the Standard Model by the introduction of the Brout–Englert–Higgs field. More precisely, these masses are the result of the spontaneous symmetry-breaking (SSB) caused by the vacuum expectation value of Brout–Englert–Higgs field, a process commonly referred to as the Higgs mechanism.

The Higgs mechanism is not only responsible for the masses of the weak bosons, but also for the masses of all the particles with which the Brout–Englert–Higgs field interacts. This field was theorized in 1964 [10–12], while its quantized excitation (Higgs boson), has been identified only in recent years by the ATLAS and CMS experiments [13, 14] with a scalar boson of mass 125GeV. The discovery of the Higgs boson or an equivalent process was a guaranteed outcome for the LHC in order to avoid the violation of unitarity for the WW scattering at high energies. Its discovery is nevertheless an astonishing result, finally obtaining all the ingredients of the SM. By the end of Run 2, not only the Higgs boson was measured with higher accuracy, but also all of the single Higgs production channels were observed, with the latest addition being $t\bar{t}H$ [15].

The standard model, however, is far from being a complete theory of nature as is not able to explain all of the phenomena that we experience. Some examples are the observation of dark matter through its gravitational effects, the oscillation between different flavours of neutrinos due to their masses, the asymmetry between matter and anti-matter, and the absence of gravity among the forces comprehend by the theory [16]. For these reasons, it is of extreme importance

to produce the utmost precise predictions to resolve the SM background and expose any deviation that can be used to constrain its possible extensions.

In the near future, the LHC will be upgraded to its high luminosity version (HL-LHC) designed to reach the target integrated luminosity of 3000fb^{-1} . This will be one order of magnitude higher than the integrated luminosity reached at the end of Run 2. The increased luminosity will have the effect of reducing the experimental uncertainties on many observables. For example, the uncertainty associated with $pp \rightarrow H + X$ is currently at the level of 8% and is expected to reduce at around 3% for the HL-LHC [17, 18].

Our computation for the differential Higgs production has been restricted to the gluon fusion channel. This channel represents the dominant contribution to the Higgs boson cross-section at 13TeV, accounting for more than 88% of the total result. The gluon fusion is loop-induced, in which a fermionic loop mediates the interaction between the Higgs boson and the gluons. As a further simplification, we work in an effective theory (EFT) where the mass of the top quark is taken to be infinite. In this approximation, the gluons interact directly with the Higgs boson, and the remaining five quark flavours are considered massless [19–25]. The same approximation was used to obtain the next-to-next-to-next-to-leading order (N^3LO) inclusive Higgs cross-section, first as an expansion around the production energy of the Higgs boson in 2015 [26] and three years later at all orders in the threshold expansion [27].

With the results presented in the thesis, we move past the inclusive cross-section and compute the differential distribution for the Higgs boson in the threshold expansion approximation. The theoretical uncertainty for the gluon fusion channel is dominated by the scale variation when considering a truncation of the perturbative expansion at next-to-next-to-leading order (NNLO). This uncertainty is reduced by more than 50% for rapidities $|Y| < 3$ when including the N^3LO correction. The reduced uncertainty has two major implications: the first is allowing to make predictions that will be valid also for the increase experimental accuracy achieved by the HL-LHC, the second is bringing the scale variation uncertainty at a level where other uncertainties become relevant (e.g. parton distribution functions [28]).

The analytic computation of the rapidity distribution has been the result of a tremendous effort and was successfully completed only as a threshold expansion. These kind of difficulties are not an anomaly when computing high order corrections. In many cases, the analytic computation of observables for the LHC in perturbative QCD employs well-established techniques that rely on the combination of differential equations and integration by part identities. In particular, the Feynman integrals are expressed as a linear combination of simpler expressions called master integrals [29–50] and then computed by building differential equations in the different scales of the problem [51–70]. These master integrals, when expressed as a series in the

dimensional regulator, take the form of iterated integrals such as harmonic polylogarithms [54] and elliptic functions [68–72].

All of these tools will be rendered inefficient in front of a growing number of scales due to the presence of additional masses or the resolution of additional differential quantities in the final states. It is therefore vital the development of alternative techniques which could help us in the computation of physical observables. One alternative is to employ a more numerical approach to perform the integration over the loop momenta and extract phenomenologically relevant predictions for the LHC also from those processes that are so far prohibitive for a fully analytical approach. There are several alternatives for performing a numerical integration which in essence can be summarized in the fact that they perform a Monte-Carlo integration that relies on an efficient evaluation and sampling of the integrand, whether in Feynman-parameters space [73, 74], four dimensional Minkowski space [75–77], or three-dimensional Euclidean space [78–81].

In this thesis, we focus our attention on the method that uses Loop-Tree duality (LTD), where the integration over the energies of the loop momenta is performed analytically by means of the residue theorem [78–81]. This method has been recently extended to the case of multi-loop scalar integrals, providing an algorithmic way to build the LTD integrand [81, 82]. We show how to endow these multi-loop numerical integrations with a deformation of the loop momenta in order to reproduce the causal prescription of the Feynman propagators, allowing to compute integrals that contain threshold singularities.

The derivation of the Loop-Tree Duality as a sum of cut diagrams is subject to the presence of spurious singularities that can be source of numerical instabilities. These numerical instabilities are particularly severe in the ultraviolet region of integration. To solve this problem, we present a way to analytically combine terms to obtain an expression which is rendered free of all spurious singularities, resulting in a manifestly causal representation of the Loop-Tree Duality (cLTD).

The increased stability of the numerical LTD integration yields a reliable tool that can be implemented for the computation of physical quantities by exploiting the fact that we are working in momentum space. One of these applications is the integration of amplitudes after they have been regulated to remove all the infrared divergences [83]. The full potential is made manifest in the computation of cross-sections. Given a gauge theory, one can combine LTD with reverse unitarity in order to obtain an infrared safe quantity at every point in the integration space. The first application of such cancellations was performed in 1999 in ref. [84] and has been extended to more general cases in ref. [6].

The thesis is organized as follows.

The first part is divided into three chapters. In chapter 1 we present the analytic computation of the Higgs boson differential cross-section up to NNLO in the perturbative expansion. In particular, we present the results for the rapidity and p_T distributions, and obtain all the ingredients contributing to the N³LO computation. In chapter 2 we show how we expand on methods used for the NNLO computation to tackle the N³LO correction, which is performed as a threshold expansion. The chapter concludes with the validation of the threshold expansion for the computation of the rapidity distribution of the Higgs boson. In the last chapter of this first part, namely chapter 3, the threshold series is extended to include six terms from the two computed in chapter 2 and is used to make predictions on the rapidity distribution.

The second part is divided into two chapters. We start by reviewing the LTD method in chapter 4 and present how to supply it with a general deformation of the integration variables to match the Feynman prescription. We then use this deformation for the computation of a physical amplitude by introducing suitable counterterms for the $q\bar{q} \rightarrow \gamma\gamma$ and $q\bar{q} \rightarrow \gamma\gamma\gamma$ processes. In chapter 4 it becomes clear that the numerical instabilities due to the spurious singularities of the LTD integrands can have a harmful impact on the integration. In chapter 5 we address this problem by deriving an alternative representation of LTD where we remove all the spurious singularities and drastically improve the numerical stability.

Part I

HIGGS DIFFERENTIAL



HIGGS DIFFERENTIAL CROSS SECTIONS

The work presented in this chapter consists of the computation of the Higgs-differential cross-section in perturbative QCD. The perturbative series is truncated at NNLO in the strong coupling and was presented for the first time in ref. [1]. The differential distribution for the Higgs boson at NNLO in QCD were already obtained several years ago in refs. [85–88]. More recently, the $pp \rightarrow H + 1 \text{ jet}$ fully differential cross section has been computed at NNLO [89–93]. Combined with the $N^3\text{LO}$ inclusive cross section, this has allowed to compute the $N^3\text{LO}$ Higgs cross section with a jet-veto [94]. This is a first example of a differential cross section in gluon-fusion at this perturbative order. If a fully differential parton-level Monte-Carlo at $N^3\text{LO}$ is achieved in the future, it will become possible to assess the efficiency of the majority of event selection criteria at the same level of accuracy in perturbative QCD as the jet-veto efficiency. To achieve this goal, one could attempt to generalise any of the available methods at NNLO (sector-decomposition [95–98], slicing [85, 99–101], subtraction [102–105], reweighting [106] and other methods [107]) to the next perturbative order. A generalisation of any of these methods would be a formidable task. An intermediate goal could therefore be to compute first some specific differential distributions of particular importance, which are the main ingredients for a fully differential $N^3\text{LO}$ parton-level Monte-Carlo within a slicing method.

Our aim is computing the Higgs cross-section fully differential in all components of the Higgs momentum and its decay products, treating the associated QCD radiation inclusively at NNLO. Moreover, by maintaining the full dependence of the Higgs-differential cross-section on the dimensional regulator we enables the construction of the counter terms for ultraviolet and initial-state collinear divergences at $N^3\text{LO}$.

1.1 KINEMATICS

At the LHC the Higgs boson is produced by colliding two protons at high energy. The production of the boson in most cases will not be an isolated event; instead, there will be

additional radiated particles in the final state. We can schematically represent a general process that contains at least one Higgs boson in the form of an equation:

$$\text{Proton}(P_1) + \text{Proton}(P_2) \rightarrow H(p_h) + X, \quad (1.1)$$

P_1 and P_2 are the momenta of the colliding protons and p_h the momentum of the Higgs boson. All the extra radiations, denoted by X , are treated completely inclusively.

Since the protons are not fundamental particles, their interaction is not explicitly contained in the Standard Model (SM) Lagrangian. In order to make predictions for such scattering processes, we have to look at their constituents, the partons. If the scattering energy is high enough, we can consider the partons within a single proton as non-interacting due to the asymptotic freedom of QCD [108]. These high energies allow to consider the scattering as happening between two partons coming from different hadrons. The probability distribution of finding a specific parton j with fractional momentum $p_j \equiv xP_i$ is encoded in the *parton distribution function* (PDF) $f_{ij}(x, \mu_F)$, where μ_F is the factorization scale separating the hard from the soft-collinear process.

The hard process can be computed using perturbation theory and is described by the partonic cross-section, while the soft radiations with energies below μ_F are ascribed to the PDFs. The parton distribution functions resulting from this separation are process independent and can therefore be fit from different scattering experiments such as DIS or Drell-Yan, and then used for other hard processes. The specific value taken by the distributions will depend on the chosen factorization scale, with a different scale resulting in a different set of PDFs. The evolution between different scales is governed by the Dokshitzer-Gribov-Lipatov-Altarelli-Parisi (DGLAP) equations [109–111].

The computation of the Higgs-differential cross-section gives access to the probabilities related to the observables that solely depend on the four-momentum of the Higgs boson, while all other final state particles in X are treated inclusively. The mass associated with the collective four-momentum of the particles in X depends on the relative collinearity and softness of its constituents. We consider the experimental framework to be symmetric under rotation around its azimuthal angle (i.e. around the beam axis), reducing the number of independent degrees of freedom by one. The observables can then be expressed in terms of the rapidity Y , transverse momentum p_T and mass m_h of the Higgs boson.

The four-momentum p_h can be expressed in full generality in terms of these quantities together with the azimuthal angle ϕ as,

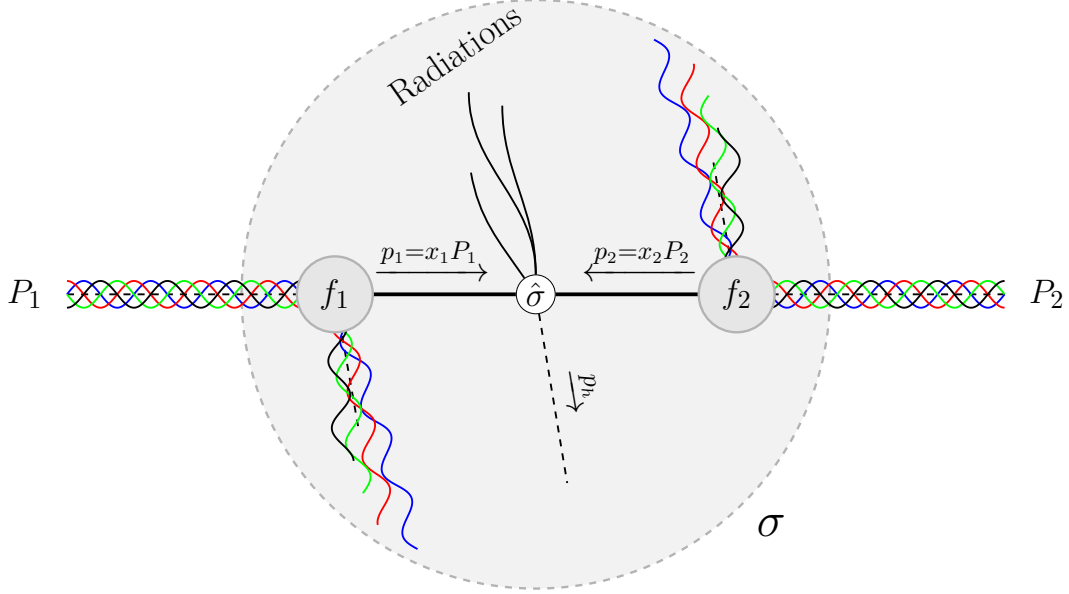


FIGURE 1.1: Schematic representation of a hadron collision where two partons originated by the parent hadrons interact to give rise to the Higgs boson together with radiation particles. The hadronic momenta are represented with capital letters, while the partonic momenta are written in lower-case. The regions of interest for the hadronic and partonic cross-sections are denoted by σ and $\hat{\sigma}$, respectively.

$$p_h \equiv (E, p_x, p_y, p_z) = \left(\sqrt{p_T^2 + m_h^2} \cosh Y, p_T \cos \phi, p_T \sin \phi, \sqrt{p_T^2 + m_h^2} \sinh Y \right), \quad (1.2)$$

where

$$Y = \frac{1}{2} \log \left(\frac{E + p_z}{E - p_z} \right), \quad p_T = \sqrt{E^2 - p_z^2 - m_h^2}. \quad (1.3)$$

E , p_T and p_z are the energy, transverse momentum and momentum along the beam axis, respectively. The Lorentz boost along the z -axis is expressed in terms of rapidity by noticing that $\cosh(Y) = \gamma$ and $\sinh(Y) = \beta\gamma$, where γ is the Lorentz factor and β the boost velocity. The major advantage in describing the boost of the Higgs along the z -axis in terms of the rapidity is that it is an additive quantity when multiple Lorentz boosts are combined.

The rapidity is reference-frame dependent, and it takes a particularly nice form in the hadronic center of mass. With the two protonic momenta being back to back, we obtain:

$$P_1 = \frac{\sqrt{S}}{2}(1, \vec{0}_\perp, 1), \quad P_2 = \frac{\sqrt{S}}{2}(1, \vec{0}_\perp, -1), \quad \Rightarrow \quad \frac{E + p_z}{E - p_z} = \frac{2P_2 p_h}{2P_1 p_h}, \quad (1.4)$$

where $S = (P_1 + P_2)^2$ is the hadronic collision energy. The momenta of the colliding partons are related to the proton momenta by $p_1 = x_1 P_1$ and $p_2 = x_2 P_2$, and can be used to write the rapidity:

$$Y = \frac{1}{2} \log \left(\frac{x_1}{x_2} \cdot \frac{p_2 p_h}{p_1 p_h} \right). \quad (1.5)$$

The bounds of the rapidity can be found by noticing that it reaches its extrema when there is no additional radiation beside p_h , since any additional radiation will reduce the boost in the beam direction due to energy conservation. In this framework one has $p_1 + p_2 + p_h = 0$ with a maximised boost when $x_1 x_2 = \tau$ which results in:

$$\exp(2Y) \in \left[\tau, \frac{1}{\tau} \right], \quad (1.6)$$

where $\tau \equiv \frac{m_h^2}{S}$ is the inelasticity factor measuring the fraction of the total hadronic energy that goes into the creation of the Higgs.

At the core of the predictive power of QCD lies the *factorization theorem* [112], allowing for the independent computation of the PDFs and the hard process. For the Higgs-differential cross-section, we can write, together with the convolution with the PDFs, the integration over the differential quantities. By representing the integration corresponding to some observable \mathcal{O} with the jet function $\mathcal{J}_{\mathcal{O}}$ yields:

$$\begin{aligned} \sigma_{PP \rightarrow H+X}[\mathcal{O}] = \tau \sum_{ij} \int_{\tau}^1 \frac{dz}{z} \int_{\frac{\tau}{z}}^1 \frac{dx_1}{x_1} \int_0^1 dx \int_0^1 d\lambda \int_0^{2\pi} \frac{d\phi}{2\pi} \\ \times f_i(x_1) f_j \left(\frac{\tau}{x_1 z} \right) \frac{1}{z} \frac{d^2 \hat{\sigma}_{ij}}{dx d\lambda} (z, x, \lambda, m_h^2) \mathcal{J}_{\mathcal{O}}(x_1, z, x, \lambda, \phi, m_h^2). \end{aligned} \quad (1.7)$$

where the sum over i and j ranges over all contributing partons. The variables x and λ are related to the more familiar Higgs boson rapidity and transverse momentum by

$$Y = \frac{1}{2} \log \left[\frac{x_1}{x_2} \frac{1 - \frac{\bar{z}\bar{\lambda}}{1 - \bar{z}\lambda x}}{1 - \bar{z}\lambda} \right], \quad p_T^2 = s \frac{\bar{z}^2 \lambda \bar{\lambda} \bar{x}}{1 - \bar{z}x\lambda}. \quad (1.8)$$

where we use the notation $\bar{x} \equiv 1 - x$, $\bar{\lambda} \equiv 1 - \lambda$ and $\bar{z} \equiv 1 - z$.

The advantage of a differential cross section lays in the possibility of going beyond an inclusive quantity, where one integrates over the whole range of possible outcomes, and ask questions about the distribution of the final state. This ability is highlighted in eq.(1.7) by the presence of the measurement function $\mathcal{J}_{\mathcal{O}}(x_1, z, x, \lambda, \phi, m_h^2)$ which acts as a filter, selecting only those region of the phase space which we are of interest. For example, if one wants to compute

the probability for a Higgs boson to be produced in the rapidity interval $Y \in [y_{min}, y_{may}]$, the measurement function would take the form

$$\mathcal{J}_O(x_1, z, x, \lambda, \phi, m_h^2) = \theta(y_{max} - Y(x_1, z, x, \lambda, \phi, m_h^2)) \theta(Y(x_1, z, x, \lambda, \phi, m_h^2) - y_{min}). \quad (1.9)$$

Moreover, the Higgs-differential cross-sections can be combined with subsequent decays of the Higgs boson to allow for the prediction of fiducial cross-sections for Higgs boson decay products as we are going to present at the end of this chapter.

1.2 PHASE SPACE

The strong coupling constant grows smaller as the process energy grows larger, a behaviour that is known as *asymptotic freedom* [113, 114]. The details on its running are outside the scope of this thesis and can be found in many places and are nicely summarized in the Particle Data Group review [16]. What is important is that at high energies the strong coupling becomes small enough, taking a value of $\alpha_s(m_Z) = 0.1181(11)$, allowing for the computation of theoretical predictions in QCD perturbation theory (pQCD).

When considering the partonic cross-section $\hat{\sigma}$ at a given order in pQCD, one has to sum over different contributions that differ by their kinematic configurations. In particular, the perturbative corrections can manifest themselves as being either real or virtual. Each virtual correction corresponds to an additional loop in the Feynman integral compared with the born level cross-section. On the other hand, real corrections correspond to additional particles in the final state. At fix order in pQCD, we can have different combinations of real and virtual correction with their total multiplicity being related to the specific perturbative order. In order to obtain the cross-section, one needs to sum over the different multiplicities that can be written as:

$$\hat{\sigma}_{ij} \approx \sum_m \int d\Phi_{H+m} \mathcal{M}_{ij \rightarrow H+X}, \quad (1.10)$$

were X here represents a set of m final state partons and Φ_{H+m} the corresponding process phase space.

The integration over the phase space for a fixed multiplicity m will lead to a divergent integral when performed in a 4-dimensional space. These local divergences correspond to kinematic configurations where particular propagators become soft and/or collinear, together with the possibility that the matrix element becomes divergent for large loop momenta. We regulate such divergences by relying on dimensional regularization [115, 116].

The expression for the Higgs phase space with m additional massless particles in the final state can be written in d dimensions as:

$$d\Phi_{H+m} = \frac{d^d p_h}{(2\pi)^d} (2\pi)\delta_+(p_h^2 - m_h^2) \left[\prod_{i=3}^{m+2} \frac{d^d p_i}{(2\pi)^d} (2\pi)\delta_+(p_i^2) \right] (2\pi)^d \delta^d \left(p_1 + p_2 + p_h + \sum_{i=3}^{m+2} p_i \right) \quad (1.11)$$

where the distribution δ_+ denotes a Dirac delta function where only the positive energy solution of the on-shell condition is considered,

$$\delta_+(p^2 - m^2) \equiv \theta(-p^0 - m) \delta(p^2 - m^2). \quad (1.12)$$

Being the aim the computation of a cross-section which is differential in the Higgs boson kinematic variables, it is convenient to separate the integration over the phase space of the Higgs from the integration over the radiations. This can be achieved by considering the $2 \rightarrow 1 + m$ scattering as happening in two steps. In the first step, the two incoming partons give rise to two particles, one being the Higgs and the other carrying the collective momentum of all the partons. The latter will then split into m massless elements. The split of the phase space can be represented by the insertion of unity in the form of an integration over Dirac delta functions:

$$1 = \int \frac{d^d k}{(2\pi)^d} (2\pi)^d \delta^d \left(k - \sum_{i=3}^{m+2} p_i \right) \int_0^\infty \frac{d\mu}{2\pi} (2\pi)\delta_+(k^2 - \mu^2). \quad (1.13)$$

Plugging this identity into eq.(1.11) casts the expression in the wished factorized form:

$$d\Phi_{H+m} = \int_0^\infty \frac{d\mu}{2\pi} d\Phi_{HX}(\mu^2) d\Phi_m(\mu^2) \quad (1.14)$$

where,

$$d\Phi_{HX} = \frac{d^d p_h}{(2\pi)^d} (2\pi)\delta_+(p_h^2 - m_h^2) \frac{d^d k}{(2\pi)^d} (2\pi)\delta_+(k^2 - \mu^2) (2\pi)^d \delta^d(p_1 + p_2 + p_h + k), \quad (1.15)$$

$$d\Phi_m = \left[\prod_{i=3}^{m+2} \frac{d^d p_i}{(2\pi)^d} (2\pi)\delta_+(p_i^2) \right] (2\pi)^d \delta^d \left(k - \sum_{i=3}^{m+2} p_i \right). \quad (1.16)$$

From this definition, it is clear that the integration over the additional degrees of freedom, here represented by Φ_m , is not affected by the particular choice of Higgs observable in which we decided to be differential. Any dependence on specific Higgs kinematics is decoupled and only contained into the phase space Φ_{HX} , where the additional final state partons are only present as a collective recoil object with momentum k and mass μ .

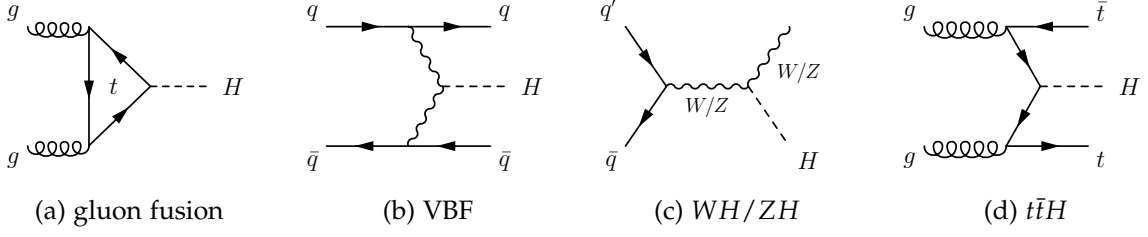


FIGURE 1.2: Feynman diagrams corresponding to the LO contribution to the various production channels for the Higgs Boson.

$S[\text{TeV}]$	ggF	VBF	WH	ZH	ttH	$\sigma_{tot}[pb]$
13	$48.6^{+4.6\%}_{-6.7\%}$	$3.78^{+2.2\%}_{-2.2\%}$	$1.37^{+2.6\%}_{-2.6\%}$	$0.88^{+4.1\%}_{-3.5\%}$	$0.50^{+4.8\%}_{-9.9\%}$	55.1
14	$54.7^{+4.6\%}_{-6.7\%}$	$4.28^{+2.2\%}_{-2.2\%}$	$1.51^{+1.9\%}_{-2.0\%}$	$0.99^{+4.1\%}_{-3.7\%}$	$0.60^{+6.8\%}_{-9.8\%}$	62.1

TABLE 1.1: The different contribution to the inclusive cross section as reported in ref. [16] collecting the results for the LHC for an Higgs boson mass of $m_H = 125\text{GeV}$ from refs. [28, 117–119].

1.3 GLUON FUSION

No theoretical prediction has value if it is not compared with reality through an experiment. In our case, the experimental apparatus is the LHC with particular attention at those processes that create a Higgs boson through the collision of two protons. We can divide into four main categories the production mechanisms that have a single Higgs boson in the final state and are shown in figure 1.2 with their LO diagrams.

With the collision energy at the LHC set at 13TeV, we have that the largest contribution to the cross-section comes from the gluon fusion channel. Other channels ordered by their relative importance are vector boson fusion, associated production with one heavy electroweak boson, and $t\bar{t}H$. The detail of their different contribution to the inclusive cross-section are collected table 1.1 for both 13TeV and 14TeV.

The enhanced contribution of the gluon fusion channel is a consequence of the distribution of partons within the two incoming hadrons. This distribution is shown in figure 1.3, where it becomes clear that the probability of having a gluon taking part in the collision is much higher than for any other parton. When considering a fixed collision energy τ , the probability of two partons to collide can be seen as a function of the partonic centre of mass energy expressed in terms of luminosity:

$$L_{ij}(z) = \int_{\frac{\tau}{z}}^{\frac{\tau}{z}} \frac{dx}{x} f_i(x) f_j\left(\frac{\tau}{z \cdot x}\right), \quad z = \frac{m_h}{s}. \quad (1.17)$$

From the plot in figure 1.4 we can see how, for low partonic energies, the collision probability is greatly enhanced for two gluons. The probability for two gluons is falling faster than the one

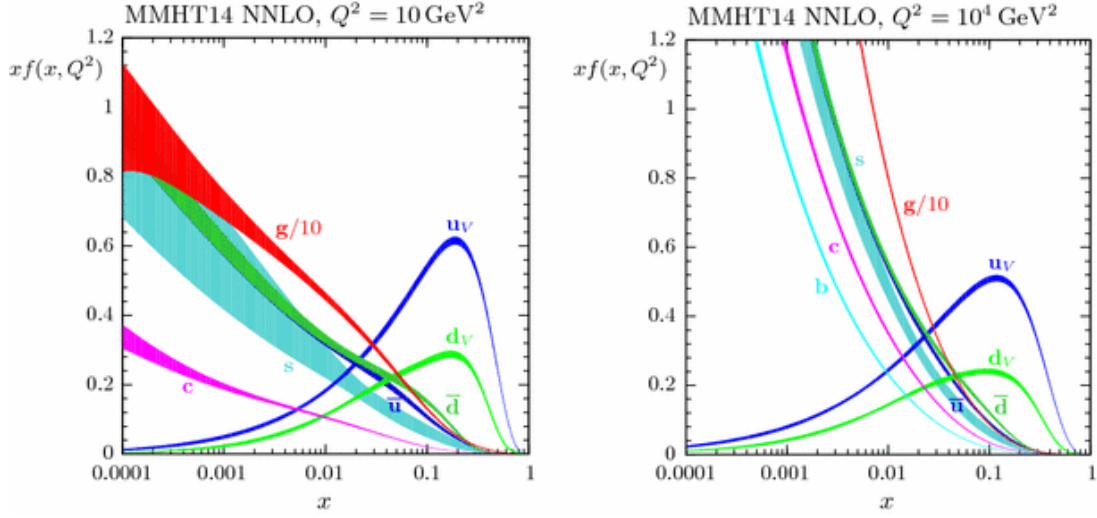


FIGURE 1.3: MMHT2014 NNLO PDFs at a collision energy of $Q^2 = 10 \text{ GeV}^2$ and $Q^2 = 10^4 \text{ GeV}^2$, with associated 68% confidence-level uncertainty bands as presented in ref. [120].

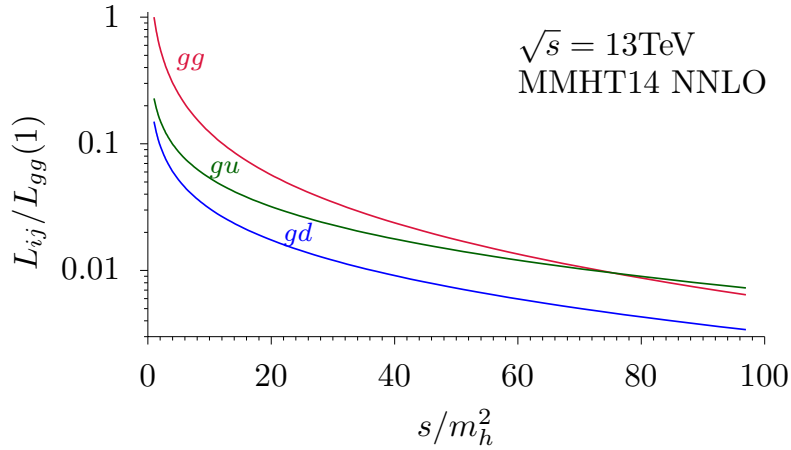


FIGURE 1.4: Plot showing the relative probability of two partons to collide for a collision energy of 13 TeV. The convolution has been done by means of the PDF grid given by MMHT14 from ref. [120] through LHAPDF [121] for the top three collision probabilities where only the mean value of the grid is used.

involving fermions, and they become of the same size around $9m_h$. Since most of the probability is concentrated close to $s = m_h$ we can also understand why the threshold expansion of the Higgs cross-section is such a reliable tool for making predictions.

In the Standard Model (SM) the Feynman rules connecting the quarks and the Higgs field are describe by the Yukawa interaction, where the coupling is directly proportional to the mass of the quark. As a consequence, we have that the top quark represents the primary mediator for the gluon fusion production, having a mass of 172 GeV.

When computing the higher-order corrections to the gluon fusion channel, it becomes challenging to calculate the partonic cross-section with the full top mass dependence. These difficulties arise from the computation of multi-loop integrals in the presence of massive propagators. An approximation that has shown itself to be extremely reliable is to consider the theory in the limit of a top with infinite mass, while all other quarks are massless. This approximation was used for the computation of the inclusive cross section for the gluon fusion channel at NLO [122–124], at NNLO [125–127], and also at N³LO [26, 128]. The results obtained using this effective theory can be improved by rescaling the contribution coming from the LO cross-section by its exact top mass dependence [28]. Through this rescaling, the NNLO cross-section is estimated to have an error due to the infinite top mass limit at the percent level [129, 130]. The uncertainty related to the top mass has been further reduced in ref. [131] by expanding around the top mass threshold and approximating over the whole range by means of the Padé approximation.

The *effective field theory* (EFT) is built by matching the standard model in the infinite top mass limit to the effective lagrangian where the Higgs boson couples directly to the gluons via an effective dimension five operator given by

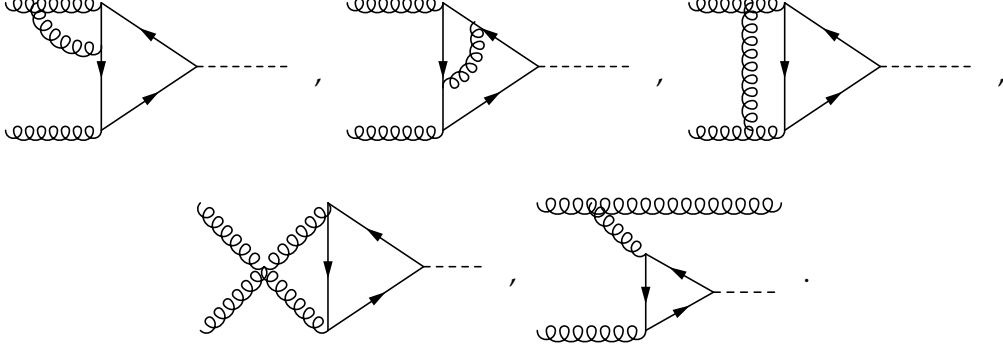
$$\mathcal{L}_{eff} \equiv -\frac{1}{4}C_1 G_{\mu\nu}^a G^{a\mu\nu} H, \quad \text{with} \quad C^0 \equiv \frac{C_1}{v}. \quad (1.18)$$

where is $G_{\mu\nu}^a$ the gluon field strength tensor, a the color index, H the Higgs field, $v \approx 246\text{GeV}$ the vacuum expectation value and C_1 the Wilson coefficient. Because of the presence of the gluon field strength tensor, the effective vertex can have from two to four gluons interacting with the Higgs. The corresponding Feynman rules can be schematically represented as a crossed circle, where at LO can be directly matched to the top quark loop,

$$(1.19)$$

At higher orders, the structure of the interaction is richer, and it is necessary to consider also the corrections due to additional gluons, either as real emission or virtual loops [123]. Some

of the interactions that need to be considered for the α_s^2 correction to the effective vertex are illustrated by the following diagrams:



We can see that the first four diagrams consist of pure virtual corrections and will still be encoded in the same effective vertex as the one shown for the LO case in eq.(1.19). The last diagram is more interesting as it includes a real correction to the LO interaction. The real emission contribution will appear in the effective theory as a 4-point interaction between three gluons and one Higgs boson. The effective lagrangian of eq.(1.18) allows up to 5-point interactions which will appear only when looking at NNLO or higher corrections. All the corresponding Feynman rules are shown in appendix A.

The Wilson coefficient corresponding to the infinite top mass limit has been computed up to four loops in refs. [20, 22, 132, 133]:

$$\begin{aligned}
C_1(\mu^2) = & -\frac{\alpha_s}{3\pi} \left\{ 1 + \frac{11}{4} \frac{\alpha_s}{\pi} + \left(\frac{\alpha_s}{\pi}\right)^2 \left[\frac{19}{16} L_t + \frac{2777}{288} + N_F \left(\frac{1}{3} L_t - \frac{67}{96} \right) \right] \right. \\
& + \left(\frac{\alpha_s}{\pi}\right)^3 \left[\frac{897943}{9216} \zeta_3 + \frac{209}{64} L_t^2 + \frac{1733}{288} L_t - \frac{2892659}{41472} \right. \\
& + N_F \left(-\frac{110779}{13824} \zeta_3 + \frac{23}{32} L_t^2 + \frac{55}{54} L_t + \frac{40291}{20736} \right) \\
& \left. \left. + N_F^2 \left(-\frac{1}{18} L_t^2 + \frac{77}{1728} L_t - \frac{6865}{31104} \right) \right] + \mathcal{O}(\alpha_s^4) \right\}, \tag{1.20}
\end{aligned}$$

where $\alpha_s \equiv \alpha_s(\mu)$ is the \overline{MS} strong coupling constant, $n_f = 5$ is the number of effective flavours after the absorption of the top quark into the effective Lagrangian, and $L_t \equiv \log\left(\frac{\mu^2}{m_t^2}\right)$ with μ the renormalization scale.

1.4 SETUP OF THE CALCULATION

For the production of a Higgs boson with the observed mass of $m_h = 125\text{GeV}$ with a transverse momentum below the top-pair threshold, the process can be safely described in terms of the EFT where the top quark is infinitely heavy. The Higgs-differential partonic cross-section can be written in the following form,

$$\frac{1}{z} \frac{d^2 \hat{\sigma}_{ij}}{dx d\lambda} = (C^0)^2 \hat{\sigma}_0 \eta_{ij}(z, x, \lambda) \quad (1.21)$$

$$= (C^0)^2 \hat{\sigma}_0 \sum_{k=0}^{\infty} \left(\frac{\alpha_S}{\pi} \right)^k \eta_{ij}^{(k)}(z, x, \lambda), \quad (1.22)$$

where η_{ij} denotes the partonic coefficient function (PCF), that is obtained by factorizing out the Born cross section,

$$\hat{\sigma}_0 = \frac{\pi}{8(n_c^2 - 1)}. \quad (1.23)$$

This expression represents the starting point of the computation. In this section, we will define more precisely the partonic coefficient function for the differential cross-section and then transform the phase space to adapt to the differential variables used to describe the system.

1.4.1 Partonic coefficient function

The PCF corresponding to the n -th order in the perturbative expansion can be written explicitly as:

$$\eta_{ij}^{(n)}(z, x, \lambda) = \frac{N_{ij}}{2m_h^2 \sigma_0} \sum_{m=0}^n \int d\Phi_{H+m} \delta \left(x - \frac{s(p_1 + p_2 + p_h)^2}{(s + 2p_1 \cdot p_h)(s + 2p_2 \cdot p_h)} \right) \times \delta \left(\lambda - \frac{s + 2p_1 \cdot p_h}{s - m_h^2} \right) \mathcal{M}_{ij \rightarrow H+m}^{(n)}. \quad (1.24)$$

where $\mathcal{M}_{ij \rightarrow H+m}^{(n)}$ is the modulus squared of the amplitudes proportional to α_S^n for partons i and j producing a final state Higgs boson and m partons summed over polarizations and colours. To obtain the n -th order correction to the partonic coefficient function, one has to consider all the l -loop matrix elements with m final state partons such that that $m + l = n$. In the above, we impose the choice of differential variables defined in eq.(1.8) employing explicit delta function acting on the phase space Φ_{H+m} . This choice of variable can be better understood if

one considers the collective radiated momentum $k = -\sum_{i=3}^{m+1} p_i$ as defined in eq.(1.13) to be parametrized by \bar{z} , λ , $\tilde{\lambda}$ and k_\perp :

$$k = -\bar{z} (\lambda p_1 + \tilde{\lambda} p_2 + k_\perp). \quad (1.25)$$

with $p_{1,2}$ being the momenta of the two incoming partons with a center of mass energy of $(p_1 + p_2)^2 = s$. In this explicit parametrization, one can see how the variable \bar{z} is related to the distance from the threshold energy for the Higgs production, with the limit $\bar{z} = 0$ corresponding to the radiation X becoming soft. Moreover, from momentum conservation, it follows that the transverse component of k is equal and opposite to p_T , provided that we work in the rest frame of the collision. The parameter $\tilde{\lambda}$ can be easily replaced by the introduction of an alternative variable x that relates directly to the relative hardness of the extra radiation via,

$$k^2 = x\lambda\tilde{\lambda}\bar{z}^2 \quad (1.26)$$

The new set of variables x , λ and z can be defined in terms of scalar products as

$$x = \frac{s k^2}{(2k \cdot p_1)(2k \cdot p_2)}, \quad \lambda = -\frac{2k \cdot p_2}{s - m_h^2}, \quad z = \frac{p_h^2}{s}. \quad (1.27)$$

These variables have the advantage of developing physical singularities independently, a property that will be discussed in more details in the next section.

At any order in perturbation theory it is possible to categorize the initial state configurations in 6 different groups involving different combinations of partons:

$$\begin{aligned} g(p_1) + g(p_2) &\rightarrow H(p_h) + X \\ q(p_1) + g(p_2) &\rightarrow H(p_h) + X \\ g(p_1) + q(p_2) &\rightarrow H(p_h) + X \\ q(p_1) + \bar{q}(p_2) &\rightarrow H(p_h) + X \\ q(p_1) + q(p_2) &\rightarrow H(p_h) + X \\ q(p_1) + q'(p_2) &\rightarrow H(p_h) + X \end{aligned} \quad (1.28)$$

In the above g , q , \bar{q} and q' represent a gluon, a quark, an anti-quark and a quark with a different flavour respectively. From the configuration above, one can obtain all other combinations of

explicit (anti-)quark flavours and gluons. The initial state dependent factors N_{ij} in eq.(1.24) can be explicitly written for all the specific cases and are given by:

$$\begin{aligned} N_{gg} &= \frac{1}{4(1-\epsilon)^2(n_c^2-1)^2}, \\ N_{gq} &= N_{qg} = \frac{1}{4(1-\epsilon)(n_c^2-1)n_c}, \\ N_{q\bar{q}} &= N_{q\bar{q}} = N_{q\bar{q}'} = \frac{1}{4c^2}. \end{aligned} \quad (1.29)$$

To obtain all the contributing Feynman diagrams required for computing the n -th order correction to the gluon fusion channel, we generate all the relevant graphs using QGRAF [134]. Since in $\mathcal{M}_{ij \rightarrow H+m}^{(n)}$ we are summing over all polarizations, we do not have any open index. We perform all the algebraic operation involving traces over spinor and colour indices using FORM [135].

1.4.2 Higgs differential phase space

We now consider the phase space discussed in section 1.2 in the context of a differential cross-section as defined in eq.(1.24). More precisely, we want to cast the Higgs dependent phase space Φ_{HX} as an integration over the differential variables by explicitly absorbing the Dirac delta functions.

We can take advantage of the fact that the variables we want to map to only depend on the energy, z -component and the magnitude of the transverse momentum of k as made explicit in eq.(1.25). First, we notice that we can rewrite the d -dimensional integration measure for some momentum p as follows:

$$\frac{d^d p}{(2\pi)^d} = \frac{1}{(2\pi)^d} dE d p^z d^{d-2} p^\perp = \frac{1}{2(2\pi)^d} dE d p^z d|p^\perp|^2 d\Omega_{d-2} \left(|p^\perp|^2\right)^{\frac{d}{2}-2}. \quad (1.30)$$

Then we take the definition of Φ_{HX} and remove p_h by solving the momentum conservation condition, and replace the remaining measures with the above parametrization:

$$\begin{aligned} d\Phi_{HX} &= \frac{(2\pi)^{2-d}}{2} dE_k d k^z d|k^\perp|^2 d\Omega_{d-2} \left[(k^\perp)^2\right]^{\frac{d}{2}-2} \\ &\quad \times \theta(-E_k - \mu) \theta(E_k + \sqrt{s} - m_h) \delta(k^2 - \mu^2) \delta(s + 2p_{12}k + k^2 - m_h^2). \end{aligned} \quad (1.31)$$

The integration over k^\perp is performed by resolving the on-shell condition, giving as result $|k^\perp|^2 = E_k^2 - (k^z)^2 - \mu^2$. By means of eq.(1.27), we can rewrite the integral in terms of λ , $\tilde{\lambda}$ and x . The integration measure is transformed under the change of variables as:

$$dE_k dk^z = s \bar{z}^2 d\lambda d\tilde{\lambda}. \quad (1.32)$$

While the scalar products can be written as follows:

$$\begin{aligned} 2p_1 \cdot k &= -s \bar{z} \tilde{\lambda}, & |k^\perp|^2 &= (1-x) \bar{z}^2 \lambda \tilde{\lambda}, \\ 2p_2 \cdot k &= -s \bar{z} \lambda, & \mu^2 &= x \bar{z}^2 \lambda \tilde{\lambda}. \end{aligned}$$

where we hide the dependence in μ into the variable x . Thus the phase space becomes:

$$\begin{aligned} d\Phi_{HX} &= \frac{(2\pi)^{2-d}}{4} s \bar{z}^2 d\lambda d\tilde{\lambda} d\Omega_{d-2} [s \bar{z}^2 \lambda \tilde{\lambda} (1-x)]^{\frac{d}{2}-2} \theta(s \bar{x} \bar{z}^2 \lambda \tilde{\lambda}) \\ &\quad \times \theta(-E_k - \mu) \theta(E_k + \sqrt{s} - m_h) \delta(s \bar{z} (1 - \lambda - \tilde{\lambda} (1 - \bar{z} \lambda x))). \end{aligned} \quad (1.33)$$

We can then integrate out the dependence in $\tilde{\lambda}$ and solve the θ constrains for the new set of variables obtaining:

$$\begin{aligned} d\Phi_{HX} &= \frac{(2\pi)^{2-d}}{4} s^{\frac{d}{2}-2} \bar{z}^{d-3} d\lambda d\Omega_{d-2} (\lambda(1-\lambda))^{\frac{d}{2}-2} (1-x)^{\frac{d}{2}-2} (1-\bar{z}\lambda x)^{1-\frac{d}{2}} \\ &\quad \times \theta(\lambda) \theta(1-\lambda) \theta(1-x) \theta(\bar{z}) \theta(s). \end{aligned} \quad (1.34)$$

By plugging this result into the factorized phase space presented in eq.(1.14) we translate the implicit dependence of μ in x :

$$\begin{aligned} d\Phi_{H+m} &= \int_0^\infty \frac{d\mu}{2\pi} d\Phi_{HX} d\Phi_m \\ &= \frac{s^{\frac{d}{2}-1}}{4(2\pi)^{d-1}} \bar{z}^{d-1} d\lambda d\Omega_{d-2} \theta(\bar{z}) \theta(s) \int dx \theta(x) \theta(1-x) \theta(\lambda) \theta(1-\lambda) \\ &\quad \times (\lambda(1-\lambda))^{\frac{d}{2}-1} (1-x)^{\frac{d}{2}-2} (1-\bar{z}\lambda x)^{-\frac{d}{2}} d\Phi_m. \end{aligned} \quad (1.35)$$

The analytic partonic coefficient functions for Higgs-differential cross-sections are now obtained by performing the integration of the squared matrix over the m -parton final state elements using the above measure.

1.5 REGULARIZATION OF COEFFICIENT FUNCTIONS

The PCFs contain single poles in the variables \bar{z} , x , and λ . They correspond to vanishing transverse momentum for the Higgs boson or vanishing virtuality of the system of associated radiations. The set of such singularities reads:

$$\left\{ \bar{z}^{-1+a_1\epsilon}, x^{-1+a_2\epsilon}, (1-x)^{-1+a_3\epsilon}, \lambda^{-1+a_4\epsilon}, (1-\lambda)^{-1+a_5\epsilon} \right\}, \quad (1.36)$$

where the coefficients a_i are small integer numbers. It may happen that one or more of these singularities lay within the integration volume of a given observable. For example, it is the case when computing the rapidity distribution or the inclusive cross-section for the Higgs boson. In order to regulate them, we proceed as in ref. [1].

Consider a function $f(x) = x^{-1+a\epsilon} f_h(x)$, for some integer a and with $f_h(x)$ holomorphic around $x = 0$. We are interested in integrating the function over a test function $\phi(x)$ on the range $[0, 1]$. In the case of our Higgs-differential cross-section, the test function $\phi(x)$ corresponds to the product of the parton luminosity and the measurement function. The divergence at $x = 0$ can be extracted explicitly from the integral:

$$\begin{aligned} \int_0^1 dx f(x) \phi(x) &= \int_0^1 x^{-1+a\epsilon} f_h(x) \phi(x) \\ &= \int_0^1 dx x^{-1+a\epsilon} [f_h(x) \phi(x) - f_h(0) \phi(0)] + \frac{1}{a\epsilon} f(0) \phi(0). \end{aligned}$$

We now want to give an expression for the partonic cross-section that is finite even if all-inclusive integrations are performed. To this end we define in a slight abuse of notation,

$$f_s(0) \equiv \delta(x) \left[x^{-1+a\epsilon} - \frac{1}{a\epsilon} \right] f_h(0). \quad (1.37)$$

Here the δ -distribution is to be understood as acting only on the test function and not on its coefficient in the square bracket. It is easy to see that $f_s(0)$ integrates to zero. We can therefore regulate the integrand $f(x)$ by subtracting $f_s(0)$,

$$I = \int_0^1 dx f(x) \phi(x) = \int_0^1 dx (f(x) - f_s(0)) \phi(x), \quad (1.38)$$

so that every term of its ϵ expansion can be integrated numerically.

In the particular case of the Higgs-differential cross-section, we need to regulate potential end-point divergences in the three remaining variables \bar{z} , x and λ , c.f. eq. (1.7). We define the distributions σ_s that subtract the limits of $\sigma(\bar{z}, x, \lambda)$ and label them by the kinematic limit of the cross-section that they reproduce. For example, $\sigma_s(\bar{z}, 0, \lambda)$ takes care of the limit for the

cross-section as x goes to zero, meaning that everything but the regulated pole in ϵ is evaluated at $x = 0$. After partial-fractioning, to avoid simultaneous singularities on both end-points of the integral, we obtain the following decomposition,

$$\begin{aligned} \sigma_f(\bar{z}, x, \lambda) &\equiv \sigma(\bar{z}, x, \lambda) - \sigma_s(\bar{z}, x, 1) - \sigma_s(\bar{z}, x, 0) - \sigma_s(\bar{z}, 1, \lambda) - \sigma_s(\bar{z}, 0, \lambda) - \sigma_s(0, x, \lambda) \\ &+ \sigma_s(\bar{z}, 1, 1) + \sigma_s(\bar{z}, 1, 0) + \sigma_s(\bar{z}, 0, 1) + \sigma_s(\bar{z}, 0, 0) + \sigma_s(0, x, 1) + \sigma_s(0, x, 0) \\ &+ \sigma_s(0, 1, \lambda) + \sigma_s(0, 0, \lambda) - \sigma_s(0, 1, 1) - \sigma_s(0, 1, 0) - \sigma_s(0, 0, 1) - \sigma_s(0, 0, 0). \end{aligned} \quad (1.39)$$

More generally one can treat the case of n variables x_i that have each a set of limits \mathbf{a}_i . To produce the correct finite expression one has to consider all the limits and their combinations. This procedure can be summarized in a compact form by

$$\sigma_f(x_1, \dots, x_n) = \left[\prod_{i=1}^n \left(1 - \sum_{a \in \mathbf{a}_i} \lim_{x_i \rightarrow a} \right) \right] \sigma_s(x_1, \dots, x_n). \quad (1.40)$$

The limit appearing in this expression has to be applied to the arguments of the function σ_s as opposite to its content. It is then straight forward to insert the single limit for \bar{z} and the two end-point limits for λ and x to obtain all the 18 terms that are shown in eq.(1.39) with the correct relative signs.

1.6 MASTER INTEGRALS

As mentioned before, to compute all the relevant Feynman diagrams necessary for the computation of the N³LO correction to the Higgs differential cross-section, we use QGRAF [134] and then perform all the spinor and colour algebra by means of a private code written in FORM [135]. The final result of this procedure is a set of integrals consisting of a product of squared propagators at the denominator and a combination of scalar products at the numerator. To be able to compute the double-differential cross-section, it is crucial to reduce the number of integrals that appear in the final expression, which is of the order of thousands at NNLO and 10⁵ when considering N³LO.

The first step is casting each diagram in terms of a set of linearly independent propagators by means of partial fractioning. Assuming we have an integral described by a set of n propagators D_i which are linearly dependent, we can then write:

$$\sum_{i=1}^n \beta_i D_i = 0 \quad \Rightarrow \quad 1 = \frac{\sum_{i=2}^n \beta_i D_i}{\beta_1 D_1}. \quad (1.41)$$

By applying this identity to the integrand, we will obtain a sum of integrals that depend on $n - 1$ denominators. The procedure is repeated till all the integrands are written in terms of linearly independent propagators.

The second step consists of writing the scalar products appearing at the numerator in terms of squared propagators. To this end, we notice that for a given set of kinematics with E independent external momenta and L loops, the number of the linearly independent propagator is bounded. In particular, the number of possible scalar propagator that involve at least one loop momentum corresponds to $N_t = E \cdot L + \frac{L(L+1)}{2}$. By taking advantage of this, one can cast any scalar product that appears at the numerator as a linear combination of a completed and independent set of propagators of size N_t , leaving us with scalar integrals of the form:

$$I_{(v_1, v_2, \dots, v_{N_t})} = \int \left[\prod_{i=1}^L \frac{d^d l_i}{(2\pi)^d} \right] \prod_{j=1}^n \frac{1}{D_j^{v_j}}. \quad (1.42)$$

where $v_i \in \mathbb{Z}$, and the denominators D_j of the form:

$$D_j = \left(\sum_{i=1}^L \alpha_{ji} l_i + \sum_{i=1}^E \beta_{ji} p_i + m_j \right)^2. \quad (1.43)$$

All the integrals that can be described by the same set of propagators D_i differing only in their powers v_i are said to correspond to the same *topology*.

By exploring the invariance of the integral under transformations of the loop momenta, one can find that two topologies are isomorphic to one another and can be merged. Additional symmetries can be applied to map different topologies into each other, for example by an exchange of the external kinematics like $p_1 \leftrightarrow p_2$. The resulting integrals can be computed analytically in the context of a different, isomorphic, topology with the only condition that at the end we swap back the definitions of the external momenta.

By mapping different topologies into each other, we are able to reduce the number of integrals. However, in most practical cases, this number remains too large or involves integrals which are too difficult to be computed analytically. The success of many high-order computations in QCD is due to reducing this problem to a smaller set of Master Integrals (MI) by means of the application of integration by part identities (IBP). There are several public tools to perform this reduction to master integrals; some notable examples are refs. [42, 43, 48]. The implementation of the Laporta algorithm [136] is very demanding in computing power. For the case of the N³LO Higgs-differential cross-section as computed in refs. [2, 3], a direct reduction was unfeasible due to the complexity of the coefficients involved. To recover the coefficients describing the reduction to master integrals, we had to rely on multiple evaluations over

different finite fields and then reconstruct the expressions. The details of this procedure will be discussed in the next chapter.

1.6.1 Integration by parts (IBP) identities

The IBP identities have been a reliable and successful tool to rewrite scalar integrals in terms of master integrals. These identities arise from exploiting the condition that in dimensional regularisation our functions have to vanish on the contour at infinity. This translates into the following relation [29, 30, 115]:

$$\int \frac{d^d l}{(2\pi)^d} \frac{\partial}{\partial l^\mu} F(l, \{p_i\}) = 0, \quad (1.44)$$

where the function F can be any combination of propagators, scalar products and loop momentum vectors. For the case of several loops, one can build a set of relations that connect different integrals $I_{(\nu_1, \dots, \nu_{N_l})}$ within the same topology by acting with different derivative and vector structures:

$$\int \left(\prod_{k=1}^L l_k \right) \frac{\partial}{\partial l_q^\mu} \left(l_r^\mu \prod_{m=1}^M \frac{1}{[D_m(\{p_i \cdot l_j\}, \{l_i \cdot l_j\}, m_j)]^{d_m}} \right), \quad q, r \in \{1, \dots, L\} \quad (1.45a)$$

$$\int \left(\prod_{k=1}^L l_k \right) \frac{\partial}{\partial l_q^\mu} \left(p_r^\mu \prod_{m=1}^M \frac{1}{[D_m(\{p_i \cdot l_j\}, \{l_i \cdot l_j\}, m_j)]^{d_m}} \right), \quad \begin{array}{l} q \in \{1, \dots, L\} \\ r \in \{1, \dots, E\}, \end{array} \quad (1.45b)$$

The number of identities that can be written with this procedure depends on the number of linearly independent external momenta p_i and loop momenta l_i . In the case of L loops and E independent external momenta, we obtain a total of $L \cdot (L + E)$ different identities.

EXAMPLE

Let us consider the simple example of the massless triangle, whose topology is defined by the scalar integral:

$$Tri((p_1 + p_2)^2; \nu_1, \nu_2, \nu_3) = \int \frac{d^d l}{i\pi^{\frac{d}{2}}} \frac{1}{l^{2\nu_1} (l + p_1)^{2\nu_2} (l + p_1 + p_2)^{2\nu_3}}, \quad p_1^2 = p_2^2 = 0.$$

The case where all the ν_i 's are 1 can be easily solved in terms of a bubble by summing the single IBP identity coming from eq.(1.45a) together with the one corresponding to eq.(1.45b) with $r = 1$, yielding:

$$\text{Triangle}(p_1, p_2) = \frac{2}{d-4} \text{Bubble}(p_{12})$$

This can be checked against the explicit integration of the triangle and the bubble performed by using Feynman parameters. In the case of the triangle, we restrict to the case at hand where all the propagators come with a unit power:

$$\text{Tri}((p_1 + p_2)^2; 1, 1, 1) = ((p_1 + p_2)^2)^{-1-\epsilon} \frac{1}{\epsilon^2} \frac{\Gamma(1-\epsilon)^2 \Gamma(1+\epsilon)}{\Gamma(1-2\epsilon)} \quad (1.46)$$

For the bubble, we are going to integrate the corresponding expression in the case of general powers for the two denominators:

$$\begin{aligned} \text{Bub}(p^2; \nu_1, \nu_2) &= \int \frac{d^d l}{i\pi^{d/2}} \frac{1}{[l^2]^{\nu_1} [(l+p)^2]^{\nu_2}} \\ &= (p^2)^{\frac{d}{2}-\nu_1-\nu_2} (-1)^{\frac{d}{2}} \frac{\Gamma(\nu_1 + \nu_2 - \frac{d}{2}) \Gamma(\frac{d}{2} - \nu_1) \Gamma(\frac{d}{2} - \nu_2)}{\Gamma(\nu_1) \Gamma(\nu_2) \Gamma(d - \nu_1 - \nu_2)}, \end{aligned} \quad (1.47)$$

where we can see that the relation between the two integrals is indeed correct.

This generic bubble integral is all one needs in order to compute any massless triangle. This can be shown by summing the same two IBP identities as before, but this time for generic exponents ν_i 's. The result can be represented in a diagrammatic way as follows:

$$\text{Triangle}(\nu_1, \nu_2, \nu_3) = \frac{1}{d - \nu_1 - 2\nu_2 - \nu_3} \left(\nu_3 \times \text{Bubble}(\nu_3, \nu_1) + \nu_1 \times \text{Bubble}(\nu_3, \nu_1 + 1) \right),$$

where the exponent corresponding to each propagator is written on its side. It is clear from this identity that is always possible to make the propagator with power ν_2 disappear ($\nu_2 = 0$). By removing one propagator from the massless triangle, we are reducing the problem to a linear combination of bubble integrals with different powers ν_i as expected.

1.6.2 *Lorentz invariance identities*

There is also another family of identities that can be used to relate different diagrams within the same topology. These identities exploit the fact that any integral whose elements are all expressed in terms of scalar products is invariant under Lorentz transformations.

Let us consider the infinitesimal version of a Lorentz transformation:

$$p^\mu \rightarrow p^\mu + \delta\epsilon_\nu^\mu p^\nu, \quad \delta\epsilon_\nu^\mu = -\delta\epsilon_\mu^\nu, \quad (1.48)$$

where $\delta\epsilon_\nu^\mu$ is an antisymmetric tensor. The invariance of an integral $I(p_1, \dots, p_n)$ can then be translated into the following condition:

$$\delta\epsilon_\nu^\mu \left[\sum_{i=1}^n \left(p_i^\nu \frac{\partial}{\partial p_i^\mu} - p_i^\mu \frac{\partial}{\partial p_i^\nu} \right) \right] I(p_1, \dots, p_n) = 0. \quad (1.49)$$

Using the fact that this condition must hold for any arbitrary choice of Lorentz transformation leads to the production of 6 identities. In ref. [37] was shown that the Lorentz invariance identities could be expressed as a combination of IBP identities. Despite being redundant, they can still be useful during the reduction to MI providing alternative representations of the relations between integrals.

1.7 CUTKOSKY'S RULE

The reduction to master integrals by means of the IBPs identities is a formidable tool which shows its full potential when combined with *reverse unitarity* [86, 126, 137–139]. This method has already been successfully used in the computation of the inclusive Higgs cross-section [26, 128, 140–145]. In this framework one casts the on-shell delta functions appearing in the phase space of eq.(1.11) as propagators, allowing to use the reduction machinery directly to the matrix elements.

In order to illustrate the procedure, let us consider the simple case of the LO cross-section for the Higgs as computed in the infinite top mass effective theory. The partonic cross-section $\sigma_{gg \rightarrow H}$ in the collision rest frame is written as the integration of the tree-level amplitude squared:

$$\sigma = \frac{1}{2S} \int \Phi_H |\mathcal{A}|^2, \quad (1.50)$$

where S is the energy of the process, Φ_H the phase space and \mathcal{A} the amplitude. In this simple case the phase space becomes:

$$d\Phi_H = \frac{d^d p_h}{(2\pi)^d} (2\pi) \delta_+(p_h^2 - m_h^2) (2\pi)^d \delta^d(p_1 + p_2 + p_h). \quad (1.51)$$

At leading order in EFT the only contribution to the amplitude comes from the three-point interaction between the two incoming gluons and the Higgs. The cross-section is then given by:

$$2S \sigma = \int \Phi_H \left(\underbrace{\left(\begin{array}{c} \text{diagram 1} \\ \text{---} \\ \text{diagram 2} \end{array} \right)}_{\mathcal{A}} \right) \left(\underbrace{\left(\begin{array}{c} \text{diagram 3} \\ \text{---} \\ \text{diagram 4} \end{array} \right)}_{\mathcal{A}^*} \right) =: \text{diagram 5} \cdot \text{diagram 6}. \quad (1.52)$$

The integration over the final particle phase space, here represented by a single Higgs, is being replaced by a forward scattering with the addition of a dashed line across the particle that has to be considered on-shell. The d -dimensional delta function that imposes energy-momentum conservation is solved by imposing that the final state satisfies $p_h = p_1 + p_2$.

This procedure can be extended to more complicated diagrams, that may include multiple particles in the final state. By means of the Cutkosky's rule [146] we express the on-shell constraints appearing in phase space integrals as cut propagators:

$$\delta_+(q^2) \rightarrow \left[\frac{1}{q^2} \right]_c = \frac{1}{2\pi i} \text{Disc} \left(\frac{1}{q^2} \right) = \frac{1}{2\pi i} \left(\frac{1}{q^2 + i0} - \frac{1}{q^2 - i0} \right). \quad (1.53)$$

The Cutkosky's rule can be used to "glue" together the two ends of the diagrams that interfere in \mathcal{M} , which can be represented as:

$$\int d\Phi \left| \begin{array}{c} \text{diagram 7} \\ \text{---} \\ \text{diagram 8} \end{array} \right|^2 \equiv \text{diagram 9} \cdot \text{diagram 10}.$$

The reduction to master integrals can be applied directly to the integral appearing on the right-hand side by noticing that the cut propagators can be differentiated similarly as ordinary propagators,

$$\frac{\partial}{\partial q_\mu} \left(\left[\frac{1}{q^2} \right]_c \right)^v = -v \left(\left[\frac{1}{q^2} \right]_c \right)^{v+1} 2q^\mu. \quad (1.54)$$

The fact that the cut propagator represents a delta function is reflected by the constraint that any integral containing a cut propagator raised to a negative power must vanish:

$$\left(\left[\frac{1}{q^2} \right]_c \right)^{-n} = 0 \quad \text{for} \quad n \geq 0, \quad (1.55)$$

which simplifies the reduction.

In refs. [86, 138, 139], it was introduced a modification of the reverse unitarity framework in order to allow for the computation of differential quantities, such as the rapidity distribution. Here we want to be fully differential in the Higgs momentum. Effectively, we apply reverse unitarity treating p_h as an additional external momentum together with p_1 and p_2 . After factorizing the phase space one may write:

$$\hat{\sigma}_{ij}(S, x, \lambda, m_h^2) \sim \sum_m \int_0^\infty \frac{d\mu^2}{2\pi} d\Phi_{HX} \times \underbrace{\left[\int d\Phi_m \mathcal{M}_{ij \rightarrow H+X} \right]}_{\text{Reverse Unitarity}}. \quad (1.56)$$

The explicit factorization of the Higgs boson phase space and the QCD radiation phase space achieved by eq.(1.35) allows us to use different methods for the two phase spaces without having to renounce to any of the differential quantities relative to the Higgs boson. The analytic integration over the QCD radiation is performed inclusively in *conventional dimensional regularization* (CDR) [116, 147], where the matrix elements, as well as the integration over the phase space, are calculated in d -dimensions. This differs from the 't Hooft Veltman dimensional regularization (HV) [115] in the fact that the latter treats the observed states as four-dimensional while CDR treats all the states as being d -dimensional. The latter leads to a more convenient computational framework when dealing with infrared divergencies on the external momenta. In both these prescriptions, it is possible to maintain a 4-dimensional spinor space. Then, in CDR, the fermions still have two polarizations, while the gluons have $d - 2$ spin degrees of freedom.

1.8 NNLO MASTER INTEGRALS

In this section, we elaborate on the computation of the master integrals that serve as building blocks for our partonic cross-section at NNLO. To validate our results, we follow two different strategies. The first is based on the method of differential equations as described in refs. [51, 52, 56] to express the master integrals as a Laurent series in the dimensional regulator ϵ whose coefficients are written in terms of harmonic polylogarithms or more generally elliptic functions. The second approach is based on the direct evaluation of phase space and loop integrals. As

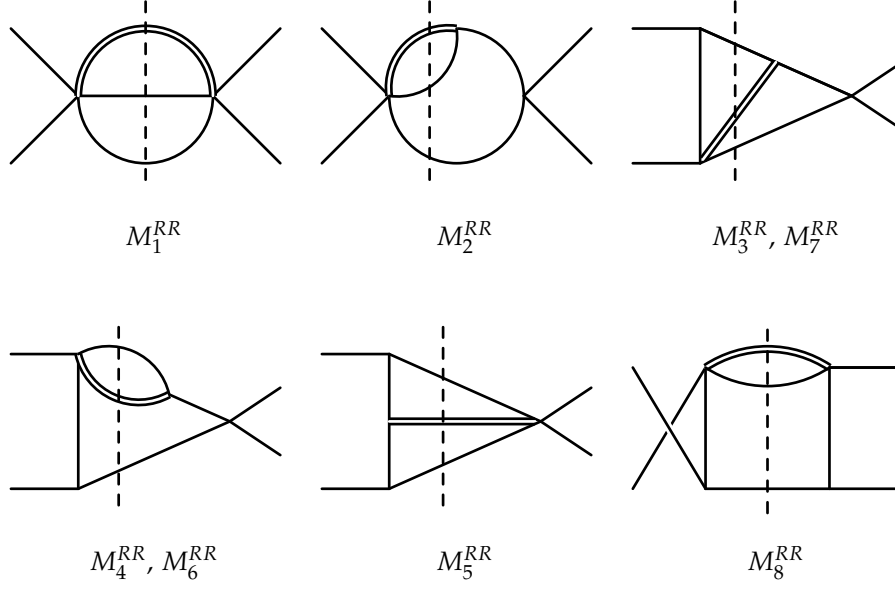


FIGURE 1.5: Double-real master integrals, the double line represents the Higgs propagator with associated mass m_h , and the external lines allow for the momenta p_1 and p_2 , while the dashed line represents the unitarity cut.

both strategies lead to identical results, and since the first method is well established in the field of high order computations, we will not discuss it in more details. Moreover, we limit the discussion to master integrals involving at least one final state parton as purely virtual corrections are well known [148, 149].

1.8.1 Double-real master integrals

At NNLO we find that the differential cross-section involving two partons in the final state can be written in terms of eight master integrals M_i^{RR} , corresponding to the six diagrams in figure 1.5. Propagators crossing the dashed line in the diagrams represent cut propagators, while the double line marks the massive Higgs boson propagator. The fact that we are interested in Higgs-differential master integrals means that the momentum of the Higgs boson is completely fixed.

Following the factorization of the phase-space shown in eq.(1.14), all the double-real (RR) master integrals can be written in the form

$$I(p, q; \alpha, \beta) \equiv \int \frac{d^d l}{(2\pi)^{d-2}} \frac{\delta(l^2) \delta((l-k)^2)}{(l+p)^{2\alpha} (l+q)^{2\beta}} \quad \begin{array}{l} k^2 \neq 0, \\ p^2 = 0, \\ q^2 \in \mathbb{R} \end{array} \quad (1.57)$$

where again we denoted with k the momentum of the collective system of final state partons. The generalised exponents α and β and the momenta q and p specify the propagators that appear in the respective master integral. In particular, p and q are linear combinations of p_1 , p_2 and k . The integral over l stands for the integration over one of the two final state parton momenta. The integral $I(p, q; \alpha, \beta)$ can be evaluated for generic values of the parameters in terms of Appell's Hypergeometric function [150]:

$$I(p, q; \alpha, \beta) = (-1)^{\alpha+\beta} \frac{\pi^{-1+\epsilon} 2^{-3-\beta+2\epsilon} (k^2)^{-\epsilon} \Gamma(1-\beta-\epsilon)}{\Gamma(2-\beta-2\epsilon)} \frac{(q^2 - q \cdot k)^{\alpha-\beta}}{(k^2(q \cdot p) - q^2(k \cdot p))^\alpha} \times \\ \times F_1 \left(\alpha; 1-\beta-\epsilon, 1-\beta-\epsilon; 2-\beta-2\epsilon; 1 - \frac{1 + \sqrt{1-4v_{11}}}{2v_{12}}, 1 - \frac{1 - \sqrt{1-4v_{11}}}{2v_{12}} \right) \quad (1.58)$$

where we have defined the auxiliary quantities,

$$1 - 4v_{11} \equiv \frac{(q \cdot k)^2 - k^2 q^2}{(q^2 - q \cdot k)^2} \xrightarrow{q^2=0} 1, \\ 2v_{12} \equiv \frac{q^2(k \cdot p) - k^2(q \cdot p)}{(p \cdot k)(q^2 - q \cdot k)} \xrightarrow{q^2=0} \frac{k^2(q \cdot p)}{(p \cdot k)(q \cdot k)}.$$

The eight master integrals, shown in Figure 1.5, contributing to the RR partonic cross-section, expressed in terms of the function $I(p, q; \alpha, \beta)$, are given by

$$M_1^{RR} = C_{RR}(1-2\epsilon) I(0, 0; 0, 0), \\ M_2^{RR} = -C_{RR} \frac{\bar{z}\epsilon}{1-\lambda x \bar{z}} I(0, p_1 + p_2; 0, 1), \\ M_3^{RR} = C_{RR} \frac{\lambda \bar{z} \epsilon (\lambda^2 x \bar{z}^2 - 2\lambda x \bar{z} + x \bar{z} - \bar{z} + 1)}{1-\lambda x \bar{z}} I(p_2, k - (p_1 + p_2); 1, 1), \\ M_4^{RR} = C_{RR}(1-\lambda) \bar{z} \epsilon I(p_1, p_1 + p_2; 1, 1), \\ M_5^{RR} = -C_{RR} \frac{(1-\lambda)\lambda(1-x)\bar{z}^2 \epsilon}{1-\lambda x \bar{z}} I(p_2, k - p_1; 1, 1), \\ M_6^{RR} = C_{RR} \frac{\lambda \bar{z} \epsilon (1-x \bar{z})}{1-\lambda x \bar{z}} I(p_2, p_1 + p_2; 1, 1), \\ M_7^{RR} = C_{RR} \frac{(1-\lambda) \bar{z} \epsilon (\lambda^2 \bar{z}^2 x (1-x) - \bar{z} + 1)}{(1-\lambda x \bar{z})^2} I(p_1, k - (p_1 + p_2); 1, 1), \\ M_8^{RR} = C_{RR} \frac{(1-\lambda)\lambda x \bar{z}^2 \epsilon}{1-\lambda x \bar{z}} I(p_2, p_1; 1, 1), \quad (1.59)$$

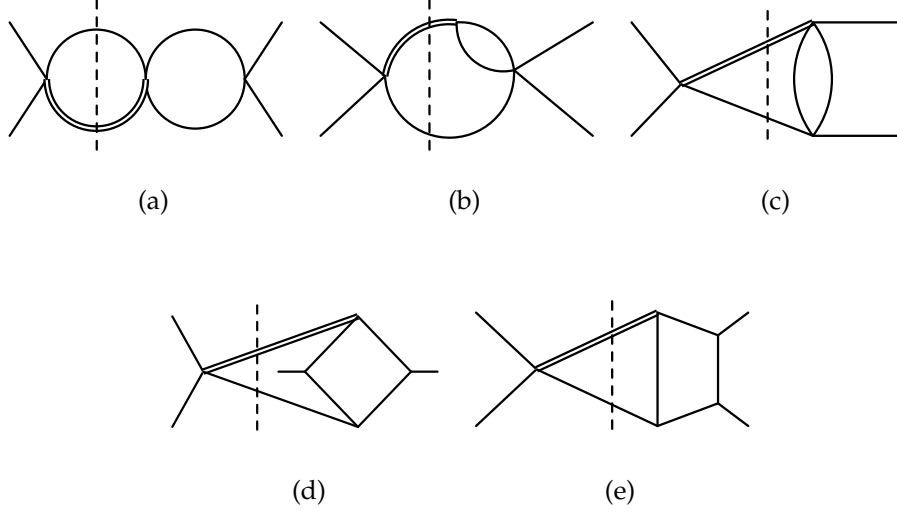


FIGURE 1.6: Set of real-virtual integrals to build the set of master integrals M_i^{RV} where the dashed line represents the Cutkosky cuts, the double line represents the Higgs propagator with associated mass m_h and the external lines allows for the momenta p_1 and p_2 , meaning that the diagrams (c, e) can have two possible configurations while all the other are symmetric under exchange $p_1 \leftrightarrow p_2$.

where M_6^{RR} and M_7^{RR} are related to M_4^{RR} and M_3^{RR} under the exchange of p_1 with p_2 , respectively. In the prefactor C_{RR} we absorb additional factors that result from the phase space measure of the integration over the Higgs boson momentum,

$$C_{RR} = \epsilon^3 (\mu^2)^{2\epsilon} e^{2\epsilon\gamma_E} \frac{(4\pi)^{-2-\epsilon} (m_h^2)^{-\epsilon} z^\epsilon}{\Gamma(1-\epsilon)} \bar{z}^{-2\epsilon} (\lambda\bar{\lambda})^{-\epsilon} (1-x)^{-\epsilon} (1-\bar{z}x\lambda)^\epsilon. \quad (1.60)$$

The rational prefactors and the C_{RR} in the above definitions of the master integrals make most of them pure functions of uniform transcendental weight [56]. This is true for all but M_2^{RR} which still contains a root of a polynomial in our variables.

1.8.2 Real-virtual master integrals

In the case of the RV master integrals, the integration over the final state parton phase space becomes trivial, and all master integrals are simply given by one-loop integrals. The masters

necessary to describe the RV differential cross-section are shown in figure 1.6. To express them, we define the shorthand notation for two well-known integrals:

$$\begin{aligned} \text{Bub}(p^2) &= \frac{1}{(4\pi)^{\frac{d}{2}}} \text{Bub}(p^2; 1, 1) \\ &= \frac{(4\pi)^{-2+\epsilon} (-p^2)^{-\epsilon} \Gamma(1-\epsilon)^2 \Gamma(\epsilon+1)}{\epsilon(1-2\epsilon)\Gamma(1-2\epsilon)}, \\ \text{Box}(q_1, q_2, q_3) &= \int \frac{d^d l}{i(2\pi)^d} \frac{1}{l^2(l+q_1)^2(l+q_1+q_2)^2(l+q_1+q_2+q_3)^2}, \end{aligned} \quad (1.61)$$

where the box integral can be found, for example, in ref. [151]. The master integrals can then be written as:

$$\begin{aligned} M_1^{RV} &= -\frac{2}{3}\epsilon(1-2\epsilon) C_{RV} \text{Re} [\text{Bub}((p_1+p_2)^2)], \\ M_2^{RV} &= -\frac{2}{3}\epsilon(1-2\epsilon) C_{RV} \text{Re} [\text{Bub}(p_h^2)], \\ M_3^{RV} &= -\frac{2}{3}\epsilon(1-2\epsilon) C_{RV} \text{Re} [\text{Bub}((p_2-p_h)^2)], \\ M_4^{RV} &= -\epsilon^2 s^2 \bar{\lambda} \bar{z} C_{RV} \text{Re} [\text{Box}(p_2, p_1, -p_h)], \\ M_5^{RV} &= \epsilon^2 s^2 \lambda \bar{z} C_{RV} \{11\bar{z}\bar{\lambda} \text{Re} [\text{Box}(p_2, -p_h, p_1)] - 23 \text{Re} [\text{Box}(p_1, p_2, -p_h)]\}, \\ M_6^{RV} &= -\frac{2}{3}\epsilon(1-2\epsilon) C_{RV} \text{Re} [\text{Bub}((p_1-p_h)^2)], \\ M_7^{RV} &= \epsilon^2 s^2 \lambda \bar{z} C_{RV} \{-\bar{z}\bar{\lambda} \text{Re} [\text{Box}(p_2, -p_h, p_1)] + 2 \text{Re} [\text{Box}(p_1, p_2, -p_h)]\}. \end{aligned} \quad (1.62)$$

The normalisation factor C_{RV} absorbs part of the integration measure of the Higgs boson momentum and is given by

$$C_{RV} = \epsilon^2 (\mu^2)^{2\epsilon} e^{2\epsilon\gamma_E} \frac{(4\pi)^{-1-\epsilon} (m_h^2)^{-\epsilon} z^\epsilon}{2\Gamma(1-\epsilon)} \bar{z}^{-2\epsilon} (\lambda\bar{\lambda})^{-\epsilon}. \quad (1.63)$$

1.8.3 Expansion in the dimensional regulator

For further numerical evaluation, we need to expand the master integrals as a Laurent series in the dimensional regulator ϵ . The Laurent expansions for the RV master integrals are well known, so we comment here only on the expansion of the RR integrals. For the masters M_1^{RR} , M_4^{RR} and M_5^{RR} , their Appell's hypergeometric function can be reduced to Gauss hypergeometric functions ${}_2F_1$, and can be expanded in ϵ with public tools such as the HypExp package [152, 153].

For the remaining master integrals, we have to directly expand the Appell's hypergeometric function through weight three, starting from the following integral representation:

$$\begin{aligned}
F_1(1; -\epsilon, -\epsilon; 1 - 2\epsilon; x, y) &= (-2\epsilon) \int_0^1 dt (1-t)^{-1-2\epsilon} (1-yt)^\epsilon (1-xt)^\epsilon \\
&= (-2\epsilon) \bar{x}^\epsilon \bar{y}^\epsilon \int_0^1 dt t^{-1-2\epsilon} \left[\left(1 - (1-tx')^\epsilon\right) \left(1 - (1-ty')^\epsilon\right) \right. \\
&\quad \left. - \left(1 - (1-tx')^\epsilon\right) - \left(1 - (1-ty')^\epsilon\right) \right] \\
&\quad + (-2\epsilon) \bar{x}^\epsilon \bar{y}^\epsilon \int_0^1 dt t^{-1-2\epsilon}. \tag{1.64}
\end{aligned}$$

Here we have defined $x' = \frac{x}{x-1}$ and similarly for y' . From this reparametrization and rearrangement, we obtain that the first element inside the squared parenthesis integrates to a finite quantity when ϵ vanishes and can therefore be expanded at the integrand level around $\epsilon = 0$. The divergent behaviour is captured by the remaining terms, which can be easily integrated for generic ϵ in terms of ${}_2F_1$. Combining these contributions back together yields the following expansion for the F_1 :

$$\begin{aligned}
F_1(1; -\epsilon, -\epsilon; 1 - 2\epsilon; x, y) &= 1 + \epsilon \ln(\bar{x}\bar{y}) - 2\epsilon^2 \left[\text{Li}_2(x) + \text{Li}_2(y) + \frac{1}{4} \ln^2\left(\frac{\bar{x}}{\bar{y}}\right) \right] \\
&\quad - 2\epsilon^3 \left\{ 2 \text{Li}_3(x) + 2 \text{Li}_3(y) - \text{Li}_3\left(\frac{x}{y}\right) + \text{Li}_3\left(\frac{\bar{x}}{\bar{y}}\right) + \text{Li}_3\left(\frac{y\bar{x}}{x\bar{y}}\right) \right. \\
&\quad \left. - \ln\left(\frac{\bar{x}}{\bar{y}}\right) \text{Li}_2\left(\frac{y\bar{x}}{x\bar{y}}\right) - \zeta_3 - \frac{1}{12} \ln^3\left(\frac{\bar{x}}{\bar{y}}\right) \right. \\
&\quad \left. - \frac{1}{6} \ln^3\left(-\frac{x}{y}\right) + \frac{1}{2} \ln(x) \ln^2\left(\frac{\bar{x}}{\bar{y}}\right) \right\} + \mathcal{O}(\epsilon^4). \tag{1.65}
\end{aligned}$$

The above expression is real-valued for $x \in [0, 1], y < 0$. This allows us to express all coefficients in the Laurent series in terms of real valued classical polylogarithms, enabling a fast and stable numerical evaluation [154].

1.9 NUMERICAL RESULTS FOR THE HIGGS DIPHOTON SIGNAL

In this section, we carry out numerically the remaining integrations which are necessary in order to obtain the hadronic Higgs-differential cross-sections. We present results for the LHC at 13TeV in order to showcase the types of observables which can be readily computed with our approach.

While our analytical results are original and extend the literature of NNLO Higgs-differential cross-sections at $\mathcal{O}(\epsilon)$, our numerical predictions for the finite part can be compared to available

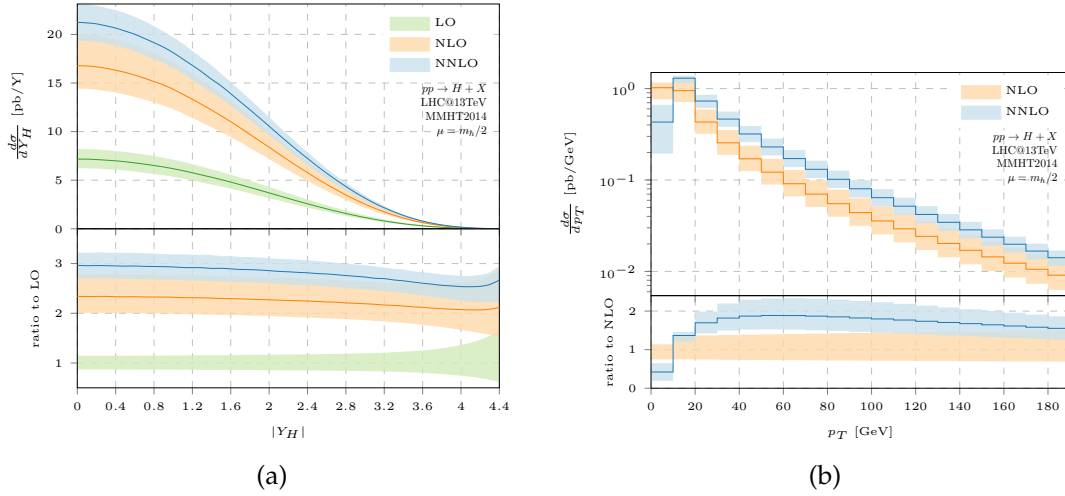


FIGURE 1.7: Rapidity and p_T distributions for the inclusive production of a Higgs boson via gluon fusion for different orders in perturbative QCD through NNLO. The bands represent the variation of the cross section under changes of the unphysical scale μ w.r.t. the central value (thick lines) by a factor of two.

computer codes. We have validated our numerical implementation against the predictions of HNNLO [85] and MCFM [155] and we have found good agreement within Monte-Carlo uncertainties.

For our numerical studies we use NNLO MMHT parton distribution functions [120] throughout, as available from LHAPDF [121]. Their default value for the strong coupling constant $\alpha_s(m_Z) = 0.118$ and the corresponding three-loop running are also adopted. We set the Higgs boson mass to $m_h = 125$ GeV and neglect its width. We equate the renormalisation and factorisation scales for simplicity and we choose $\mu = m_h/2$ as a central value. As it is common practice, we estimate the effect of missing higher order corrections by varying μ by a factor of two around its central value.

We start by showing distributions for the inclusive production of a Higgs boson via gluon fusion. In Figure 2.6a we present the unbinned rapidity distribution of the Higgs boson. The bands correspond to the variation of the cross-section at LO, NLO and NNLO in our default μ scale range. In Figure 1.7b we show the p_T distribution of the Higgs boson. In order to have a non-vanishing transverse momentum, the Higgs boson needs to recoil against additional radiation and therefore its p_T distribution is trivial at LO.

In addition to simple inclusive distributions for a stable Higgs boson, we can also investigate its decays. Specifically, we present differential distributions for the Higgs diphoton signal after the application of typical selection cuts for the photons. The decay of the Higgs boson to two photons allows for precise measurements of numerous properties (see e.g. [156–162]) due to its

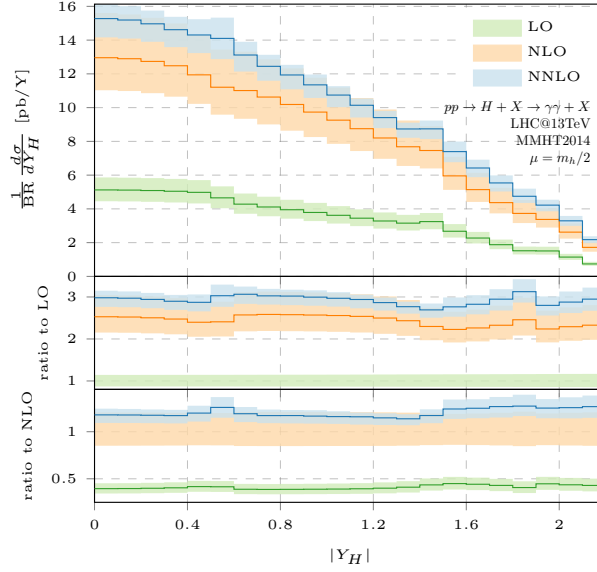


FIGURE 1.8: The Higgs boson rapidity distribution for different orders in pQCD through NNLO in the fiducial volume for the diphoton decay. The bands represent the variation of the cross-section under changes of the unphysical scale μ w.r.t. the central value (thick lines) by a factor of two.

exceptionally clean experimental signature and it has played a crucial role in the discovery of the Higgs boson itself [13, 14].

We impose photon selection cuts which follow as closely as possible the diphoton analysis of ATLAS [162]. We require that the pseudorapidities of both photons satisfy $\eta_\gamma < 2.37$, together with $\eta_\gamma \notin [1.37, 1.52]$, which implies that there are no photons in these regions. Furthermore, we require the photon with larger transverse momentum to satisfy $p_{T,\gamma_1} > 0.35 m_h$ and the one with smaller transverse momentum to have $p_{T,\gamma_2} > 0.25 m_h$. Since we have integrated out the associated radiation in the production of the Higgs boson, our analysis ignores photon isolation which is important for removing most of the diphoton background due to fragmentation [18], but it effects in a minor way the Higgs signal that is studied here.

In Figure 1.8, we present the rapidity distribution of the Higgs boson after the application of the photon selection cuts described above. The bands correspond to the values of the cross-section at LO, NLO and NNLO in our default μ scale range. Due to the restrictions in the coverage of the pseudorapidity of the photons, the Higgs rapidity distribution manifests some non-smooth changes. In the middle panel, we show the conventional K -factors, i.e. we normalise the rapidity distribution at LO, NLO and NNLO for a general scale μ to the LO prediction evaluated at a fixed scale $\mu = m_h/2$. We observe that the relative size of QCD corrections at NLO and NNLO has a pattern which is similar to the one seen for the inclusive cross-section, although the K -factors are not entirely uniform across bins due to the effect of

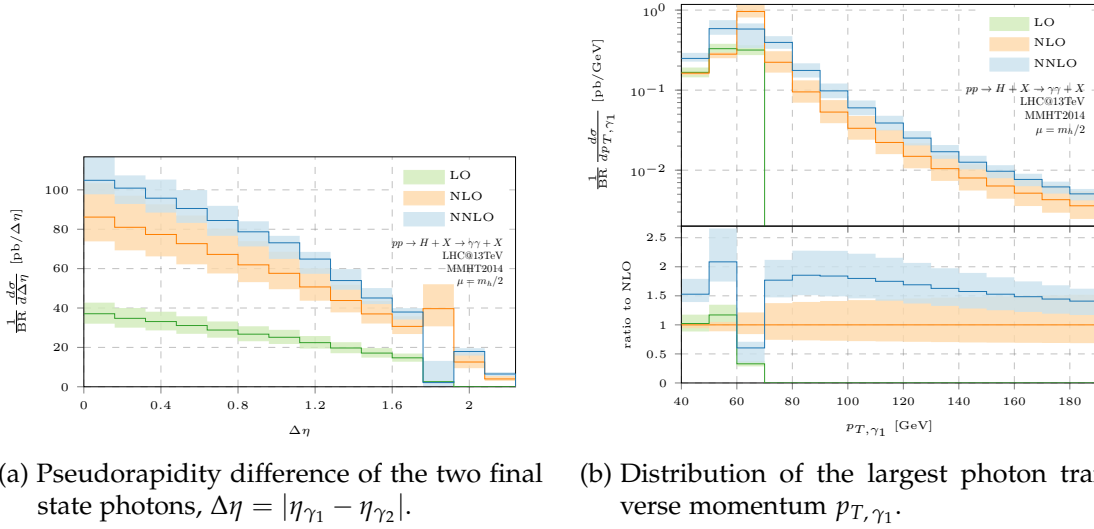


FIGURE 1.9: Differential distributions for the decay products of the Higgs boson for different orders in perturbative QCD through NNLO in the fiducial volume for the diphoton decay. The bands represent the variation of the cross section under changes of the unphysical scale μ w.r.t. the central value (thick lines) by a factor of two.

the photon cuts. In the lower panel, we normalise the rapidity distribution at LO, NLO and NNLO for a general scale μ to the NLO prediction at NLO at a fixed scaled $\mu = m_h/2$. This shows that the relative K -factor from NLO to NNLO is more uniform in rapidity.

In Figure 1.9a, we present the distribution of the pseudorapidity difference of the two photons. The distribution has a kinematic edge at leading order at $\Delta\eta \simeq 1.79$. The perturbative expansion contains logarithms in terms of the ratio $\frac{p_T}{m_H}$ which becomes large as the transverse momentum of the Higgs boson becomes smaller. In order to improve the fixed order perturbative corrections a resummation of these logarithms is required [163]. However, the bulk of the distribution can be calculated in fixed order perturbative QCD.

In Figure 1.9b, we present the p_T distribution of the leading photon. At LO, the photon p_T cannot exceed the value of $m_h/2$. In addition, the experimental selection imposes a lower p_T value at $0.35 m_h$. This severe restriction of the phase space leads to large corrections to the available perturbative results. As such, resummation would be required to obtain stable predictions in this kinematical regime. Beyond LO the phase space for larger values of p_T opens up and the distribution becomes more well-behaved beyond 100 GeV.

These distributions are just a small selection of possible observables that can be computed in our framework. Combining the production with other decay modes is straightforward and can be used to study a number of phenomenologically relevant observables.

The analytic computation of the partonic coefficient functions $\eta_{ij}^{(k)}(z, x, \lambda)$ as defined in eq.(1.24) has been published in ref. [1] together with a finite version with all 18 different

kinematic configurations of these coefficient functions as in section 1.5 each as a sum of products of rational coefficients and master integrals, provided in Mathematica readable form in an ancillary file together with the arXiv submission.

1.10 CONCLUSION

In this chapter, we presented differential distributions for Higgs boson observables at NNLO in perturbative QCD, obtained within our Higgs-differential framework. Our computational method is a departure from common frameworks for differential calculations in that it avoids explicit subtraction of infrared divergences at the cost of being inclusive in jet observables. This is achieved by separating the QCD radiation phase space from the phase space of the produced colour-neutral final state. By integrating the QCD radiation phase space inclusively in dimensional regularisation, soft and collinear divergences are made explicit as poles in the regulator. Furthermore, this separation enables us to employ reverse unitarity and related techniques that have been developed in inclusive calculations, in order to simplify the phase-space integrations over final-state partons which are produced in association with the Higgs boson.

The NNLO cross section has been cast in terms of few master integrals, which we compute in an arbitrary number of dimensions in terms of standard hypergeometric functions that admit expansions to arbitrarily high order in the dimensional regulator. We have presented results that go beyond the finite term in the ϵ expansion, which were unknown in the literature. These new results are essential ingredients for the construction of collinear and UV counter terms for Higgs-differential cross sections at N³LO. The master integrals encountered here do not depend on the exact nature of the colourless final state produced and could be directly re-used in a similar differential Drell-Yan calculation.

The main achievement of this chapter is laying down the mathematical framework for the computation of the N³LO differential Higgs distribution that will be discussed in the next chapter in the context of a threshold expansion.

THRESHOLD EXPANSION

In this chapter, we discuss the problems arising when dealing with the computation of the Higgs-differential cross-section at one order higher in the perturbative expansion, namely N³LO in the effective theory.

We start by showing a tool that has been key in order to enable us to explore the large complexity of the problem; the implementation of the reconstruction of rational functions with the aid of finite fields. In particular, the reconstruction of the coefficients of the reduction to master integrals.

We then present two ways to perform the threshold expansion, one performed at the integrand level, and another by building a system of differential equations.

At last, we present the result of the analytic computation for the first and second term of the threshold expansion of the partonic N³LO coefficient functions for the Higgs-differential cross-section. These results were first published in refs. [2]. In order to perform the computation we also strongly rely on techniques recently developed in refs. [26, 128, 140, 141] together with [1] as presented in the previous chapter.

2.1 RATIONAL FUNCTION RECONSTRUCTION

The reduction of an integral $I_{(v_1, \dots, v_n)}$, defined in eq.(1.42), to master integrals $M_k(p_1, \dots, p_n; \{m_i\})$ can be written as:

$$I_{(v_1, \dots, v_n)} = \sum_k c_k M_k(p_1, \dots, p_n; \{m_i\}). \quad (2.1)$$

were the master integrals depend on the external momenta p_i and a number of massive propagators with arbitrary masses m_j . The coefficients c_k that define the integral in terms of master integrals are the result of the application of IBP identities as presented in eq.(1.45). By combining them, it is possible to explore a growing number of relations between integrals that differ only in their denominator powers by following the Laporta algorithm [136]. Solving the system to retrieve the coefficients c_k is performed with a simple Gaussian elimination, which consists in the repetition of simple arithmetic operations such as addition, subtraction,

multiplication and division. Since each IBP relation in eq.(1.45) corresponds to a linear combination of integrals $I_{(v_1, \dots, v_n)}$ with varying powers v_i and multiplied by coefficients that are rational functions of the external kinematics $s_{ij} = (p_i + p_j)^2 - \delta_{ij} p_i^2$, it follows that also the coefficients c_k appearing in eq.(2.1) must be rational functions.

The evaluation of the coefficients c_k is still far from simple, and performing all the steps of the Gaussian elimination analytically may be beyond our current computing power. This is especially true for topologies with many loops, masses or external legs, which significantly increase the structure that such rational functions can take.

One of the limiting factors is that to reach the expression for the coefficients c_k one needs to evaluate all the intermediate steps of the Gaussian elimination, which could involve expressions much more complicated than the final result. As has been pointed out in ref. [62], the evaluation of all these steps is extremely fast when performed numerically. We can then perform multiple evaluations to gather enough information to reconstruct the rational structure of the coefficients c_k . Since we want this reconstruction to be exact, we are not allowed to approximate any of the numerical evaluation (e.g. by using float numbers), to this end we use finite fields to minimize the loss of information without affecting the evaluation speed.

The exact analytic expression for the reduction coefficients is recovered by performing the rational reconstructions over multiple finite fields. The procedure used to go from the finite field representation to the one involving rational numbers is illustrated in figure 2.1. In particular, using the Chinese Remainder Theorem (CRT) one can build a representation over \mathbb{Z}_m with m large enough to allow for the unique identification of a rational number through the Rational Reconstruction Theorem (RRT). The details on the work of the CRT and RRT are discussed in the dedicated subsections.

2.1.1 Finite Field

The use of finite fields in physics has gained increasing popularity from its first applications in refs. [39, 62] and was an important ingredient when we were working on the threshold expansion presented in ref. [2]. Other examples of works that relied on the use of finite fields in order to circumvent problems related to the complexity of the expressions can be found in refs. [164–169].

In mathematics, finite field (or Galois field) are defined as commutative division ring.

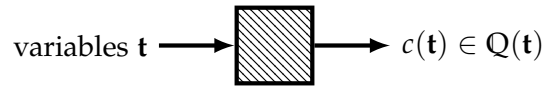
COMMUTATIVE DIVISION RING :

A **Ring** $(R, +, \circ)$ is a set R together with two binary operations $+ : R \times R \rightarrow R$ and $\circ : R \times R \rightarrow R$ and fulfils the following conditions:

- (1) R is an abelian group with respect to the operation $+$ with the identity element denoted by 0
- (2) the operation \circ is associative
- (3) Distributivity of multiplication over addition: $(a + b) \circ c = a \circ c + b \circ c$

A Ring is said to be a commutative division ring if $R \setminus \{0\}$ is an abelian group under \circ . From this definition it follows that \mathbb{Z}_p is a finite field if and only if p is a prime number. For example, if $p = 3 \cdot 5$ then \mathbb{Z}_{15} cannot be a commutative division ring since $(3 \cdot 5 = 0 \pmod{15})$, meaning that neither 3 nor 5 can have a multiplicative inverse.

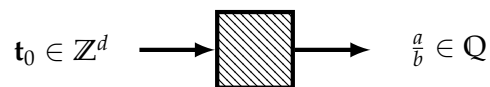
We now want to incorporate the use of finite fields into the evaluation of the reduction coefficients. We can represent the evaluation of these coefficients as a black-box which contains the set of instructions one need to follow to obtain their expressions. The only constraint that we impose to the black-box is that all the internal operations must be represented as a combination of addition, subtraction, multiplication and division. Assuming the reduction coefficient depend on a set of variables \mathbf{t} , we can represent the evaluation as,



where $\mathbb{Q}(\mathbf{t})$ represents the space of rational functions over the field \mathbb{Q} with variables \mathbf{t} .

This operation could become extremely time-consuming. For our computation, we have used FERMAT [170] to perform all the algebraic manipulations necessary to build the reduction coefficients. These instructions were provided by a private C++ implementation of the reduction algorithm that was already used for the inclusive N^3LO Higgs cross-section in refs. [26, 128, 140, 141]. This direct manipulation of the algebraic expression became so complicated for the N^3LO Higgs-differential cross-section that, even after running the corresponding code for two months, we couldn't recover the coefficients. Considering that this was the reduction for a single topology out of more than 200, this method quickly showed its limitations.

The evaluation time is drastically reduced when considering numerical values for the variables \mathbf{t} . This new evaluation can be represented as:



with d the number of variables. For practical applications this numerical evaluation is not optimal since, when sampling to reconstruct a rational function, the resulting rational numbers may become extremely large in both the numerator and denominator. As the size of these numbers grows so does the amount of time need for the evaluation of any algebraic operation among them. To avoid this problem we can perform the evaluation over a finite field \mathbb{Z}_p . By using $p < 2^{63}$ we ensure that all the operations are performed between machine size integers allowing to exploit the full potential of the hardware used for the computation.

2.1.2 Rational Function Reconstruction

UNIVARIATE CASE

The reconstruction of rational functions in one variable is a well known problem, and there are several ways to do it. Here we are going to present the procedure followed for our computations.

Let us assume that a function $f(t)$ over a field \mathbb{K} can be written in the form:

$$f(t) = \frac{\sum_{i=0}^n a_i t^i}{1 + \sum_{i=1}^m b_i t^i} =: \frac{g(t)}{h(t)}, \quad (2.2)$$

where we choose to normalize the constant coefficient to one. In case the function cannot be brought directly into this form, we can either apply a shift to the variable t or considering the inverse function $1/f(x)$. It is also convenient to define the degree of a rational function:

$$\deg[f(t)] \equiv 2 \cdot \max\{\text{rank}[g(t)], \text{rank}[h(t)]\},$$

which is related to the number of points needed to complete the interpolation.

To reconstruct the expression of the rational function, we make use of *Thiele's interpolation* formula:

$$T(t; \{t_j, a_j\}_{j=0, \dots, n}, a_{n+1}) = a_0 + \frac{t - t_0}{a_1 + \frac{t - t_1}{\ddots a_n + \frac{t - t_n}{a_{n+1}}}}, \quad (2.3)$$

where t is the variable we are reconstructing in, t_j the points where we have evaluated the function we want to interpolate, and a_n the coefficients that need to be fixed.

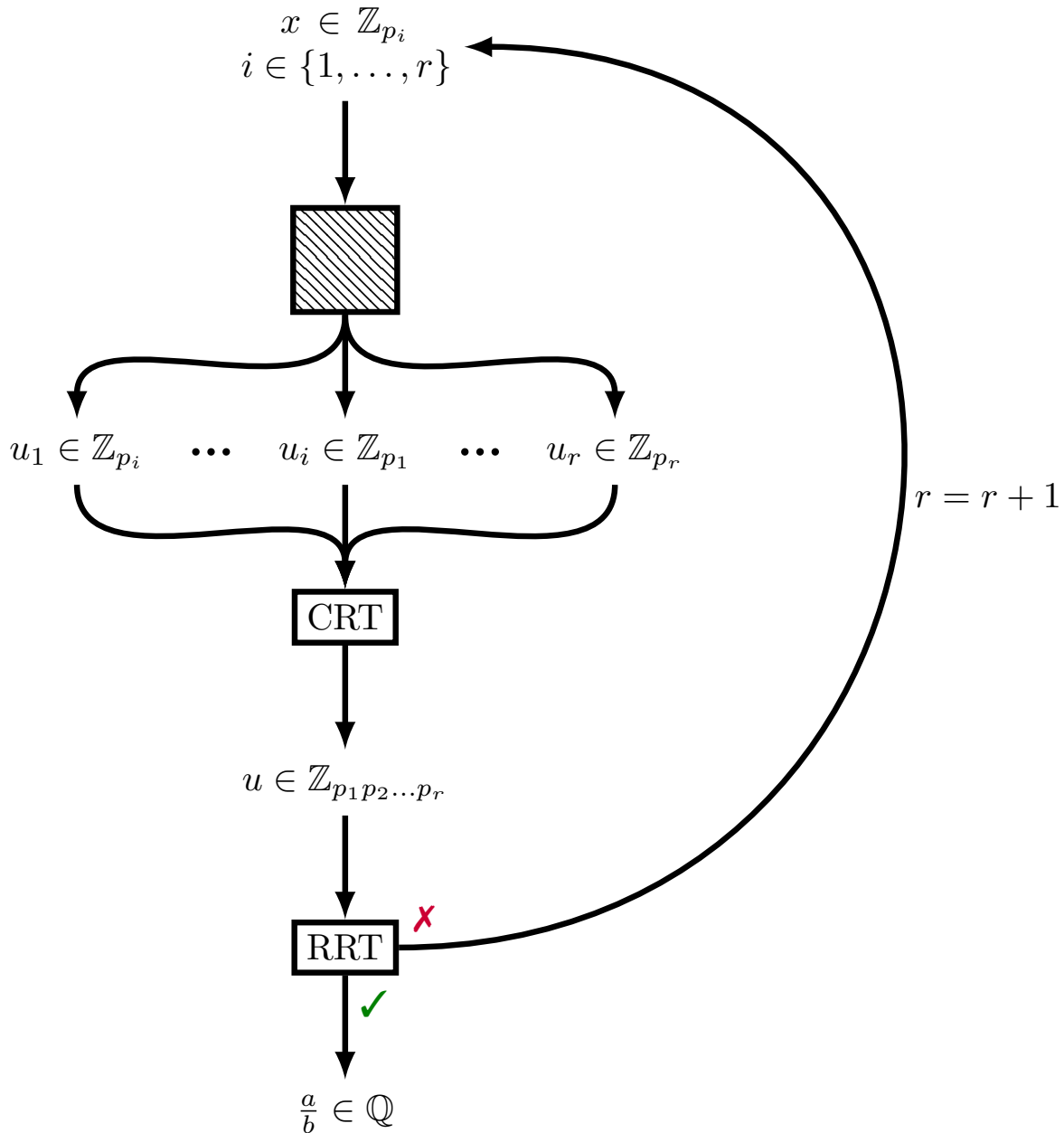


FIGURE 2.1: Schematic representation on how the reconstruction of rational numbers is performed. In the first step, the numerical input is an element of the finite field \mathbb{Z}_{p_i} implying that we are going to perform all the operations inside of the black-box over \mathbb{Z}_{p_i} . In the third layer, we see that the evaluation is repeated for a set of different primes p_i resulting in different representation of the rational number. All these results are then combined using the Chinese Remainder Theorem (CRT) to create a new number u which is the representation of the rational number modulus the product of all the primes used so far. We then try to use the Rational Reconstruction Theorem (RRT) to recover the expression of the rational number, if such an operation fails then we evaluate over an extra finite field with size p_{r+1} to increase the size of $\mathbb{Z}_{p_1 p_2 \dots p_r}$ till the RRT is successful.

In order to illustrate how the coefficients a_n are fixed, it is useful to write the interpolation formula in a recursive form. First, we introduce the shorthand notation:

$$T_j^i(t; \{t_k, a_k\}, a_{n+1}) := T(t; \{t_k, a_k\}_{k=i, \dots, j}, a_{j+1}), \quad T_j^{j+1}(t; \{t_j, a_j\}, a_{n+1}) = a_{n+1} \quad (2.4)$$

where the second condition represents the end of the recursion that will reproduce eq.(2.3). In particular, the recursive step that unfolds into the expression for Thiele's interpolation formula is written as:

$$T_n^m(t; \{t_j, a_j\}, a_{n+1}) = a_m + \frac{(t - t_m)}{T_n^{m+1}(t; \{t_j, a_j\}, a_{n+1})}. \quad (2.5)$$

The number of different evaluations necessary to successfully reconstruct a function of the form of eq.(2.2) is given by $\deg[f(t)]$, corresponding to the degrees of freedom that need to be fixed. The first coefficient of the interpolation is trivially set, assuming that the first evaluation at t_0 corresponds to a value f_0 , then $a_0 = f_0$.

Let us assume that we have all the coefficients up to a_n and we want to fix the next one. This means that we have already evaluated some rational function $f(t)$ in $(n + 1)$ different points and fit to the corresponding Thiele's interpolation T_{n-1}^0 . The next step is to evaluate the function in one extra point and solve for a_{n+1} . The system generated by this additional evaluation corresponds to:

$$T_{n-1}^0\left(t_{n+1}; \{t_j, a_j\}, a_n + \frac{(t_{n+1} - t_n)}{a_{n+1}}\right) = f_{n+1}. \quad (2.6)$$

If either the reconstruction is already completed or the point is by chance aligned with the current state of the reconstruction, one gets the following condition:

$$T_{n-1}^0\left(t_{n+1}; \{t_j, a_j\}, a_n + \frac{(t_{n+1} - t_n)}{a_{n+1}}\right) = T_{n-1}^0(t_{n+1}; \{t_j, a_j\}, a_n) \quad (2.7)$$

$$\Rightarrow \frac{(t_{n+1} - t_n)}{a_{n+1}} = 0. \quad (2.8)$$

Since by assumption $t_n \neq t_{n+1}$, we conclude that this system has no solution. To ensure that this corresponds to the end of the reconstruction, we discard this last point and try again with a different evaluation point t'_{n+1} . If we encounter the condition in eq.(2.8) enough times we can claim with reasonable certainty that the reconstruction is concluded and take T_{n-1}^0 as being our original function $f(t)$. As we will see for the multivariate case, we can also find an upper bound for n with high confidence and avoid all the extra evaluations.

MULTIVARIATE CASE

We just saw how to reconstruct rational functions in the simple case where there is just one variable; we now want to solve it for the generic case of d -variables.

Let us introduce a shorthand notation to avoid unnecessarily messy equations:

$$\mathbf{x}^{\alpha_n} = \prod_{i=1}^{i=d} x_i^{\alpha_{n,i}}, \quad |\alpha_n| = \sum_{i=1}^{i=d} \alpha_{n,i} = n.$$

We then consider the natural extension of the 1-dimensional case of eq.(2.2):

$$f(\mathbf{x}) = \frac{\sum_{i=0}^n \sum_{\alpha_i} a_i(\alpha_i) \mathbf{x}^{\alpha_i}}{1 + \sum_{i=0}^n \sum_{\beta_i} b_i(\beta_i) \mathbf{x}^{\beta_i}} =: \frac{g(\mathbf{x})}{h(\mathbf{x})}. \quad (2.9)$$

For the multivariate case, it is in general not possible to represent the function like this. For example, the expression $\frac{x_1}{x_2}$ cannot be normalized to a constant in either the numerator or the denominator. Similarly as was discussed in the 1-dimensional case, any multivariate function $f(\mathbf{x})$ can nevertheless be brought in the form of eq.(2.9) by performing a shift in the variables and considering the new function $f'(\mathbf{x}) \equiv f(\mathbf{x} + \mathbf{x}_0)$. After a successful reconstruction, the original expression can be recovered by reversing the shift.

Also for the higher dimensional case, it is useful to introduce the concept of degree of the function as well as the rank for both numerator and denominator. We define the degree of the d -dimensional rational function as:

$$\deg[f(\mathbf{x})] \equiv 2 \cdot \max \{ \max(|\alpha_n|), \max(|\beta_m|) \}.$$

For any multivariate reconstruction, one can fall back to the problem of interpolating a 1-dimensional rational function. Assuming we have some arbitrary point \mathbf{x}_0 where we evaluate the expression, we can then rescale it by some variable t_1 and interpolate in it. By considering different starting points \mathbf{x}_0 , it is then possible to infer the multivariate structure. For our reconstruction, we used the following rescaling to systematically explore the space:

$$x_i = x_{0,i} \cdot \begin{cases} t_1, & i = 1 \\ t_1 \cdot t_i, & \text{otherwise} \end{cases} \quad (2.10)$$

By freezing the values for all t_i with $i > 1$ we obtain a univariate rational function in t_1 that can then be reconstructed by following the method discussed in the 1-dimensional case. Such rational expression will have all of its coefficients a_i and b_i from eq.(2.2) to represent

polynomials in the remaining scaling parameters t_2, \dots, t_d . By interpolating rational functions in t_1 for different values of the other t_i s, we can perform a *Newton polynomial interpolation* of each coefficient. The interpolation reads:

$$N(t; \{t_j, a_j\}_{j=0, \dots, n}, a_{n+1}) = a_0 + (t - t_0) \left(a_1 + (t - t_1) \left(\dots (t - t_{n-1}) \left(a_n + (t - t_n) a_{n+1} \right) \dots \right) \right). \quad (2.11)$$

Depending on the position of the coefficient in the univariate rational function, we can obtain an upper bound for the degree of the polynomial and use it to truncate the polynomial interpolation.

The rational reconstruction in the variable t_1 requires at least $\deg[f(t\mathbf{x}_0)]$ independent evaluations. Instead, the number of independent evaluations needed for the other t_i is related to the rank of the variable x_i . Because of this difference in the required number of evaluations, it is convenient to assign the x_1 position to the variable that appears with the highest power to reduce the overall number of points needed to complete the reconstructions.

This brings us to the problem of extracting the ranks in the individual variables. To recover the rank in the variable x_i , we can fix the starting position to be \mathbf{x}_0 and then reconstruct the rational function by rescaling only in this variable. In order to avoid accidental cancellations due to the choice of \mathbf{x}_0 , we repeat these reconstructions by sampling over different initial values.

The algorithmic reconstruction we just discussed is valid for any rational function over a field \mathbb{K} . For the purpose of computing the reduction coefficients for the Higgs-differential cross-section, we work with finite fields (i.e. $\mathbb{K} = \mathbb{Z}_p$). To restore the original expression with $\mathbb{K} = \mathbb{Q}$ we need to recover the numerical coefficients in terms of rational numbers (see figure 2.1). To this end, we need to explain two ideas, the CRT that is used to combine different results and the RRT that maps the numbers in \mathbb{Z}_m to their rational counterpart.

2.1.3 Chinese Remainder Theorem

One key ingredient in using RRT to successfully map back to a rational number its representation over \mathbb{Z}_m is to have the modulus m to be large enough. In particular, it must exceed in size the square of both the numerator and denominator of the rational number. At the same time, we want to limit the size of the finite fields to work with machine size integers allowing to compute the algebraic operations as efficiently as possible.

The CRT allows us to fulfil both conditions, also when the rational number in the final expression contains reasonably large numbers at the numerator and/or denominator. The large modulus needed for the reconstruction can be built by combining many smaller finite fields \mathbb{Z}_p over different primes $p \approx 2^{63}$.

Let us assume that we are dealing with the number $x \in \mathbb{Q}$ and all we have are its values over several finite fields:

$$u_i \equiv x \pmod{p_i}, \quad (2.12)$$

where the p_i are all co-prime. What we want to achieve is a new number u , which is the number x modulus the product of all the previous primes:

$$u \equiv x \pmod{\prod_i p_i}. \quad (2.13)$$

The Chinese remainder theorem allows building u from the information that we already have about the values u_i . What it says is that if we have any number u that fulfils

$$u \in \left[0, \prod_i p_i\right), \quad u_i = u \pmod{p_i}, \quad (2.14)$$

then it must be exactly the same as eq.(2.13).

It is self evident that if we first apply the modulus $a \cdot p_i$ for any $a \in \mathbb{N}$ and then p_i it is equivalent to applying only p_i . This means that eq.(2.13) implies eq.(2.14).

We now want to show that there is only one such expression and that it is enough to define u completely. Assume for a moment that we have two solution u and u' , then we investigate their difference $\Delta u = |u - u'|$:

$$\begin{aligned} \Delta u = 0 \pmod{p_i}, \quad \forall i &\quad \Rightarrow \quad \Delta u \propto \prod_i p_i \\ &\Rightarrow \quad \Delta u = 0 \pmod{\prod_i p_i} \\ &\Rightarrow \quad u = u' \end{aligned}$$

This result tells us that it is sufficient to find an expression that fulfils eq.(2.14) to obtain u . Such expression can be written explicitly as:

$$u = \sum_i u_i \left[\prod_{j \neq i} p_j \left(\frac{1}{p_j} \pmod{p_i} \right) \right] \pmod{\prod_i p_i}, \quad (2.15)$$

by noticing that for any pair (p, q) of co-prime we can write:

$$1 = \left[p \left(\frac{1}{p} \bmod q \right) \right] \bmod q, \quad (2.16a)$$

$$0 = \left[p \left(\frac{1}{p} \bmod q \right) \right] \bmod p. \quad (2.16b)$$

EXAMPLE

Take the number $x = 65$ and its two moduli u_1 and u_2 over \mathbb{Z}_p with $p_1 = 9$ and $p_2 = 17$. The values of the two moduli are $u_1 = 2$ and $u_2 = 14$. We can then use the CRT as presented in eq.(2.15) to build the expression for $(u = x \bmod p_1 p_2)$:

$$\begin{aligned} u &= 2 \left[17 \left(\frac{1}{17} \bmod 9 \right) \right] + 14 \left[9 \left(\frac{1}{9} \bmod 17 \right) \right] \bmod 153 \\ &= 2(17 \cdot 8) + 14(9 \cdot 2) \bmod 153 \\ &= 65 \end{aligned}$$

As expected this value satisfies the conditions that $(u = u_1 \bmod p_1)$ and $(u = u_2 \bmod p_2)$.

2.1.4 Rational Reconstruction Theorem

If we were to reconstruct any integer number $x \in \mathbb{Z}$, we would be able to recover it from its value modulus m provided that $m > 2|x|$. Also for rational numbers, there are constrains on the size of \mathbb{Z}_m that allows for a successful reconstruction. In particular, it is possible to map all rational number of the form $\pm \frac{x}{y}$ that fulfil:

$$\begin{aligned} x &\in \{n \in \mathbb{N} \mid n < \sqrt{m/2}\} \\ y &\in \{n \in \mathbb{N}_{>0} \mid n < \sqrt{m/2}, n \text{ and } m \text{ co-prime}\} \end{aligned} \quad (2.17)$$

as was proven in ref. [171].

This boundary can be understood by considering the possible rational numbers that one can write satisfying the conditions above. By counting all possible combinations, we obtain an upper bound of $2(\sqrt{m/2})^2$, where the factor two takes care of the negative numbers. The actual number of unique rational number will be smaller since \mathbb{Q} is an equivalence class. To see how the different rational numbers are represented in \mathbb{Z}_m , it is useful to consider a simple example.

Data: $x, y \in \mathbb{Z}$

Result: Bézout's coefficients and $\gcd(x, y)$ in a vector (a, b, c) . Then the solution can be written as $\gcd(x, y) = ax + by = c$.

```

begin
  v = (1, 0, a);
  u = (0, 1, b);
  while u3 ≠ 0 do
    q = v3 quot u3;
    r = v - qu;
    v = u; u = r;
  end
  return v;
end

```

Algorithm 1: Extended Euclidean Algorithm (EEA)

EXAMPLE

Take $m = 23$. By assumption we should be able to map all rational numbers of the form $\pm \frac{x}{y}$ with $0 < x \leq 3$ and $1 < y \leq 3$:

$y \backslash x$	-3	-2	-1	0	1	2	3
1	20	21	22	0	1	2	3
2	10	↗	11	↑	12	↖	13
3	↗	7	15	↑	8	16	↖

Where we omitted the equivalent fractions. We see that indeed each rational number is associated with one unique number over \mathbb{Z}_m .

To understand how to map the representation of a rational number over a modulus m to its original value, we need to review the Extended Euclidean Algorithm (EEA, see algorithm 1). This algorithm is used for the computation of the greatest common divisor between two numbers x and y together with the corresponding Bézout's coefficients a and b :

$$\gcd(x, y) = ax + by \tag{2.18}$$

This same algorithm is used to find the inverse when working over a finite field \mathbb{Z}_p . Since the number p needs to be a prime, it guarantees that the greatest common divisor between any $x \in \mathbb{Z}_p \setminus \{0\}$ and p is always one:

$$\gcd(x, p) = ax + bp = 1 \quad \Rightarrow \quad a = \frac{1}{x} \pmod{p}. \tag{2.19}$$

Notice that when performing the EEA shown in algorithm 1, each intermediate value of v satisfies:

$$v_1x + v_2m = v_3 \quad \Rightarrow \quad x = \frac{v_1}{v_3} \pmod{m}.$$

This expression can be used to find a family of rational numbers which share the same modular representation:

$$x = \frac{v_1}{v_3} \pmod{m}.$$

The RRT proved in ref. [171] tells us that only one element out of all the candidate will have v_1 and v_2 to fulfil the constraints show in eq.(2.17).

During our computations, we found that in the worst case we needed up to 10 machine size primes to successfully recover the rational coefficients coming out of the reduction to master integrals. The reconstruction was already possible with fewer prime numbers, but we intentionally increased the size of the modulus m to ensure that the reconstruction was indeed successful. A false reconstruction could always happen when we are not restricting ourself to the correct bounds of (2.17). By having consistent results over an increasingly larger modulus m , we slim this chances. As a final check, we run a slow evaluation with arbitrary precision rational numbers of the original function and compare it with the evaluation of the expression we just reconstructed.

When dealing with the Higgs-differential cross-section at N³LO , we recovered reduction coefficients that needed up to 300 independent evaluations in t_1 for a single univariate reconstruction. At the same time, the individual variables were found to reach maximal ranks of up to 100. Part of the complexity of these coefficients could be blamed on the choice of master integrals since a different basis will also change the coefficients c_k . However, we can treat the evaluation of these coefficients as being just another intermediate step of our reconstruction. By doing so, we were able to build the differential equations for the master integrals by combining all the reduction coefficients directly into the matrix elements of the differential system. The components of the differential equation take a much simpler form and therefore need also fewer evaluations and fewer finite fields to perform the rational function reconstruction. This is further proof of how powerful this method is, allowing to sidestep the evaluation of the reduction coefficients altogether.

It is also possible to combine all the coefficients c_k directly at the cross-section level. Since this expression refers now to physical observable, as opposed to the result of the reduction to master integrals, we expect these expressions to take a much simpler form.

2.2 SOFT EXPANSION OF MASTER INTEGRALS

The expression of the differential equations for the master integrals were too complicated to be solved exactly as a Laurent series in the dimensional regulator ϵ . For this reason, we opted for an expansion around the production threshold of the Higgs boson, a method that has already been successfully implemented for the inclusive computation at N³LO in ref. [151].

It has been shown in refs. [128, 172] that the master integrals for the Higgs hadroproduction can be expanded in a systematic way as power series around the threshold limit. This expansion is generally not meromorphic but can nevertheless be written as a combination of meromorphic functions. In particular, when working in $d = 4 - 2\epsilon$ dimensions, the integral takes the form

$$I_i(s, \lambda, x, \bar{z}) \equiv \sum_{r \in \text{sectors}} \bar{z}^{(\beta_{ri} - \alpha_r \epsilon)} \sum_{n=0}^{\infty} \bar{z}^n m_{in}^{(r)}(s, \lambda, x), \quad (2.20)$$

where the index r denotes what we call the different *sectors* in which the soft expansion is split. For the case of the *RRV* master integrals, these regions are three. One represents the hard region (H) and has $\alpha = 4$, while the two collinear regions (C₁, C₂) have $\alpha = 5$ and the last is the soft region (S) with $\alpha = 6$.

2.2.1 Differential Equation

We are interested in expressing the master integrals in the form shown in eq.(2.20). The problem of extracting the various expansion coefficients can be solved by looking at the differential equation in \bar{z} . In appendix B we show how to perform this derivative by acting directly to the integral representation of the master integrals with differential operators written in terms of the external momenta. The corresponding system of differential equations can be written as,

$$\frac{\partial}{\partial \bar{z}} \vec{I}(s, \lambda, x, \bar{z}) = A(s, \lambda, x, \bar{z}) \vec{I}(s, \lambda, x, \bar{z}). \quad (2.21)$$

Here \vec{I} represents a vector whose elements are master integrals and A_{ij} is the differential equation matrix.

One of the first things to notice is that the different sectors, corresponding to different α in eq.(2.20), do not mix in the differential equation. The reason for this is that the differential operator can change the powers of \bar{z} only by an integer quantity. Therefore, we can treat the expansions of each sector independently from each other. Because of this independence, we will now drop the index r and see how to build the system for a generic region.

Let us take the left-hand side of eq.(2.21) and replace \vec{I} with its expanded expression:

$$\frac{\partial}{\partial \bar{z}} \left(\bar{z}^{(\beta_i - \alpha \epsilon)} \sum_{n=0}^{\infty} \bar{z}^n m_{in}(s, \lambda, x) \right) = \bar{z}^{(\beta_i - \alpha \epsilon)} \sum_{n=0}^{\infty} \left(\frac{\beta_i - \alpha \epsilon + n}{\bar{z}} \right) \bar{z}^n m_{in}(s, \lambda, x). \quad (2.22)$$

We do the same for the right-hand side of eq.(2.21):

$$\frac{\partial}{\partial \bar{z}} \vec{I}(s, \lambda, x, \bar{z}) = \sum_j \bar{z}^{(\beta_j - \alpha \epsilon)} A_{ij} \sum_{n=0}^{\infty} \bar{z}^n m_{jn}(s, \lambda, x). \quad (2.23)$$

Taking the difference of the two expressions and dividing by $\bar{z}^{(\beta_i - \alpha \epsilon)}$ yields,

$$0 = \sum_j \sum_{n=0}^{\infty} \left(\bar{z}^{(\beta_j - \beta_i)} A_{ij} - \delta_{ij} \left(\frac{\beta_i - \alpha \epsilon + n}{\bar{z}} \right) \right) \bar{z}^n m_{jn}(s, \lambda, x), \quad (2.24)$$

where the expression for the matrix $A_{ij} = A_{ij}(s, \lambda, x, \bar{z})$ is still a function of \bar{z} and since all of its elements are rational functions we can easily expand it as Laurent series around $\bar{z} = 0$.

Each order in \bar{z} in eq.(2.24) is equally zero, providing with a system of equations that can be solved up to some boundary terms. The boundary conditions are computed by taking the integral and expanding it around the different regions following refs. [128, 172].

The extraction of the coefficients m_{jn} from the system of equations defined by eq.(2.24) has been implemented in a private C++ code that uses both GiNaC [173] for performing the Laurent expansion of the differential matrix A , and FERMAT [170] and finite fields to perform the Gaussian elimination.

2.2.2 One-loop non-planar box expansion

As mentioned at the beginning of this section, the expression of a scalar Feynman integral is in general not meromorphic around $\bar{z} = 0$, and a simple series expansion of the integrand is therefore not possible. This can be illustrated by the fact that the loop momentum can take arbitrary values that are parametrically smaller or larger compared to the expansion parameter \bar{z} . Let us consider a single propagator containing a loop momentum l and a rescaled final state momentum $\bar{z}p_3$, the expansion of the integrand is:

$$\frac{1}{(l^2 + \bar{z}2lp_3)} = \frac{1}{l^2} \sum_{i=0}^{\infty} \left(-\frac{\bar{z}2lp_3}{l^2} \right)^i. \quad (2.25)$$

This expansion is clearly not convergent if l is uniformly smaller than \bar{z} . We then need to perform the expansion around the different scaling of the loop momentum. In particular, we

can write the integrand as a sum of expansions around the loop momentum soft, hard and collinear regions [128].

At one-loop, when we have the Higgs plus m partons in the final state, we need to consider the regions where the loop momentum becomes collinear to either one of the incoming momenta p_1 and p_2 , the region where the propagators between p_1 and p_2 become soft, and the hard region with respect to the soft parameter \bar{z} . We label these regions as (C1), (C2), (S) and (H), respectively. In the threshold limit, where all the n final states become soft, the integral becomes the one of a triangle:



$$(2.26)$$

where the number of final states going soft can be written as $m = \nu_1 + \nu_2 + \nu_3 - 3$. From this observation, it is clear that the regions that one needs to explore are the same as the one of a one-loop triangle.

The integral at 1-loop can be divided into the individual sectors as,

$$I_{1\text{-loop}} = I^{(S)} + I^{(H)} + I^{(C1)} + I^{(C2)}. \quad (2.27)$$

where each sector scales in different ways in \bar{z} . Normalizing the sector integrals by the hard region gives the following scalings:

$$\begin{aligned} \frac{I^{(S)}}{I^{(H)}} &\sim \bar{z}^{d-(2\nu_1+\nu_2+\nu_3)} = \bar{z}^{(4-2\nu_1-\nu_2-\nu_3)-2\epsilon} \\ \frac{I^{(C1)}}{I^{(H)}} &\sim \bar{z}^{d-(\nu_1+\nu_3)} = \bar{z}^{(2-\nu_1-\nu_3)-\epsilon} \\ \frac{I^{(C2)}}{I^{(H)}} &\sim \bar{z}^{d-(\nu_1+\nu_2)} = \bar{z}^{(2-\nu_1-\nu_2)-\epsilon} \end{aligned} \quad (2.28)$$

We can see that the two collinear limits correspond to the sector with $\alpha = 1$ in eq.(2.20), while the soft maps to $\alpha = 2$ and the hard region to $\alpha = 0$.

In order to illustrate the ingredients used for the computation of the threshold expansion, we analyse the simple case of the non-planar box integral shown in figure 2.2. This is an example of an integral that contributes to the RRV cross-section. We define its propagator by routing the loop momentum such that its soft limit corresponds to the soft divergence of the integral:

$$A_1 = l^2, \quad A_2 = (l - \bar{z}q)^2, \quad A_3 = (l - \bar{z}q + p_2)^2, \quad A_4 = (l - p_1)^2. \quad (2.29)$$

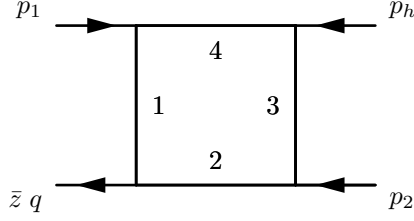


FIGURE 2.2: Non planar box for soft expansion. This could correspond to the amplitude where we have a box loop of gluon propagators and the vertex with outgoing momentum $\bar{z}q$ corresponds to a 4-gluon vertex. The numbers denotes the propagators ids and are represented in eq.(2.29).

where $l = 0$ sits on the intersection of the two pinched surfaces defining the two collinear divergences.

SOFT REGION

In the soft region the loop momentum scales in the same way as the real outgoing parton,

$$l = \bar{z}\ell.$$

This choice corresponds to having the momentum flowing through the propagators labelled by ν_1 in eq.(2.26) being soft. Then, the propagators in eq.(2.29) can be separated into leading terms and the sub-leading terms of the soft expansion:

$$\begin{aligned} A_1 &= \bar{z}^2 B_1, & B_1 &= \ell^2, \\ A_2 &= \bar{z}^2 B_2, & B_2 &= (\ell - q)^2, \\ A_3 &= \bar{z}(B_3 + \delta B_3), & B_3 &= 2p_2(\ell - q), & \delta B_3 &= \bar{z}(\ell - q)^2, \\ A_4 &= \bar{z}(B_4 + \delta B_4), & B_4 &= -2p_1\ell, & \delta B_4 &= \bar{z}\ell^2. \end{aligned}$$

Since δB_3 and δB_4 are linear in \bar{z} , it is easy to expand the last two propagators as geometric series. This expansion leads to a series of box-like integrals expressed in terms of a topology defined by the leading propagators B_i :

$$I^{(S)} = \bar{z}^{d-6} \sum_{n,m} \bar{z}^{n+m} \int \frac{d^d \ell}{B_1^{1+n} B_2^{1+m} B_3^{1-m} B_4^{1-n}}. \quad (2.30)$$

where the leading order in \bar{z} is obtained when $n = m = 0$.

This leading integral can be computed using the Feynman parameters, grouping together B_1 with B_4 and B_2 with B_3 :

$$\frac{I_0^{(S)}}{z^{D-6}} = (-1) \int \frac{d^d \ell}{i\pi^{d/2}} \int_0^\infty d\alpha_1 d\alpha_2 \frac{1}{[\ell^2 - 2\alpha_1 p_1 \ell]^2 [(\ell - q)^2 + 2\alpha_2 p_2 (\ell - q)]^2}$$

We then notice that the two propagators can be written as $(l - \alpha_1 p_1)^2$ and $(l - q + \alpha_2 p_1)^2$ corresponding to a massless bubble with propagators raised by an additional power and central energy $s = (\alpha_1 p_1 + \alpha_2 p_2 - q)^2$. The resulting expression over the two parameters α_1 and α_2 becomes:

$$\frac{I_0^{(S)}}{z^{D-6}} = -(-1)^\epsilon \underbrace{\frac{\Gamma(-\epsilon)^2 \Gamma(2+\epsilon)}{\Gamma(-2\epsilon)}}_{-2^{\frac{1+\epsilon}{\epsilon}} C_\Gamma} \int_0^\infty \frac{d\alpha_1 d\alpha_2}{\left(\tilde{\lambda} \alpha_1 + (\lambda + \alpha_1) \alpha_2 - \frac{x \lambda \tilde{\lambda}}{2}\right)^{2+\epsilon}},$$

where $\lambda = 2p_2 \cdot q$ and $\tilde{\lambda} = 2p_1 \cdot q$ are the light-cone coordinates of q as defined in eq.(1.25). The integral in these two variables leads to a second order pole in ϵ which reflects the soft divergence:

$$\frac{I_0^{(S)}}{z^{-2-2\epsilon}} = -2(-1)^{-\epsilon} \left(1 - \frac{x}{2}\right)^{-1-\epsilon} \frac{C_\Gamma (\lambda \tilde{\lambda})^{-1-\epsilon}}{\epsilon^2} \left(\epsilon B\left(\frac{x}{2}; -\epsilon, \epsilon + 1\right) + \Gamma(1-\epsilon)\Gamma(\epsilon+1)\right), \quad (2.31)$$

with $B(x; a, b)$ the incomplete beta function, and the factor

$$C_\Gamma = \frac{\Gamma(1-\epsilon)^2 \Gamma(1+\epsilon)}{\Gamma(1-2\epsilon)}.$$

By means of the IBP identities, it is possible to show that of all the contributions in eq.(2.30) beside the leading order can be reduced to a bubble with e centre of mass energy of $s = x \tilde{\lambda} \lambda$.

In the case of a massless radiation (e.g. RV corrections), we have $x = 0$. Therefore the incomplete beta function becomes exactly zero as well as all the higher order corrections to the threshold expansion.

COLLINEAR REGION C1

In the collinear region C1 the loop momentum scales as follows:

$$l^2 \sim \bar{z}, \quad l \cdot p_1 \sim \bar{z}, \quad l \cdot p_2 \sim 1.$$

The light cone coordinates are therefore the best choice to investigate this sector:

$$l = (l^+, l^-, l_\perp), \quad l^\pm = \frac{l \cdot p_{1,2}}{p_1 p_2}, \quad l_\perp \sim \sqrt{\bar{z}}.$$

We can then proceed and extract the explicit \bar{z} scaling for each of the light cone components of the loop momentum:

$$\begin{aligned} l &= (l^+, l^-, l_\perp) = (\bar{z} \ell^+, \ell^-, \sqrt{\bar{z}} \ell_\perp) \\ \Rightarrow \quad \ell^2 &\sim 1, \quad \ell \cdot p_1 \sim 1, \quad \ell \cdot p_2 \sim 1. \end{aligned}$$

Using this rescale loop momentum, we rewrite the propagators extracting the leading behaviour around $\bar{z} = 0$:

$$\begin{aligned} A_1 &= \bar{z} B_1, & B_1 &= \ell^2, \\ A_2 &= \bar{z}(B_2 + \delta B_2), & B_2 &= (\ell - \tilde{\lambda} p_2)^2, & \delta B_2 &= -[\bar{z}(2\lambda \ell p_1 - q^2) - \sqrt{\bar{z}}(2\ell q_\perp)], \\ A_3 &= B_3 + \delta B_3, & B_3 &= 2\ell p_2, & \delta B_3 &= -[-\bar{z}((\ell - \tilde{\lambda} p_2)^2 - \lambda) \\ & & & & & + \bar{z}^{3/2}(2\ell q_\perp) + \bar{z}^2(2\lambda \ell p_1 - q^2)], \\ A_4 &= \bar{z} B_4, & B_4 &= \bar{z}(\ell - p_1)^2, \end{aligned}$$

The leading propagators are not linearly independent since $B_2 + \tilde{\lambda} B_3 = B_1$. Moreover, the threshold expansion of propagator A_2 and A_3 will introduce an additional scalar product $B_5 = 2\ell q_\perp$. The integrals appearing in the expansion in the collinear region will then be represented by integrals of the form:

$$I_{(\nu_1, \nu_2, \nu_3, \nu_4, \nu_5)}^{(C1)} = \int \frac{d^d \ell}{B_1^{\nu_1} B_2^{\nu_2} B_3^{\nu_3} B_4^{\nu_4} B_5^{\nu_5}}. \quad (2.32)$$

It is possible to generate two topologies composed only by linearly independent propagators by repeated application of partial fractioning through the operator:

$$1 = \frac{B_2 + \tilde{\lambda} B_3}{B_1}. \quad (2.33)$$

The topology characterized by the absence of B_3 is identically zero. This can be seen by noticing that the integral $I_{(\nu_1, 0, \nu_3, \nu_4, \nu_5)}^{(c1)}$ can only depend on two scalar products, namely q_\perp^2 and $p_1 p_2$. We then extract the dependence in these scalar products by acting with the two

orthogonal differential operators $p_2 \frac{\partial}{\partial p_2}$ and $q_\perp \frac{\partial}{\partial q_\perp}$. This basis of differential operator takes full advantage of the presence of the two linear propagators, namely B_3 and B_5 . We then write:

$$\begin{aligned} q_\perp^\mu \frac{\partial}{\partial q_\perp^\mu} I_{(v_1,0,v_3,v_4,v_5)}^{(c1)} &= -v_5 I_{(v_1,0,v_3,v_4,v_5)}^{(c1)}, \\ p_2^\mu \frac{\partial}{\partial p_2^\mu} I_{(v_1,0,v_3,v_4,v_5)}^{(c1)} &= -v_3 I_{(v_1,0,v_3,v_4,v_5)}^{(c1)} \end{aligned}$$

which results into,

$$I_{(v_1,0,v_3,v_4,v_5)}^{(c1)} = (p_1 \cdot p_2)^{-v_4} (q_\perp^2)^{-v_5} C_{(v_1,0,v_3,v_4,v_5)}. \quad (2.34)$$

where $C_{(v_1,0,v_3,v_4,v_5)}$ represents some dimensionless function. From this we can argue that the dimension of the integral $I_{(v_1,0,v_3,v_4,v_5)}^{(c1)}$ is the same as $(p_h^2)^{-v_4-v_5}$. At the same time by looking at the integral representation in eq.(2.32), we can conclude that the dimension is $(p_h^2)^{\frac{d}{2}-v_1-v_3-v_4-v_5}$. Because of the dependence on the dimension $d = 4 - 2\epsilon$, the only way in which these two results could be compatible is if the integral itself is zero.

Now that we have all the ingredients we can get a first approximate solution for the collinear region (C1) by expanding the expression for $I^{(C1)}$ as a geometric series in the sub-leading terms:

$$\begin{aligned} I^{(C1)} &= \bar{z}^{\frac{d}{2}-3} \sum_{n,m} \int d\ell \frac{(-\delta B_2)^n (-\delta B_3)^m}{B_1^{v_1} B_2^{v_2+n} B_3^{v_3+m} B_4^{v_4}}, \\ &= \bar{z}^{\frac{d}{2}-3} \sum_{n,m} \bar{z}^m \int d\ell \frac{[\sqrt{\bar{z}} B_5 + \bar{z}(\lambda B_1 - \lambda B_4 - q^2)]^n [\lambda - B_2 + \sqrt{\bar{z}} B_5 + \bar{z}(\lambda B_1 - \lambda B_4 - q^2)]^m}{B_1^{v_1} B_2^{v_2+n} B_3^{v_3+m} B_4^{v_4}}, \end{aligned}$$

The leading order can be read by looking at the $m = n = 0$ and by using the partial fraction identity in eq.(2.33) we obtain an integral that can be reduced to a bubble yielding,

$$\begin{aligned} I_0^{(C1)} &= -\bar{z}^{-1-\epsilon} \frac{2(1-2\epsilon)}{\tilde{\lambda}(1+\epsilon)} Bub(-\tilde{\lambda}; 1, 1) \\ &= -(\tilde{\lambda}zb)^{-1-\epsilon} \frac{2C_\Gamma}{\epsilon(1+\epsilon)}. \end{aligned} \quad (2.35)$$

Where we use the expression for the bubble integral computed in eq.(1.47).

COLLINEAR REGION C2

The conditions for the loop momentum to be collinear to p_2 are:

$$l^2 \sim \bar{z}, \quad l \cdot p_1 \sim 1, \quad l \cdot p_2 \sim \bar{z}.$$

This leads to the following expansion for the propagators around $\bar{z} = 0$:

$$\begin{aligned}
A_1 &= \bar{z}B_1, & B_1 &= \ell^2, \\
A_2 &= \bar{z}(B_2 + \delta B_2), & B_2 &= (\ell - \lambda p_1)^2, & \delta B_2 &= -[\bar{z}\tilde{\lambda}(2\ell p_2 - q^2) + \sqrt{\bar{z}}(2\ell q_\perp)], \\
A_3 &= \bar{z}(B_3 + \delta B_2), & B_3 &= (\ell - \lambda p_1 + p_2)^2, \\
A_4 &= -(B_4 + \delta B_4), & B_4 &= 2\ell p_1, & \delta B_4 &= -\bar{z}\ell^2.
\end{aligned}$$

The topology defined by this set of propagators can be mapped to the one corresponding to the collinear region C1 using the shift $l \rightarrow l + \lambda p_1$. This transformation corresponds to exchanging $\tilde{\lambda} \rightarrow -\lambda$ in the integrated expressions. The leading term then reads:

$$\begin{aligned}
I_0^{(C2)} &= -\bar{z}^{-1-\epsilon} \frac{2(1-2\epsilon)}{\lambda(1+\epsilon)} \text{Bub}(-\lambda; 1, 1) \\
&= -(\lambda z b)^{-1-\epsilon} \frac{2C_\Gamma}{\epsilon(1+\epsilon)}
\end{aligned} \tag{2.36}$$

HARD REGION

We now consider the loop momentum to be hard compared with the soft scale \bar{z} , therefore scaling as $l \sim 1$. Dividing each propagator into the part that depends on \bar{z} and the one that does not leads to:

$$\begin{aligned}
A_1 &= B_1, & B_1 &= l^2, \\
A_2 &= B_1 + \delta B_1, & \delta B_1 &= -\bar{z}[2ql - \bar{z}q^2], \\
A_3 &= B_2 + \delta B_2, & B_2 &= (l + p_2)^2, & \delta B_2 &= -\bar{z}[2q(l + p_2) - \bar{z}q^2], \\
A_4 &= B_3, & B_3 &= (l - p_1)^2.
\end{aligned}$$

The number of independent propagators at leading order in the threshold expansion is reduced to three. Yet, the geometric expansion of the linear terms in \bar{z} gives rise to two terms at the numerator with a dependence on the scalar product $B_4 = 2q \cdot l$. We can use this scalar product to complete the topology. The expansion can then be written as:

$$I^{(H)} = \sum_{n,m} \bar{z}^{n+m} \int \frac{d^D l [B_4 - \bar{z}q^2]^n [B_4 - (2qp_2 + \bar{z}q^2)]^m}{B_1^{2+n} B_2^{1+m} B_3}$$

All the integrals of this expansion can be written in terms of a simple bubble diagram. This is a consequence of applying the reduction to integrals that have B_4 always appearing with $\nu_4 < 0$. In the hard case the leading order term reads:

$$\begin{aligned} I_0^{(h)} &= -\frac{2(1-2\epsilon)}{s^2(1+\epsilon)} \text{Bub}(s; 1, 1) \\ &= (-s)^{-1-\epsilon} \frac{2C_\Gamma}{\epsilon(1+\epsilon)} \end{aligned} \quad (2.37)$$

THRESHOLD EXPANSION SYSTEM

The power expansion around the threshold region $\bar{z} = 0$ is resolved in two ways. We either compute the integrals appearing in the explicit expansions as shown above or by using differential equations.

The integrand approach could become computationally expensive, like in the case of the two collinear limits, where the presence of square roots forces us to expand twice as many terms as the order we wish to reach in the soft parameter. Once the integrand expansion is completed, we still need to reduce all the integrals in terms of master integrals and then compute them. One way to compute these soft master integrals is to solve their differential equations as expansions in ϵ [51, 52, 56].

Alternatively, we can extract the threshold expansion coefficients through differential equations with respect to \bar{z} as presented in section 2.2.1, using as boundary conditions the leading terms of the expansion by regions computed above. The box integrals is cast into the topology $I_{(\nu_1, \nu_2, \nu_3, \nu_4)}$ defined by the propagators in eq.(2.29). We then end up with a set of master integrals, consisting of four bubbles and one box, for which we can write the following differential equations:

$$\frac{\partial}{\partial \bar{z}} \vec{M}(x, \lambda, x, s) = A_{\bar{z}} \cdot \vec{M}(x, \lambda, x, s), \quad \vec{M}(x, \lambda, x, s) = \begin{pmatrix} I_{(0,1,0,1)} \\ I_{(0,1,1,0)} \\ I_{(1,0,0,1)} \\ I_{(1,0,1,0)} \\ I_{(1,1,1,1)} \end{pmatrix}. \quad (2.38)$$

With the differential matrix defined as:

$$A_{\bar{z}} = \begin{pmatrix} a_{11} & 0 & 0 & 0 & 0 \\ 0 & a_{22} & 0 & 0 & 0 \\ 0 & 0 & a_{33} & 0 & 0 \\ 0 & 0 & 0 & a_{44} & 0 \\ a_{15} & a_{25} & 0 & a_{45} & a_{55} \end{pmatrix} \quad (2.39)$$

with the non-zero elements given by:

$$\begin{aligned} a_{11} &= -\frac{(x\bar{z}(\lambda x\bar{z} - 2) + 1)\epsilon}{\bar{z}(x\bar{z} - 1)(\lambda x\bar{z} - 1)}, & a_{22} &= \frac{\epsilon}{1 - \bar{z}}, \\ a_{33} &= \frac{(2 - \lambda x\bar{z})\epsilon}{\bar{z}(\lambda x\bar{z} - 1)}, & a_{44} &= -\frac{\epsilon}{\bar{z}}, \\ a_{15} &= \frac{2(\lambda x\bar{z} - 1)(1 - 2\epsilon)}{\lambda\bar{z}^2(\lambda(x - 1)\bar{z} + \bar{z} - 1)(x\bar{z} - 1)}, & a_{45} &= \frac{2(1 - 2\epsilon)}{(1 - \lambda)\bar{z}^2(\lambda\bar{z} - 1)}, \\ a_{25} &= \frac{2(\lambda x\bar{z} + \bar{z} - 2)(1 - 2\epsilon)}{(1 - \bar{z})\bar{z}(\lambda\bar{z} - 1)(\lambda(x - 1)\bar{z} + \bar{z} - 1)}, & a_{55} &= -\frac{(\lambda x\bar{z} - 2)(1 + \epsilon)}{\bar{z}(\lambda x\bar{z} - 1)}. \end{aligned}$$

The space of solutions supported by this set of differential equations is constrained to the three sectors corresponding to $-\alpha\epsilon$ with $\alpha = \{0, 1, 2\}$, matching the constraints coming from the boundary conditions. We also have that the space of solutions matches the leading powers of the boundary conditions, meaning that we only need to fix the coefficients of the leading terms. Moreover, since all higher terms coefficients are expressed in terms of these boundary terms, we can conclude that all the integrals appearing in the expansions above can be reduced using the IBP identities to the integrals appearing at leading order.

2.3 THRESHOLD EXPANSIONS FOR HIGGS-DIFFERENTIAL CROSS-SECTIONS

As we approach the production threshold, the parameter \bar{z} tends to zero. To obtain the expansion of the Higgs-differential cross-section around this limit, we perform a systematic expansion of the partonic coefficient functions:

$$\eta_{ij}^{(n)}(z, x, \lambda) = \eta_{ij}^{(n,SV)}(z, x, \lambda) + \sum_{i=0}^{\infty} \bar{z}^i \eta_{ij}^{(n,i)}(z, x, \lambda). \quad (2.40)$$

We separated the leading term in the expansion, indicated by the superscript (SV) , commonly referred to as the soft-virtual contribution. This particular term is singular as $\bar{z} \rightarrow 0$ and acts

as a distribution on the measurement function and the parton distribution functions as we explain below. All higher power terms depend on z in the form of polynomials of logarithms $\log(1-z)$. The individual terms $\eta_{ij}^{(n,i)}(z, x, \lambda)$ depend on the threshold variable \bar{z} in the form of polynomials of logarithms of the form $\log(\bar{z})$. In ref. [2] we obtain the first and second term in the threshold expansion for all required partonic coefficient functions.

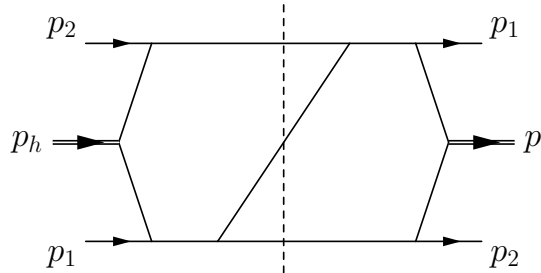
The purely virtual matrix elements are independent of the expansion parameter and were computed in refs. [174]. Matrix elements with two loop and one emission were computed in refs. [141, 144, 145] and recomputed for the purpose of our expansion and are known to all orders in \bar{z} .

In this section, we describe our method to perform a threshold expansion at the integrand level for the N³LO coefficient functions that involve two or more partons. We start by considering matrix elements that correspond to purely real radiation diagrams and contain no closed loops, and then we address the case of virtual radiations.

2.3.1 Triple-Real threshold expansion

Consider as an example the following scalar phase space integral:

$I(p_1, p_2, k) =$



$$= \int d\Phi_3 \frac{1}{p_{23}^2 p_{25}^2 p_{34}^2 p_{45}^2 p_{134}^2 p_{145}^2}, \quad p_{i_1 \dots i_n} = p_{i_1} + \dots + p_{i_n} \quad (2.41)$$

In the above picture, solid lines correspond to scalar propagators, doubled line to massive external legs, and lines crossed by the dashed line represent the on-shell constraints of the phase space integration measure.

The threshold limit corresponds to the kinematic configuration where all radiation produced in association with the Higgs boson is uniformly soft. It is thus natural to perform the variable transformation $p_f \rightarrow \bar{z} p_f$ [140]. Here, p_f indicates the momentum of any final state parton, which can be identified in (2.41) by the momenta crossing the dashed line, namely p_3 , p_4 and

p_5 . This rescaling induces a transformation on the phase space measure $d\Phi_3 \rightarrow z^{2d-6}d\Phi_3$ contained in (2.41) given that $k \rightarrow \bar{z}k$.

Performing a series expansion of the integrand yields

$$\begin{aligned} I(p_1, p_2, \bar{z}k) &= \bar{z}^{2d-14} \left[\int d\Phi_3 \frac{1}{(2p_2p_3)(2p_2p_5)p_{34}^2p_{45}^2(2p_1p_{34})(2p_1p_{45})} + \mathcal{O}(\bar{z}^1) \right] \\ &= \bar{z}^{2d-14} \left[I^{(0)} + \bar{z}I^{(1)} + \dots \right]. \end{aligned} \quad (2.42)$$

Every term in the soft expansion of a Feynman integral can be written in terms of a linear combination of soft integrals as already observed in ref. [128, 175]. Soft integrals are Feynman integrals that are independently homogeneous under rescaling of the initial momenta p_1, p_2 or all momenta in the integral simultaneously.

To illustrate this property, let us look at what happens to the integral $I^{(0)}$ in eq.(2.42) as we rescale $p_1 \rightarrow \lambda_1 p_1$.

$$I^{(0)} \rightarrow \lambda_1^{\gamma_1} I^{(0)}. \quad (2.43)$$

The associated rescaling dimension can be easily read off the integral and in this specific case we find $\gamma_1 = -2$.

More generally, for a soft integral one can write the following scaling behaviours:

$$\begin{aligned} p_1 \rightarrow \lambda_1 p_1 : \quad & I_s \rightarrow \lambda_1^{\gamma_1} I_s, \\ p_2 \rightarrow \lambda_2 p_2 : \quad & I_s \rightarrow \lambda_2^{\gamma_2} I_s, \\ \{p_1, p_2, p_f, k\} \rightarrow \lambda_3 \{p_1, p_2, p_f, k\} : \quad & I_s \rightarrow \lambda_3^{\gamma_3} I_s. \end{aligned} \quad (2.44)$$

The last relation denotes a rescaling of the momenta in the curly bracket. Note that the respective scaling dimensions γ_i will depend in general on the specific integral in question, but for simplicity we write them without any argument.

We realize that the integrated soft integrals are functions of four Lorentz invariant scalar products $s, k^2, 2p_1k$ and $2p_2k$. We can use the scaling behaviour of our soft integrals to determine its functional dependence on three of the four scalar products. Consequently, the soft integrals depend on one variable that is invariant under any of the three rescaling symmetries. This invariant cross ratio is given by the dimensionless variable $x = \frac{k^2 s}{2k p_1 2k p_2}$. Combining these properties we are able to write:

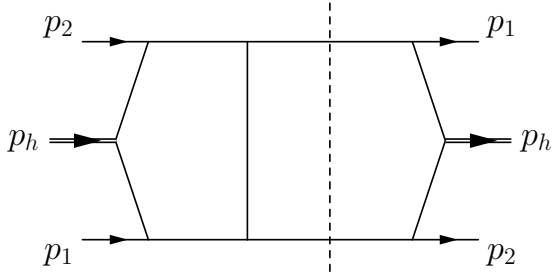
$$I_s(s, k^2, 2k p_1, 2k p_2) = s^{\gamma_1 + \gamma_2 - \gamma_3/2} (2k p_1)^{\gamma_3/2 - \gamma_2} (2k p_2)^{\gamma_3/2 - \gamma_1} \tilde{I}_s(x). \quad (2.45)$$

Once our integrand is expressed in terms of integrals that only depend on the cross ratio x we can use standard phase space integral techniques to compute these functions. In particular, we employ the framework of reverse unitarity [126, 137–139, 176] to express our differential partonic cross sections in terms of a few soft master integrals. Subsequently, we make use of the method of differential equations [51, 52, 56] to compute our soft master integrals. The soft expansion greatly simplifies these steps as in the expression above we only need to maintain functional dependence on x . The resulting functions are harmonic polylogarithms [53] in the x variable.

Note, that so-far we did not apply the relation among the invariants that arises due to the on-shell constraint for the Higgs boson, $p_h^2 - m_h^2 = s + 2kp_2 + 2kp_3 + k^2 - sz = 0$. This relation is inhomogeneous under rescaling the final state momenta k and will introduce sub-leading terms in the \bar{z} expansion. In ref. [141] this issue was solved by performing a systematic expansion of the on-shell constraint by including it in the reverse unitarity method. Here, we choose to impose the aforementioned on-shell constraint only after reduction to master integrals.

2.3.2 Double-Real-Virtual threshold expansion

Let us consider an integral that appears in with one virtual correction:



$$I(p_1, p_2, k) = \int d^d l \int d\Phi_2 \frac{1}{p_{23}^2 p_{25}^2 p_{34}^2 p_{45}^2 p_{134}^2 p_{145}^2}, \quad p_{i_1 \dots i_n} = p_{i_1} + \dots + p_{i_n} \quad (2.46)$$

When considering the threshold limit parametrizing the final states as $\bar{z}p_f$, the phase space will gain an additional overall factor transforming as $d\Phi_2 \rightarrow z^{d-4}d\Phi_2$. The computation of the family of RRV integrals follows the same procedure that was presented in the previous section for the non-planar box diagram, where one must be careful and expand around the various regions of the loop momentum. These expansions were also addressed in much details in ref. [128] and we refrain from repeating the procedure here.

Once the loop and phase space integrand is expanded, we perform a reduction of the loop integrals to loop master integrals. The initial step of performing the reduction of loop integrals allows us to determine the rescaling behaviour of the loop integrals under the scaling transformations introduced in eq. (2.44). Next, we embed the loop master integrals again in terms of their Feynman propagator representation into the phase space integration and we subsequently perform the combined loop and phase space integral in the same fashion as the pure phase space integrals discussed above (i.e. via reverse unitarity and differential equations). Again, we benefit from having only to maintain functional dependence on the cross-ratio x by inferring the dependence of our integral on the other variables from its behaviour under scaling transformations. The relations between the different orders in the threshold expansion are then compared with the expansion using the differential equations in \bar{z} .

With the techniques discussed thus far, we can perform a threshold expansion of the partonic Higgs differential cross sections at arbitrary order in the strong coupling constant and to arbitrary power in \bar{z} . Specifically, we perform the computation of tree-level partonic cross-sections with three partons in the final state and partonic cross-section with one loop and two partons in the final state to first and second order in the threshold expansion. As a result, we obtain all ingredients to compute the first and second term in the threshold expansion of the N³LO Higgs-differential cross-section. The extension of the threshold expansion to higher powers is discussed in the next chapter in the context of obtaining the Higgs rapidity distribution.

2.4 VALIDATING THE THRESHOLD EXPANSION FOR DIFFERENTIAL OBSERVABLES AT NNLO

When we consider the proton-proton collision at a fixed centre of mass energy, we can understand the probability of collision for two constituent partons as a function of the partonic centre of mass energy s . This probability is falling as s rises. In particular, it falls faster when we consider two gluons compared with two quarks or a gluon-quark pair (see for reference figure 1.3). As the main source of production of the Higgs boson at the LHC are two colliding gluons, this implies that there is a kinematic enhancement for the Higgs boson to be produced from a system of gluons with as little energy as possible.

In the past, this simple kinematic consideration was exploited to derive simplifications for the prediction of Higgs boson cross-sections. Perturbative NNLO [125] and N³LO [26] corrections were approximated in the form of an expansion around the threshold. For the

inclusive cross-section, this approximation is at an astonishing precision when compared with the result at all order in \bar{z} as computed in ref. [27]. Factorisation properties of the leading term in the threshold expansion are commonly exploited to perform all order resummation of threshold enhanced terms. In this section, we will analyse the performance of an expansion of partonic Higgs-differential cross-sections around the production threshold.

As the partonic differential cross sections were computed analytically as a function of \bar{z} in ref. [1] we can easily perform a threshold expansion a posteriori. In the following we want to study the quality of this approximation as higher and higher terms in the expansion are included for differential observables. In order to do so, we compute the rapidity and transverse momentum distribution of the Higgs boson. The threshold expansion is performed only on the matrix elements occurring at NNLO while the lower order elements are kept exact. This allows analysing the effect of performing the expansion only on the highest correction as will be the case for the N³LO distributions. We then truncate the expansion at different orders and compare with the exact results.

To derive numerical values we numerically perform the remaining integrals in eq. (1.7) over the partonic cross sections in conjunction with MMHT2014 parton distribution functions [120] in a private C++ implementation. We perform renormalisation and convolutions with the mass factorisation counter terms numerically. We only expand the partonic NNLO matrix elements around the production threshold. This leads to a mismatch in the cancellation of infrared and ultraviolet divergences which are treated in the framework of dimensional regularisation. Specifically, the cancellation of poles in the dimensional regulator is only given up to the respective order in the threshold expansion at which we truncate.

Let us first consider the inclusive cross-section produced at a perturbative scale $\mu = m_h$. In refs. [177] similar studies were performed for the inclusive cross-section at NNLO, and our findings agree. We show the inclusive cross-section through NNLO in fig. 2.3 for different truncation orders. The first few terms in the threshold expansion (in red) significantly deviate from the exact result (in blue). After the first five terms, the expansion stabilizes and subsequent terms gradually improve the result. The agreement after including five terms in the expansion is fairly good. Further improvement is achieved at a comparably slow rate. This slow convergence of the remaining difference to the exact result can be attributed to explicit divergences of the partonic coefficient functions at the high energy limit $z = 0$. Similar behaviour was observed for the expansion of the N³LO corrections to the inclusive cross-section in refs. [26, 177, 178].

In figure 2.4 we show the rapidity and transverse momentum distribution. Increasing truncation order of the threshold expansion is indicated by increasingly dark shades of red and the exact result in blue. As for the inclusive cross-section we observe that the first few terms

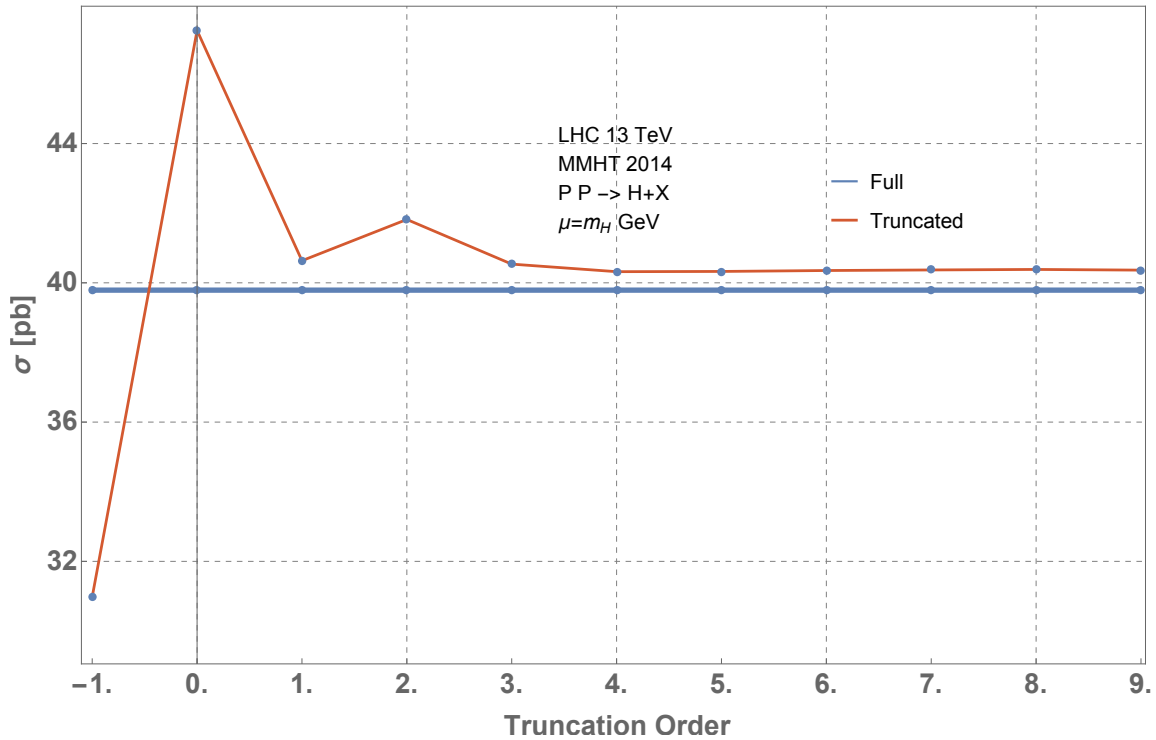


FIGURE 2.3: Inclusive production probability for a Higgs boson as a function of the truncation order of the expansion for the NNLO correction (red). The blue line represents the unexpanded NNLO inclusive cross section.

display large variations from the full result. After about five terms, the expansion stabilizes and adding higher terms shows gradual improvements on the approximation.

The actual quality of the expansion can be studied in more detail by analyzing the relative deviations of the expanded distributions from the full result. In fig. 2.5 we show the rapidity and transverse momentum distribution normalized to the respective unexpanded distributions. We note that by including only the third term in the expansion, the rapidity distribution at NNLO is approximated to a level better than five percent. The transverse momentum distribution is improved as higher terms in the expansion are included. However, even with ten terms in the expansion, the overall agreement between the exact result and the expansion is merely at the level of ten percent.

At large rapidities, the quality of the threshold expansion deteriorates as the Higgs boson is produced with a larger boost along the beam axis and thus on average more energy is in the final state system. The stark difference between the behaviour of the rapidity and of the transverse momentum distribution can be understood by considering the structure of the partonic coefficient functions. The transverse momentum of the Higgs boson is identically zero at leading order as there is no parton produced for the Higgs boson to recoil against. At the

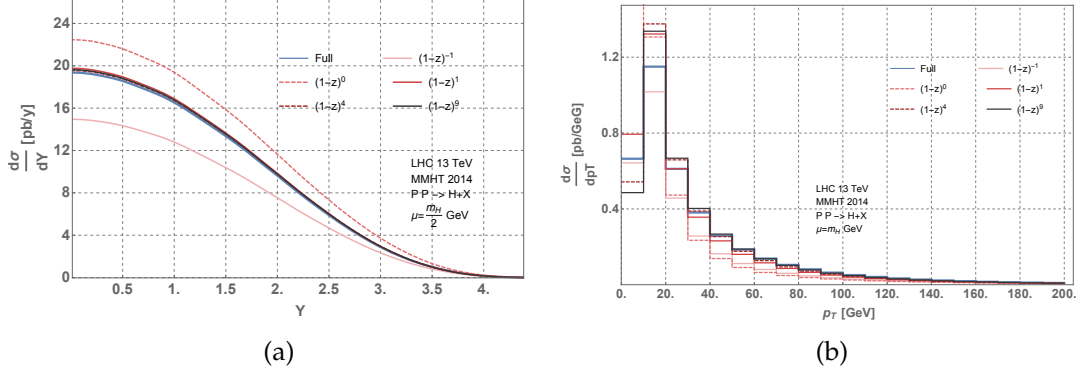


FIGURE 2.4: NNLO rapidity (left) and transverse momentum (right) distribution for the Higgs boson. The blue line represents the exact result. Increasingly darker shades of red represent higher and higher truncation order of the threshold expansion.

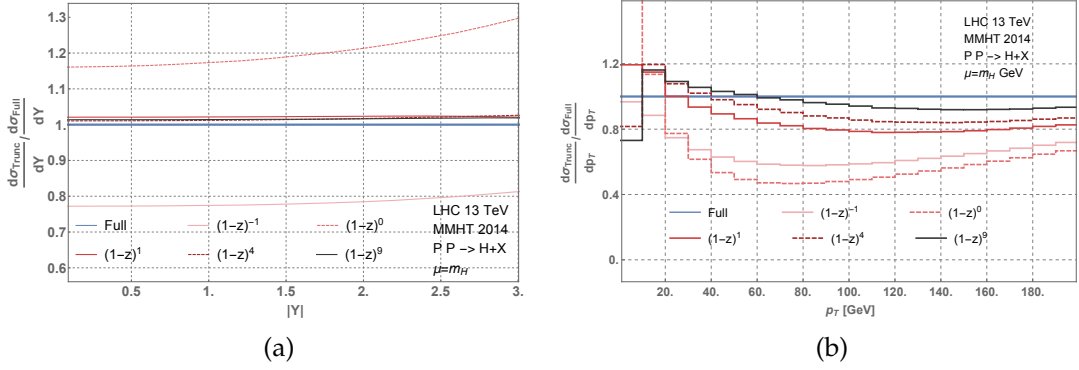


FIGURE 2.5: NNLO rapidity (left) and transverse momentum (right) distribution for the Higgs boson at different truncation orders of the threshold expansion normalized to the exact NNLO distributions.

kinematic threshold, all radiation produced in association with the Higgs boson is soft and does not provide any recoil either. Adding terms in the threshold expansion only gradually builds up the functional dependence of the matrix elements on the transverse momentum. At the same time, the partonic matrix elements are singular as the transverse momentum of the Higgs boson vanishes. The partonic transverse momentum distribution contains kinematic singularities at finite values of \bar{z} that are expanded by the threshold expansion. This leads to a slower convergence compared to the rapidity distribution.

We can conclude that the quality of a threshold expansion is subject to the particularities of individual observables. If such an expansion is to be used to approximate cross-section predictions, a dedicated analysis of the quality of the approximation has to be performed for the corresponding observable. Complementing threshold expansions with higher order in the in \bar{z} in the rapidity of the Higgs boson is the subject of the next chapter.

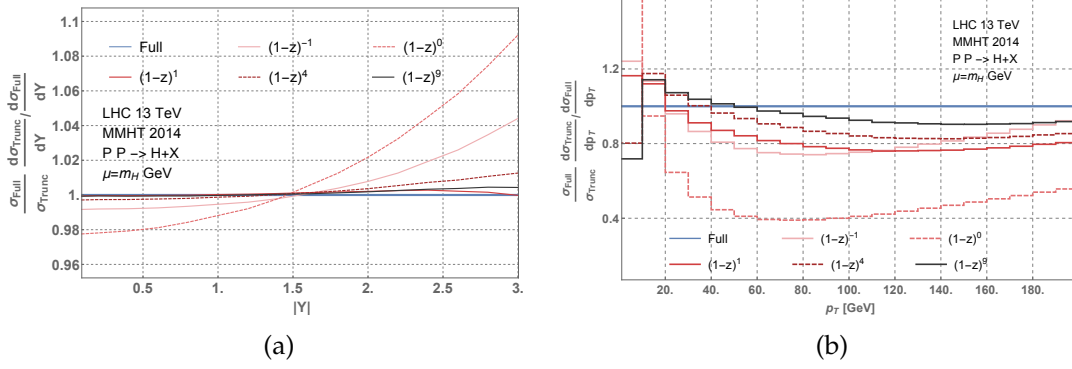


FIGURE 2.6: NNLO rapidity (left) and transverse momentum (right) distribution for the Higgs boson normalized to the exact NNLO distributions. The expanded distributions are weighted such that their cumulant reproduces the unexpanded NNLO cross section.

It is commonly the case that predictions for inclusive cross sections become available prior to predictions for exclusive observables. Suppose this was the case for NNLO Higgs differential cross sections. In this case we could approximate differential cross sections at NNLO by performing a threshold expansion. To further improve the expanded results we could ensure that the inclusive cross section is reproduced by the differential approximation and only shapes are computed by the approximated result. We define the improved Higgs differential cross section to be

$$\sigma_{PP \rightarrow H+X}^{\text{Improved}}[\mathcal{O}] = \frac{\sigma_{\text{Full}}}{\sigma_{\text{Expanded}}} \sigma_{PP \rightarrow H+X}^{\text{Expanded}}[\mathcal{O}]. \quad (2.47)$$

Here, σ_{Full} and σ_{Expanded} are the inclusive cross section without and with expanding around the threshold limit respectively. $\sigma_{PP \rightarrow H+X}^{\text{Expanded}}[\mathcal{O}]$ is the Higgs differential cross section based on partonic coefficient functions approximated by a threshold expansion.

We show predictions for the rapidity and transverse momentum distribution based on the improved approximation in fig. 2.6 normalized to their exact counterparts. The effect of the rescaling is largest for low truncation order where the difference between the inclusive cross-section based on the expansion and the full result is largest. We observe that the rapidity distribution is approximated at a level significantly better than two percent including just three terms in the threshold expansion throughout the rapidity interval $[0, 3]$. The significant deviations of the shape of the transverse momentum distribution based on the threshold expansion are only mildly impacted by rescaling the distribution to the correct inclusive cross-section.

2.5 APPROXIMATED N³LO CROSS SECTION

In this section, we discuss the final ingredients to promote the Higgs-differential cross-section to distributions. When computing any hadronic observable, we require the parton distribution functions $f(x, Q^2)$ as external inputs which are provided in the form of grids in (x, Q^2) space. We observed in [2] that default way in which LHAPDF interpolates the grid through a log-cubic spline was producing numerical artefacts due to the presence of logarithms of order 5 in the rapidity distribution. This problem has been resolved by using LHAPDF for performing the μ evolution of the PDFs and then using a private interpolator that uses polynomial of order 16 in $\log(x)$ space. By means of this higher order interpolation, it was possible to obtain smooth distributions.

2.5.1 Exact Scale Variation at N³LO

After ultraviolet (UV) renormalization of the coupling constant and the Wilson coefficient, and after suitable redefinition of the parton distribution function, the Higgs differential cross-section takes its final and finite form. The coefficient of α_S^3 can be written as

$$\tilde{\eta}_{ij}^{(3)}(z, x, \lambda, L_\mu) = \sum_{i=-3}^0 \left[\epsilon^i \left(\frac{m_h^2}{\mu^2} \right)^{-3\epsilon} \eta_{ij}^{(3,i)}(z, x, \lambda) + \epsilon^i C_T^{(3,i)}(z, x, \lambda, L_\mu) \right] + \mathcal{O}(\epsilon). \quad (2.48)$$

Here $L_\mu = \log\left(\frac{m_h^2}{\mu^2}\right)$. The coefficients $C_T^{(3,i)}$ correspond to the Laurent series coefficients of the sum of UV renormalization counter term and mass factorization counter term. They are constructed in the usual way in terms of lower order cross-sections and universal anomalous dimensions and splitting functions [1]. The renormalized coefficient function is finite as the residual poles of the partonic coefficient function and the counter terms cancel. consequently we find

$$\eta_{ij}^{(3,i)}(z, x, \lambda) = -C_T^{(3,i)}(z, x, \lambda, 0), \quad i < 0. \quad (2.49)$$

It is thus easy for us to construct these coefficients explicitly. Utilizing the above identity we may write the finite term of the N³LO coefficient function as

$$\begin{aligned} \tilde{\eta}_{ij}^{(3,0)}(z, x, \lambda, L_\mu) &= \eta_{ij}^{(3,0)}(z, x, \lambda) + C_T^{(3,0)}(z, x, \lambda, L_\mu) + 3C_T^{(3,-1)}(z, x, \lambda, 0) L_\mu \\ &\quad - \frac{9}{2} C_T^{(3,-2)}(z, x, \lambda, 0) L_\mu^2 + \frac{9}{2} C_T^{(3,-3)}(z, x, \lambda, 0) L_\mu^3 \end{aligned} \quad (2.50)$$

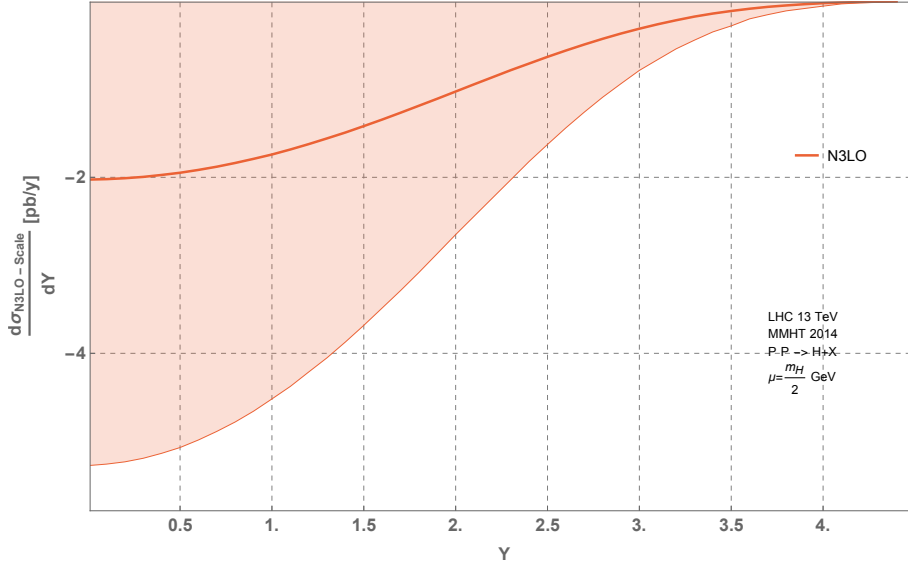


FIGURE 2.7: $N^3\text{LO}$ correction to the rapidity distribution arising from coefficients of logarithms of the perturbative scale μ . The band corresponds to a variation of the scale within the interval $\mu \in [m_h/4, m_h]$.

Where all contributions explicitly depending on the perturbative scale μ of the $N^3\text{LO}$ coefficient functions are known. Additional dependence on the perturbative scale μ arises due to the multiplication of the partonic coefficient functions with the Wilson coefficient and due to the dependence of the strong coupling constant, the Wilson coefficient and the parton distribution functions on the perturbative scale.

We now present the impact of all contributions of the α_S^3 coefficient on the Higgs-differential cross-sections. Specifically, we compute contributions to the rapidity distribution for the Higgs boson given by all ingredients that explicitly contain a logarithm L_μ . We include the partonic coefficient function at $N^3\text{LO}$ as

$$\tilde{\eta}_{ij, \text{RGE}}^{(3,0)}(z, x, \lambda, L_\mu) = \tilde{\eta}_{ij}^{(3,0)}(z, x, \lambda, L_\mu) - \tilde{\eta}_{ij}^{(3,0)}(z, x, \lambda, 0) \quad (2.51)$$

as well as all contributions to the α_S^3 coefficient of the cross section containing renormalization group logarithms that arise due to the multiplication of the Wilson coefficient with lower order coefficient functions. We thus obtain all contributions to the $N^3\text{LO}$ correction to the Higgs differential cross section involving explicit RGE logarithms.

We show the numerical impact of the contributions involving RGE logarithms on the $N^3\text{LO}$ corrections to the rapidity distribution of the Higgs boson in fig. 2.7. We choose $\mu = \frac{m_h}{2}$ as a central scale which results in the prediction given by the solid line. The red bands correspond to a variation of the perturbative scale in the interval $\mu \in [\frac{m_h}{4}, m_h]$. The contribution is monotonously rising as we increase the perturbative scale. At $\mu = m_h$ the argument of the RGE

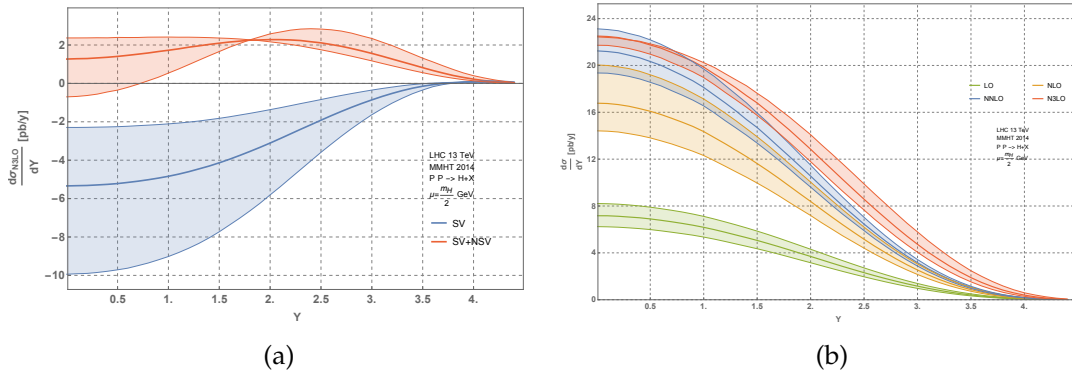


FIGURE 2.8: The left plot shows the contribution of the N³LO partonic cross section to the distribution of the absolute value of the rapidity of the Higgs boson approximated by including the first (blue) and by including the first and second (red) term in the threshold expansion. N³LO contributions were approximated by performing a threshold expansion through the second term.

logarithm is one, and the contribution considered here is identically zero. The corresponding inclusive cross-section agrees for all scales with the results of ref. [26]. The contribution presented here on its own does not allow for an improved prediction at N³LO since the finite coefficient functions without any RGE logarithms are still missing. However, it represents one more essential stepping stone towards Higgs differential cross sections at N³LO.

2.5.2 Numerical Results for approximate differential Distributions at N³LO

In section 2.4 we discussed the phenomenological implications of performing a threshold expansion for Higgs-differential cross-sections at NNLO. The findings clearly indicate that several terms in the expansion are required. Particularly, predictions made by performing the threshold expansion to only the first or second order displayed sizable deviations from the true result.

We implemented the analytical results we obtained for the partonic coefficient functions in terms of the first and second term in the threshold expansion into a private C++ code. Furthermore, we combine our new results with our computation of the exact scale variation contributions obtained in section 2.5.1. We show our results for the N³LO corrections to the rapidity distribution of the Higgs boson in figure 2.8a. Results including only the first term in the threshold expansion are shown in blue and including also the second term in red. The bands correspond to variations of the perturbative scale around the central value $\mu = \frac{m_h}{2}$ by a factor of two. It is evident that the two predictions based on the first and second order expansion wildly differ which confirms our expectation from the analysis at NNLO. While the scale variation of the correction to the rapidity distribution based on the leading term in the

threshold expansion is monotonously increasing with the scale the second order approximation is not. The negative contributions arising from the the explicit RGE logarithms are, depending on the exact value of the scale, compensated by the positive contributions arising from the $N^3\text{LO}$ coefficient function and the Wilson coefficient. In figure 2.8b we combine the predictions for the corrections to the rapidity distribution at $N^3\text{LO}$ based on the the first and second term in the threshold expansion with lower order results (in red). Exact lower order results are shown for LO, NLO and NNLO in green, yellow and blue respectively. We observe a fairly large impact of the approximate $N^3\text{LO}$ corrections on the rapidity distributions.

The inclusive cross section obtained with our current next-to-soft coefficient functions differs significantly from the inclusive cross section obtained in ref. [26]. Our approximate results show large differences between the two newly computed terms. This confirms our NNLO analysis that demonstrates that an approximation based only on the first and second term in the threshold expansion is insufficient in order to improve on currently existing phenomenological predictions. Further subleading terms in the threshold expansion or a complete computation are required.

2.6 CONCLUSION

We achieve several key steps towards predicting differential observables to $N^3\text{LO}$ in pQCD. We illustrate how a systematic expansion around the production threshold of Higgs-differential cross-sections can be performed to arbitrary order and presented a set of tools to perform such an expansion. We apply this method to obtain the first and second term in the threshold expansion of the $N^3\text{LO}$ coefficient functions in analytical form. This analytic data represented a cornerstone of a complete $N^3\text{LO}$ calculation as it constitutes the complete soft limit of the cross-section and contains vital boundary information for the computation of master integrals via differential equations and are provided as ancillary files in ref. [2] in the form of Mathematica readable regularized expressions as presented in section 1.5. Furthermore, the obtained information may in future work serve as data to extract anomalous dimension for the resummation of logarithms in the transverse momentum of the Higgs boson.

Furthermore, we analyze the performance of a threshold expansion for the Higgs-differential cross-section. We start by considering corrections at NNLO, for which also the exact result is known. Analyzing the analytic structure of the NNLO coefficient functions shows that their threshold expansion is convergent within the unit interval of the threshold parameter \bar{z} . When studying the inclusive cross-section in the threshold expansion, we observe an oscillatory behaviour of the series when only including the first three powers in \bar{z} . The series then stabilizes

within the inclusion of the first five coefficients, resulting in a difference of 3% compared to the full NNLO result. Further improvements due to including even higher order terms are comparably slow.

Next, we analyze the quality of differential predictions obtained with threshold expansions. The rapidity distribution of the Higgs boson at NNLO displays similar behaviour as the inclusive cross-section. Including about five terms stabilizes initial oscillatory pattern and leads to good approximations of the full result. The distribution starts to deviate from the full result at high rapidities as more and more energy is required in the final state. Assuming that the same relation between the inclusive cross-section and the rapidity distribution observed for the NNLO case holds true also at N^3LO , would mean that there is great potential in the predictions that can be produced via threshold expansion for this observable. Especially on the light of the recent result presented in ref. [27] where is presented the inclusive Higgs boson cross-section at N^3LO together with a comparison with the threshold expansion approximation of ref. [142].

The second observable we analyze is the transverse momentum distribution of the Higgs boson. The quality of the approximation obtained, including the same amount of terms in the threshold expansion as for the rapidity distribution, is greatly reduced. While including higher and higher terms in the expansion is improving the approximation, the convergence is so slow that even with ten terms in the expansion the deviations from the exact result are at the level of ten percent.

In general, the approximations based on threshold expansions can be improved by normalizing the differential cross-sections such that their cumulant reproduces the exact inclusive result. Our analysis at NNLO shows that the threshold expansion for Higgs-differential cross-sections can be a powerful tool. The quality of the approximation has to be carefully assessed for every observable under consideration. Even for comparatively inclusive observables, as the total cross-section or the rapidity distribution, several terms in the threshold expansion are required to obtain a reliable approximation. We also had a first look at the rapidity distribution of the N^3LO coefficient function. The resulting rapidity distribution displays a similar pattern as we observed for the corresponding NNLO coefficient function. An analysis with higher orders in the threshold expansion is the subject of the next chapter.

3

RAPIDITY DISTRIBUTION

In this chapter, we present the results that were first shown in ref. [3], where predictions for the rapidity distribution are presented through N³LO in pQCD computed as a threshold expansion. The same quantity has also been computed by other means, in particular through the so-called q_t -subtraction scheme [85, 179, 180] and presented in ref. [181]. In this alternative and independent prediction, the authors observed a slight deviation from an entirely uniform N³LO correction, but the two predictions are still compatible within the scale variation uncertainties.

Having access to these differential quantities is of high importance, especially given that the ATLAS and CMS experiments have accomplished remarkable results [182, 183] ever since the discovery of the Higgs boson [13, 14]. It is then important to produce matching theoretical predictions for the standard model, more so on the light of the fact that we are getting closer to the high-luminosity LHC phase, where the experimental error is estimated to be ultimately reduced to the level of 3% [17, 18].

Taking into account effects due to the neglected quark masses as well as electro-weak corrections and appraising residual uncertainties from missing higher-order effects, the current state-of-the-art prediction for the Higgs production cross-section in gluon fusion was obtained in [178, 184].

The following computations for the rapidity distribution in gluon fusion are performed in the same framework as the rest of the thesis, where the interaction of the Higgs boson with the partons is represented in term of an EFT in the limit of an infinite top mass. The Wilson coefficient corresponding to this EFT is written in eq.(1.20). The computation takes advantage of the results obtained in chapter 1 by using the NNLO expansion of the cross section up to linear terms in the dimensional regulator, together with the partial results obtained in chapter 2 for the rapidity distribution. In particular, we follow on the conclusion from the previous chapter and increase the accuracy of the threshold expansion by computing four extra orders in the series. We also renormalize the distribution to match the inclusive cross-section in order to improve its accuracy.

3.1 THRESHOLD EXPANSION

For the current computation, we decide to employ a different set of variables compared with those used in the case of the double differential computation in the previous chapter. The probability of producing a Higgs boson with a given rapidity Y is then expressed as,

$$\frac{d\sigma_{PP \rightarrow H+X}}{dY} = \hat{\sigma}_0 \sum_{ij} \int_0^1 dx_1 dx_2 dy_1 dy_2 f_i(y_1) f_j(y_2) \delta(\tau - x_1 x_2 y_1 y_2) \times \delta\left(Y - \frac{1}{2} \log\left(\frac{x_1 y_1}{x_2 y_2}\right)\right) \eta_{ij}(x_1, x_2), \quad (3.1)$$

where $f_i(y)$ are parton distribution functions (PDFs) and $\eta_{ij}(x_1, x_2)$ are the partonic coefficient functions. The sum runs over all possible combinations of initial state partons and we integrate over the energy fraction of the incoming partons, namely y_1 and y_2 . The goal of our computation is to analytically determine the partonic coefficient functions in perturbative QCD through N³LO which can be expanded in the strong coupling as a power series as in

$$\eta_{ij}(x_1, x_2) = \sum_{i=0}^3 \left(\frac{\alpha_S}{\pi}\right)^i \eta_{ij}^{(i)}(x_1, x_2) + \mathcal{O}(\alpha_S^4). \quad (3.2)$$

The partonic coefficient functions are comprised of squared partonic matrix elements with up to three unresolved partons in the final state integrated over the available phase space. We compute them by employing the tools presented for the double differential study, where the first two order in the threshold expansion at N³LO were computed. In particular, we improve the threshold expansion by computing an additional four terms in the expansion in \bar{z} .

In eq.(3.1), we presented the new set of variables through the introduction of Dirac delta functions. These variables can be related to physical quantities by expressing them in terms of scalar products of initial state partons p_1 and p_2 , together with the final state Higgs momentum. These variables are then written as,

$$\frac{x_1}{x_2} = \frac{p_h p_2}{p_h p_1}, \quad x_1 x_2 = z. \quad (3.3)$$

where $z = \frac{m_h^2}{s}$.

For the computation of the threshold expansion, we can introduce a new parameter δ and redefine x_i as being functions of this parameter. In particular, we want that in this

parametrization the threshold limit corresponds to a vanishing δ . We first notice that the \bar{z} dependence can be expressed in terms of x_1 and x_2 as follows,

$$\bar{x}_1 + \bar{x}_2 - \bar{x}_1\bar{x}_2 = \delta\bar{z}. \quad (3.4)$$

where the bar over the variable corresponds to $\bar{x}_i = 1 - x_i$. A parametrization in which both sides vanish as δ goes to zero is provided by:

$$\bar{x}'_1(\delta) = \delta \bar{x}_1 \frac{1 - \bar{x}_2}{1 - \delta \bar{x}_2}, \quad \bar{x}'_2(\delta) = \delta \bar{x}_2, \quad (3.5)$$

giving a one-to-one correspondence between the expansion of the partonic coefficients around $\delta = 0$ and $\bar{z} = 0$.

3.2 EXPLOITING THE DIVERGENCE STRUCTURE

The bare PCFs at N³LO, arising from the calculation of contributing squared matrix elements, in $d = 4 - 2\epsilon$ dimensions, take the form

$$\begin{aligned} \eta_{ij,\text{bare}}^{(3)}(\bar{x}_1, \bar{x}_2) &= \eta_{ij,\text{virt}}^{(3)} \delta(\bar{x}_1) \delta(\bar{x}_2) \\ &+ \sum_{n,m=1}^3 \bar{x}_1^{-1-m\epsilon} \bar{x}_2^{-1-n\epsilon} \eta_{ij,\text{bare}}^{(3,m,n)}(\bar{x}_1, \bar{x}_2). \end{aligned} \quad (3.6)$$

The term $\eta_{ij,\text{virt}}^{(3)} \delta(\bar{x}_1) \delta(\bar{x}_2)$ corresponds to the purely virtual contributions with a leading divergence of $1/\epsilon^6$. The functions $\eta_{ij,\text{bare}}^{(3,m,n)}(\bar{x}_1, \bar{x}_2)$ are holomorphic around $\bar{x}_i = 0$ and contain fourth order poles in ϵ . The sum over m and n is the consequence of the threshold expansion around various divergent regions. This sum will get contributions from (SS) , (SC) , (SH) , (CC) , (CH) and (HH) for double virtual corrections, and (S) , (C) and (H) for single virtual ones, denoting the soft, collinear and hard regions, respectively.

To make the expansion of the PCFs in the dimensional regulator explicit, we perform a standard expansion of singular factors in terms of delta functions $\delta(\bar{x}_i)$ and plus-distributions

$$\begin{aligned} \int_0^1 d\bar{x}_i \phi(\bar{x}_i) \bar{x}_i^{-1+a\epsilon} &= \int_0^1 d\bar{x}_i \phi(\bar{x}_i) \frac{\delta(\bar{x}_i)}{a\epsilon} \\ &+ \int_0^1 d\bar{x}_i \phi(\bar{x}_i) \sum_{n=0}^{\infty} \frac{(a\epsilon)^n}{n!} \left[\frac{L_i^n}{\bar{x}_i} \right]_+, \end{aligned} \quad (3.7)$$

with $L_i = \log(\bar{x}_i)$. The test function $\phi(\bar{x})$ corresponds in our calculation to a product of the parton luminosity and the observable function.

We obtain our finite renormalised N³LO coefficient function by combining the bare PCF with a suitable mass factorisation and ultraviolet renormalisation counter term $CT_{ij}^{(3)}$, which is defined by the QCD β -function, the three-loop splitting functions and the lower order contribution to the process. The expression for the counterterm will equally contain distribution which will cancel against those of our partonic coefficient function for the singular terms rendering it finite,

$$\begin{aligned}\eta_{ij}^{(3)}(x_1, x_2) &= \lim_{\epsilon \rightarrow 0} \left[\eta_{ij, \text{bare}}^{(3)}(x_1, x_2) + CT_{ij}^{(3)}(x_1, x_2) \right] \\ &= \sum_{k,l} D_k(\bar{x}_1) D_l(\bar{x}_2) \eta_{ij, (k,l)}^{(3)}(x_1, x_2).\end{aligned}\quad (3.8)$$

We isolate the structures that are singular in the limit $\bar{x}_i \rightarrow 0$ into the functions $D_k(\bar{x}_i)$ such that the coefficients $\eta_{ij, (k,l)}^{(3)}(x_1, x_2)$ are either real numbers or holomorphic functions in the limit. The non-holomorphic function $D_k(\bar{x}_i)$ corresponds to the k^{th} entry of the following list of 12 possible structures that can appear in the cross section through N³LO ,

$$\left\{ \delta(\bar{x}_i), \left[\frac{L_i^0}{\bar{x}_i} \right]_+, \dots, \left[\frac{L_i^5}{\bar{x}_i} \right]_+, L_i^0, \dots, L_i^4 \right\}.\quad (3.9)$$

The fact that all the poles in the regulator have to cancel among the different contributions in eq.(3.8) allows us to derive relations among the various bare partonic coefficients in eq.(3.6) and the counter term. Knowing that only the genuine two loop contributions can produce bare coefficient functions contributing to the $n = 1$ or $m = 1$ terms in eq. (3.6), becomes a powerful tool to determine many of the coefficients $\eta_{ij, (k,l)}^{(3)}(x_1, x_2)$ exactly.

All coefficients of terms proportional to two distributions were already computed in ref. [2] and presented in the previous chapter and can also be deduced from the inclusive cross-section at threshold (c.f. ref. [142, 175]) as was done in ref. [185]. Furthermore, we observe that if we consider only the leading power term in either one of the \bar{x}_i , a reduced number of exponents contributes to eq.(3.6), such that $n \leq m$, which further constrains our system of equations.

Using these relations, we were able to determine all coefficients in eq. (3.8) exactly in \bar{x}_i , except for the terms,

$$\begin{aligned}
\eta_{ij, \text{missing}}^{(3)}(x_1, x_2) = & \left[\delta(\bar{x}_1) \log(\bar{x}_2) \eta_{ij, (1,9)}^{(3)}(0, x_2) \right. \\
& + \delta(\bar{x}_1) \eta_{ij, (1,8)}^{(3)}(0, x_2) \\
& + \left[\frac{1}{\bar{x}_1} \right]_+ \eta_{ij, (2,8)}^{(3)}(0, x_2) \\
& + \log(\bar{x}_2) \eta_{ij, (8,9)}^{(3)}(x_1, x_2) \left. \right] + \left[(x_1 \leftrightarrow x_2) \right] \\
& + \eta_{ij, (8,8)}^{(3)}(x_1, x_2) + \log(\bar{x}_1) \log(\bar{x}_2) \eta_{ij, (9,9)}^{(3)}(x_1, x_2).
\end{aligned} \tag{3.10}$$

While the above terms could not be determined exactly from our current knowledge of unexpanded matrix elements, we obtained them via a threshold expansion as described above. Notice, that the above contributions contain maximally one power of a logarithm that is enhanced as $\bar{x}_i \rightarrow 0$.

In our final approximation of the PCF we choose to re-organise the terms without any distributions such that all terms proportional to threshold logarithms $\log^i(\bar{z})$ with $i \geq 3$ are maintained exactly. We approximate terms with lower powers of threshold logarithms using the threshold expansion as discussed above. Note, that the relations among the different components of the PCF provide a highly non-trivial consistency check on the results from our threshold expansion.

The partonic coefficient functions also depend explicitly on logarithms of the perturbative scale μ and we can rearrange them as,

$$\eta_{ij}^{(3)}(x_1, x_2) = \sum_{l=0}^3 \eta_{ij}^{(3,l)}(x_1, x_2) \log^l \left(\frac{m_h^2}{\mu^2} \right). \tag{3.11}$$

Naturally, the functions $\eta_{ij}^{(3,l)}(x_1, x_2)$ can be decomposed into distribution-valued or logarithmically enhanced terms. However, the coefficients with $l \geq 1$ can be derived exactly from lower order cross sections by solving the DGLAP evolution equations. Consequently, we determine them exactly, with one exception: The derivation of the non-distribution valued, non-logarithmically enhanced term of the coefficient of $\log(m_h^2/\mu^2)$ involves rather cumbersome convolution integrals. We approximate this particular term using a threshold expansion which modifies our approximation at terms beyond the claimed formal accuracy.

3.3 MATCHING TO THE INCLUSIVE CROSS SECTION

As we show for the rapidity distribution at NNLO, the prediction coming from the threshold expansion can be improved by rescaling the result such that it reproduced the inclusive cross-section once the differential quantity is integrated over. The inclusive partonic coefficient functions for the Higgs gluon fusion production at N³LO was computed exactly in ref. [27] and can therefore be used to this end. This inclusive quantity is written as a one-parameter function in the threshold variable z , and we can perform a change of variable to match it.

Let us consider the transformation from \bar{x}_i to (x, \bar{z})

$$\bar{x}_1 = \frac{(1 - \bar{x})\bar{z}}{1 - \bar{x}\bar{z}}, \quad \bar{x}_2 = \bar{x}\bar{z} \quad (3.12)$$

where now the soft limit can be taken without effecting the variable x . By looking at eq.(3.6) we can write the second term in these new variables which now reads,

$$\bar{x}_1^{-1-m\epsilon} \bar{x}_2^{-1-n\epsilon} = x^{-1-n\epsilon} \bar{x}^{-1-m\epsilon} \bar{z}^{-2-(n+m)\epsilon} (1 - \bar{x}\bar{z})^{-1-n\epsilon}.$$

Note that the last term is never singular since the upper value of \bar{z} will reach unit only in the case of infinite energies. This expression could give the impression to have a non-regularizable divergence around the threshold. However, by looking at the measure, we can see that an additional power of \bar{z} is produced,

$$dx_1 dx_2 = \frac{\bar{z}}{1 - \bar{x}\bar{z}} dx d\bar{z}.$$

removing the enhanced pole in \bar{z} . The variable x hit the singularity at the endpoints when the radiation k goes on-shell and collinear to one of the two incoming momenta $p_{1,2}$. By writing the partonic rapidity for the Higgs:

$$y = \frac{1}{2} \log\left(\frac{x_1}{x_2}\right) = \frac{1}{2} \log\left(\frac{z}{(1 - \bar{x}\bar{z})^2}\right)$$

we see that x parameterizes the rapidity in the partonic system between z and $\frac{1}{z}$.

With the use of the variables x and z we can now relate the differential PCF to the inclusive one by integrating over the additional degree of freedom as in,

$$\eta_{ij}^{(3),\text{inc.}}(z) = \int_0^1 \frac{\bar{z} d\bar{x}}{(1 - \bar{z}\bar{x})} \eta_{ij}^{(3)}\left(\frac{(1 - \bar{x})\bar{z}}{1 - \bar{x}\bar{z}}, \bar{x}\bar{z}\right). \quad (3.13)$$

This relation provides an enormously stringent check on our partonic coefficient functions. Indeed, our threshold expansion agrees with the threshold expansion of the inclusive partonic coefficient function for all computed orders.

Furthermore, eq. (3.13) allows us to modify our differential partonic coefficient functions by terms of higher order in the threshold expansion such that the exact inclusive cross-section is automatically obtained if the integral over the rapidity distribution is performed,

$$\eta_{ij}^{(3),\text{matched}}(x_1, x_2) = \eta_{ij}^{(3),\text{app.}}(x_1, x_2) + \frac{x_1 + x_2}{2(1 - x_1 x_2)} \left[\eta_{ij}^{(3),\text{inc}}(x_1 x_2) - \eta_{ij}^{(3),\text{inc, app.}}(x_1 x_2) \right]. \quad (3.14)$$

Here, $\eta_{ij}^{(3),\text{app.}}$ corresponds to the approximation of the PCF obtained as described in the previous sections and $\eta_{ij}^{(3),\text{inc, app.}}$ is its inclusive counterpart obtained by virtue of eq. (3.13). Furthermore, $\eta_{ij}^{(3),\text{inc}}$ is the inclusive partonic coefficient function obtained in ref. [27]. Therefore the term in the square bracket of eq.(3.14) contains only terms that are of higher order in the threshold expansion than those obtained as described above. This modification of the PCF ensures that if the integration over the Higgs boson rapidity is performed, then the correct inclusive cross-section is obtained for each partonic centre of mass energy. The approximation defined in eq.(3.14) will be the basis for our numerical results presented below.

3.4 PHENOMENOLOGICAL RESULTS

In the previous sections, we derive an analytic approximation to the PCF for the Higgs boson cross-section differential in the rapidity through N³LO in QCD. We now use MMHT2014 PDFs [186] to derive predictions for hadronic Higgs boson rapidity distribution at the LHC with a centre of mass energy of 13 TeV by means of eq.(3.1). We implement our coefficient functions into a private C++ code and use LHAPDF [121] to perform the μ^2 evolution of the PDF grids and evaluate them with a private grid interpolator that uses a polynomial of order 16 in the $\log(x)$ space as mention in section 2.5. The Cuba library [187] is used to perform the numerical integration over the momentum fractions of the partons.

As validation, we first derive the NNLO analogue of the approximation of the PCF used at N³LO and show the resulting predictions in the left panel of fig. 3.1 normalised to the exact rapidity distribution through NNLO with a central scale of $\mu = m_h/2$. The blue band corresponds to the cross-section obtained by varying the common scale μ in the interval $[m_h/4, m_h]$. The coloured lines show the cross-section obtained by truncating the threshold expansion in our approximation at different orders. We observe that our approximation describes the NNLO rapidity distribution very well for central rapidities ($|Y| < 3$) and even

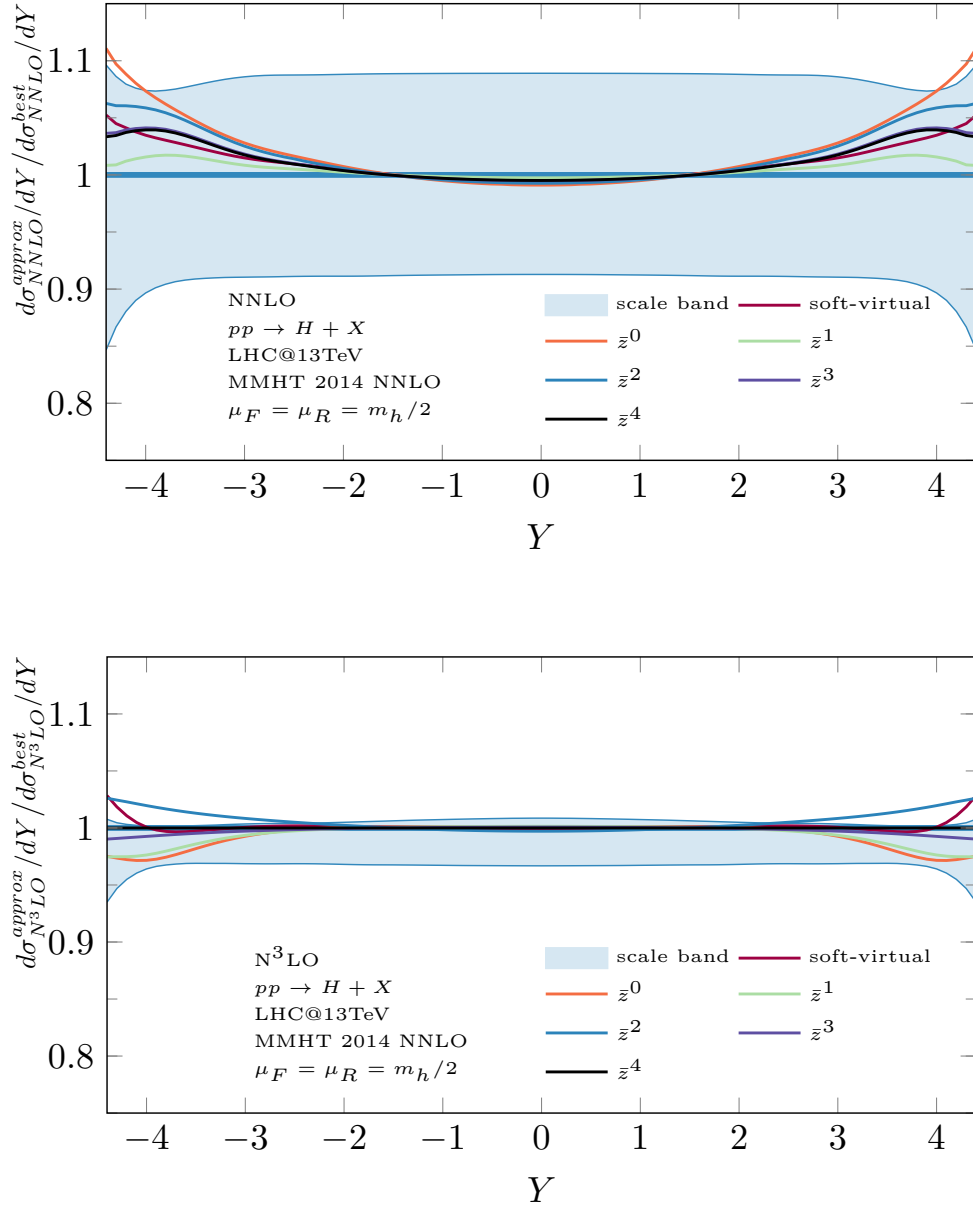


FIGURE 3.1: Approximate Higgs boson rapidity distribution with threshold expansion truncated at different orders. The top panel shows the ratio of the approximate NNLO to the exact result, the bottom panel shows the approximate N³LO result to the best prediction obtained in this work.

performs fine for larger rapidities. Deterioration of the threshold approximation at larger rapidities can be expected as on average the final state of the scattering process is more energetic, i.e. further from the production threshold. Including an increasing number of terms systematically improves the approximation. We also observe that all rapidity distributions obtained from truncated threshold expansions fall well within the scale variation band of the exact NNLO cross-section.

In the right panel of fig. 3.1 we show predictions for the N³LO rapidity distribution truncating the threshold expansion at different orders normalised to our best approximation. Similarly to the case at NNLO, including more terms in the expansion systematically stabilises our approximation. Central rapidities are remarkably stable under the inclusion of more and more expansion terms. In particular, all truncated approximations are once again contained within the scale variation band for central rapidities. We explored relaxing some of the ingredients of our approximation (less exact distributions or no matching to the exact inclusive cross-section) which amounts to a modification of terms beyond those computed in our threshold expansion and find only slight variations in our prediction. For example, basing our calculation purely on a threshold expansion with six terms underestimates the inclusive cross-section by 0.25% and only slightly varies the shape of the rapidity distribution. Similarly, we checked that a simple reweighting of the threshold-expanded N³LO rapidity distribution to the exact inclusive cross-section at N³LO produces results that are very close to our best prediction including the matching procedure according to eq. (3.13). We observe that at NNLO we approximate the exact PCF to better than one percent for $|Y| < 2$ and better than two percent for $|Y| < 3$. In order to be conservative, we estimate that our prediction is at the same level of precision relative to the exact result at N³LO.

3.5 STABILITY

In figure 3.2 we show the rapidity distribution truncated at different order in QCD perturbation theory. Our newly derived N³LO prediction display a stabilisation of the perturbative series as well as a drastic reduction of the size of the perturbative scale dependence. We observe that the ration of the rapidity distribution at N³LO relative to NNLO is uniform over the entire range of Higgs boson rapidities. Consequently, the N³LO rapidity distribution can be reproduced to very high accuracy by rescaling the NNLO prediction by the inclusive N³LO *K-factor*.

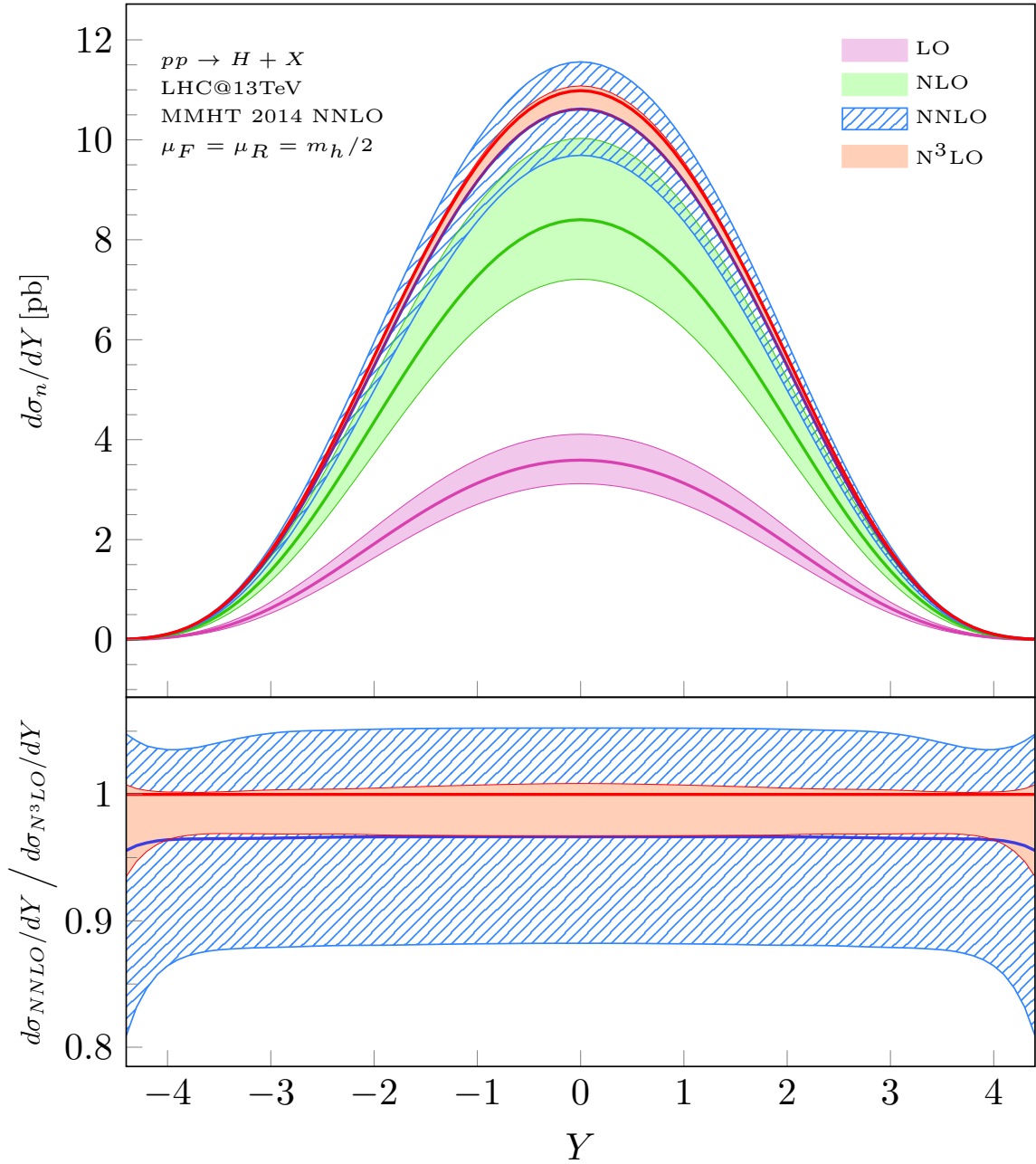


FIGURE 3.2: The Higgs boson rapidity distribution at different orders in perturbation theory. The lower panel shows the N³LO and NNLO predictions normalised to the N³LO prediction for $\mu = m_h/2$.

3.6 CONCLUSION

In chapter 2, we studied the behaviour of the Higgs-differential cross-section around the threshold limit and concluded that the approximation was suitable for computing the rapidity distribution. In this chapter, we have focused our attention on this particular observable and made predictions by computing six terms in the threshold expansion, four more than the one computed in chapter 2. The final result has been rescaled at higher order in the threshold expansion in order to match to the inclusive cross-section for each partonic center of mass energy.

We have analyzed the behaviour of the threshold expansion for the correction coming from different truncation orders of the PCFs and compared it with the NNLO equivalent. We see that the series converges to a stable value in the central region of rapidity which also corresponds to the most relevant from the phenomenological point of view, being the region that is probed with the highest accuracy at the LHC.

Although the central value of the correction to the expansion in the strong coupling is shown to be homogenous in rapidity, and therefore compatible with a simple rescaling by a K -factor of the NNLO distribution, we managed to significantly reduce the uncertainty due to scale variation. In particular, in the range of rapidity $|Y| < 3$ is reduce to a level of $[-3.4\%, +0.9\%]$. From the observation of the behaviour of the power expansion at different order in the soft parameter \bar{z} at NNLO we estimate the error coming from the truncation to be less than 1% for $|Y| < 2$ and less than 2% for $|Y| < 3$.

As was observed in the inclusive cross-section when compared with the threshold expansion, the inclusion of additional order will marginally improve this prediction. In fact, the missing part is mostly due to the high-energy behaviour, and the expansion of poles located in that region. This is particularly evident in the behaviour in the tails of the rapidity $|Y| > 3$ were the contributions coming from a Higgs with large momentum become dominant. We expect the result of this work to be the cornerstone of future fully differential Higgs boson phenomenology.

Part II

DIRECT INTEGRATION

4

LOOP-TREE DUALITY

In this second part, we want to present an alternative approach to the computation of phenomenologically relevant quantities. Especially if we consider that, despite impressive advances in the mathematical aspects of the reduction of scattering amplitudes to master integrals [29–50], and their subsequent computation by means of differential equations [51–70], it is believed that the computation of many relevant higher-order corrections to important processes (e.g. NNLO corrections to $pp \rightarrow t\bar{t}H$ and $pp \rightarrow t\bar{t}b\bar{b}$) will remain intractable with this traditional approach. The difficulties can, for example, be due to the increase in the number of scales relevant to the problem and to the appearance of new mathematical structures in the form of generalised elliptic functions [68–72]. Here we decide to explore a purely numerical integration of the virtual contribution in momentum space.

Working in momentum space is especially appealing when also performing the loop energy integrals analytically using the residue theorem. This energy integration yields the Loop-Tree Duality [79–81] (LTD) which provides an alternative representation for the loop integral containing terms with as many on-shell constraints as there are loops, making them effectively trees. This aligns the measure of phase-space and LTD integrals, thus making LTD ideally suited to pursue the ambitious goal of directly combining real-emission and virtual contributions and compute them numerically at once by realising the local cancellation of their infrared singularities.

This chapter starts with the natural follow-up to ref. [81]: regulating threshold singularities in order to numerically integrate loop integrals evaluated with physical kinematics. We achieve this by constructing a contour deformation in the $(3L)$ -dimensional complex integration space, designed in accordance with the constraints imposed by the causal prescription of Feynman propagators and by the matching conditions stemming from analytic continuation.

Contour deformations for numerical integration have been considered in the past [75, 77, 188], and we present a novel variant well-suited to the multi-loop LTD expression of ref. [81]. In order to ensure that our construction is correct for arbitrary (multi-)loop integrals, we apply it to more than a hundred qualitatively different examples, always finding agreement with the analytical benchmark (when available). We also demonstrate in this way that the convergence rate of our current numerical implementation already renders it competitive.

We then proceed and show how to regulate divergent one-loop integrals by building counterterms that are compatible with the LTD derivation. We analyze divergent integrals also in the context of amplitudes where, thanks to the factorisation of the infrared singularities, the counterterms can be written in a simple form.

4.1 LOOP-TREE DUALITY

In this section, we fix the notation and summarise the findings presented in ref. [81]. A general n -loop integral in four-momentum Minkowskian space can be rewritten as an integral over the Euclidean space of the three-dimensional spatial part of the loop momenta. The integrand, in that case, is the sum of residues obtained by iteratively integrating out the energy variables one after the other by applying the residue theorem. Each residue identified in this manner corresponds to a particular *spanning tree* (i.e. a tree graph that connects all vertices) of the underlying loop graph, or equivalently, to a particular *loop momentum basis* (i.e. the n edges that complete a spanning tree back to the original n -loop graph) together with a specific set of signs for the energy solutions of the on-shell conditions fixing the residue location, which we call the *cut structure*.

More precisely, we start from the following n -loop integral

$$I = \int \prod_{j=1}^n \frac{d^4 k_j}{(2\pi)^4} \frac{N}{\prod_{i \in \mathbf{e}} D_i}, \quad D_i = q_i^2 - m_i^2 + i\delta, \quad (4.1)$$

where \mathbf{e} is the set of indices labelling the edges of the connected graph identifying the integral considered and the numerator N is a regular function of the loop momenta. We assume the Feynman propagators to be pairwise distinct with on-shell energies $\pm E_i = \pm \sqrt{\vec{q}_i^2 + m_i^2} - i\delta$ and discuss the extension to the case of repeated propagators in appendix C. The momentum flow in a graph is uniquely determined by the choice of (consistent) signature vectors $\mathbf{s}_i = (s_{i1}, \dots, s_{in})$, $s_{ij} \in \{\pm 1, 0\}$ for each propagator, such that $q_i^\mu = \sum_{j=1}^n s_{ij} k_j^\mu + p_i^\mu$, where p_i^μ is a shift that depends on external momenta.

We consider the integration of the energies in a fixed arbitrary order, set by (k_1^0, \dots, k_n^0) , each along the real line and closing on an arc of infinite radius in *either* the upper (with winding number $\Gamma_j = +1$) *or* the lower ($\Gamma_j = -1$) complex half-plane. We assume the integrand to vanish for large loop momenta, so that we can consider the integral along this arc to be zero, thus allowing us to relate the original integral to the sum of residues at poles located within the contour.

When carrying out this iterative integration of the loop energies and collecting residues, one finds that some residues may lie within or outside the integration contour depending on the spatial part of the loop momenta. It has been conjectured and verified explicitly in ref. [81] that only the residues that unconditionally lie within the integration contour contribute to the integral. We write the *dual integrand* corresponding to one particular residue of the original integrand $f = N / \sum_{i \in \mathbf{e}} D_i$ identified by the loop momentum basis choice $\mathbf{b} = (b_1, \dots, b_n)$, $b_j \in \mathbf{e}$ (corresponding to the list of propagators put on-shell for this residue) as

$$\text{Res}_{\mathbf{b}}[f] = \frac{1}{\prod_{i \in \mathbf{b}} 2E_i} \frac{N}{\prod_{i \in \mathbf{e} \setminus \mathbf{b}} D_i} \Big|_{\{q_j^0 = \sigma_j^{\mathbf{b}} E_j\}_{j \in \mathbf{b}}} \quad (4.2)$$

with $\sigma^{\mathbf{b}} = (\sigma_1^{\mathbf{b}}, \dots, \sigma_n^{\mathbf{b}})$, $\sigma_j^{\mathbf{b}} \in \{\pm 1\}$. It describes a residue that is within the contour for all loop momentum configurations if

$$\prod_{r=1}^n \Theta(\Gamma_r \text{Im}[k_{\mathbf{b},r}^{\sigma}]) = 1, \quad \forall \vec{k}_j \in \mathbb{R}^3, \quad (4.3)$$

where

$$\text{Im}[k_{\mathbf{b},r}^{\sigma}] = \frac{\det \begin{pmatrix} & \sigma_1 \text{Im}[E_{i_1}] \\ (s_{b_{j_1 j_2}})_{\substack{1 \leq j_1 \leq r \\ 1 \leq j_2 < r}} & \vdots \\ & \sigma_r \text{Im}[E_{i_r}] \end{pmatrix}}{\det((s_{b_{ij}})_{1 \leq j \leq r})}, \quad (4.4)$$

which for a choice of integration order, contour closure and momentum routing (determined by $(\vec{k}_1, \dots, \vec{k}_n)$, Γ_j and s_{ij} respectively), is satisfied unconditionally for exactly *one* configuration of signs, the cut structure, denoted by $\sigma^{\mathbf{b}}$.

Therefore, the original integral of eq. (4.1) is identically equal to the resulting LTD expression

$$I = (-i)^n \int \prod_{j=1}^n \frac{d^3 \vec{k}_j}{(2\pi)^3} \sum_{\mathbf{b} \in \mathcal{B}} \text{Res}_{\mathbf{b}}[f], \quad (4.5)$$

where \mathcal{B} is the set of all loop momentum bases.

We stress again that the functional form of the LTD expression is implicitly dependent on the chosen order for the integration of loop energies, the contour closure choices and the particular momentum routing chosen for the original integral. but nevertheless evaluate to the same expression.

The dual integrands can become singular on surfaces which may be labeled by the residue corresponding to the particular dual integrand in which they appear (specified through the loop basis \mathbf{b}) and the particular propagator of that dual integrand that becomes on-shell (specified through the propagator index i). These *singular surfaces* are of the form

$$\tilde{\zeta}_{\mathbf{b},i,\alpha_i} \equiv \sum_{j \in \mathbf{b}} \alpha_j E_j + \alpha_i E_i + \tilde{p}_i^{0,\mathbf{b}} = 0, \quad (4.6)$$

with $\alpha_i \in \{\pm 1\}$ for $i \in \mathbf{e} \setminus \mathbf{b}$ and $\alpha_j = s_{ij}^{\mathbf{b}} \sigma_j^{\mathbf{b}} \in \{0, \pm 1\}$ for $j \in \mathbf{b}$, where $s_{ij}^{\mathbf{b}}$ and $\tilde{p}_i^{\mu,\mathbf{b}}$ are implicitly defined through the change of basis $q_i^\mu = \sum_{j \in \mathbf{b}} s_{ij}^{\mathbf{b}} q_j^\mu + \tilde{p}_i^{\mu,\mathbf{b}}$ induced by the loop momentum basis \mathbf{b} identifying this surface. The singular surfaces ζ can be separated into two classes: *E-* and *H-surfaces*. E-surfaces are defined by the property of having all the non vanishing prefactors α_k that multiply the energies with equal sign, we refer to this sign as the *surface sign*. We factor out the surface sign and name the resulting E-surface $\eta^{\mathbf{b},i}$. From this point on, we consider every E-surface to have a positive sign for all energies:

$$\eta_{\mathbf{b},i} \equiv \sum_{j \in \mathbf{b}} E_j + E_i + p_\eta^0 = 0. \quad (4.7)$$

E-surfaces are convex and bounded. H-surfaces are then defined by having at least one positive and at least one negative α_k and they are labelled $\gamma_{\mathbf{b},i,\alpha_i}$.

A particularly elegant feature of LTD is that the sum of dual integrands forming eq. (4.5) only becomes singular on E-surfaces, as the singularities from H-surfaces cancel pairwise thanks to a mechanism referred to as *dual cancellations* [79, 189]. As will be discussed in more details later, this cancellations are source of numerical instabilities that effect many practical applications in particular when the integrator approaches e UV region. The E-surface has a non-empty set of real solutions in $\vec{k} = (\vec{k}_1, \dots, \vec{k}_n) \in \mathbb{R}^{3n}$ for $\delta = 0$ if it satisfies

$$(p_i^{0,\mathbf{b}})^2 - (\tilde{p}_i^{\mathbf{b}})^2 \geq \left(\sum_{j \in \mathbf{b}} \alpha_j m_j + \alpha_i m_i \right)^2 \quad \text{and} \quad p_i^{0,\mathbf{b}} < 0. \quad (4.8)$$

When both sides of this inequality are exactly zero, the E-surface has no interior since its minor axis is zero, and the E-surface corresponds to the location on an infrared collinear and/or soft singularities of the integral. We refer to them as *pinched* E-surface, with the important property that singularities they correspond to cannot be regularised via a contour deformation of the loop momenta integration phase-space.

For $\delta > 0$ an E-surface η is uniquely regulated by the imaginary prescription

$$\text{sgn Im}[\eta] = -1. \quad (4.9)$$

We do not find it particularly useful to work out the imaginary part of the squared propagators appearing in eq. (4.5) (referred to as *dual propagator* in ref. [79]). Instead, we prefer to stress that the relevant imaginary part of the E-surface equations induced by the causal prescription has a simple definite sign. As it will be made clear later, this observation is indeed the only relevant one in regard to the construction of a contour deformation that satisfies physical requirements and regulates threshold singularities.

4.2 CONTOUR DEFORMATION

Numerical integration of Feynman diagrams and physical amplitudes in momentum space originated with the early attempts by Davison E. Soper in [84] and [78], in which the LTD formalism was applied to virtual diagrams at one loop in order to then integrate the cross-section directly. Interestingly, the author also explicitly mentions and utilises the mechanism of *local* real-virtual cancellations to render the integrand finite at the location of the non-integrable soft and collinear singularities. In order to avoid so-called scattering singularities, referred to in our work as one-loop E-surfaces, the author devised a contour deformation capable of satisfying the relevant constraints.

Several methods have since been developed for integrating diagrams and amplitudes directly in four-dimensional loop momentum space. A first success was the computation of one-loop photon amplitudes in ref. [75], followed by refs. [190–192] which generalised the formalism beyond one loop and applied it to more challenging integrals. The especially inspiring feature of these two series of publications is the focus on constructing a provably exact deformation, through the concept of anti-selection and dynamic scaling of the deformation.

Around the same time when these techniques were developed, a different line of work expanded on LTD and, specifically, on its aspects relevant for the $(3n)$ -dimensional numerical integration of integrals, amplitudes and cross sections [188, 193, 194]. The contour deformation presented in these works is based on a linear combination of vectors normal to the existing E-surfaces, weighted by adjustable parameters and dampened by exponential functions with unspecified width; the deformation proves to be correct for simple threshold structures and in the limit of arbitrarily small dampening widths. Results obtained in this way however highlighted for the first time the potential of numerical integration over the spatial degrees of freedom resulting from the LTD identity.

In this section we will construct a reliable and exact deformation that is valid for an arbitrary number of loops and legs. We will give specific examples in order to illustrate how to implement the deformation constraints for complicated singular structures, especially on intersections of multiple E-surfaces.

As long as an integral only features non-pinned threshold singularities, it is possible to engineer a contour deformation yielding a finite result for the integral. The absorptive part of the integral is correct provided that the contour deformation considered satisfies requirements imposed by physical conditions, in particular *causality*. In relativistic quantum mechanics, causality is originally realised in Feynman propagators via the $i\delta$ -prescription or, equivalently, by the request that the theory is in the range of validity of Gell-Mann and Low's theorem [195]. In the LTD formalism, an imaginary prescription on propagators remains and, although its formal expression is more complicated than $i\delta$, it still holds that on E-surfaces this prescription sign is fixed (i.e. it does not depend on either external nor loop kinematics, see eq. (4.9)).

Contour integration of threshold singularities requires to analytically continue the LTD integrand by replacing its dependence on the chosen basis of loop momenta \vec{k} , by the complex variable $\vec{k} - i\vec{\kappa} \in (\mathbb{C}^3)^n$, where $\vec{k} = (\vec{k}_1, \dots, \vec{k}_n) \in (\mathbb{R}^3)^n$ and $\vec{\kappa} = (\vec{\kappa}_1, \dots, \vec{\kappa}_n) \in (\mathbb{R}^3)^n$. The spatial momenta associated with each propagator are a linear combination of the vectors in the chosen loop momentum basis plus an affine term:

$$\vec{q}_j(\vec{k}) = \sum_{i=1}^n s_{ji} \vec{k}_i + \vec{p}_j = \vec{Q}_j(\vec{k}) + \vec{p}_j. \quad (4.10)$$

Once analytically continued, these spatial momenta then also acquire an imaginary part:

$$\vec{q}_j(\vec{k} - i\vec{\kappa}) = \vec{q}_j(\vec{k}) - i\vec{Q}_j(\vec{\kappa}). \quad (4.11)$$

Each surface η has an associated energy shift p_η^0 , defined in eq. (4.7) as a specific linear combination of the energies of external particles.

An approximation of the imaginary part of the E-surface η can be obtained from the first order term of its Taylor expansion in $\|\vec{\kappa}\|$:

$$\text{Im}[\eta(\vec{k} - i\vec{\kappa})] = -\vec{\nabla}_{\vec{k}}\eta(\vec{k}) \cdot \vec{\kappa} + \mathcal{O}(\|\vec{\kappa}\|^2), \quad (4.12)$$

The quantity $\vec{\nabla}_{\vec{k}}\eta(\vec{k})$, henceforth denoted as $\vec{\nabla}\eta$, is the outward pointing normal vector to the surface $\eta(\vec{k}) = 0$. The contour deformation is defined in the $(3n)$ -dimensional complex space and we parametrise it as $\vec{k} - i\vec{\kappa}(\vec{k})$. It must satisfy constraints affecting two of its key characteristics, the direction and magnitude of the vector field $\vec{\kappa}(\vec{k})$:

DIRECTION: The deformation vector $\vec{\kappa}(\vec{k})$ must induce a sign of the imaginary part of the E-surface equation that matches the sign enforced by the causal prescription whenever \vec{k} lies on a singular E-surfaces. This imposes conditions on the direction of the vector field $\vec{\kappa}(\vec{k})$. We derive these conditions by comparing the sign of the LTD prescription on E-surfaces (eq. (4.9)) with the sign of the imaginary part of E-surfaces that results from the deformation (eq. (4.12)). We obtain:

$$\text{sgn}[\vec{\nabla}\eta \cdot \vec{\kappa}] = +1, \text{ when } \eta(\vec{k}) = 0. \quad (4.13)$$

MAGNITUDE: The norm of the deformation vector is limited by three constraints:

INTEGRAND CONTINUITY: The LTD expression can be seen as a function of the on-shell energies of the internal particles $E_i = \sqrt{\vec{q}_i^2 + m_i^2 - i\delta}$. These square roots have to be evaluated on a well-defined Riemann sheet. Thus the contour must not cross the branch cuts of any of the involved square roots.

COMPLEX POLE CONSTRAINT: By extending the domain of the LTD integrand from \mathbb{R}^{3n} to \mathbb{C}^{3n} through the replacement of its functional dependency on \vec{k} with $(\vec{k}, \vec{\kappa})$, we find that in addition to real-valued poles (corresponding to the existing E-surfaces), the integrand also features complex-valued poles located at $(\vec{k}, \vec{\kappa})$, with $\vec{\kappa} \neq \vec{0}$. We stress that these *complex poles* exist for *all* E-surface equations: those (pinched or not) already having solutions for real loop momenta $(\vec{k}, \vec{0})$ as well as those that do not and which are referred to as *non-existing* E-surfaces (in regard to the fact that their existence condition of eq. (4.8) is not fulfilled).

According to Cauchy's theorem, the result of the contour-deformed integral will only be identical to that of the original defining integral over the spatial part of the loop momenta in the real hyper-plane, if and only if the volume defined by this real hyper-plane and the deformed contour does not contain any of such complex poles. The magnitude of the contour deformation must therefore be constrained to be small enough so as to exclude these complex poles.

EXPANSION VALIDITY: The causal constraint on the direction of the contour deformation as well as the complex pole constraint are derived from the Taylor expansion of each energy function E_i . We must therefore impose that the norm of the contour deformation vector field is such that the complex argument of each square root defining an energy remains within the range of validity of its expansion.

The fulfillment of these conditions is discussed at length in ref. [4] together with the deformation for a general intersections of different E-surface at multi-loop. To the end of presenting the

integration of a divergent integral we limit ourself to the one loop case and we do it by considering the following example.

4.2.1 Construction at one loop

Consider a one-loop scalar box diagram in the LTD representation after having explicitly solved the on-shell constraint:

$$\begin{aligned}
I &= -i \int \frac{d^3\vec{k}}{(2\pi)^3} \sum_{b=1}^4 \frac{1}{2E_b} \prod_{\substack{i=1 \\ i \neq b}}^4 \frac{1}{D_i} \Big|_{q_b^0=E_b} = -i \int \frac{d^3\vec{k}}{(2\pi)^3} \sum_{b=1}^4 \frac{1}{2E_b} \prod_{\substack{i=1 \\ i \neq b}}^4 \frac{1}{\eta_{bi}\gamma_{bi}} \\
&= -i \int \frac{d^3\vec{k}}{(2\pi)^3} \sum_{b=1}^4 \frac{1}{2E_b} \prod_{\substack{i=1 \\ i \neq b}}^4 \frac{1}{(E_b + E_i - p_b^0 + p_i^0)(E_b - E_i - p_b^0 + p_i^0)}.
\end{aligned} \tag{4.14}$$

where we used that at one loop the dual propagator factorises into the product of an E- and an H-surface, as $D_i(k)|_{q_b^0=E_b} = \eta_{bi}(\vec{k})\gamma_{bi}(\vec{k})$. At one loop, one can also simplify the loop basis identifier \mathbf{b} and write it as the index $b \in \mathbf{e} = \{1, 2, 3, 4\}$ corresponding to the single LTD cut considered. Thanks to the mechanism of dual cancellations, the sum of all dual integrands is only singular on E-surfaces which, at one loop, are two-dimensional rotational ellipsoids in spatial loop momentum space. All of the potential singular E-surfaces of this scalar box appear as zeros of the functions

$$\eta_{bi}(\vec{k}) \equiv \sqrt{(\vec{k} + \vec{p}_b)^2 + m_b^2} + \sqrt{(\vec{k} + \vec{p}_i)^2 + m_i^2} - p_b^0 + p_i^0, \quad p_i \equiv \sum_{j=1}^i p_j^{\text{ext}}, \tag{4.15}$$

with $i, b \in \mathbf{e}$, $i \neq b$, and for given four-momenta of the four external legs p_j^{ext} , $j \in \{1, 2, 3, 4\}$. The number of E-surfaces that have solutions for real loop momenta has an upper bound based on the topology and the number of legs N . For one-loop topologies, an upper bound on the total number of *existing* E-surfaces is $N(N-1)/2$, since we require $b \neq i$ and using the fact that if η_{bi} exists, η_{ib} cannot exist.

The singularity structure of the LTD expression can be studied by focusing on particular singular E-surfaces and their intersections. In order to do this, we define the boundary and interior operators as

$$\partial\eta_{bi} = \{\vec{k} \in \mathbb{R}^3 \mid \eta_{bi}(\vec{k}) = 0\}, \tag{4.16}$$

$$\partial^-\eta_{bi} = \{\vec{k} \in \mathbb{R}^3 \mid \eta_{bi}(\vec{k}) < 0\}. \tag{4.17}$$

The E-surface η_{bi} exists, that is $\partial\eta_{bi} \neq \emptyset$, if $(p_b^0 - p_i^0)^2 - (\vec{p}_b - \vec{p}_i)^2 \geq (m_i + m_b)^2$ and $p_b^0 - p_i^0 \geq 0$. If two ellipsoids η , η' exist and intersect, then $\partial\eta \cap \partial\eta' \neq \emptyset$. Furthermore, if they intersect without being tangent, they also *overlap*: $\partial^-\eta \cap \partial^-\eta' \neq \emptyset$. As an illustrative example, we now set particular values for the external box kinematics, which we refer to as Box4E,

$$\begin{aligned} p_1^{\text{ext}} &= (14.0, -6.6, -40.0, 0), \\ p_2^{\text{ext}} &= (-43.0, 15.2, 33.0, 0), \\ p_3^{\text{ext}} &= (-17.9, -50.0, 11.8, 0), \\ p_4^{\text{ext}} &= -p_1^{\text{ext}} - p_2^{\text{ext}} - p_3^{\text{ext}} \end{aligned} \quad (4.18)$$

and list the resulting four members of the set of existing E-surfaces $\mathcal{E} = \{\eta_{12}, \eta_{13}, \eta_{42}, \eta_{43}\}$,

$$\begin{aligned} \eta_{12} &= \sqrt{(-6.6 + k_x)^2 + (-40 + k_y)^2 + k_z^2} + \sqrt{(8.6 + k_x)^2 + (-7 + k_y)^2 + k_z^2} - 43, \\ \eta_{13} &= \sqrt{(-6.6 + k_x)^2 + (-40 + k_y)^2 + k_z^2} + \sqrt{(-41.4 + k_x)^2 + (4.8 + k_y)^2 + k_z^2} - 60.9, \\ \eta_{42} &= \sqrt{k_x^2 + k_y^2 + k_z^2} + \sqrt{(8.6 + k_x)^2 + (-7 + k_y)^2 + k_z^2} - 29, \\ \eta_{43} &= \sqrt{k_x^2 + k_y^2 + k_z^2} + \sqrt{(-41.4 + k_x)^2 + (4.8 + k_y)^2 + k_z^2} - 46.9. \end{aligned} \quad (4.19)$$

The four E-surfaces in eq. (4.19) are coloured according to the colour scheme used in figure 4.1. A focal point is the loop momentum (k_x, k_y, k_z) that sets the argument of an energy square root to zero. Each ellipsoid has two focal points, indicated with red dots in the figure. The energy shift $p_i^0 - p_b^0$ is the length of the major axis. The particular external kinematic configuration chosen in eq. (4.18) has no component along the k_z -axis and therefore the particular section $k_z = 0$ corresponds to the plane where the four E-surfaces have a maximal extent.

According to eq. (4.9) we require the imaginary part on any E-surface η to always be negative: $\text{sgn}(\text{Im}[\eta]) = -1$. By replacing $\vec{k} \rightarrow \vec{k} - i\vec{k}(\vec{k})$ and expanding the E-surface equations to first order in $||\vec{k}||$, we find that the prescription reads

$$\vec{k} \cdot \vec{\nabla}\eta_{bi} = \vec{k} \cdot \left(\frac{\vec{k} + \vec{p}_b}{E_b} + \frac{\vec{k} + \vec{p}_i}{E_i} \right) > 0, \quad \forall \vec{k} \in \partial\eta_{bi}, \quad \forall \eta_{bi} \in \mathcal{E}, \quad (4.20)$$

which imposes that on any point on the E-surface, $\vec{k}(\vec{k})$ should point outwards of the E-surface. On the intersection of many E-surfaces, the combined prescriptions impose that $\vec{k}(\vec{k})$ must simultaneously point outwards of all of the intersecting E-surfaces.

One choice that always satisfies the condition of eq. (4.20) for one single E-surface as well as for two intersecting E-surfaces is the sum of their respective normal vector fields, as shown in figure 4.2. A similar deformation was proposed in ref. [188], where the deformation field $\vec{k}(\vec{k})$

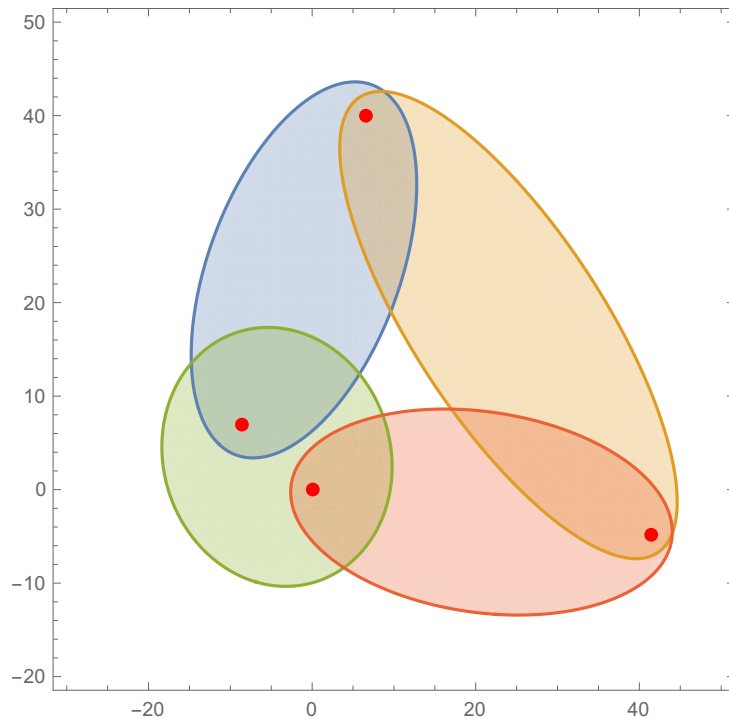


FIGURE 4.1: A $k_z = 0$ section of the singular structure of the example configuration Box4E. It has four singular E-surfaces with four (partially shared) focal points coloured in red.

is written as a linear combination of the normal fields weighted by an exponential dampening factor that ensures that each normal field vanishes away from its defining E-surface. This particular choice of deformation vector is unsatisfactory when more than two E-surfaces exist, since

- there could be triple intersections where the sum of the normal vectors is not guaranteed to be correct, unless the coefficients of the decomposition on normal vector fields is fine-tuned (and made dynamical functions of the real part of the loop momenta) so as to induce a vector with a valid direction and
- contributions from various E-surfaces may spoil the validity of the deformation direction on another surface. Again this must be avoided by fine-tuning the strength of the dampening factors affecting each normal field.

In figure 4.3 we give an example with three E-surfaces, where a naive unweighted sum of normal vectors does not yield a valid deformation. By using fine-tuned dampening of the normal vector fields from each E-surface, such cases may be avoided but this does require an ad-hoc treatment and can lead to poor numerical convergence.

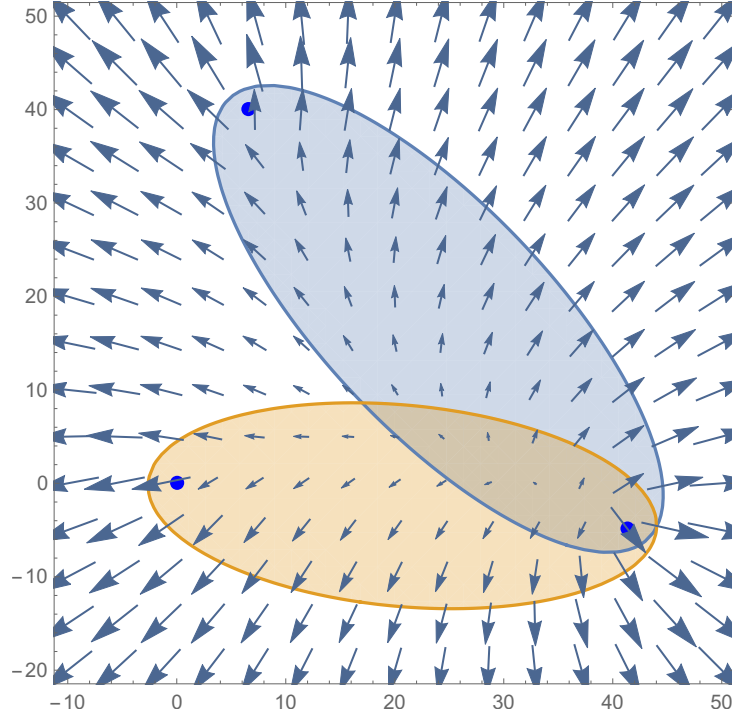


FIGURE 4.2: A correct deformation for two E-surfaces represented in the $k_z = 0$ plane constructed by summing the normal vector fields of each of the two E-surfaces.

The next subsection introduces the concept of *deformation sources* which we will use to build a deformation that avoids the shortcomings discussed in this section when considering normal fields.

DEFORMATION SOURCES

Since E-surfaces are convex surfaces, given a point \vec{s} within the interior of an E-surface $\partial^- \eta$, the radial field $\vec{v}_{\vec{s}}(\vec{k}) \equiv \vec{k} - \vec{s}$, centered at \vec{s} , satisfies the causal prescription $\text{Im}[\eta]|_{\vec{k}-i\vec{v}_{\vec{s}}} < 0$ on any point on the surface, where $\eta(\vec{k}) = 0$. We note that the interior of the *intersection* of a set $F \subseteq \mathcal{E}$ of E-surfaces again defines a convex volume and therefore we analogously have that, for any given point \vec{s} in this volume, that is $\vec{s} \in \bigcap_{\eta \in F} \partial^- \eta$, the corresponding radial field $\vec{v}_{\vec{s}}$ simultaneously satisfies the causal prescription of *all* of the E-surfaces in F and, especially, on their intersections. We call such a point \vec{s} a *deformation source* for the overlapping set F . For a case in which there exists a single point \vec{s} simultaneously in the interior of *all* of the existing E-surfaces, then the radial deformation field $\vec{\kappa}(\vec{k}) \propto (\vec{k} - \vec{s})$ satisfies the causal prescription on all the threshold singularities (see figure 4.4).

When there is no single point simultaneously in the interior of all E-surfaces, one can construct a deformation vector written as the sum of radial fields centered at different locations,

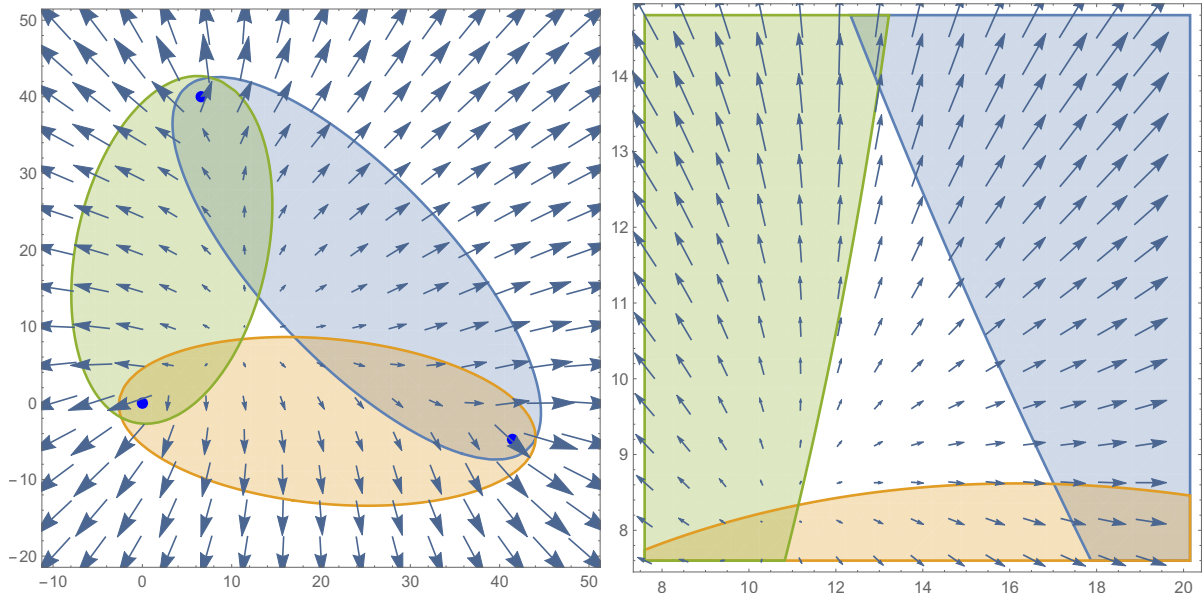


FIGURE 4.3: An example of an incorrect deformation vector field constructed by adding the normal vector fields of three E-surfaces. The picture on the right is an enlargement of the problematic center region in the left image. This particular case requires fine-tuning of the normalisation of each of the three fields added in order to obtain a valid deformation.

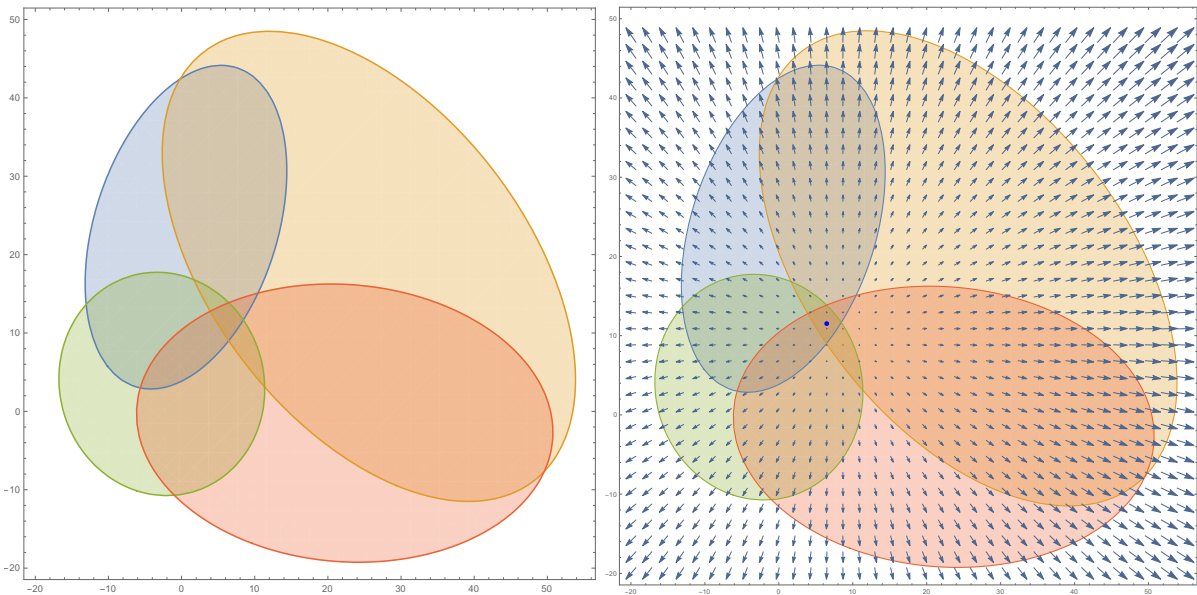


FIGURE 4.4: A correct deformation using the radial field $\vec{k} - \vec{s}$ generated by a single source \vec{s} contained in the interior of all four E-surfaces.

and adequately multiplied by an anti-selector function disabling the effect of the radial field on all the E-surfaces in which the point is not contained. The anti-selection is constructed such that the individual terms building the deformation vector fields are always “additive” in their ability to satisfy the causality requirements. Indeed, a crucial aspect of our design of the deformation is the adoption of a model in which contributions that may spoil the direction on a particular threshold singularity are excluded (i.e. “anti-selected”), as opposed to a model that enables (i.e. “selects”) the correct contributions on the particular thresholds they are designed for.

We illustrate more specifically how an *anti-selection* model is preferable to a *selection* one by highlighting the shortcomings of the latter when applied to the previously introduced Box4E configuration whose four E-surfaces are shown in figure 4.5 in the $k_z = 0$ plane. The “selection” model would in this case amount to combine all four radial fields as follows (the discussion of the analogous construction of ref. [188] that involves normal fields would be similar):

$$\begin{aligned}\vec{\kappa}_{\text{selection_model}} = & \vec{v}_{\vec{s}_{124}} (\bar{T}(\eta_{12}) + \bar{T}(\eta_{42})) \\ & + \vec{v}_{\vec{s}_{213}} (\bar{T}(\eta_{12}) + \bar{T}(\eta_{13})) \\ & + \vec{v}_{\vec{s}_{134}} (\bar{T}(\eta_{13}) + \bar{T}(\eta_{43})) \\ & + \vec{v}_{\vec{s}_{342}} (\bar{T}(\eta_{43}) + \bar{T}(\eta_{42})),\end{aligned}\quad (4.21)$$

where the subscripts on the source indicate the focal points of the involved ellipsoids and the selection function¹ simply is one minus the anti-selection function $T(\eta_{bi})$ defined as follows:

$$\bar{T}(\eta_{bi}) = 1 - T(\eta_{bi}) \quad (4.22)$$

$$T(\eta_{bi}) = \frac{\eta_{bi}(\vec{k})^2}{\eta_{bi}(\vec{k})^2 + M^2 (p_i^0 - p_b^0)^2}, \quad (4.23)$$

where M is an adjustable free parameter, and $p_i^0 - p_b^0$ is the length of the major axis of the E-surfaces η_{bi} , which provides a measure for the size of the E-surfaces. Another possible choice is to substitute the normalisation $-p_b^0 + p_i^0$ with $\sqrt{(p_i^0 - p_b^0)^2 - (\vec{p}_i - \vec{p}_b)^2 - (m_i + m_b)^2}$, which is the minor axis length of the E-surface. The choice of M provides an estimate of how rapidly $T(\eta)$ saturates to one when \vec{k} is further away from the surface η_{bi} .

The deformation of eq. (4.21) stemming from the selection model is problematic for mainly two reasons:

¹ The selection function chosen in ref. [188] is an exponential Gaussian of adjustable width A_{bi} : $\exp\left(-\frac{(\eta_{bi}(\vec{k}) - \gamma_{bi}(\vec{k}))^2}{A_{bi}}\right)$.

- On the threshold E-surface η_{12} , the deformation receives contributions mostly from $\vec{v}_{\vec{s}_{124}}$ and $\vec{v}_{\vec{s}_{213}}$ (which do satisfy the causal prescription) but also from $\vec{v}_{\vec{s}_{134}}$ and $\vec{v}_{\vec{s}_{342}}$ (which may not satisfy the causal prescription) since the suppression factor induced by their respective selection function is *small* on this surface, but *not zero*. This implies the necessity of fine-tuning the suppression parameters which may be a difficult task when E-surfaces with very different causal constraints lie close to each other.
- On the intersection of two E-surfaces, for example $\partial\eta_{12} \cap \partial\eta_{13}$, three of the four radial deformation fields $\vec{v}_{\vec{s}_{124}}, \vec{v}_{\vec{s}_{213}}$ and $\vec{v}_{\vec{s}_{134}}$ are active *without any* suppression, even though only $\vec{v}_{\vec{s}_{213}}$ is guaranteed to be correct on this particular intersection.

One may think of alleviating the intersection problem by simply removing such intersections from the selector function applied to the deformation sources that are invalid:

$$\begin{aligned}
\vec{\kappa}_{\text{selection_model_improved}} &= \vec{v}_{\vec{s}_{124}} (\bar{T}(\eta_{12})T(\eta_{13}) + \bar{T}(\eta_{42})T(\eta_{43})) \\
&+ \vec{v}_{\vec{s}_{213}} (\bar{T}(\eta_{12})T(\eta_{42}) + \bar{T}(\eta_{13})T(\eta_{43})) \\
&+ \vec{v}_{\vec{s}_{134}} (\bar{T}(\eta_{13})T(\eta_{12}) + \bar{T}(\eta_{43})T(\eta_{42})) \\
&+ \vec{v}_{\vec{s}_{342}} (\bar{T}(\eta_{43})T(\eta_{13}) + \bar{T}(\eta_{42})T(\eta_{12})). \tag{4.24}
\end{aligned}$$

However, this solution is again not exact since even though $\bar{T}(\eta_{42})T(\eta_{43})$ and $\bar{T}(\eta_{43})T(\eta_{42})$ are small quantities on $\partial\eta_{12} \cap \partial\eta_{13}$, they are not identically zero. In fact, it is impossible to build a *continuous* selection function that identically vanishes on a particular intersection of E-surfaces while at the same time being identically unity when evaluated anywhere on one of the intersecting E-surfaces but outside of the intersection.

The above shows that if the the contour deformation is required to be correct (i.e. independently of its parameters), the radial deformation fields must be combined using an *anti*-selection paradigm that also avoids referring directly to intersections of E-surfaces, since one cannot continuously (anti-)select them. In the example of Box4E, we achieve this by constructing the final deformation vector $\vec{\kappa}$ as follows:

$$\begin{aligned}
\vec{\kappa} &= \vec{v}_{\vec{s}_{124}} T(\eta_{13})T(\eta_{43}) \\
&+ \vec{v}_{\vec{s}_{213}} T(\eta_{42})T(\eta_{43}) \\
&+ \vec{v}_{\vec{s}_{134}} T(\eta_{42})T(\eta_{12}) \\
&+ \vec{v}_{\vec{s}_{342}} T(\eta_{12})T(\eta_{13}) \tag{4.25}
\end{aligned}$$

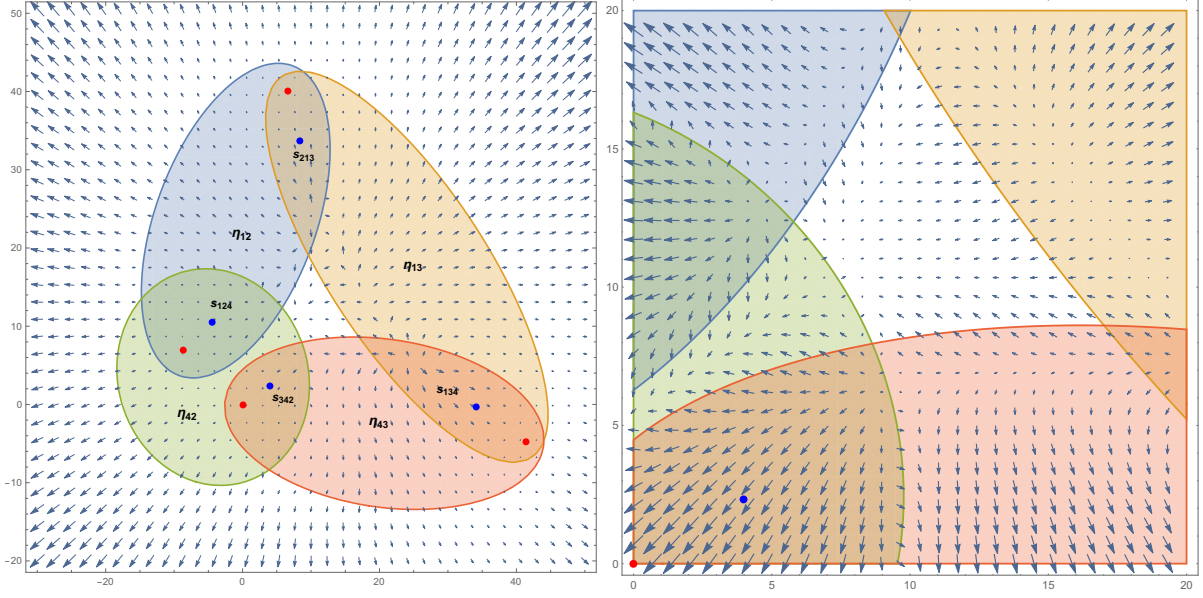


FIGURE 4.5: A correct deformation direction with functional form described by eq. (4.25) for Box4E using four sources which are excluded on those E-surfaces whose interior does not contain the source. The right plot is a zoom-in on the central region.

which *exactly* satisfies the causal requirements for \vec{k} on $\partial\eta_{12}$ and $\partial\eta_{12} \cap \partial\eta_{13}$:

$$\begin{aligned} \vec{k}(\vec{k})|_{\vec{k} \in \partial\eta_{12}} &\stackrel{!}{=} \vec{v}_{s_{124}} T(\eta_{13}) T(\eta_{43}) + \vec{v}_{s_{213}} T(\eta_{42}) T(\eta_{43}) \\ \vec{k}(\vec{k})|_{\vec{k} \in \partial\eta_{12} \cap \partial\eta_{13}} &\stackrel{!}{=} \vec{v}_{s_{213}} T(\eta_{42}) T(\eta_{43}). \end{aligned} \quad (4.26)$$

In general, the minimal set of sources required for constructing a valid deformation with this anti-selection model is obtained by determining the *maximal overlap structure* of the E-surfaces [4]. For the kinematical case of a box with the intersection of four distinct E-surfaces, this structure is $\{\{\eta_{12}, \eta_{13}\}, \{\eta_{13}, \eta_{43}\}, \{\eta_{42}, \eta_{43}\}, \{\eta_{12}, \eta_{42}\}\}$. After the maximal overlap structure has been determined, one has to construct source points in the interior of each overlap listed in the maximal overlap structure. In appendix C we present the results we obtain by testing our deformation for a range of finite topologies with a different number of external legs and internal loops. These results show that this method can produce reliable results, and we will discuss in the next chapter a way to stabilize even further the integration by removing the spurious H-surface analytically. Now that we have introduced and illustrated the key concepts underlying our construction of a valid deformation of the integration variables, we can apply them for the case of one-loop divergent integrals.

4.3 SUBTRACTION

All the results presented in appendix C refer to integrals that do not have singularities for loop momenta of large magnitude (ultraviolet (UV) singularities) or soft and/or collinear to external legs (infrared (IR) singularities). For practical applications, such as computing amplitudes of physical processes, this will not be the case, as individual diagrams can contain both UV and IR divergences.

After transforming the integrand using LTD, non-integrable singularities manifest themselves as pinched (squeezed) E-surfaces. For the case of Feynman diagrams with massless internal propagators, this will happen when one or more of the massless external legs become on-shell. It is still possible to compute these integrals provided that the non-integrable singularities are regulated first. In general, this is achieved by subtracting from the integrand an expression that contains the same pinched E-surface(s) and that approximates the original integral in the limit where the singular surface is approached. If these subtraction terms (also known as counterterms) are significantly simpler than the original integral, one can integrate them analytically in dimensional regularisation and add them back to the final expression in order to recover the original integral, including all its poles in the dimensional regulator. In this section, we start by presenting a method to regulate divergent scalar integrals at one-loop without the introduction of propagators linear in the loop momentum featured in ref. [196]. We then discuss the introduction of counterterms for physical amplitudes [83] where only one term is introduced to remove all IR divergences. This regulated expression can then be integrated using LTD and the contour deformation discussed in section 4.2.

For the rest of this section, we will refer to the external momenta as p_i for ease of reading.

4.3.1 *Regularizing Divergent scalar integrals*

We start by investigating scalar integrals subject to IR divergences at one-loop. In general, it is convenient to express counterterms in terms of the same building blocks as the original integrand, namely quadratic propagators. This allows to use the LTD formalism that has been introduced for the case of finite scalar integrals. At one-loop, we will show that we can always achieve such subtraction using a linear combination of triangles built by a subset of the original propagators and with coefficients expressed in terms of the kinematic invariants s_{ij} . Since the counterterms involve only propagators already present in the original diagram, they do not introduce any new E-surfaces.

GENERAL ONE-LOOP MASSLESS SCALAR INTEGRAL

Let us consider an n -point function with all the internal propagators massless and with external momenta p_j with $p_j^2 = m_j^2$. We first consider the case where only one leg i is massless ($m_i = 0$). As a consequence, the corresponding scalar integrand will develop a collinear singularity when the loop four-momentum k becomes collinear to the corresponding momentum p_i :

$$\left(\text{Diagram with } n \text{ external legs } p_{i+2}, p_{i+1}, p_i, p_{i-1}, p_{i-2} \text{ and internal lines } q_{i+1}, q_i, q_{i-1} \right) \xrightarrow{q_i = x p_i} \left(\text{Bubble diagram with } p_i \right) \times \underbrace{\left(\text{Diagram with } n \text{ external legs } p_{i+2}, p_{i+1} + x p_i, p_{i-1} + \bar{x} p_i, p_{i-2} \right)}_{=: c_i(x)}. \quad (4.27)$$

In the expression above (where we consider the loop momentum to flow clockwise) we can see how the integrand factorises in the collinear limit. The integration of this counterterm can be performed as shown in ref. [196]. The variable x is a function of the loop momentum and is defined as follows:

$$q_i = x p_i + y v + q_{i,\perp}, \quad \text{where} \quad \begin{cases} v^2 = 0, \\ v \cdot p_i \neq 0. \end{cases} \quad (4.28)$$

The expression on the l.h.s of eq. (4.27) can be written in an integral form as follows:

$$\mathcal{I}_n \equiv \int d^4 k I_n(k, \{p_i\}), \quad \text{where} \quad \begin{cases} I_n(k, \{p_i\}) = \frac{1}{\prod_i^n (q_i)^2}, \\ q_i = k + \sum_{j=1}^i p_j, \end{cases}, \quad (4.29)$$

$$\mathcal{I}_n \xrightarrow{q_i = x p_i} \int d^4 k \frac{c_i(x)}{(q_{i-1})^2 (q_i)^2}. \quad (4.30)$$

The coefficient $c_i(x)$ that multiplies the bubble propagators corresponds to the remaining hard propagators with the loop momentum evaluated in the collinear limit:

$$c_i(x) = \frac{1}{\prod_{j=i+1}^{n+i-2} (x p_i + q_{ji})^2}, \quad q_{ji} \equiv q_j - q_i. \quad (4.31)$$

The limit shown on the right-hand side of eq. (4.30) could be used to build an IR finite expression by subtracting it from \mathcal{I}_n , however such a counterterm introduces propagators that

are linear in the loop momentum. Linear propagators yield singular surfaces that are not akin to E-surfaces, implying that the general construction of the contour deformation presented in section 4.2 cannot directly control the properties of the imaginary part of the loop momentum on them. We leave the investigation of solutions for accommodating linear propagators to future work and for now aim at casting the subtraction terms $c_i(x)$ in terms of propagators already present in the original divergent one-loop integral.

We start by considering all possible triangles that factorise the same divergent bubble in the collinear limit. This condition fixes two of the three propagators of the triangle to be the ones that become singular in a specific collinear limit, whereas the third propagator can be chosen to be any of the other ones appearing in the original n -point integral. All such triangles are:

$$T(i, j) \equiv \begin{array}{c} q_i \\ \diagup \quad \diagdown \\ \text{---} \quad \text{---} \\ \diagdown \quad \diagup \\ q_{i-1} \end{array} q_j, \quad j \in \mathcal{J}_i \equiv \{i + 1, i + 2, \dots, i + n - 2\}. \quad (4.32)$$

with periodic conditions on the loop momenta labels. In the collinear limit, each element $T(i, j)$ factorises one hard propagator t_{ij} whose expression reads:

$$t_{ij}(x) = \frac{1}{(xp_i + q_{ji})^2}.$$

Note that each squared momentum in the denominator of our coefficient functions is linear in x because p_i is on-shell, resulting in only one simple pole in the variables x .

In order to cancel the divergences of the n -point function we need to find a linear combination of $T(i, j)$ with coefficients $a_{ij}(x)$ that satisfies:

$$\sum_{j \in \mathcal{J}_i} t_{ij}(x) a_{ij}(x) = c_i(x).$$

We can multiply both sides of this expression by the denominator of $c_i(x)$ which is equal to the product of all the possible t_{ij} with $i \neq j$. We then obtain a polynomial of degree $(n - 3)$ in x :

$$\sum_{j \in \mathcal{J}_i} \left(\prod_{\substack{r \in \mathcal{J}_i \\ r \neq j}} t_{ir}^{-1}(x) \right) a_{ij}(x) = 1.$$

Since we have $(n - 2)$ degrees of freedom and we insist that coefficients $a_{ij}(x)$ are free of poles in x , one needs to involve all terms $T(i, j)$ in order to solve the equation above (assuming all

the poles $t_{ij}(x)$ are distinct). In particular, an explicit solution can be found by using the roots of the inverse coefficients t_{ij}^{-1} :

$$a_{ij} = \prod_{\substack{r \in \mathcal{J}_i \\ r \neq j}} t_{ir} \left(-\frac{(q_{ji})^2}{2p_i \cdot q_{ji}} \right), \quad (4.33)$$

resulting in coefficients that depend only on the external kinematics.

This procedure does not work in the case of degenerate (raised) propagators. This can be resolved by considering a subset $\tilde{\mathcal{J}}_i \subset \mathcal{J}_i$ which contains only one member of each degenerate subset of propagators with multiplicity v_j for $j \in \tilde{\mathcal{J}}_i$. Moreover, we need to generalise eq. (4.33) in order to support the degeneracy of the involved propagators. In the collinear limit, the linear combination of the elements of this set gives the same singularities as the original integral, provided that:

$$\sum_{j \in \tilde{\mathcal{J}}_i} \left(\prod_{\substack{r \in \tilde{\mathcal{J}}_i \\ r \neq j}} t_{ir}^{-v_r}(x) \right) a_{ij}(x) = 1.$$

In this case we have $|\tilde{\mathcal{J}}_i|$ parameters a_{ij} to constrain a polynomial of degree n with $(|\tilde{\mathcal{J}}_i| - 1)$ distinct roots. It is then clear that the coefficients a_{ij} take the same values as those given in equation (4.33). From this point onward, we will only consider one-loop scalar integrals with non-degenerate propagators.

We are now equipped with a method that removes single collinear singularities from integrals with one off-shell external momentum by writing a linear combination of the triangular elements $T(i, j)$. When more than one external leg has a vanishing mass, we can apply the same procedure for each of them. In this case, we have to be careful when one of the triangles appears in more than one regularisation. For example, when two adjacent momenta are on-shell at the same time, one has $T(i, i+1) = T(i+1, i-1)$. In this kinematic configuration the corresponding coefficients will be same:

$$a_{i,i+1} = a_{i+1,i-1}, \quad \text{when} \quad p_i^2 = p_j^2 = 0.$$

Thus, one has to be careful when summing the regulator corresponding to each of the massless external legs in order to avoid double-counting.

We can write one general subtraction term, referred to as CT_n , that can be used for any combination of on/off-shell external momenta of a scalar one-loop n -point integral:

$$\mathcal{I}_{n|\text{subtracted}} = \mathcal{I}_n - \text{CT}_n,$$

$$\text{CT}_n = \sum_{i=1}^n \left(\beta_i T(i, i+1) + \sum_{j=i+2}^{n+(i-3)} a_{ij} T(i, j) \right), \quad (4.34)$$

where we introduced the coefficients β_i used to avoid double counting. Their expression is

$$\beta_i = \begin{cases} a_{i,i+1} & : p_i^2 = 0 \\ a_{i+1,i-1} & : \text{otherwise} \end{cases}, \quad (4.35)$$

where we make explicit use of the fact that whenever p_i and p_{i+1} are on-shell at the same time the two coefficients a_{ij} coincide.

Because the constructed collinear counterterms do not depend on the parameter x , they completely remove the singularities from pinched E-surfaces, implying that they regulate *both* collinear and soft divergences. As a consequence, we have that the integral $\mathcal{I}_n - \text{CT}_n$ is finite for all loop momentum configurations. The original expression \mathcal{I}_n can be recovered by adding back the integrated counterterms. The integrated counterterm consists of $n(n-3)$ distinct one-loop scalar triangles that are straightforward to compute analytically for general external kinematics using dimensional regularisation. We leave to future work the investigation of the possible multi-loop generalisation of this construction of counterterms that do not involve any propagators that are linear in the loop momenta.

EXPLICIT EXAMPLE OF SUBTRACTION FOR A DIVERGENT ONE-LOOP SCALAR BOX

For the four-point box topology with massless propagators, there are four counterterms since the sum in eq. (4.34) over the coefficients a_{ij} is empty. Only the β_i are present and take the following expression:

$$\beta_i = \begin{cases} \frac{s_{i,i+1} - p_{i+1}^2}{s_{i,i+1}s_{i-1,i} - p_{i+1}^2 p_{i-1}^2} & : p_i^2 = 0 \\ \frac{s_{i,i+1} - p_i^2}{s_{i,i+1}s_{i+1,i+2} - p_i^2 p_{i+2}^2} & : \text{otherwise} \end{cases}, \quad (4.36)$$

where $s_{ij} = (p_i + p_j)^2$. In the particular case where all external momenta are massless and on-shell (i.e. $p_i^2 = 0$), the final expression of the counterterms reads:

$$\begin{aligned} \text{CT}_n &= \sum_{i=1}^4 \beta_i T(i, i+1) \\ &= \frac{T(1,2)}{s_{23}} + \frac{T(2,3)}{s_{12}} + \frac{T(3,4)}{s_{23}} + \frac{T(4,1)}{s_{12}}, \end{aligned} \quad (4.37)$$

which coincides with the results presented in ref. [196], in which this same expression corresponds to the counterterm built for the subtraction of soft singularities (and the authors also concluded that the counterterm cancels all IR divergences in that particular case). In other cases however, and especially beyond one-loop, the counterterms from ref. [196] introduce linear propagators of the form of eq. (4.27).

4.3.2 One-loop amplitudes

Loop-Tree Duality has already been applied directly to the computation of amplitudes in cases where no contour deformation was needed, for example in refs. [194, 197]. In this section, we consider an amplitude that has both IR and UV divergences as well as threshold singularities: the production of photons from the scattering of a quark and an anti-quark. For simplicity, the order of the photons is kept fixed during this discussion, as performing the integration over all permutations of the final states does not add any complications.

The tree-level contribution for $q\bar{q} \rightarrow (N-2)V$ is defined as

$$i\mathcal{A}_0 = \begin{array}{c} p_2 \\ \swarrow \\ \text{---} \text{---} \text{---} \\ \text{---} \text{---} \text{---} \\ \nwarrow \\ p_1 \end{array} \begin{array}{c} p_3 \\ \swarrow \\ \text{---} \text{---} \text{---} \\ \text{---} \text{---} \text{---} \\ \nwarrow \\ p_4 \\ \vdots \\ p_N \end{array} = C_0 \left(\prod_{i=3}^{N-1} \frac{1}{(\sum_{j=2}^i p_j)^2} \right) \bar{v}_2 T_0 u_1, \quad (4.38)$$

where all the fermions are assumed to be massless and the coefficients C_0 , T_0 depend on the vector boson considered as a final state. If only photons are considered as final states such coefficients are given by:

$$T_0 = \not{\epsilon}_3(-\not{p}_{23})\not{\epsilon}_4 \cdots (\not{p}_{15})\not{\epsilon}_N, \quad C_0 = g^3 q^3. \quad (4.39)$$

These formulas can easily be extended to the electroweak bosons W^\pm and Z by substituting the photon polarisation vectors with generic ones $\not{\epsilon}_i \rightarrow \hat{\not{\epsilon}}_i$ which also encode the information about the axial and vectorial part of the corresponding boson:

$$\hat{\not{\epsilon}}_i \equiv \not{\epsilon}_i P_i, \quad P_i \equiv c_V - c_A \gamma^5, \quad (4.40)$$

with projectors defined as

$$P_L \equiv \frac{1 - \gamma^5}{2}, \quad P_Z \equiv \frac{c_V^d - c_A^d \gamma^5}{2}. \quad (4.41)$$

In order to obtain a more general expression we will use this new definition for the polarisation vectors. In the case of photons, all the P_i s are proportional to the identity matrix.

In order to compute the one-loop QCD correction to eq. (4.38) one needs to consider all possible insertions of a gluon along the fermionic line. The IR structure of the relevant diagrams features one or two pinched collinear singularities if the gluon is attached to one or both the external fermion lines, respectively. In the latter case, the diagram also features a soft singularity.

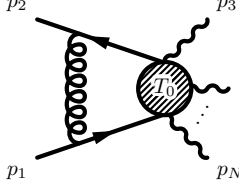
COUNTERTERMS

If the photons are physically polarised, the only pinched divergences contributing to the IR sector involve a gluon connecting one of the propagators of the tree-level diagram with the external quarks. There are no singularities originating from two internal quarks and an external photon meeting at a vertex and becoming collinear, since the numerator vanishes:

$$[\dots](\not{k} - \not{p}_i) \hat{\not{\epsilon}}_i \not{k} [\dots] \xrightarrow{k=x p_i} \bar{x} x [\dots] \not{p}_i \hat{\not{\epsilon}}_i \not{p}_i [\dots] = 0. \quad (4.42)$$

Since the pinched singularities originate uniquely from insertions of gluons connecting an external fermion to an internal fermion, the Ward identity can be used to regulate all the collinear and soft divergences with a general counterterm. However, it is necessary to fix a consistent choice of routing for the loop momentum in order for cancelling divergences to

be localised in the same region in momentum space, even though they belong to different diagrams. The general counterterm I_{IR} reads:



$$= \frac{C_1 \mu^{2\epsilon} (4\pi)^2}{\prod_{i=3}^{N-1} (\sum_{j=2}^i p_j)^2} \int \frac{d^d k}{(2\pi)^d} \frac{\bar{v}_2 \gamma^\mu (\not{k} - \not{p}_2) T_0 (\not{k} + \not{p}_1) \gamma_\mu u_1}{k^2 (k + p_1)^2 (k - p_2)^2}, \quad (4.43)$$

where

$$C_1 = -iC_0 \frac{C_F \alpha_s}{4\pi}. \quad (4.44)$$

This integration can be performed analytically using Feynman parametrisation, and we obtain:

$$I_{\text{IR}} = i \frac{C_1}{\prod_{i=3}^{N-1} (\sum_{j=2}^i p_j)^2} \left(\frac{4\pi\mu}{-s_{12}} \right)^\epsilon \frac{C_\Gamma}{2-2\epsilon} \left(-2M_0 \frac{2-2\epsilon+\epsilon^2}{\epsilon^2} + \frac{M_1}{2\epsilon} + \frac{M_2}{-s} \right), \quad (4.45)$$

where

$$\begin{aligned} M_0 &= [\bar{v}_2 T_0 u_1], \\ M_1 &= [\bar{v}_2 \gamma^\mu \gamma^\nu T_0 \gamma_\nu \gamma_\mu u_1], \\ M_2 &= [\bar{v}_2 \gamma^\mu \not{p}_1 T_0 \not{p}_2 \gamma_\mu u_1], \\ C_\Gamma &= \frac{\Gamma(1-\epsilon)^2 \Gamma(1+\epsilon)}{\Gamma(2-2\epsilon)}. \end{aligned} \quad (4.46)$$

Although subtracting eq. (4.43) from the original integrand allows to completely regulate IR singularities, the subtracted integrand is still divergent in the UV sector. This divergence can manifest itself locally, in spite of the integral itself being finite, either due to symmetries of the integrated expression or because the IR and UV poles cancel for integrals that are scaleless in dimensional regularisation. The behaviour for large momenta is inferred by the scaling of the integrand in these regions, and as a result all log-divergent triangles (one gluon, two fermions) and linearly divergent bubbles (one gluon, one fermion) that appear in the amplitude have to be regulated. The construction of the counterterm is done by taking the UV limit of each diagram by replacing

$$\frac{\not{k} + \not{p}}{(k+p)^2} \rightarrow \frac{\not{k}}{k^2 - \mu_{\text{UV}}^2}, \quad (4.47)$$

where the only relevant momentum is now the loop momentum carried by the exchanged gluon. The bubble diagram has a leading UV divergence that is linear in the loop momentum. In the context of an analytic integration such contribution integrates to zero because of radial symmetry, although the integrand is locally divergent. It is therefore necessary to also regulate

this leading UV divergence together with the sub-leading one obtained by computing the second order in the Taylor expansion around the UV approximation given by eq. (4.47). An explicit example of this subtraction can be found in appendix C, where eq. (C.1.11) represents the UV counterterm of a triangle and eq. (C.1.10) represents the counterterm of a bubble. The IR counterterm that we introduced is UV divergent and requires regulation as well. Its divergence can be expressed as as a triangle integral and can be subtracted by means of eq. (4.47).

The combination of counterterms can be used to build a finite amplitude expression that can be integrated using LTD:

$$\mathcal{A}_{\text{finite}} = \mathcal{A} - I_{\text{CT}}, \quad \text{where} \quad I_{\text{CT}} = \sum_{\text{UV div.}} I_{\text{UV}} + I_{\text{IR}} - I_{\text{UVIR}}. \quad (4.48)$$

The counterterm can be integrated analytically with the use of dimensional regularisation. In the UV contribution to the integrated counterterm we notice that the bubble and the triangle lead to the same value in norm and opposite in sign if constructed according to the substitution rule (4.47). Thus, the only remaining contribution is

$$\sum_{\text{UV div.}} I_{\text{UV}} = -i \frac{C_1}{\prod_{i=3}^{N-1} (\sum_{j=2}^i p_j)^2} \left(\frac{4\pi \mu^2}{\mu_{\text{UV}}^2} \right)^\epsilon \Gamma(1+\epsilon) \frac{(1-\epsilon)^2}{\epsilon} M_0. \quad (4.49)$$

Finally, regulate the IR counterterm with the same technique. The corresponding analytically integrated counterpart reads:

$$I_{\text{UVIR}} = -i \frac{C_1}{\prod_{i=3}^{N-1} (\sum_{j=2}^i p_j)^2} \left(\frac{4\pi \mu^2}{\mu_{\text{UV}}^2} \right)^\epsilon \Gamma(1+\epsilon) \frac{1}{4\epsilon} M_1. \quad (4.50)$$

The complete expression I_{CT} can then be expanded in ϵ up to finite terms and be used to recover the original amplitude once combined with the value coming from numerical integration. The integrated counterterm for $q\bar{q}$ to photons at one loop takes the simple form:

$$I_{\text{CT}} = -i \frac{C_1}{\prod_{i=3}^{N-1} (\sum_{j=2}^i p_j)^2} M_0 \frac{(4\pi)^\epsilon}{\Gamma(1-\epsilon)} \left[\frac{1}{\epsilon^2} + \frac{1}{\epsilon} \left(\frac{1}{2} + \ln_\mu \right) + \left(4 + \frac{1}{2} (3 + \ln_\mu) \ln_\mu \right) \right] + \mathcal{O}(\epsilon), \quad (4.51)$$

where $\ln_\mu = \log\left(\frac{\mu^2}{-s_{12}}\right)$. Any dependence on μ_{UV} has dropped from this final expression. As a consequence, the integration of the finite amplitude will also not depend on the choice of μ_{UV} . This condition can be used as a further check for the proper cancellation of the divergences.

ULTRAVIOLET BEHAVIOUR

When integrating the LTD expression, one has to take into account that the superficial degree of UV divergence of each dual integrand is higher than that of the sum of its cuts. This is because once the LTD on-shell cuts of the residues are applied, every quadratic propagator scales as $1/|\vec{k}|$ in the UV instead of $1/k^2$. As a consequence, contrary to the Minkowskian case, the addition of more fermion propagators to the diagram is not suppressing the scaling of the deformation in the UV sector:

$$\int d^4k \delta_+(q_j^2) \frac{1}{k^2} \prod_i^N \frac{q_i}{q_i^2} \sim k^{2 \vee N}, \quad (4.52)$$

compared to the original scaling of the 4D integrand being

$$\int d^4k \frac{1}{k^2} \prod_i^N \frac{q_i}{q_i^2} \sim k^{2-N}. \quad (4.53)$$

Summing over all the different cuts will however recover the original scaling of k^{2-N} .

If the dual integrand scales faster than $1/|\vec{k}|$ in the UV, the numerical cancellation of large numbers becomes prone to numerical instabilities. One way avoid such numerical instabilities in the UV region is to approximate the integrand with a better behaved function in the corresponding sector, obtained by taking a UV approximation of the integrand. The most convenient choice is to replace all the propagators with a common UV one:

$$q^2 \rightarrow (k + p_{UV})^2. \quad (4.54)$$

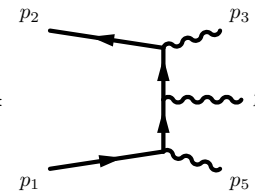
This ensures that the approximating function only features a single dual integrand, which directly scales as the 4-dimensional integrand. The numerator can be left unchanged for this approximation. In section 4.3.2 we discuss the effects of this UV approximation. The UV counterterms can be constructed as shown there for most integrals, but in the case of a bubble integral, the subleading logarithmic divergence must also be regulated. The relevant part of the approximation is shown below:

$$\begin{aligned} \frac{\gamma^\mu \not{q} \gamma_\mu}{q^2} &\approx \frac{\gamma^\mu \not{q} \gamma_\mu}{(k + p_{UV})^2} - 2k \cdot (q - k - p_{UV}) \frac{\gamma^\mu \not{q} \gamma_\mu}{(k + p_{UV})^3} \\ &= \frac{\gamma^\mu \not{q} \gamma_\mu}{(k + p_{UV})^2} - \frac{\gamma^\mu \{k, (q - k - p_{UV})\} \not{q} \gamma_\mu}{(k + p_{UV})^3}. \end{aligned} \quad (4.55)$$

Since the UV counterterms have higher-order poles, the LTD formula shown in section 4.1 cannot be applied directly. We discuss how to apply LTD to integrals featuring raised propagators in appendix C.

ONE-LOOP AMPLITUDE FOR $q\bar{q} \rightarrow \gamma_1\gamma_2\gamma_3$

We now study the specific case of the one-loop $d\bar{d} \rightarrow \gamma_1\gamma_2\gamma_3$ amplitude. The tree-level diagram of this amplitude is

$$i\mathcal{A}_0 = \text{Diagram} = C_0 \frac{M_0}{\prod_{i=3}^4 (\sum_{j=2}^i p_j)^2},$$


where the coefficients are given by

$$M_0 = \bar{v}_2 \not{\epsilon}_1(-\not{p}_{23}) \not{\epsilon}_2(\not{p}_{15}) \not{\epsilon}_3 u_1, \quad C_0 = g^3 q^3. \tag{4.56}$$

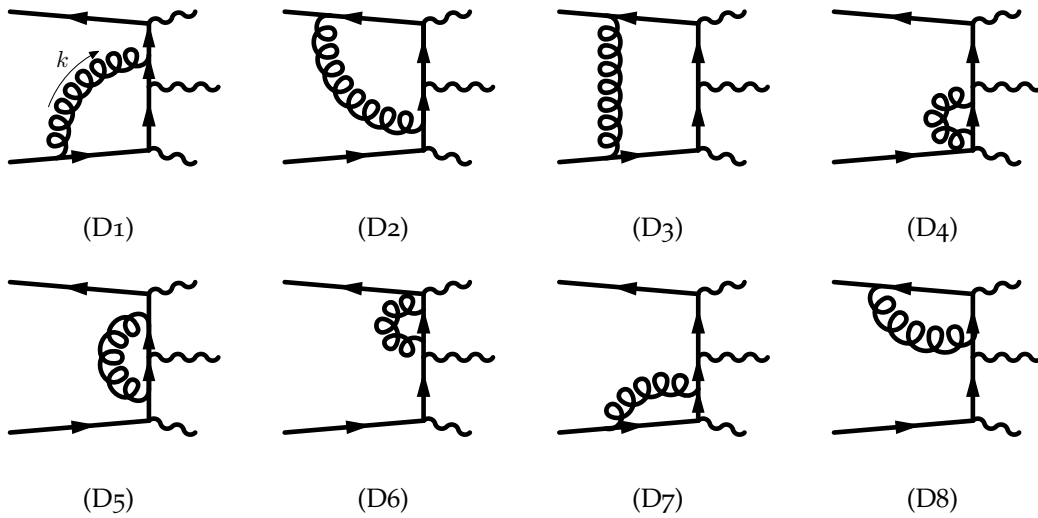


FIGURE 4.6: Diagrams contributing to one-loop QCD correction to $q\bar{q} \rightarrow 3\gamma$ amplitude.

figure 4.6 shows all the diagrams involved in the one-loop QCD correction.

Diagrams $D_1 - D_3$ and $D_7 - D_8$ are IR divergent: D_1 and D_7 are divergent when k is collinear to p_1 and D_2 and D_8 are divergent k is collinear to p_2 , whereas the diagram D_3 is divergent in both cases and also has a soft divergence.

Despite the fact that the integrated amplitude is UV finite, the local behaviour of the integrand in the UV region needs to be regulated. This can be done by writing the corresponding counterterms for all UV divergent integrals, specifically $D_4 - D_8$.

In order to ensure that the cancellation occurring across diagrams at the integrated level are also reflected at the local integrand level for the whole amplitude, one must carefully choose the the loop momentum routing of each diagram so as to localise cancelling divergences in the same region of momentum space. The case at hand is quite easy in that regard, as one can choose the gluon line to have momentum k with momentum flow against the fermionic line for all the diagrams.

figure 4.6 shows the different behaviours when approaching the soft, collinear, and UV limits. The different limits are approached by rescaling the loop momentum k by a factor δ for the soft and UV limit, while for the collinear limit we use the Sudakov parametrisation of eq. (4.28) with y and k_\perp rescaled by δ and $\sqrt{\delta}$ respectively. The different asymptotic scaling δ^1 , $\delta^{\frac{1}{2}}$ and δ^{-1} , prove that the divergences are properly subtracted.

Despite the use of quadruple precision (f128) to rescue some unstable evaluation of the UV region, we see that the cancellations between dual integrands are broken around $\delta > 10^8$ due to numerical instabilities. In figure 4.8 we show how these instabilities spoil the final result in the case of double precision (f64) with and without the use of the approximating function discussed in section 4.3.2. In the latter case it is possible to push the instability in the far UV and reproduce the behaviour of the quadruple precision evaluation. Where the transition between the approximated function and the all-order amplitude expression occurs, one has to ensure that the deformation goes to zero, since this region is not analytic. In both figure 4.7 and figure 4.8 the rescaled loop momentum is taken to be real and of the same order as s_{12} .

4.3.3 Divergent one-loop four- and five-point scalar integrals

We apply the subtraction scheme presented in section 4.3 to one-loop four- and five-point functions with massless propagators. For a randomly selected phase-space configuration, we go through all combinations of setting external momenta on-shell. For both the box and pentagon kinematics, we set $s_{12} = 1$. For the box topology, when one of the external momenta is massive, we set $m_1^2 = \frac{1}{4}$, $m_2^2 = \frac{1}{8}$, $m_3^2 = \frac{2}{9}$, $m_4^2 = \frac{1}{9}$, respectively. For the pentagon topology, the masses are set to $m_1 = 0.10$, $m_2 = 0.11$, $m_3 = 0.12$, $m_4 = 0.13$, $m_5 = 0.14$. The results for these different

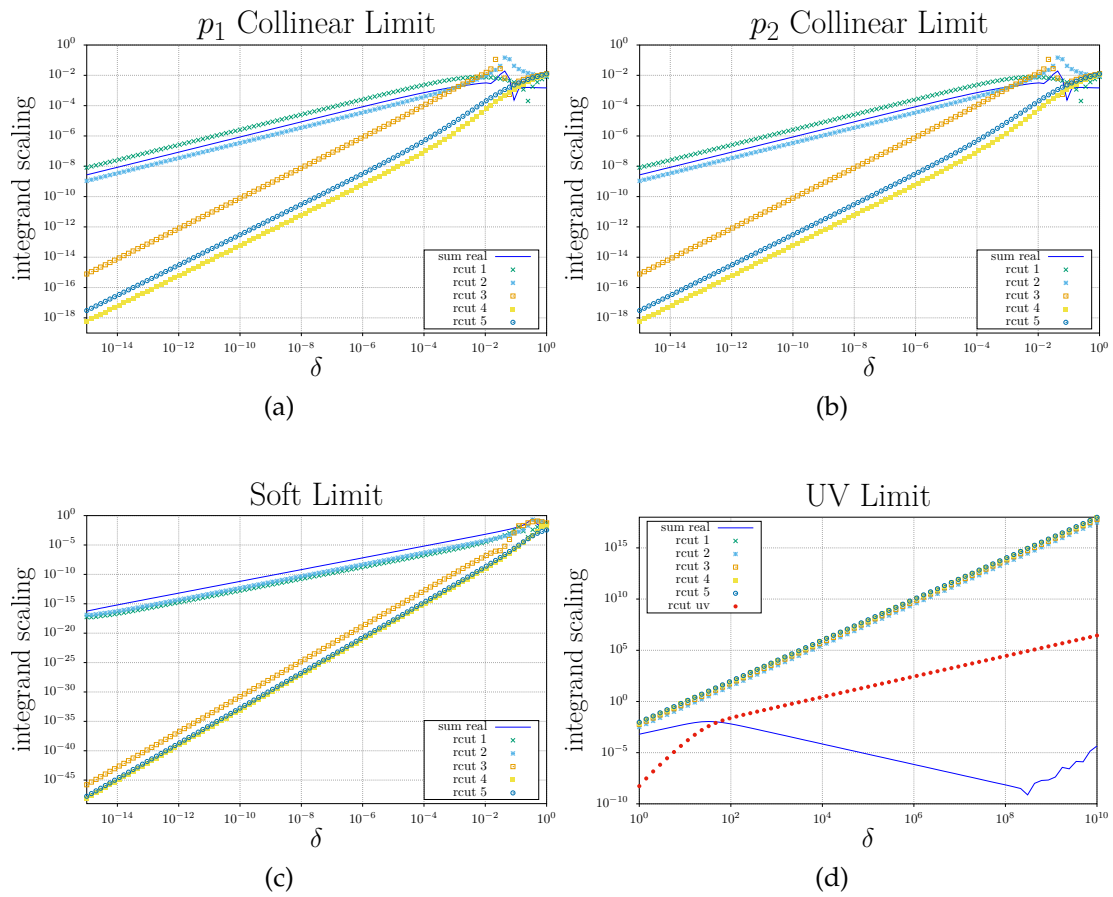


FIGURE 4.7: Behaviour of the $q\bar{q} \rightarrow 3\gamma$ in the different regulated limits. When the various limits are approached linearly in δ the plots (a–b) show a scaling as $\delta^{\frac{1}{2}}$ whereas (c) goes like δ^1 and (d) as δ^{-1} .

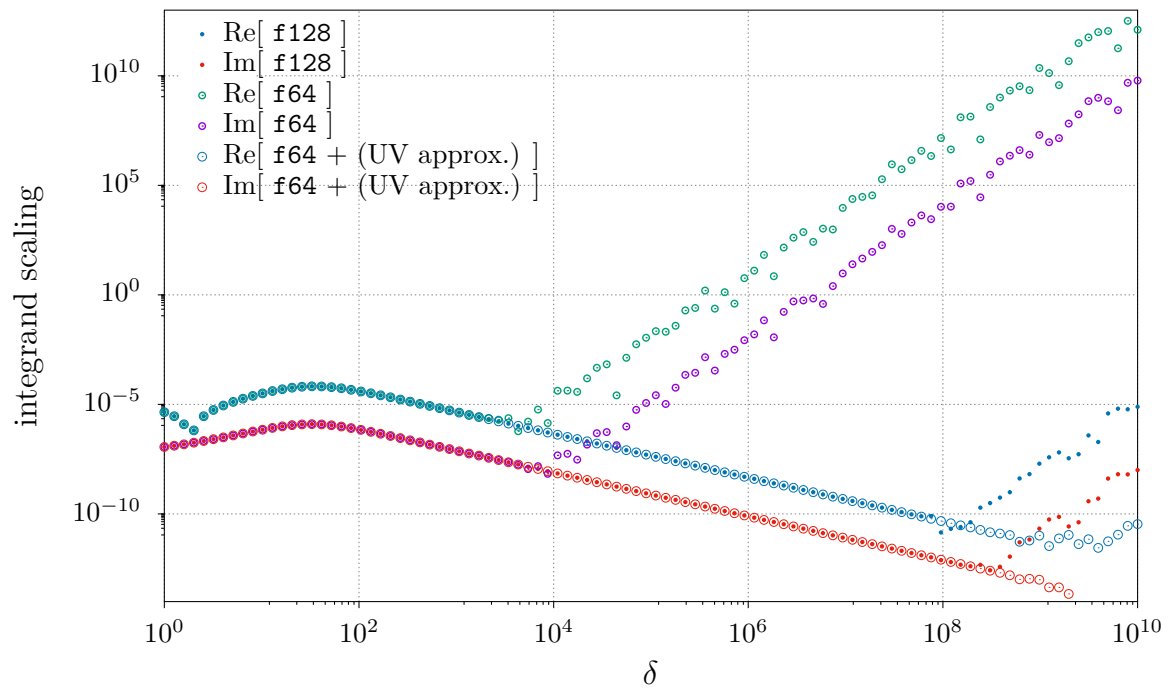
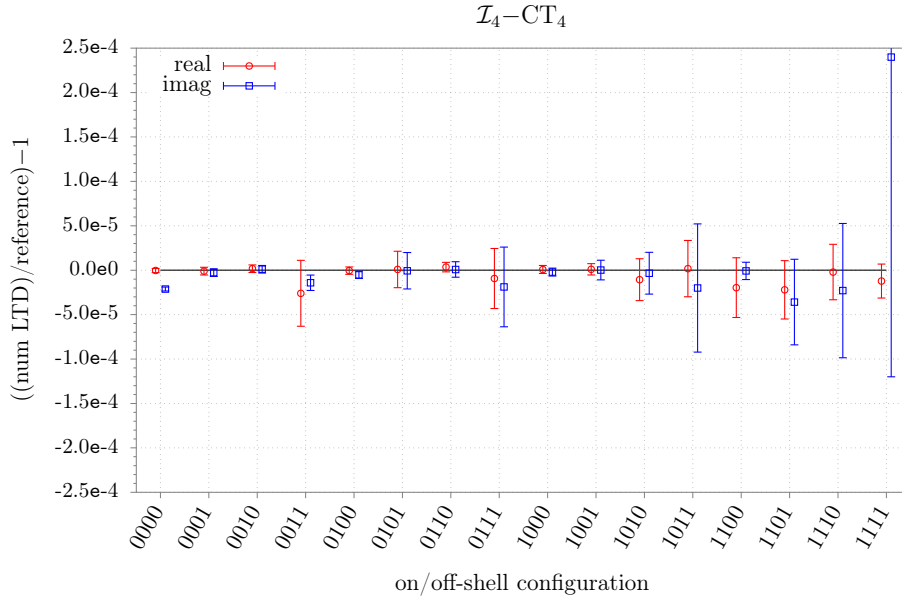
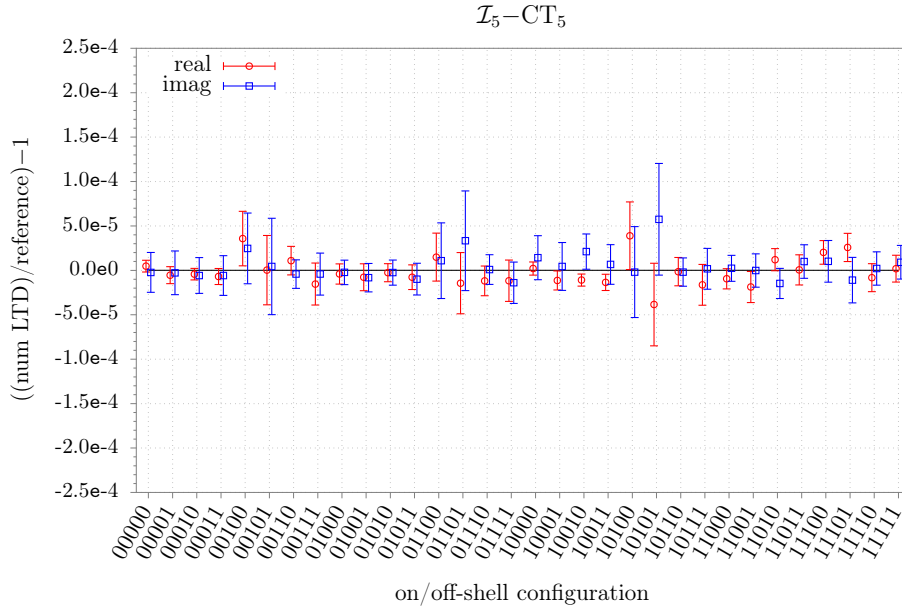


FIGURE 4.8: Behaviour of numerical instability in the UV due to imprecise cancellations between large numbers from each each dual integrand. The loop momentum k is rescaled by a factor δ and the real and imaginary part of the amplitude are presented with different precision (double and quadruple) and by expanding the expression around the UV limit as an approximation (see section 4.3.2).



(a) Divergent box topology.



(b) Divergent pentagon topology.

FIGURE 4.9: Results for the computation of divergent four- and five-point scalar one-loop integrals. We show the real and imaginary part of the expression integrated with LTD, compared with the analytic expression computed with MadLoop5 [198, 199](ML5) and qcdLoop [200]. The (nominal) horizontal axis shows different phase-space configurations using a binary notation, where a 1 (resp. 0) in the i th position signifies that the i th external momentum is on-shell with $p_i^2 = 0$ (resp. off-shell, that is with $p_i^2 \neq 0$). All but one of the central values are within 0.005% of the analytical result. The outlier with configuration 1111 lies within 0.024% of the analytical result and has a relative standard error of 0.036%.

configurations are shown in figure 4.9, where the particular combination of masses for the external momenta is labelled by a binary number with the convention that a 1 in the i -th position means that the i -th external momentum is massless. We use the Cuhre integrator from Cuba package [187] with 200 million sample points. The time for each evaluation is independent of the mass configuration and is similar with the one presented in table C.1.

Both the four-point (“box”) and five-point (“pentagon”) function can be integrated with high accuracy and precision: all but one of the central values are within a 0.005% of the analytical result. Only the imaginary part of the box topology with all the external momenta on-shell has a large uncertainty. The reason is that the central value of this integral is ten times smaller than for the other box configurations. However, even this point lies within 0.024% of the analytical result and has a relative standard error of 0.036%.

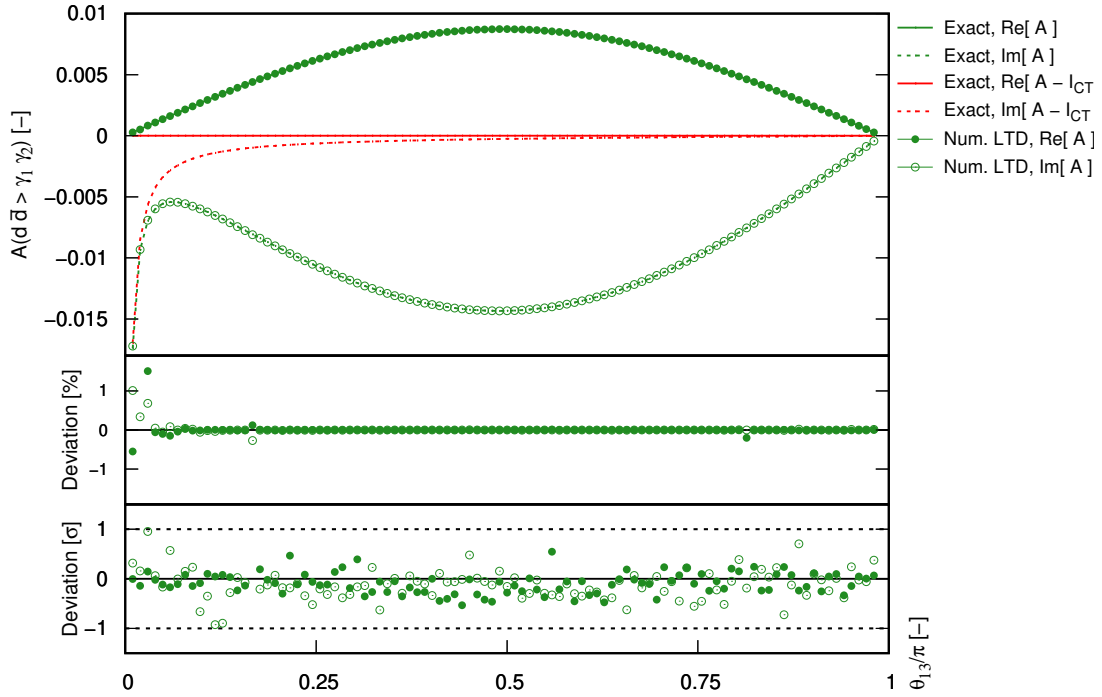
The analytic expression of the box integral and the triangle integrals required to construct the analytical expression for the counterterms have been computed using `qcdloop` [200]. The pentagon integral has been obtained using `MadLoop5` [198, 199] (ML5 henceforth).

4.3.4 One-loop amplitude for $q\bar{q} \rightarrow \gamma_1\gamma_2$ and $q\bar{q} \rightarrow \gamma_1\gamma_2\gamma_3$

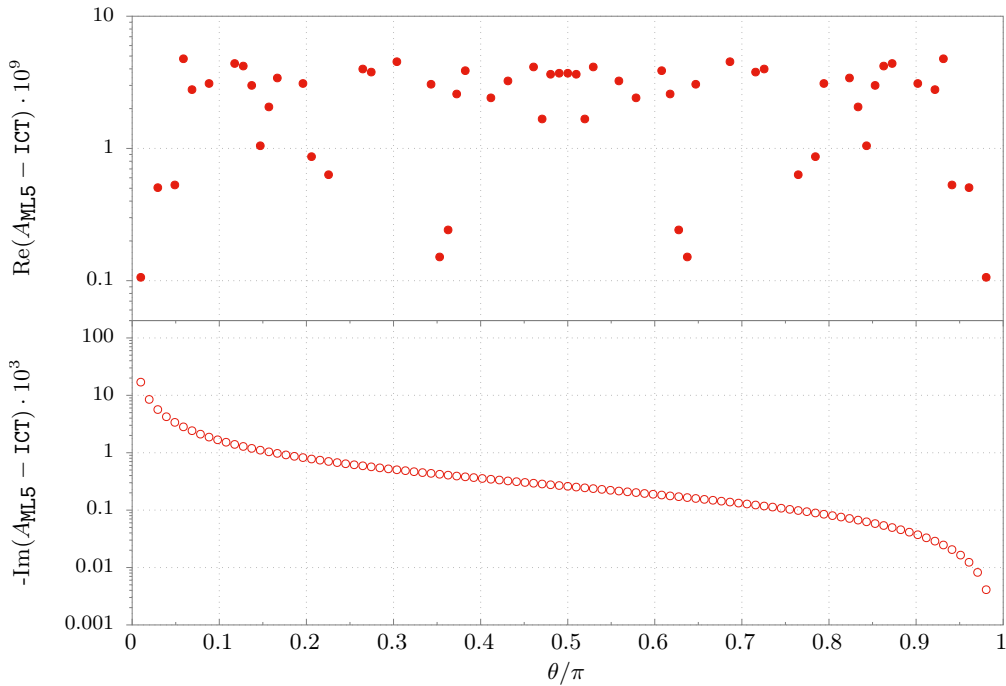
In this section we present the results from the integration of the amplitudes $d\vec{d}$ to two and three photons. For simplicity, we kept the order of the final photons fixed; the actual result for the amplitude can then be recovered by permuting through the final-state photon momenta. The helicities are defined following the HELAS convention [201], and are taken positive for all the external particles. The evaluation of the numerator, involving contractions of Lorentz and spinor indices, is performed numerically at run-time. This is not an efficient way to perform the numerator algebra, but the aim of this work is to highlight how LTD can be used to obtain results for physical and divergent expressions.

The analytic expressions have been compared with ML5 with $g_s = 1.21771$, $g = 0.30795$ and $\mu_r = 91.1880$ as couplings. We also remind the reader that the results from ML5 are rescaled by an overall factor $(4\pi)^\epsilon / \Gamma(1 - \epsilon)$.

For the $d\vec{d} \rightarrow \gamma_1\gamma_2$ process, we consider the process in its centre-of-mass rest frame, with the quarks aligned along the z -axis. The result will only depend on the scattering energy and angle. The former is kept fixed and corresponds to a simple rescaling of the integral and the latter is varied in a scan and plotted in figure 4.10. We used the Cuhre integrator from Cuba package [187] with two million evaluations. In the last plot of figure 4.10 we notice that the result is almost completely determined by the integrated counterterms. This is especially true



(a) Integration of the one-loop $d\bar{d} \rightarrow \gamma_1 \gamma_2$ amplitude.



(b) Regulated one-loop $d\bar{d} \rightarrow \gamma_1 \gamma_2$ amplitude.

FIGURE 4.10: A scan of our results using numerical LTD for the $d\bar{d} \rightarrow \gamma\gamma$ amplitude for various scattering angle θ_{13} . In figure (a-b) we can see the results computed with LTD compared with the analytic expression obtained with MadLoop5 [198, 199] (ML5). In the last plot we show the result of the integral of the the finite regulated integrand that we actually integrate numerically. This corresponds to subtracting the integrated counterterms to the exact analytic result for the amplitude.

for the real part, where one can see that resulting regulated integral is six orders of magnitude smaller than the finite part of the analytic expression.

As for the case of scalar divergent integrals, we use the Cuhre integrator with however only 2 million sample points in this case. Despite this relatively low statistics, a large fraction of the results already have relative error below 0.05%. In the upper plot of figure 4.10 we show the relative deviation with a large scale in order to highlight the few points that are not within this small error. One important observation however is that the Monte-Carlo error reported is reliable, as highlighted by the fact that all discrepancies are smaller than one (in modulus) when expressed in unit of the Monte-Carlo standard deviation σ .

In figure 4.11 we show a scan of $d\vec{d} \rightarrow \gamma_1\gamma_2\gamma_3$. In the same way as for the two-photon production case, we consider the scattering in the centre-of-mass rest frame. This time however, the number of unspecified and non-trivial degrees of freedom is four so that keeping a fixed energy $s_{12} = 1$ leaves us with three parameters. For the kinematic configuration $d(p_1)\vec{d}(p_2) \rightarrow \gamma_1(p_3)\gamma_2(p_4)\gamma_3(p_5)$, we choose to scan in the angle $\theta_{13} = \angle(p_1, p_3)$, and s_{45} which gives an indication of how collinear the momenta p_4 and p_5 are. We fix the remaining degree of freedom by forcing the process on a plane, which allows for the configuration where p_4 is collinear to p_1 , thus resulting in the valley shown in plots (a – b) of figure 4.11. For $d\vec{d} \rightarrow \gamma_1\gamma_2\gamma_3$, we observe that the relative contribution from the integrated counterterms is not as large as for $d\vec{d} \rightarrow \gamma_1\gamma_2$, because this five-point amplitude has more contributions that are IR-finite (specifically D4-6 from figure 4.6) and therefore not captured by the counterterms.

We can see that the relative error is $< 1\%$ for most of the points in the scan as shown in the upper plane of plot (e–f) from figure 4.11). In the lower part of the same plots, the precision of the result with an error that is also $< 1\%$ for most of the points. Along the valley, the *relative* accuracy is not as good as in the other regions, which is to be expected when the central value of the integrated expression becomes smaller than the values around it. Similarly as to elsewhere in this subsection, the results were obtained using the Cuhre integrator and 2 million sample points. The low number of samples is due to two mainly two reasons: first, we used a naive implementation of the numerator containing spinor chains that are recomputed numerically for each evaluation and second, despite the measure taken for improving the UV behaviour of the integrand, probing that region still requires many evaluations in quadruple precision thus increasing the overall evaluation time by roughly one order of magnitude when compared to the corresponding scalar topologies.

In the present work, we put no effort in optimising the numerator expression which we leave to future work. The main objective of these results is to demonstrate the viability of computing physical amplitudes with numerical LTD by combining the contour deformation together with the necessary infrared and ultraviolet counterterms. Optimising the implementation of

the numerator will allow us to handle more complicated amplitudes and to consider higher integration statistics.

4.4 CONCLUSION

We have established a contour deformation for regulating the threshold singularities exhibited by loop integrals when considering physical scattering kinematics. In accordance with our long-term goals, we built a solution that is prone to automation and made no compromise regarding the generality of numerical LTD: availability of computational resources should remain the only limiting factor. Moreover, we insisted that the validity of the contour deformation should be independent of the particular values of its hyperparameters, thus guaranteeing the predictive power of numerical LTD. We demonstrated that our construction and implementation achieves these objectives by applying it to over 100 different representative configurations, ranging from one-loop boxes to four-loop 2x2 fishnets.

We also presented our first step towards computing divergent integrals and physical amplitudes. This requires combining the LTD expression with *local* integrand-level counterterms regularising divergences occurring for ultraviolet, soft and/or collinear loop momenta configurations. We described this subtraction procedure at one loop and showcase explicit examples for divergent scalar four- and five-point integrals, as well as for the one-loop amplitude of the production of two and three photons. This paves the way for a first application of numerical LTD to the numerical computation of two-loop divergent scalar integrals and of complete two-loop amplitudes, using the local counterterms introduced in refs. [83, 196]. In the integration of these amplitudes we encounter numerical instabilities in the UV region, their regulation by building a manifestly causal LTD expression is the central subject of the next chapter.

In this chapter, we focused on further developing numerical LTD in a way that is provably correct, general and that demonstrates predictive power. Therefore, we did not tune our hyperparameters for the hundreds of cases we studied and, although already satisfactory, the numerical convergence and run-time speed showcased by our results are by no means final. We leave their improvement to future work.

The ability to locally regulate ultraviolet and infrared singularities at higher loops and the performance of the numerical convergence are two key difficulties whose resolution will determine the eventual viability of numerical LTD. Our work shows a clear path for this novel approach to significantly contribute to the effort of meeting the theoretical accuracy goal set by the needs of current collider experiments.

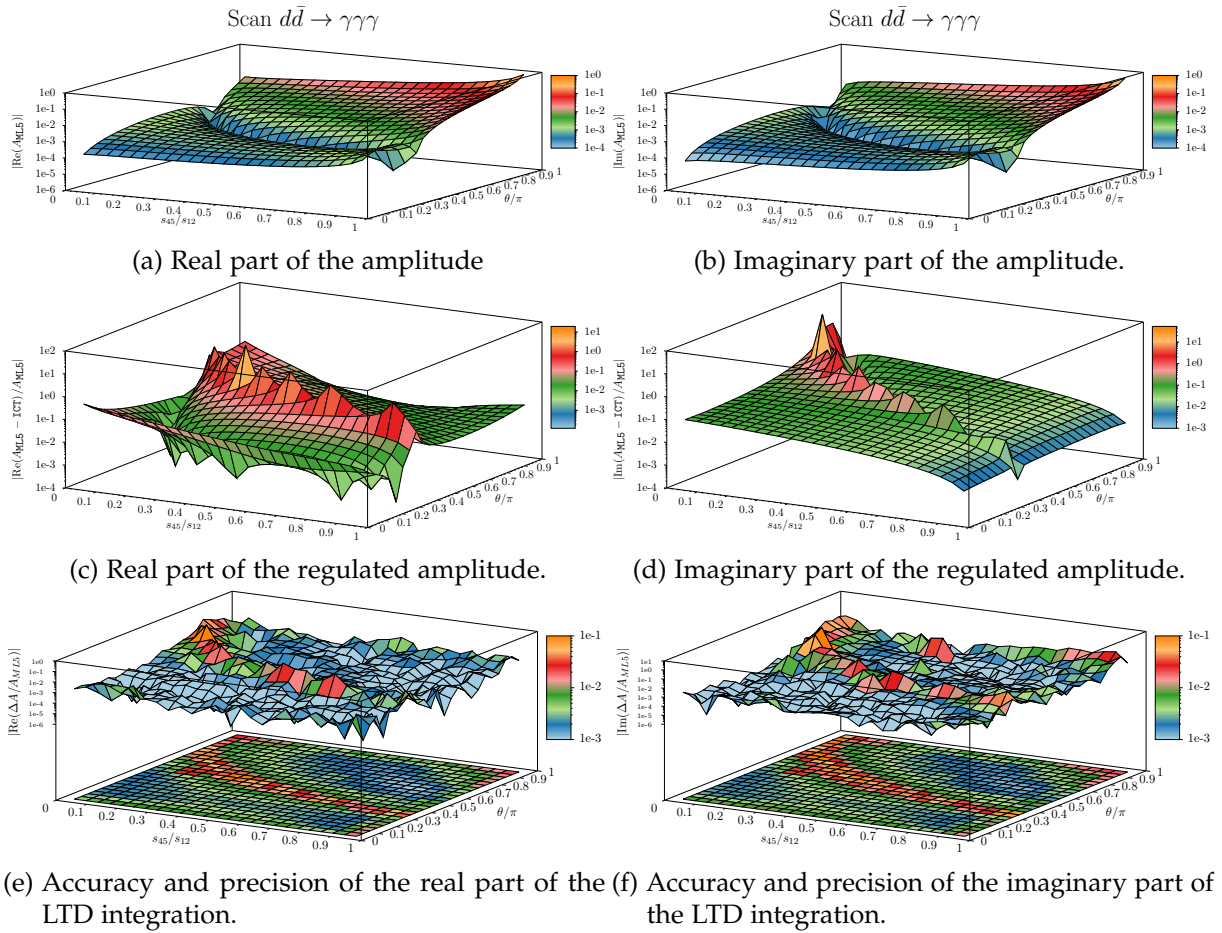


FIGURE 4.11: A scan for $d\bar{d} \rightarrow \gamma_1\gamma_2\gamma_3$. The results are absolute values plotted on a log scale. The first row (a – b) shows the real and the imaginary part of the amplitude computed with ML5. The second row (c – d) shows the relative difference between the analytic expression and the integrated counterterms. The last row (e – f) shows the LTD integration. They are a combination of two plots: the surface above shows the relative error of the central value compared with the analytic expression, the flat surface below shows the Monte Carlo error for the point right above.

In the loop-tree duality approach, the four-dimensional integrand is rewritten as a sum of functions (dual integrands) in the spatial components of the loop momenta, and the singularities are defined by the roots of their denominator; polynomials in the on-shell energies of the virtual particles involved in the process together with the energies of the external kinematics. Such polynomials can be factorised into linear combinations of its variables and the singular surfaces defined by each of these factors are represented by a (convex) manifold embedded in the integration space. These manifolds can be divided into two groups, namely H- and E-surfaces. The H-surfaces are characterised by mixed signs in the linear combination of energies, whereas the E-surfaces have a common sign.

Previous work on the analysis of the singular structure of LTD expressions [79, 81, 189] revealed that each of these dual integrands could contain poles defined by both H- and E-surface, whereas the sum of all the contributions only retains the singularities corresponding to E-surfaces. The elimination of all the H-surfaces from the final expression is referred to as dual-cancellation. Each E-surface that satisfies the existence condition and is not pinched, requires an ad-hoc contour deformation [4], or other means of regulation as e.g. subtraction of thresholds as in refs. [202] and if it is pinched, requires counterterms [83, 196, 203–207] or some other local cancellation mechanism subject of ref. [6].

Given the polynomial nature of these H-surface singularities, one can resolve the cancellations happening among different dual integrands through an algebraic manipulation: one can obtain a sum of terms which involve only E-surface kind of singularities that is locally equivalent to the original LTD expression. Such representation was studied previously for selected cases [208–210], including three- and four-loop scalar topologies. Here we propose a systematic and algorithmic procedure that yields such a representation for *any* multi-scale, multi-loop Feynman diagram with an arbitrary numerator. We refer to this new representation as *Manifestly Causal LTD* (cLTD).

The general cLTD representation presented here and introduced in ref. [5] for the first time, contains a sum of terms which grows exponentially with the number of propagators. However, these many terms are functions of a limited number of combinations of on-shell energies, thus

offering great potential in optimising their numerical implementation by identifying common sub-expressions.

The cLTD expression improves numerical stability w.r.t. that of the LTD representation whenever evaluated in the vicinity of dual-cancelling H-surfaces, which is always the case in the ultraviolet (UV) region. The UV scaling of each dual integrand of the original LTD expression is often many orders of magnitude larger than that of the original four-dimensional representation, and it is only due to dual cancellations that one eventually retrieves the original scaling of the four-dimensional integrand. Especially for physical theories, dual cancellations occur across several orders of magnitude due to the presence of a numerator. For example, in the case of the NLO $q\bar{q} \rightarrow \gamma\gamma\gamma$ amplitude presented in the previous chapter, the cancellation occurs between diverging terms that scale as k^2 , down to a scaling of $1/k^2$. In cLTD, each summand has directly the same scaling as the four-dimensional counterpart and is, therefore, more numerically stable in the UV region.

The outline of this chapter is as follows. In section 5.1 we will start by presenting a general framework for removing spurious divergences which arise from applying residue theorem to an integral with poles in the integration variable. In section 5.2, we will explain how this general formula can be applied to physical cases, realising cLTD. Finally, in section 5.3 we present several examples illustrating the cLTD procedure.

5.1 ALGEBRAIC CANCELLATION OF SPURIOUS SINGULARITIES

We consider the case of a function F defined as the integral over the real line of an integrand consisting of a general *regular* function \mathcal{N} in the numerator and a polynomial with $n + \bar{n}$ distinct roots in the denominator. We will now present a general procedure to rewrite F as a function which is manifestly regular. Within our procedure, we first perform the integral by using residue theorem. We then re-express the result by iteratively factoring each of its spurious poles. This yields terms involving divided differences of the numerator \mathcal{N} which evaluate to a finite quantity on the spurious poles, thus establishing that each term of our resulting expression is regular at these locations. In sect. 5.1.3 we specialise to the case of polynomial numerators for which the divided differences can be explicitly evaluated algebraically. Finally, we show in sect. 5.1.2 how our procedure can accommodate higher-order poles in F by regarding them as the limiting case of coinciding roots of \mathcal{N} .

5.1.1 Generic case

We start by introducing a general function defined as a real integral in z of the ratio of a numerator and a polynomial in z with roots not lying on the real line

$$F \left(\begin{matrix} \mathbf{x} \\ \bar{\mathbf{x}} \end{matrix}; \mathcal{N} \right) \equiv \frac{-1}{2\pi i} \int_{\mathbb{R}} dz \frac{\mathcal{N}(z)}{\prod_{i=1}^n (z - x_i) \prod_{i=1}^{\bar{n}} (z + \bar{x}_i)}, \quad (5.1)$$

where $\mathbf{x} \in (\mathbb{H}^*)^n$ and $\bar{\mathbf{x}} \in (\mathbb{H}^*)^{\bar{n}}$, whose components lie in the lower complex half-plane \mathbb{H}^* . As we intend to perform the integral using residue theorem, we assume the numerator \mathcal{N} to be regular such that the integrand is holomorphic on $\mathbb{C} \setminus \{\mathbf{x}, \bar{\mathbf{x}}\}$ with vanishing residue at infinity. We can therefore close the contour arbitrarily on an arc in either the upper or the lower complex half-plane so as to correctly evaluate eq.(5.1).

If all components of \mathbf{x} as well as all components of $\bar{\mathbf{x}}$ are pairwise distinct, the integrand only has single poles in the complex plane. Otherwise, the integrand exhibits higher-order poles. Although the treatment of higher-order poles may seem more involved at first, the expressions in this section are valid in this case as well, and have to be understood as the limit where single poles merge. The case of coinciding roots is discussed in section 5.1.2.

In order to keep our expressions compact we introduce the shorthand notation for a slice of a vector \mathbf{y} , as

$$\mathbf{y}_{(i,j)} \equiv (y_i, \dots, y_j), \quad \mathbf{y}_{(i)} \equiv \mathbf{y}_{(i, \dim(\mathbf{y}))}, \quad [\mathbf{y}, x_1, \dots, x_n] \equiv [y_1, \dots, y_{\dim(\mathbf{y})}, x_1, \dots, x_n], \quad (5.2)$$

as well as the following two recurring function and functional:

$$E(x_i | \bar{\mathbf{y}}) \equiv \frac{1}{\prod_{j=1}^{\dim(\bar{\mathbf{y}})} (x_i + \bar{y}_j)}, \quad (5.3)$$

$$\mathbf{N}_{\mathcal{F}}([\mathbf{y}, x_i, x_j]) \equiv \frac{\mathbf{N}_{\mathcal{F}}([\mathbf{y}, x_j]) - \mathbf{N}_{\mathcal{F}}([\mathbf{y}, x_i])}{x_j - x_i}, \quad \mathbf{N}_{\mathcal{F}}([x_i]) \equiv \mathcal{F}(x_i), \quad (5.4)$$

for any regular function \mathcal{F} and arbitrary vectors $\mathbf{y} \in (\mathbb{H}^*)^{\dim(\mathbf{y})}$ and $\bar{\mathbf{y}} \in (\mathbb{H}^*)^{\dim(\bar{\mathbf{y}})}$. We point out that the recursion for $\mathbf{N}_{\mathcal{F}}$ is commonly referred to as the algorithm of *divided differences*. Divided differences are symmetric in their arguments, meaning that $\mathbf{N}_{\mathcal{F}}([\mathbf{y}])$ is independent of the order in \mathbf{y} . Furthermore, we emphasise that the recursive step in eq.(5.4) does not introduce a pole if $x_j = x_i$ but instead translates into a derivative at x_i , as we will see in more detail in section 5.1.2. Note as well that each factor in $E(x_i | \bar{\mathbf{y}})$ with $x_i \in \mathbb{H}^*$ has a definite imaginary

part, i.e. $\text{Im}(x_i + \bar{y}_j) < 0$ and therefore cannot be singular.¹ Making these observations, we can already conclude that whereas $N_{\mathcal{F}}$ has spurious poles in its arguments, E is already manifestly free of spurious poles.

We carry on with the calculation of the integral eq.(5.1) by applying the residue theorem, such that we arrive at

$$F \left(\begin{matrix} \mathbf{x} \\ \bar{\mathbf{x}} \end{matrix}; \mathcal{N} \right) = \sum_{i=1}^n \frac{N_{\mathcal{N}}([x_i])E(x_i|\bar{\mathbf{x}})}{\prod_{j \neq i} (x_i - x_j)}, \tag{5.5}$$

which sums the residues located in the lower-half complex plane. If $n = 1$ we define the empty product to be one. Of course, the representation of eq.(5.5) as the sum of residues is formally different but equivalent when closing the contour in the upper complex half-plane. We can therefore choose a contour closure in the lower complex half-plane, thus allowing us to use the representation in eqs. (5.5).

The poles at $x_i = x_j$ are spurious since such limit corresponds to an higher order pole in the integrand of F in which can still be integrated to a finite expression via the residue theorem. As derived explicitly in appendix D, this procedure can be summarized in a generic recursive step

$$F \left(\begin{matrix} \mathbf{y} \\ \bar{\mathbf{y}} \end{matrix}; \mathcal{F}(z) \right) = -N_{\mathcal{F}}([y_1]) \sum_{j=1}^{\dim(\bar{\mathbf{y}})} E(y_1|\bar{\mathbf{y}}_{(j)}) F \left(\begin{matrix} \mathbf{y}^{(2)} \\ \bar{\mathbf{y}}_{(1,j)} \end{matrix}; 1 \right) + F \left(\begin{matrix} \mathbf{y}^{(2)} \\ \bar{\mathbf{y}} \end{matrix}; \mathcal{F}'(z) \right), \tag{5.6}$$

$$\mathcal{F}'(z) \equiv N_{\mathcal{F}}([y_1, z]),$$

which systematically removes all spurious poles in y_1 , as each summand in the expression is manifestly free of denominators $(y_1 - y_j)$ for $1 < j \leq \dim(\mathbf{y})$. Of course, such denominators are still hidden in the divided difference $N_{\mathcal{F}}([y_1, z])$. However, as mentioned before, $N_{\mathcal{F}}$ is regular if \mathcal{F} is and therefore does not introduce singularities to F . Also, note that this recursion holds for $\dim(\mathbf{y}) > 1$. Then, one can iterate the recursion for the remaining instances of F on the right-hand side of eq.(5.6) so as to explicitly and successively remove each spurious poles in y_j . Eventually one arrives at the case $\dim(\mathbf{y}) = 1$, the boundary condition, where the resulting expression for eq.(5.5) is then already manifestly free of spurious poles. Notice as well that the recursion simplifies whenever the numerator function is constant, since in that case the divided difference appearing in the last summand in eq.(5.6) vanishes.

¹ It can be singular in the limit where the imaginary part vanishes, as in the physical case (see section 5.2, where E will correspond to a product of E-surfaces), which however does not affect the discussion here.

We now apply the generic algorithm in eq.(5.6) to the expression in eq. (5.5) and unfold it into

$$F \begin{pmatrix} \mathbf{x} \\ \bar{\mathbf{x}} \end{pmatrix}; \mathcal{N} = \sum_{i=1}^n (-1)^{n+i} \mathbf{N}_{\mathcal{N}}([\mathbf{x}_{(1,i)}]) \sum_{\vec{j} \in T_{n+1-i}^n} \prod_{k=i}^n E(x_k | \bar{\mathbf{x}}_{(j_k, j_{k-1})}) \quad (5.7)$$

where we defined,

$$T_k^m \equiv \left\{ \vec{j} \in \mathbb{N}^k \mid j_{i+1} \leq j_i \leq m \text{ and } j_k = 1 \right\}, \quad (5.8)$$

with the additional boundary term defined as $j_0 \equiv \bar{n}$. We also used the property that the function $\mathcal{F}(z)$ in (5.6) can itself represent a divided difference with an additional \mathbf{y} arguments referring to the initial uni-variate numerator function \mathcal{N} as $\mathbf{N}_{\mathcal{N}}([\mathbf{y}, z])$ which will then fulfil,

$$\mathbf{N}_{\mathcal{F}([\mathbf{y}, z])}([x_i]) = \mathbf{N}_{\mathcal{N}([\mathbf{y}, z])}([x_i]) = \mathbf{N}_{\mathcal{N}}([\mathbf{y}, x_i]). \quad (5.9)$$

We emphasise that the expression in eq.(5.7) is the main result in this section. It is an alternative representation of eq.(5.5) as well as eq.(5.1). Although eq.(5.5) provides a compact expression as the sum of residues for the integral representation in eq.(5.1), it features spurious singularities that render each residue potentially singular. Only in the sum of residues are these singularities subject to exact cancellations. Our alternative representation in eq.(5.7) is manifestly free of those spurious singularities, as each individual summand cannot become singular. This means that eq.(5.7) also does not rely on large cancellations around singularities unlike eq.(5.5). Although formally more complicated, the representation in eq.(5.7) can be evaluated in a straight-forward fashion, especially because the divided differences $\mathbf{N}_{\mathcal{F}}$ are a well-known mathematical concept.

Furthermore, it is important to note that eq.(5.7) is not the only representation of eq.(5.5) that is free of spurious singularities. Indeed, a different choice of order in \mathbf{x} and $\bar{\mathbf{x}}$ or contour closure will in general yield a different formal representation of eq.(5.7). We emphasize that such different functional representations locally evaluate to the same quantity and thus all possess the property of being explicitly free of spurious singularities.

Despite ambiguities in the representation of eq.(5.7), the algorithm is symmetric under the exchange of $\mathbf{x} \leftrightarrow \bar{\mathbf{x}}$ when picking the opposite contour closure. This implies that if $\dim(\mathbf{x}) = \dim(\bar{\mathbf{x}})$ the final number of summands in eq.(5.7) is always the same given a particular numerator \mathcal{N} . In general however, the total number of terms varies and depends on the particular choice of numerator. When considering a constant numerator all but the first summand in equation (5.7) drop out. Also, for a polynomial \mathcal{F} of degree k , the divided

differences $N_{\mathcal{F}}([\mathbf{y}])$ with $\dim(\mathbf{y}) > k + 1$ vanish. The final number of terms generated with a given numerator function can be computed by noticing that

$$|T_n^m| = \binom{n+m-2}{m-1}. \quad (5.10)$$

For example, if the numerator \mathcal{N} is a polynomial of degree $k < n$ the expression in eq.(5.7) has a total number of

$$N_{\text{terms}}(n, \bar{n}, k) = \sum_{i=1}^{k+1} |T_{n-i+1}^{\bar{n}}| = \frac{1}{\bar{n}!} \left(\frac{(n+\bar{n}-1)!}{(n-1)!} - \frac{(n-k+\bar{n}-2)!}{(n-k-2)!} \right) \quad (5.11)$$

summands, where setting $k = n - 1$ establishes an upper bound for an arbitrary numerator \mathcal{N} and yields

$$\max_k [N_{\text{terms}}] (n, \bar{n}) = \frac{(n+\bar{n}-1)!}{\bar{n}!(n-1)!}. \quad (5.12)$$

This bound is especially important because it highlights a potential computational challenge with the representation in eq.(5.7). As we see in eq.(5.11), the total number of terms grows exponentially in n regardless of the value of k . Regarding computational efficiency, this is an evident drawback of eq.(5.7) when comparing to the representation in eq.(5.5), which only has n summands. On the other hand, we will demonstrate for polynomial numerators that eq.(5.7) is numerically much better behaved than eq.(5.5) and that the numerical implementation of the many summands can be drastically optimised by identifying common sub-expressions so that it can be made competitive for physical applications.

5.1.2 Degenerate case

As we have already touched upon in the previous section, the integrand as defined in eq.(5.1) exhibits higher-order poles if the components of \mathbf{x} or $\bar{\mathbf{x}}$ are not pairwise distinct but two or more components are equal. This raises the question of whether the computation of the integral in eq.(5.5) can still be correct in this case, since it is given by a sum of single pole residues. As we will see in this section, the case of higher-order poles, the *degenerate case*, does not require special treatment but can be understood as the limit in which multiple single poles merge. This means that equations in the previous section 5.1 are still valid when considered in this limit. Although the limit is not straight-forward to apply to the sum of residues in eq.(5.5), it can easily be computed in the final expression in eq.(5.7). We will now explicitly evaluate the limit

of the degenerate case and show that the result is the same as if residues of higher-order poles were used directly to compute the integral in eq.(5.1).

We start by computing the divided difference in eq.(5.4) in the case where r of its arguments are equal. Since divided differences are symmetric in their arguments, we can arrange them such that the equal components are last. It follows from the mean value theorem that the degenerate divided difference evaluates to

$$N_{\mathcal{N}}(\underbrace{[x, y, \dots, y]}_{r\text{-times}}) = \frac{1}{(r-1)!} \frac{d^{r-1}}{dy^{r-1}} N_{\mathcal{N}}([x, y]), \quad (5.13)$$

the $(r-1)^{\text{th}}$ derivative of the divided difference without degenerate arguments. In the special case where all of the n single poles merge into one pole located at x of order n , eq.(5.7) becomes

$$\begin{aligned} F\left(\begin{matrix} x \cdot \mathbf{1} \\ \bar{x} \end{matrix}; \mathcal{N}\right) &= \frac{1}{(n-1)!} \sum_{r=0}^{n-1} \binom{n-1}{r} \left[\frac{d^r \mathcal{N}(x)}{dx^r} \right] \left[\frac{d^{n-1-r}}{dx^{n-1-r}} E(x|\bar{x}) \right] \\ &= \frac{1}{(n-1)!} \frac{d^{n-1}}{dx^{n-1}} \left[\mathcal{N}(x) E(x|\bar{x}) \right], \end{aligned} \quad (5.14)$$

where we used Leibniz's rule and

$$\sum_{\vec{j} \in \Gamma_m^n} \prod_{k=1}^m E\left(x|\bar{x}_{(j_k, k-1)}\right) = \frac{(-1)^{m-1}}{(m-1)!} \frac{d^{m-1}}{dx^{m-1}} E(x|\bar{x}), \quad (5.15)$$

which follows from eq.(5.7) when one considers all x_j to be equal, which allows to identify the overlaps of denominators in the product of E -functions as raised powers induced by the action of the derivative on x .

Notice that eq.(5.14) shows that the integral commutes with the limit so that we can treat the degenerate case with higher-order poles in the same fashion as the non-degenerate one with single poles only. This however raises a question regarding numerical evaluation in the degenerate limit. In general, one then still expects to rely on the computation of derivatives, unless the numerator is a polynomial as we will now demonstrate.

5.1.3 Manifest cancellations for polynomial numerators

For most physical applications of our procedure, the numerator \mathcal{N} will be a polynomial. For example, Feynman integrals that arise from gauge theories such as the the Standard Model are analogous to F and have a non-trivial polynomial numerator \mathcal{N} . More specifically, as we

will see in section 5.2, the numerator of a Feynman integral will translate into a polynomial numerator in the loop energy variables, as in eq.(5.1), while the variables \mathbf{x} will correspond to on-shell energies.

As discussed in the previous section 5.1.2, the divided differences defined in eq.(5.4) are not singular for degenerate arguments as they correspond to a derivative in this limit. This however means that a naive evaluation at $x_j = x_i$ of the divided difference in eq.(5.4) is not possible without computing the derivative. Furthermore, an evaluation even close to the degenerate case, i.e. close to $x_j = x_i$ is numerically unstable, such that the expression eq.(5.4) is in general computationally not very useful. We will now demonstrate that this does not pose an issue whenever we deal with polynomial numerators, as we can evaluate divided differences algebraically. More explicitly, if the numerator \mathcal{N} is a polynomial of finite degree with coefficients α_i , we can always explicitly cancel the potentially singular denominator $(x_j - x_i)$ from eq.(5.4) and rewrite the divided differences as polynomials of smaller degree, depending on the same coefficients α_i . This implies that in practice, using the following manipulations for polynomial numerators, the treatment of the degenerate as well as the non-degenerate case is identical. In the application to loop integrals this means that raised propagators as well as intersections of singular surfaces do not require special attention regarding the derivation of the cLTD expression.

We start by writing a generic polynomial numerator of degree r as

$$\mathcal{N}(x) = \sum_{i=0}^r \alpha_i x^i.$$

Making use of the geometric sequence one can rearrange the differences appearing in the numerator function in such a way that factorizes the spurious singularity,

$$(x_1^n - x_2^n) = (x_1 - x_2) \sum_{k=0}^{n-1} x_1^{n-k-1} x_2^k. \quad (5.16)$$

Removing all the explicit cancellations in the recursive definition in eq.(5.4), we can express the divided difference $N_{\mathcal{N}}([\mathbf{x}])$ directly as

$$N_{\mathcal{N}}([x_1, \dots, x_n]) = \sum_{s=0}^{r-(n-1)} \alpha_s^{(1, \dots, n-1)} x_n^s, \quad (5.17)$$

where

$$\alpha_s^{(1, \dots, m)} = \sum_{k=s+1}^{r-(m-1)} \alpha_k^{(1, \dots, m-1)} x_m^{k-s-1}, \quad \alpha_s^{(1)} = \sum_{k=s+1}^r \alpha_k x_1^{k-s-1}. \quad (5.18)$$

The iteration presented above can be completely unfolded to yield

$$N_{\mathcal{N}}([x_1, \dots, x_n]) = \sum_{i_0=0}^r \sum_{i_1=1}^{i_0} \sum_{i_2=1}^{i_0-i_1} \dots \sum_{i_n=1}^{i_0-\sum_{m=1}^{n-1} i_m} \alpha_{i_0} x_n^{i_0-\sum_{m=1}^n i_m} \prod_{m=1}^{n-1} x_m^{i_m-1}$$

On a side note, another interesting property of a divided difference of polynomials is its correspondence to the quotient Q in Euclid's division theorem $\mathcal{N}(x_1) = Q(x_1)(x_1 - x_2) + \mathcal{R}$, which allows to identify $\mathcal{R} = \mathcal{N}(x_2)$ and therefore $Q(x_2) = N_{\mathcal{N}}([x_1, x_2])$.

In general the numerator may not be a polynomial, for example if one applies the partial fractioning procedure to manifestly remove infrared singularities in cross-sections, in which case the numerator can include an observable function, as in ref. [6]. If the numerator function is not a polynomial, the explicit cancellation of factors cannot be carried out explicitly and the divided differences will be subject to the same numerical instabilities as the original expression in eq.(5.5). One can nevertheless cure those cases locally by performing a Taylor expansion around such points to analytically remove such instabilities with arbitrary precision. However, the degenerate case of raised propagators can also be treated globally by computing derivatives, as we showed in section 5.1.2.

5.2 MANIFESTLY CAUSAL LTD

In this section we present an alternative to the multi-loop LTD expression presented in refs. [80, 81], which is manifestly free of spurious singularities (denoted as H-surfaces in ref. [81] or non-causal threshold singularities in refs. [209, 210]). The procedure outlined in this section will explicitly perform cancellations of spurious singularities (known as dual cancellations [79]), such that the expression does not contain any H-surfaces but only contains causal threshold singularities, known as E-surfaces [81].

The extension to the multi-loop case uses the procedure laid out in sect. 5.1 for the integration over one loop energy. Then, both this integration step and the extraction of spurious poles can be repeated for the integrals over each of the remaining loop energies. We formally write this iterative procedure by showing how the individual terms generated at each step satisfy the necessary requirements for the identity of eq. (5.7) to apply again. Although the formal derivation of the iterative procedure may seem involved, the algorithm can be expressed in a short python code that was provided in the ancillary files of ref. [5].

5.2.1 Multi-loop derivation

We consider an L -loop integrand with P propagators and perform j loop energy integrations, as in

$$\mathcal{I}_j = \left(\prod_{i=1}^j \frac{1}{2\pi i} \int dk_i^0 \right) \frac{\mathcal{N}(k_1^0, \dots, k_L^0)}{\prod_{i=1}^P D_i}, \quad (5.19)$$

which, for $j = L$ corresponds to same analytically performed integration when deriving the multi-loop LTD expression as in ref. [81]. We define the numerator \mathcal{N} as a regular function in the loop energies, such that the integrand has a vanishing residue at infinity, and the Feynman propagator as

$$\begin{aligned} \frac{1}{D_i} &= \frac{1}{(\ell_i + p_i)^2 - m_i^2 + i\delta} = \frac{1}{2E_i} \left(\frac{1}{\ell_i^0 + p_i^0 - E_i} - \frac{1}{\ell_i^0 + p_i^0 + E_i} \right) \\ &= \frac{1}{2E_i} \left(\langle -\hat{e}_i | \hat{e}_i | \vec{\lambda}_i \rangle - \langle \hat{e}_i | \hat{e}_i | \vec{\lambda}_i \rangle \right) = \frac{1}{2E_i} \sum_{\sigma_i \in \{-1, 1\}} \sigma_i \langle -\sigma_i \hat{e}_i | \hat{e}_i | \vec{\lambda}_i \rangle, \end{aligned} \quad (5.20)$$

where we introduced the loop line momentum $\ell_i = \sum_{j=1}^L \lambda_{ij} k_j$, $\lambda_{ij} \equiv (\vec{\lambda}_i)_j$ as a linear combination of the loop integration momenta, the shift of the propagator p_i as a linear combination of the external momenta, the mass m_i and the canonical basis vector \hat{e}_i , i.e. $(\hat{e}_i)_j = \delta_{ij}$. The on-shell energy $E_i = \sqrt{(\vec{\ell}_i + \vec{p}_i)^2 + m_i^2} - i\delta$ satisfies $\text{Im } E_i < 0$ since the causal prescription satisfies $\delta > 0$. Furthermore, we introduced the generic linear propagator i with the notation

$$\langle \vec{v}_i^E | \vec{v}_i^S | \vec{\lambda}_i \rangle \equiv \frac{1}{(\vec{\lambda}_i \cdot \vec{k}_0 + \vec{v}_i^E \cdot \vec{E} + \vec{v}_i^S \cdot \vec{p}_0)}, \quad \vec{k}_0 = \begin{pmatrix} k_1^0 \\ \vdots \\ k_L^0 \end{pmatrix}, \quad \vec{p}_0 = \begin{pmatrix} p_1^0 \\ \vdots \\ p_P^0 \end{pmatrix}, \quad \vec{E} = \begin{pmatrix} E_1 \\ \vdots \\ E_P \end{pmatrix},$$

where $\vec{v}_i^E \in \mathbb{R}^P$ and $\vec{v}_i^S \in \mathbb{R}^P$ define the linear combination of on-shell energies and shifts of propagators, respectively. The vector $\vec{\lambda}_i \in \mathbb{R}^L$ encodes the flow of the loop energies, introduced in the previous chapter as the signature of the propagator. Note that the linear combination $\vec{v}_i^S \cdot \vec{p}_0$ has a unique representation if expressed in terms of external momenta, as they define a basis of propagator shifts. Furthermore, we point out that a linear propagator i whose non-zero components of \vec{v}_i^E are all equal corresponds to an E-surface. Otherwise it is an H-surface.

The product of Feynman propagators in eq.(5.19) can then be rewritten in terms of linear propagators as

$$\frac{1}{\prod_{i=1}^P D_i} = \left(\prod_{i=1}^P \frac{1}{2E_i} \right) \sum_{\vec{\sigma} \in \{-1, 1\}^P} \prod_{i=1}^P \sigma_i \langle -\sigma_i \hat{e}_i | \hat{e}_i | \vec{\lambda}_i \rangle, \quad (5.21)$$

such that inserting this relation in eq.(5.19) yields an integral over a sum of terms, each containing a product of P linear propagators. In the next section we will see that each of those summands can be identified with a function F as in eq.(5.5) and show that this will eventually allow us to iteratively perform one integration after the other following the partial fractioning procedure in section 5.1, effectively solving it loop-by-loop. The final expression after carrying out this procedure is free of spurious H-surface singularities and only contains E-surfaces.

5.2.2 Loop-by-loop iteration

In order to apply the partial fractioning procedure of section 5.1 in an iterative fashion, we have to identify the linear propagators appearing at each stage of the integration with those of eq.(5.1). We will characterise each iteration by a single integral over a loop energy and perform one loop energy integral after the other. Therefore, it is necessary to pick an (arbitrary) order k_1^0, \dots, k_L^0 , with their respective integration contours with winding numbers $\Gamma_j, j \in \{1, \dots, L\}$. Evidently, the integral will be independent of the choice of integration order, as well as the contour closure. Note however that the representation of the result, including the number of summands, will depend on those choices. Furthermore, the representation of the result will also be affected by the order in which the recursion of eq.(5.6) is applied to cancel the spurious singularities explicitly. On top of this, there is a freedom of changing the loop momentum routing through the loop diagram. This is of particular interest since it effects the number of terms generated in this recursion and can therefore be used to reduce the size of the final expression.

INDUCTION HYPOTHESIS In order to make the identification clear with the procedure given in sect. 5.1, we will provide a systematic iteration step. This iteration will eventually allow us to write the cLTD expression. We set out our induction hypothesis to be the following: After explicitly performing $(j - 1)$ loop energy integrations, \mathcal{I}_j can be expressed as a sum of integrals over k_j^0 of the form

$$\mathcal{I}_j = \left(\prod_{i=1}^P \frac{1}{2E_i} \right) \sum_{\vec{h} \in \Omega_j} I_{j\vec{h}}, \quad I_{j\vec{h}} = \frac{-1}{2\pi i} \int_{\mathbb{R}} dk_j^0 \mathcal{F}_{\vec{h}}(k_j^0) \prod_{i \in S_{j\vec{h}}} \langle \vec{v}_{\vec{h}i}^E | \vec{v}_{\vec{h}i}^S | \vec{\lambda}_{\vec{h}i} \rangle. \quad (5.22)$$

where Ω_j is a set of indices and $S_{j\vec{h}} \subseteq \{1, \dots, P\}$. $I_{j\vec{h}}$ is the one-dimensional integral of a product between a regular function \mathcal{F} in k_j^0 and $|S_{j\vec{h}}|$ linear propagators, whose argument $\vec{v}_{\vec{h}i}^E$ is such that all of its non-zero components have the same sign. In other words, all linear propagators are E-surfaces. Since H-surfaces are defined as linear propagators whose energy

vectors do not have a consistent sign across their components, this induction will effectively allow to construct an iterative procedure yielding a representation of multi-loop amplitudes that is manifestly free of spurious H-surface singularities. In the following, we will perform the integration for $I_{\vec{h}}$ and suppress the index \vec{h} for simplicity.

If this assumption holds true, we can identify I_j in eq. (5.22) with the starting expression F in eq. (5.1) in the partial fractioning procedure in sect. 5.1. To now make this identification explicit, we first have to split the product of the $|S_j|$ linear propagators into three factors,

$$\prod_{i \in S_j} \langle \vec{v}_i^E | \vec{v}_i^S | \vec{\lambda}_i \rangle = \left(\prod_{i \in S_j^0} \langle \vec{v}_i^E | \vec{v}_i^S | \vec{\lambda}_i \rangle \right) \left(\prod_{i \in S_j^+} \langle \vec{v}_i^E | \vec{v}_i^S | \vec{\lambda}_i \rangle \right) \left(\prod_{i \in S_j^-} \langle \vec{v}_i^E | \vec{v}_i^S | \vec{\lambda}_i \rangle \right),$$

characterised by the disjoint sets defined as

$$S_j^0 \equiv \left\{ i \in S_j \mid \lambda_{ij} = 0 \right\}, \quad (5.23)$$

$$S_j^\pm \equiv \left\{ i \in S_j \mid \lambda_{ij} \neq 0 \text{ and } \pm \frac{\Gamma_j}{\lambda_{ij}} \vec{v}_i^E \geq \vec{0} \right\}, \quad (5.24)$$

which is sufficient as a characterisation of all possible factors due to our induction hypothesis requiring that the non-zero components of \vec{v}_i^E all have the same sign. Indeed, because of the induction hypothesis it follows that $S_j = S_j^+ \cup S_j^- \cup S_j^0$. Notice that the linear propagators in S_j^0 are constant in k_j^0 and therefore they are to be treated as simple prefactors of the whole partial fractioning procedure. Each linear propagator $i \in S_j^\pm$ however, has a single pole at $k_j^0 = k_{ji}^0$, where

$$k_{ji}^0 \equiv k_j^0 - \frac{1}{\lambda_{ij}} \left(\vec{\lambda}_i \cdot \vec{k}_0 + \vec{v}_i^E \cdot \vec{E} + \vec{v}_i^S \cdot \vec{p}_0 \right) = -\frac{1}{\lambda_{ij}} \left(\sum_{\substack{r=1 \\ r \neq j}}^L \lambda_{ir} k_r + \vec{v}_i^E \cdot \vec{E} + \vec{v}_i^S \cdot \vec{p}_0 \right) \quad (5.25)$$

lies either in the lower or the upper complex half-plane. Note that k_{ji}^0 is independent of k_j^0 since the first term cancels against the k_j^0 dependency of the first scalar product inside the parenthesis. Since the causal prescription $\delta > 0$ implies that $\text{Im } E_i < 0$ for all on-shell energies $i \in \{1, \dots, P\}$ and since we assume that \vec{v}_i^E have consistent signs, it follows that $\text{Im } k_{ji}^0$ has a definite sign that fixes its location on either the lower or the upper complex-half plane, for all possible values of spatial loop momenta. This effectively makes for the absence of residues that are sometimes in and sometimes out of the integration contour, which appeared in the derivation of our original work [81], although they dropped out in the final expression.

We therefore conclude that S_j^+ and S_j^- enumerate the linear propagators with poles in k_j^0 lying inside and outside the contour, respectively. Each linear propagator $i \in S_j^\pm$ can now be written as

$$\langle \bar{v}_i^E | \bar{v}_i^S | \bar{\lambda}_i \rangle = \frac{1}{\lambda_{ij}} \frac{1}{k_j^0 - k_{ji}^0}. \quad (5.26)$$

We now explicitly express our induction hypothesis in eq. (5.22) as the expression in eq. (5.1). According to eq. (5.26), we identify

$$z \equiv k_j^0, \quad \mathbf{x} \equiv \mathbf{k}_j^0 = \left(k_{ji}^0 \right)_{i \in S_j^+}, \quad \bar{\mathbf{x}} \equiv \bar{\mathbf{k}}_j^0 = \left(-k_{ji}^0 \right)_{i \in S_j^-}, \quad (5.27)$$

$$I_j = \left(\prod_{i \in S_j^+} \frac{1}{\lambda_{ij}} \right) \left(\prod_{i \in S_j^-} \frac{1}{\lambda_{ij}} \right) \left(\prod_{i \in S_j^0} \langle \bar{v}_i^E | \bar{v}_i^S | \bar{\lambda}_i \rangle \right) F \left(\begin{matrix} \mathbf{x} \\ \bar{\mathbf{x}} \end{matrix}; \mathcal{F} \right). \quad (5.28)$$

where the notation $(x_i)_{i \in S}$ denotes a vector of components whose index runs over the (integer) elements of S sorted in ascending order. Now that we have seen that the induction hypothesis takes the exact same form as the starting expression in eq. (5.1), we are finally ready to carry out the partial fractioning procedure laid out in sect. 5.1.

To prove the assumption we will first show that it is satisfied for the base case $j = 1$. Then we show that performing both the integration over k_j^0 and as the partial fractioning procedure for I_j implies that \mathcal{I}_{j+1} satisfies the induction hypothesis in eq. (5.22).

BASE CASE First we show that the assumption holds for the base case, where $j = 1$. We consider the expression in eq. (5.19). Notice that the very first integral over k_1^0 in eq. (5.19) together with the decomposition into linear propagators in eq. (5.21) is a sum of terms, each a product of a regular numerator,

$$\mathcal{F} = \left(\prod_{i=1}^P \sigma_i \right) \mathcal{N} \quad (5.29)$$

as well as P linear propagators. Furthermore, $\Omega_1 = \{\pm 1\}^P$. To prove that the hypothesis in eq. (5.22) is indeed satisfied for each of those summands, we have to show that all the non-zero components of \bar{v}_i^E have the same sign for each linear propagator i . For $j = 1$ the linear propagators are given as in eq. (5.20) and all satisfy $\bar{v}_i^E = -\sigma_i \hat{e}_i$. Thus, all components of \bar{v}_i^E are zero except for its i^{th} component, which proves our hypothesis for $j = 1$.

INDUCTIVE STEP To prove the hypothesis for $j > 1$, we assume that it holds true for j and show that it holds true for $j + 1$. Thanks to the identifications in eq. (5.28) we can directly apply

the partial fractioning procedure outlined in sect. 5.1. We can now express eq. (5.7) again in linear propagators. To achieve this, we have to introduce some more notation.

We define $\vec{w}^\pm \in \mathbb{N}^{|S_j^\pm|}$ and $\vec{w}^0 \in \mathbb{N}^{|S_j^0|}$ to be the vectors collecting the elements of S_j^\pm and S_j^0 respectively as entries in an ascending order. That is, $\vec{w}^\pm = (i)_{i \in S_j^\pm}$ and $\vec{w}^0 = (i)_{i \in S_j^0}$. For simplicity, we write $s = |S_j^+|$ and $\bar{s} = |S_j^-|$. Then

$$I_j = \sum_{i=1}^s \sum_{\vec{m} \in T_{s-i+1}^s} J_{j\vec{i}\vec{m}} \quad (5.30)$$

with

$$J_{j\vec{i}\vec{m}} = \frac{(-1)^{i-1} N_{\mathcal{F}}([\mathbf{k}_j^{(1,i)}])}{\prod_{i \in S_j^+} \lambda_{ij} \prod_{i \in S_j^-} \lambda_{ij}} \left[\prod_{k=1}^{s-i+1} \prod_{l=m_k}^{m_{k-1}} \lambda_{w_l^-} \langle \vec{v}_{w_l^-}^E | \vec{v}_{w_l^-}^S | \vec{\lambda}_{w_l^-} \rangle \Big|_{k_j^0 = k_{jw_k^+}^0} \right] \prod_{i \in S_j^0} \langle \vec{v}_i^E | \vec{v}_i^S | \vec{\lambda}_i \rangle \quad (5.31)$$

and $\mathbf{k}_j^{(1,i)} = ((\mathbf{k}_j^0)_1, \dots, (\mathbf{k}_j^0)_i)$ the analogue of $\mathbf{x}_{(1,i)}$. For an arbitrary linear propagator with index r , the evaluation at $k_j^0 = k_{ji}^0$ induces the transformation

$$\langle \vec{v}_r^{E'} | \vec{v}_r^{S'} | \vec{\lambda}_r' \rangle \equiv \langle \vec{v}_r^E | \vec{v}_r^S | \vec{\lambda}_r \rangle \Big|_{k_j^0 = k_{ji}^0} = \left\langle \vec{v}_r^E - \frac{\lambda_{rj}}{\lambda_{ij}} \vec{v}_i^E \Big| \vec{v}_r^S - \frac{\lambda_{rj}}{\lambda_{ij}} \vec{v}_i^S \Big| \vec{\lambda}_r - \frac{\lambda_{rj}}{\lambda_{ij}} \vec{\lambda}_i \right\rangle, \quad (5.32)$$

which is trivial if $\lambda_{rj} = 0$. For each linear propagator on the right-hand side of eq. (5.31), since $w_l^- \in S_j^-$ and $w_k^+ \in S_j^+$, it therefore follows that its energy vector $\vec{v}_i^{E'}$ has non-zero entries that have a consistent sign between them. Since the linear propagator transforms into another linear propagator with different coefficients, we conclude that it is a sum of terms just like the starting expression in eq. (5.22) with $k_j^0 \rightarrow k_{j+1}^0$ for $j < N$ replaced. This implies that the final expression \mathcal{I}_L involves denominators featuring at most $L + 1$ on-shell energies. In summary, re-instating the \vec{h} index, we can thus see that \mathcal{I}_{j+1} can be written as a sum of integrals

$$\mathcal{I}_{j+1} = \left(\prod_{i=1}^P \frac{1}{2E_i} \right) \sum_{\vec{h} \in \Omega_{j+1}} I_{j+1\vec{h}} \quad (5.33)$$

where Ω_{j+1} can be written in terms of Ω_j as

$$\Omega_{j+1} = \left\{ (\vec{h}, \vec{m}, i) \Big| \vec{h} \in \Omega_j, \vec{m} \in T_{s-i+1}^{\bar{s}}, i = 1, \dots, s, s = |S_{j\vec{h}}^+|, \bar{s} = |S_{j\vec{h}}^-| \right\}. \quad (5.34)$$

The inductive step together with the base case prove the induction hypothesis.

Finally, by construction, \mathcal{I}_{j+1} depend on one less loop energy variable with respect to \mathcal{I}_j . Ultimately \mathcal{I}_L no longer depends on any loop integration energies, which terminates the recursion. After the final iteration, \mathcal{I}_L will still be expressed as a sum of terms in the form of eq. (5.31), where each linear propagator has a definite imaginary part, determined by the causal prescription $\delta > 0$ alone. These linear propagators define precisely the causal threshold singularities, i.e. the E-surfaces of the LTD integrand. As each term in the final expression is free of non-causal singularities, i.e. H-surfaces, we have hereby proven that those spurious singularities are indeed absent in the multi-loop LTD integrand.

5.2.3 Comparison of the cLTD and LTD representations

Despite the different functional forms of LTD and cLTD, all numerical tests up to six-loop Feynman integrals have shown that this cLTD expression corresponds to the one previously conjectured in ref. [81]. This equivalence holds locally at any value of spatial integration momenta. The singular thresholds one needs to deform around are therefore the same by construction in both expressions. The cLTD therefore serves as a proof of the hypothesis posed in ref. [4] regarding dual cancellations. However, it does not offer an alternative algorithm for deriving the cut structures appearing in the LTD expression.

Because the original LTD expression in ref. [81] suffers from dual cancellations, each of its *dual integrands* [79] cannot be integrated individually. In contrast, each summand building the cLTD expression can be integrated separately with a dedicated contour deformation and importance sampling.

The main practical advantage of the cLTD expression regards its numerical stability in the vicinity of H-surfaces. In the UV region, one is always close to an H-surface, as reflected by a worsened UV scaling of the LTD expression compared to original the four-dimensional integrand. More specifically, the superficial degree of UV divergence of each dual integrand is λ^{3-P} for a one-loop scalar integral with a constant numerator and P loop propagators, whereas that of the original four-dimensional integrand is λ^{4-2P} . Especially for physical theories, dual cancellations in the LTD expression occur across several orders of magnitude. For example, in the case of the NLO $q\bar{q} \rightarrow \gamma\gamma\gamma$ amplitude (see section 4.3.2), the cancellation is between diverging terms in k^2 across four orders of magnitude, down to a scaling of $1/k^2$ of the summand. As a consequence, an approximate stabilisation procedure based on a Taylor expansion in the UV region was introduced to cope with such numerical instabilities. In contrast, each summand of the cLTD expression directly reproduces the UV behaviour of the original Feynman integral and thus renders such approximate stabilisation unnecessary.

5.2.4 Numerical stability

One main benefit from the cLTD expression is its improved numerical stability. In this section we explore this statement by considering the two scalar integrals depicted figure 5.1. Our selection is motivated by the fact that together these two integrals explore the numerical stability obtained in terms of the three relevant complexity parameters: the loop count, the multiplicity of external momenta and the rank of the polynomial numerator.

In order to probe the numerical stability in different relevant kinematic regions and be definite, we fixed the external real four-momenta components to randomly chosen quantities of order $\mathcal{O}(1)$ and probe the LTD and cLTD integrands along a particular one-dimensional section of the spatial loop momenta phase-space defined by $\vec{k}_i = \lambda \vec{c}_i$ with a variable λ spanning both the IR (small λ) and UV (large λ) regions. The defining direction \vec{c}_i are chosen with random real-valued components of order $\mathcal{O}(1)$. The numerical instabilities are correlated with the proximity of the sampling point to H-surfaces which are not isotropically distributed so that we expect quantitative differences when varying the choice of the directions \vec{c}_i . In practice however, we tested several directions and found a similar qualitative behaviour of the stability for all of them. Moreover, results from direct integration (which explores the phase-space much more democratically) corroborate our findings presented in this section. To facilitate the rendering of the results of both the IR and UV regions we choose to normalise the integrand (which does not include any jacobian) by multiplying it with the factor $(1 + \lambda^{\alpha_{UV}}) \frac{\lambda^{\alpha_{IR}}}{1 + \lambda^{\alpha_{IR}}}$, with α_{UV} and α_{IR} chosen so as to obtain a constant asymptotic behaviour in both limits.

The first plots in figure 5.1 shows the results for the 2x2 4-loop fishnet topology with a constant numerator set to one. We find that the double-precision result from the LTD representation (LTD_f64) reaching the asymptotic flat behaviour (which loosely speaking coincides with a region of lesser interest as the integrals are UV finite). This demonstrates that for such integrals, a numerical implementation in double-precision only is inapplicable, as the truncation of the UV region that would be necessary in this case would cause a non-negligible approximation error in the result of the Monte-Carlo integration. We notice small spikes in the numerical stability pattern of the LTD_f64 evaluation which we attribute to accrued proximity to dual canceling H-surfaces for such values of λ . When considering an implementation of the LTD expression using quadruple precision arithmetic (LTD_f128), the occurrence of numerical instabilities is delayed by about four order in magnitude in λ but remain as severe as for LTD_f64. Instead, we see that the cLTD representation completely removes the need for such regularisation procedure as it offers unconditional numerical stability over the entirety of the UV range. We remind the reader that the flooring at 10^{-15} of the relative accuracy of cLTD_f128 w.r.t cLTD_f64 is due to the fact the double-precision floating point representation only includes

about 17 significant digits. In the IR region and for the integral for the fishnet we find all representations and implementations to be numerically stable.

We now turn to the discussion of the results shown in the second plot of fig. 5.1, where we consider the case of a 2-loop 6-point integrals with a rank-2 numerator which is arguably more relevant to collider phenomenology. Indeed, physics applications often involve a lower loop count than that of the 2x2-fishnet but include IR subtraction/cancellation patterns, complex-valued loop kinematics and complicated numerators. The rank-2 numerator $(k_1 + k_2) \cdot p_1 + k_1 \cdot k_2$ chosen for the integral for the second integrand worsens its UV behaviour and is a first step towards exploring the benefits of the cLTD expression in the presence of such complications. In the UV region, we found the same qualitative behaviour as for the 4-loop integral, except that the numerical stability of the LTD_f128 implementation breaks down two orders of magnitude earlier. In the IR region however, we observe a degradation of the numerical stability of the cLTD_f64 implementation compared to that of its LTD counterparts. It is harder to pin-point the origin of this feature, but it is important to note that this numerical stability breakdown is far less severe than that of the LTD representation in the UV region and that the cLTD_f128 implementation remains stable throughout the entire λ -range and can thus be considered to be a reliable ground truth.

5.3 EXAMPLES

In the following section we will showcase a variety of example Feynman diagrams whose cLTD representation is computed explicitly. We will vary the number of loops, the number of external momenta and the rank of the numerator.

In order to write out explicitly the cLTD representations, we unfold the one-loop procedure discussed in section 5.1 and the multi-loop procedure of section 5.2.2, while also extending the notion of divided differences to multi-loop integrands. In doing so, we will illustrate the main features and delicate issues that arise in the derivation of the cLTD expression.

We will consider three simple examples:

- (1) In section 5.3.1 we illustrate how physical numerators are treated in the framework we laid out in sections 5.1 and 5.2 with a photon one-loop self-energy diagram. This also showcases how divided differences can be computed explicitly for polynomial numerators.
- (2) In section 5.3.2 we investigate a box diagram that highlights the intricate way in which the number of propagators per loop line affects the structure of the linear propagators and divided differences. Furthermore, using the same box diagram, we will consider

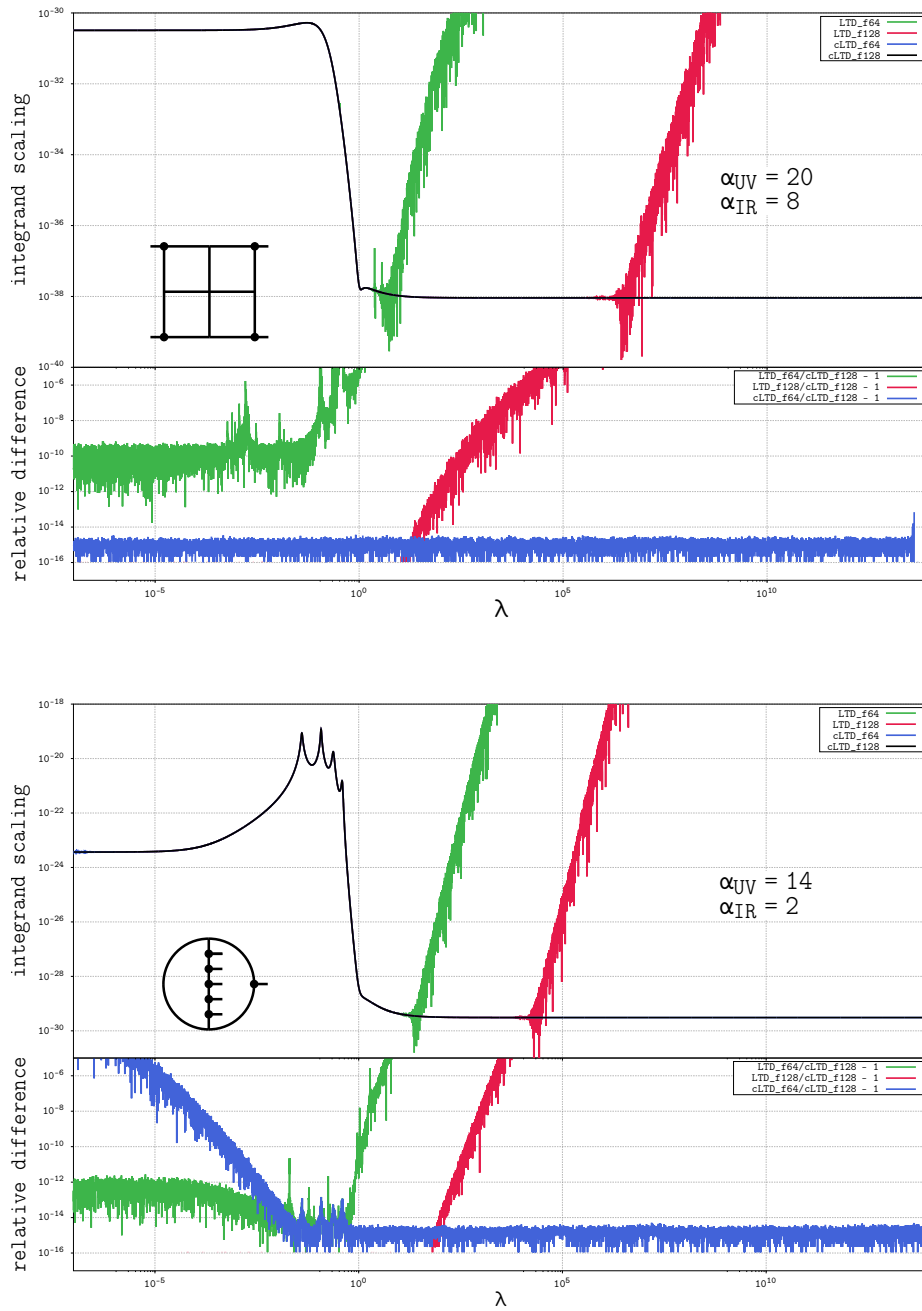


FIGURE 5.1: Study of the numerical stability of two different functional forms of the Loop-Tree Duality integrand representation of ref. [4] (LTD) and the new manifestly causal one introduced here (cLTD). Each representation is compared using double-precision arithmetic (f64) and quadruple-precision arithmetic (f128). The top plot refers to the 2x2-fishnet diagram, a 4-loop topology with four external legs and the bottom corresponds to a 2-loop 6-point topology (epta-triangle).

the degenerate case of a tadpole diagram with a propagator raised to the fourth power, corresponding to the UV limit of the box itself, whose cLTD representation is obtained directly as a limit of the non degenerate case.

- (3) In section 5.3.3 we address the application of the partial fractioning procedure beyond one loop by giving explicit examples for the two-loop sunrise diagram.

In ref. [5] we will provide a PYTHON code in the ancillary material of the ArXiv submission, which provides the cLTD expression for any Feynman diagram with an arbitrary external multiplicity, loop count, and numerator.

5.3.1 One-loop photon self-energy

This first example investigates the one-loop photon self-energy:



Despite its simplicity, this case already highlights the subtleties arising when considering a non-trivial, physical numerator. It is also the simplest setup in which it is possible to see the basic pattern of dual cancellation as it always involves terms cancelling pairwise.

The energy integration of the one-loop vacuum polarisation diagram is given by

$$\Pi = - \int dk^0 \frac{\epsilon_\mu(p, \lambda) \text{tr}((-ie\gamma^\nu)\mathbf{i}(\mathbf{k} + m)(-ie\gamma^\mu)\mathbf{i}(\mathbf{k} - \mathbf{p} + m))\epsilon_\nu^*(p, \lambda)}{(k^2 - m^2 + i\delta)((k - p)^2 - m^2 + i\delta)}, \quad (5.35)$$

whose numerator then reads:

$$\mathcal{N}(k^0) \equiv - \frac{1}{(2\pi)^4} \epsilon_\mu(p, \lambda) \text{tr}((-ie\gamma^\nu)\mathbf{i}(\mathbf{k} + m)(-ie\gamma^\mu)\mathbf{i}(\mathbf{k} - \mathbf{p} + m))\epsilon_\nu^*(p, \lambda) \quad (5.36)$$

$$= \frac{-1}{2\pi i} \frac{i\alpha}{2\pi^2} (c_0 + c_1 k^0 + c_2 (k^0)^2), \quad (5.37)$$

where

$$c_0 = 4m^2 + 4\vec{k} \cdot (\vec{k} - \vec{p}) + 8 (\vec{\epsilon} \cdot \vec{k}) (\vec{\epsilon}^* \cdot \vec{k}) \quad (5.38)$$

$$c_1 = 4p^0 - 8 \left[+\epsilon^0 (\vec{\epsilon}^* \cdot \vec{k}) + (\epsilon^0)^* (\vec{\epsilon} \cdot \vec{k}) \right] \quad (5.39)$$

$$c_2 = 8\epsilon^0 (\epsilon^0)^* - 4. \quad (5.40)$$

The numerator \mathcal{N} is a second degree polynomial in the integration variable k_0 . As argued in section 5.1, the numerator rank affects the total number of summands building the cLTD expression. We start by considering the usual LTD representation [81] of the vacuum polarization bubble, which features two dual integrands, each corresponding to one of the two internal propagators of the fermion bubble being cut with positive on-shell energy:

$$\Pi = \frac{2\alpha}{(2\pi)^6 i} \left[\frac{c_0 + c_1 E_1 + c_2 E_1^2}{2E_1((E_1 + p_0)^2 - E_2^2)} + \frac{c_0 + c_1(E_2 - p_0) + c_2(E_2 - p_0)^2}{2E_1((E_2 - p_0)^2 - E_1^2)} \right]. \quad (5.41)$$

We can rewrite each propagator evaluated at the on-shell condition as the difference of two linear propagators multiplied by the inverse on-shell energy of the momentum flowing in that propagator:

$$\frac{1}{(E_1 + p_0)^2 - E_2^2} = \frac{1}{2E_2} \left(\frac{1}{E_1 + p_0 - E_2} - \frac{1}{E_1 + p_0 + E_2} \right), \quad (5.42)$$

which makes it clear that the zeros of the inverse propagator is the union of the zeros of an E-surface $E_1 + p_0 + E_2 = 0$ and an H-surface $E_1 + p_0 - E_2 = 0$. The E-surface, characterised by its consistent sign across all on-shell energies involved, is bounded. It corresponds to a physical threshold. Instead, the H-surface contains different on-shell energy signs and its imaginary prescription therefore depends on kinematics. We now show the explicit cancellation of this H-surface by substituting eq. (5.42) in eq. (5.41) for both dual integrands:

$$\Pi = \frac{-\alpha/2}{(2\pi)^6 i E_1 E_2} \left[\frac{\mathcal{N}(E_1)}{E_1 + p_0 + E_2} + \frac{\mathcal{N}(E_2)}{E_2 - p_0 + E_1} - \frac{c_1(E_1 - E_2 + p_0) + c_2(E_2^2 - (E_2 - p_0)^2)}{E_1 - E_2 + p_0} \right]. \quad (5.43)$$

Each dual integrand yields two new summands after this substitution: one corresponding to an H-surface singularity and one to an E-surface singularity. We see that the H-surface summands have a common denominator and can be written as the last term of eq. (5.43). This combination is what manifestly realises the pairwise cancellation pattern that underlies dual cancellations. Indeed, because the numerator is a polynomial in the energy, it is possible to explicitly perform the polynomial division. As a result, we obtain our final expression

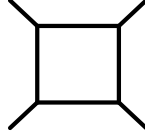
$$\Pi = \frac{-\alpha/2}{(2\pi)^6 i E_1 E_2} \left[\frac{\mathcal{N}(E_1)}{E_1 + p_0 + E_2} + \frac{\mathcal{N}(E_2)}{E_2 - p_0 + E_1} - c_1 - c_2(E_1 + E_2 - p_0) \right]. \quad (5.44)$$

The expression is now manifestly free of spurious poles, and dual cancellations have been realized algebraically. The remaining singularities of Π are located at the zeros of E-surfaces which, as mentioned earlier, have a prescription with a well-defined sign across all kinematic configurations and identify bounded surfaces.

5.3.2 Box topology

As we increase the number of propagators per loop line (at one-loop this corresponds directly to an increase of the multiplicity of the external momenta), the cancellation of spurious singularities induces more terms in the cLTD representation.

We observe that for the box diagram



the original four dual integrands forming the LTD representation of ref. [81] increase to up to 35 summands in the cLTD representation. More precisely, we consider the general box integral over the loop energy

$$\text{Box}_{\text{LTD}} = \frac{1}{2\pi i} \int dk^0 \frac{\mathcal{N}(k^0)}{\prod_{i=1}^4 ((k + p_i)^2 - m_i^2 + i\delta)}. \quad (5.45)$$

The corresponding cLTD expression following from our recursive procedure of section 5.2.2 reads:

$$\begin{aligned} \left[\prod_{i=1}^4 (2E_i) \right] \text{Box}_{\text{LTD}} = & + \frac{\mathcal{N}_{\mathcal{N}}([z_1])}{d_{21}d_{31}d_{41}} + \frac{\mathcal{N}_{\mathcal{N}}([z_1])}{d_{21}d_{24}d_{34}} + \frac{\mathcal{N}_{\mathcal{N}}([z_1])}{d_{21}d_{31}d_{34}} + \frac{\mathcal{N}_{\mathcal{N}}([z_1])}{d_{21}d_{23}d_{43}} + \frac{\mathcal{N}_{\mathcal{N}}([z_1])}{d_{21}d_{41}d_{43}} \\ & + \frac{\mathcal{N}_{\mathcal{N}}([z_1])}{d_{21}d_{23}d_{24}} + \frac{\mathcal{N}_{\mathcal{N}}([z_1])}{d_{31}d_{32}d_{42}} + \frac{\mathcal{N}_{\mathcal{N}}([z_1])}{d_{31}d_{41}d_{42}} + \frac{\mathcal{N}_{\mathcal{N}}([z_1])}{d_{31}d_{32}d_{34}} + \frac{\mathcal{N}_{\mathcal{N}}([z_1])}{d_{41}d_{42}d_{43}} \\ & + \frac{\mathcal{N}_{\mathcal{N}}([z_2])}{d_{12}d_{32}d_{42}} + \frac{\mathcal{N}_{\mathcal{N}}([z_2])}{d_{12}d_{14}d_{34}} + \frac{\mathcal{N}_{\mathcal{N}}([z_2])}{d_{12}d_{32}d_{34}} + \frac{\mathcal{N}_{\mathcal{N}}([z_2])}{d_{12}d_{13}d_{43}} + \frac{\mathcal{N}_{\mathcal{N}}([z_2])}{d_{12}d_{42}d_{43}} \\ & + \frac{\mathcal{N}_{\mathcal{N}}([z_2])}{d_{12}d_{13}d_{14}} + \frac{\mathcal{N}_{\mathcal{N}}([z_3])}{d_{13}d_{23}d_{43}} + \frac{\mathcal{N}_{\mathcal{N}}([z_3])}{d_{13}d_{14}d_{24}} + \frac{\mathcal{N}_{\mathcal{N}}([z_3])}{d_{13}d_{23}d_{24}} + \frac{\mathcal{N}_{\mathcal{N}}([z_4])}{d_{14}d_{24}d_{34}} \\ & - \frac{\mathcal{N}_{\mathcal{N}}([z_1, z_2])}{d_{32}d_{42}} - \frac{\mathcal{N}_{\mathcal{N}}([z_1, z_2])}{d_{32}d_{34}} - \frac{\mathcal{N}_{\mathcal{N}}([z_1, z_2])}{d_{42}d_{43}} - \frac{\mathcal{N}_{\mathcal{N}}([z_1, z_3])}{d_{23}d_{43}} - \frac{\mathcal{N}_{\mathcal{N}}([z_1, z_3])}{d_{23}d_{24}} \\ & - \frac{\mathcal{N}_{\mathcal{N}}([z_1, z_4])}{d_{24}d_{34}} - \frac{\mathcal{N}_{\mathcal{N}}([z_2, z_3])}{d_{13}d_{43}} - \frac{\mathcal{N}_{\mathcal{N}}([z_2, z_3])}{d_{13}d_{14}} - \frac{\mathcal{N}_{\mathcal{N}}([z_2, z_4])}{d_{14}d_{34}} - \frac{\mathcal{N}_{\mathcal{N}}([z_3, z_4])}{d_{14}d_{24}} \\ & + \frac{\mathcal{N}_{\mathcal{N}}([z_1, z_2, z_3])}{d_{43}} + \frac{\mathcal{N}_{\mathcal{N}}([z_1, z_2, z_4])}{d_{34}} + \frac{\mathcal{N}_{\mathcal{N}}([z_1, z_3, z_4])}{d_{24}} + \frac{\mathcal{N}_{\mathcal{N}}([z_2, z_3, z_4])}{d_{14}} \\ & - \mathcal{N}_{\mathcal{N}}([z_1, z_2, z_3, z_4]). \end{aligned} \quad (5.46)$$

Although eq.(5.46) is a sum of 35 terms, it features an underlying structure, made manifest by the fact that there are only 12 distinct linear propagators, denoted with

$$d_{ij} = E_i + E_j + p_i^0 - p_j^0. \quad (5.47)$$

At one loop, the four limits involved in the finite difference functional \mathcal{N} are simply defined by the respective poles of the propagators in the lower complex half-plane at

$$z_i = E_i - p_i^0. \quad (5.48)$$

It is interesting to note that some groups of terms in the expression (5.46) can be written in alternative ways, making it clear that the representation is not unique, as discussed in both section 5.1 and section 5.2. For example, one can observe that

$$\frac{\mathcal{N}_{\mathcal{N}}([z_1])}{d_{21}d_{24}d_{34}} + \frac{\mathcal{N}_{\mathcal{N}}([z_1])}{d_{21}d_{31}d_{34}} = \frac{\mathcal{N}_{\mathcal{N}}([z_1])}{d_{21}d_{24}d_{31}} + \frac{\mathcal{N}_{\mathcal{N}}([z_1])}{d_{24}d_{31}d_{34}}. \quad (5.49)$$

The non-uniqueness can also be understood by noticing that the choice of edge labelling in Feynman diagrams is arbitrary. This means that although the final expression stays invariant under such a relabelling, the partial fractioning procedure results in a different but equivalent representation. This opens the possibility of separately integrating each of the summands in the remaining spatial components of the loop variable, and finding an optimal representation in which each of the summands has an especially convenient overlap structure.

When regulating the UV behaviour, it is convenient to introduce counterterm diagrams that have the same asymptotic behaviour as the original integrand and are simple enough to be integrated analytically. These counterterms are subtracted from the integrand to make it suitable for numerical integration and their analytically integrated counterpart can be added back to the final result. As counterterm diagrams often have degenerate edges, we show the degenerate limit of the box diagram which corresponds to a tadpole with a single propagator raised to the fourth power:

$$\text{Tadpole}_{\text{LTD}}(4; m_1) = \frac{1}{2\pi i} \int dk^0 \frac{\mathcal{N}(k^0)}{((k + p_1)^2 - m_1^2 + i\delta)^4}. \quad (5.50)$$

As pointed out in section 5.1, the derivation for the manifestly causal LTD expression for diagrams with raised propagators does not require special treatment as it corresponds to the degenerate limit of pairwise distinct propagators. We can therefore consider the limit $p_i = p_1$ and $m_i = m_1$, where $d_{ij} = 2E_1 \forall i, j$ and $z_i = E_1 - p_1^0 \forall i$, and apply the formula for degenerate divided differences given in eq. (5.13). The general box expression of eq.(5.46) then reduces to

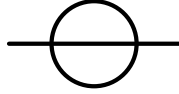
20 summands involving $\frac{\mathcal{N}(z_1)}{(2E_1)^3}$, 10 summands involving $-\frac{\mathcal{N}'(z_1)}{(2E_1)^2}$, 4 summands involving $\frac{\mathcal{N}''(z_1)}{2!(2E_1)}$ and one summand involving $-\frac{\mathcal{N}'''(z_1)}{3!}$, each with the overall prefactor $\frac{1}{(2E_1)^4}$, finally yielding

$$\text{Tadpole}_{\text{LTD}}(4; m_1) = \frac{15\mathcal{N}(z_1) - 15E_1\mathcal{N}'(z_1) + 6E_1^2\mathcal{N}''(z_1) - E_1^3\mathcal{N}'''(z_1)}{96E_1^7}. \quad (5.51)$$

This integrand reproduces the asymptotic UV behaviour of the original Box_{LTD} representation, thus rendering it finite and integrable over the remaining spatial loop degrees of freedom using a numerical Monte-Carlo procedure (see e.g. ref. [4]). Notice that depending on the particular numerator and the corresponding superficial degree of UV divergence, one may also need to include subleading terms which at one-loop always correspond to tadpole topologies, but involving different denominator powers.

5.3.3 Sunrise topology

The simplest example beyond one-loop is the sunrise diagram



which is a two-loop two-point function with three propagators. The integral over the loop energies reads

$$\text{Sunrise}_{\text{LTD}} = \frac{1}{(2\pi i)^2} \int dk_1^0 dk_2^0 \frac{\mathcal{N}(k_1^0, k_2^0)}{\prod_{i=1}^3 \left((\vec{\lambda}_i \cdot (k_1, k_2) + p_i)^2 - m_i^2 + i\delta \right)}, \quad (5.52)$$

with loop line signatures $\vec{\lambda}_1 = (1, 0)$, $\vec{\lambda}_2 = (1, -1)$ and $\vec{\lambda}_3 = (0, 1)$ with one propagator each.

The corresponding cLTD expression is given by the following four summands

$$\begin{aligned} \text{Sunrise}_{\text{LTD}} = & -\frac{\mathbf{N}_{\mathcal{N}}([z_2], [z_4])}{E_1 + E_2 + E_3 + p_1^0 - p_2^0 - p_3^0} - \frac{\mathbf{N}_{\mathcal{N}}([z_1], [z_3])}{E_1 + E_2 + E_3 - p_1^0 + p_2^0 + p_3^0} \\ & + \mathbf{N}_{\mathcal{N}}([z_1], [z_4, z_3]) + \mathbf{N}_{\mathcal{N}}([z_1, z_2], [z_4]), \end{aligned} \quad (5.53)$$

where the numerator is evaluated with the following inputs

$$\begin{aligned} z_1 &= E_1 - p_1^0, & z_2(k_2^0) &= E_2 + k_2^0 - p_2^0, \\ z_3 &= E_1 + E_2 - p_1^0 + p_2^0, & z_4 &= E_3 - p_3^0. \end{aligned} \quad (5.54)$$

Note that when evaluating the numerator $N_{\mathcal{N}}([z_2(k_2^0)], [z_4])$, the recursion in eq.(5.4) is performed first in the first argument $[z_2(k_2^0)]$, which changes the numerator's dependence on k_2^0 since $\tilde{\mathcal{N}}(k_2^0) \equiv \mathcal{N}(z_2(k_2^0), k_2^0)$. The evaluation in the second argument $[z_4]$ is then to be understood in the context of the functional recursion given in eq.(5.4), applied to the function $\tilde{\mathcal{N}}$. In order to better understand how the iteration represented by the step of eq.(5.31) works, we unfold it here explicitly for a scalar sunrise vacuum bubble. Let us start by partial fractioning each propagator in its Minkowski representation, as done in eq.(5.20):

$$\begin{aligned} \text{Sunrise}_{m=0} = & \int \frac{dk_1^0 dk_2^0 / (2\pi i)^2}{8E_1 E_2 E_3} \left[\right. \\ & + \frac{1}{(k_1^0 - E_1)(k_1^0 - k_2^0 - E_2)(k_2^0 - E_3)} - \frac{1}{(k_1^0 - E_1)(k_1^0 - k_2^0 - E_2)(k_2^0 + E_3)} \\ & - \frac{1}{(k_1^0 - E_1)(k_1^0 - k_2^0 + E_2)(k_2^0 - E_3)} - \frac{1}{(k_1^0 + E_1)(k_1^0 - k_2^0 - E_2)(k_2^0 - E_3)} \\ & + \frac{1}{(k_1^0 - E_1)(k_1^0 - k_2^0 + E_2)(k_2^0 + E_3)} + \frac{1}{(k_1^0 + E_1)(k_1^0 - k_2^0 - E_2)(k_2^0 + E_3)} \\ & \left. + \frac{1}{(k_1^0 + E_1)(k_1^0 - k_2^0 + E_2)(k_2^0 - E_3)} - \frac{1}{(k_1^0 + E_1)(k_1^0 - k_2^0 + E_2)(k_2^0 + E_3)} \right], \end{aligned} \tag{5.55}$$

and let us contour integrate in the variable k_1^0 on the usual semi-circle spanning the lower half of the complex plane. We stress that the last two terms of (5.55) vanish under this integration, whereas the integration of the first four terms contribute and yield eight new terms; of which many pair-wise cancel, eventually yielding

$$\begin{aligned} \text{Sunrise}_{m=0} = & - \int \frac{dk_2^0 / (2\pi i)}{8E_1 E_2 E_3} \left[- \frac{1}{(E_1 - k_2^0 + E_2)(k_2^0 - E_3)} - \frac{1}{(k_2^0 + E_2 + E_1)(k_2^0 - E_3)} \right. \\ & \left. + \frac{1}{(E_1 - k_2^0 + E_2)(k_2^0 + E_3)} + \frac{1}{(k_2^0 + E_2 + E_1)(k_2^0 + E_3)} \right]. \end{aligned} \tag{5.56}$$

We now perform the energy integration in k_2^0 by closing the contour, again, in the lower-half of the complex plane. This last integral yields the final cLTD expression for this example:

$$\text{Sunrise}_{m=0} = - \frac{1}{4E_1 E_2 E_3} \frac{1}{E_1 + E_2 + E_3}. \tag{5.57}$$

This cLTD expression for the sunrise diagram of eq.(5.53) agrees with the special case of a constant numerator presented recently in ref. [210].

5.4 CONCLUSION

In this work, we have introduced a new iterative and systematic procedure that, given a multi-loop multi-scale Feynman diagram with arbitrary numerator, yields a representation of the integrand that is manifestly free of spurious poles. The resulting integrand has poles at physical thresholds only, which are regulated by a Feynman prescription with a definite sign. These physical thresholds, or E-surfaces, correspond to sets of particles whose four-momenta simultaneously become on-shell. In the original LTD representation there are spurious poles in the summands, which cancel in the sum. Our work introduces, for the first time, a general procedure to realise their cancellation within each individual term.

The derivation of this representation involves two basic steps which are iterated over for the integration of each loop energy variable. At each iteration, the two steps are applied in succession: first, we analytically perform the integration in a loop energy variable using residue theorem, and then we apply a partial fractioning procedure on all the propagators involving the loop energy integrated over at this step. In this way, we show that it is possible to reabsorb spurious singularities in the definition of divided differences of the product of the numerator and physical poles of the loop integral. The analytic behaviour of divided differences of such quantities can be determined immediately, and in particular it allows us to conclude that the resulting expression is finite for all spurious poles. We refer to this new representation of the integral as the Manifestly Causal Loop-Tree Duality representation, or cLTD.

Our procedure readily applies to loop integrals with arbitrary numerators. In particular, when the numerator of the Feynman integral is a polynomial, as it is in most cases of practical interest, we recognize that divided differences can be computed explicitly. This leads to an expression in which no spurious pole appear, neither explicitly nor implicitly. We studied the resulting numerical stability of the cLTD expression and found the expected perfect numerical stability arbitrarily far in the UV region. In the IR region however, the cLTD representation yields a marginally worse numerical stability when using double precision arithmetic, which we however show to be completely cured by the promotion to quadruple precision. This highlights the complementarity of the cLTD and LTD representation for the numerical application of the Loop-Tree Duality.

One additional potential drawback of the cLTD representation is that the number of terms generated when unfolding our iterative procedure grows exponentially in the number of propagators. However, by identifying common sub-expressions among these many terms can drastically reduce the numerical complexity of the implementation of the cLTD representation

and render it competitive, and sometime even advantageous, over that of its original LTD counterpart.

The ability to systematically analyse and regularise the pole structure of Feynman diagrams, together with the engineering of integrands that are numerically stable and fast are two key steps towards the fully numerical computation of higher-order corrections to the prediction of collider observables. Our novel Manifestly Causal Loop-Tree Duality representation achieves both of these goals and offers a clear path to physics applications.

In ref. [5], we provide as ancillary material a standalone program offering an automated generation of our novel cLTD representation for arbitrary loop integrals.

Part III

OUTLOOK

CONCLUSION

The standard model of particle physics represents the legacy of the 20th century. With the discovery of all of its constituents, we have at hand the most accurate theory of subatomic physics ever written. However, it is still far from providing a complete description of nature, leaving many questions unanswered. It is up to us to challenge its predictions in the quest for understanding the mechanisms that guide the evolution of matter at the most fundamental level. The ongoing and future research programme of the LHC will measure the interactions among particles with the highest precision so far. These formidable experimental measures call for an improvement on the theoretical accuracy of the simulation of many scattering processes. By having an accurate understanding of the theoretical background, we could expose effects due to physics beyond the SM.

In this direction, we have computed the rapidity distribution through N³LO in the gluon fusion channel. For its computation, we worked in the context of the EFT of a top quark with infinite mass and included six terms in the expansion around the threshold energy. The errors coming from these approximations are estimated at the percent level, at least for central rapidities ($|Y| < 2$). We equate the renormalisation and factorisation scales to the central value $\mu = \frac{m_h}{2}$. The theoretical uncertainty due to the truncation of the perturbative expansion is then estimated by rescaling by a factor two the common scale around its central value. The scale variation uncertainty is brought to $^{+0.9\%}_{-3.4\%}$ when also the N³LO correction is included, with a relatively flat K -factor of around 1.03. The current uncertainty at the LHC for the Higgs boson cross-section is about 8% [182] considering an integrated luminosity of 139fb^{-1} and will be lowered to 3% once the target integrated luminosity of 3000fb^{-1} is reached [211]. Due to the reduction of the scale uncertainty, other uncertainties start to become relevant (e.g. the PDFs) as well as corrections coming from different channels and electroweak effects.

The rapidity distribution through N³LO computed as threshold expansion represents a cornerstone in the high order corrections for the Higgs sector. However, the path to a better understanding of nature requires a broader effort and has seen contribution coming from a large community of high energy physicist. The analytic computations necessary to reduce the

error of the theoretical predictions and expose the presence of new physics at the LHC remain in large part unresolved. In particular, computing QCD amplitudes beyond two loops and/or four scales remains exceptionally challenging, even with modern analytical techniques. We identify this as one of the main bottlenecks for computing many of the higher-order corrections necessary to decrease the theoretical uncertainty to the experimental level. This observation is what motivates our work on numerical Loop-Tree Duality, as its strength and limitations are orthogonal, and thus complementary, to those of the canonical paradigms for predicting collider observables.

We have presented and validated a method for constructing a deformation of the integration variable in the Loop-Tree Duality that is aligned with the causal prescription of Feynman propagators and fulfils the conditions originating from analytic continuation. Empowered by a general deformation, we can look past the numerical computation of integrals in the Euclidean region of phase space, and start considering any finite integral that contains threshold singularities. As a demonstration of the stability and accuracy of our method, we apply it to a diverse range of integrals.

As a further step in the direction of building a framework for the computation of physical processes, we have treated the case of divergent integrals at one-loop. Regulating integrals in the context of LTD requires counterterms that are described in terms of scalar propagators, making it particularly challenging in the presence of collinear divergences. We presented a method for regulating individual scalar integrals at one-loop that can be used for computing master integrals. However, the real potential of a numerical integration in momentum space is illustrated for the class of amplitudes $q\bar{q} \rightarrow n\gamma$ at NLO in pQCD where the IR divergences factorise. Extending the regulation of divergent scalar integral at higher loops in numerical LTD remains to this day unresolved and an engaging subject for further studies. The regulation of two-loop amplitudes for electron-positron annihilation to multi photons has been presented recently in ref. [83] and constitutes the natural next step in the implementation of amplitudes in the context of LTD.

While integrating the one-loop amplitudes, we exposed a troublesome aspect of LTD consisting of being subject to large cancellations resulting in numerical instabilities. These large cancellations happen because of the presence of spurious singularities in the LTD expression and were conjecture to cancel when summed together. We offer a proof of these cancellations together with a way to resolve them analytically. The resulting manifestly causal LTD expression is locally equivalent to the original LTD expression but has the advantage to cure all the troubling instabilities for large loop momenta.

One powerful application of the Loop-Tree Duality that is left for future work consists in its combination with reverse unitarity, where the IR divergences can be removed at the local level

without the need of introducing additional counterterms [6]. These local cancellations make it a viable alternative to other infrared subtraction methods for differential quantities.

Part IV

APPENDIX

A

FEYNMAN RULES

A.1 LAGRANGIAN

The Lagrangian used for the computations presented in part i can be separated into four contributions:

$$\mathcal{L}_{tot} = \mathcal{L}_{eff} + \mathcal{L}_{fermions} + \mathcal{L}_{gauge} + \mathcal{L}_{ghosts}. \quad (\text{A.1.1})$$

The effective Lagrangian in the one that appears in eq.(1.18) corresponding to the infinite top mass limit:

$$\mathcal{L}_{eff} = -\frac{C_1}{4v} G_{\mu\nu}^a G^{a\mu\nu} H, \quad (\text{A.1.2})$$

where C_1 is the Wilson coefficient shown in eq.(1.20).

In the infinite top mass limit, all the remaining fermions have to be considered massless yielding:

$$\mathcal{L}_{fermions} = i \sum_{k=1}^{n_f} \bar{q}_k \not{D} q_k = i \sum_{j=1}^{n_f} \bar{q}_{ki} (\not{\partial} \delta_{ij} - i g_s \gamma^\rho T_{ij}^a G_\rho^a) q_{kj} \quad (\text{A.1.3})$$

where $n_f = 5$ is the number of flavours, $\not{D} = \gamma^\mu D_\mu$ contains the covariant derivative defined as $D_\mu := (\mathbb{1} \partial_\mu - i g_s T^a G_\mu^a)$, and q_k is a three dimensional vector whose elements have different color charges (red, green and blue) $q_k = (g_{kr}, g_{kg}, g_{kb})$.

For the gauge Lagrangian, we consider only the $SU(3)_{QCD}$ field of the strong interaction and is written in terms of the gluon strength tensor:

$$\mathcal{L}_{gauge} = \frac{1}{4} G_{\mu\nu}^a G^{a\mu\nu}. \quad (\text{A.1.4})$$

$$G_{\mu\nu}^a = \partial_\mu G_\nu^a - \partial_\nu G_\mu^a + g_s f^{abc} G_\mu^b G_\nu^c, \quad [T^a, T^b] = i f^{abc} T^c. \quad (\text{A.1.5})$$

where the T^a are the generators of the Lie algebra of $SU(3)_{QCD}$.

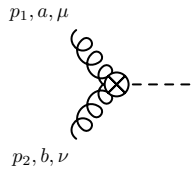
The ghost Lagrangian will depend on the choice of gauge and results from the Faddeev-Popov procedure [212], it will be discuss in more details in the following section.

A.2 INTERACTIONS AND PROPAGATORS

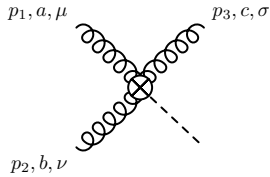
To derive the Feynman rules coming from the effective Lagrangian of eq.(A.1.2) we write it using the definition of the strength tensor in eq.(A.1.5):

$$\begin{aligned} \mathcal{L}_{eff} &= -\frac{C_1}{4v} G_{\mu\nu}^a G^{a\mu\nu} H \\ &= -\frac{C_1}{4v} [2\partial_\nu G_\mu^a \partial^\mu G^{a\nu} - 2\partial_\mu G_\nu^a \partial^\nu G^{a\mu} \\ &\quad + 4g_s f^{abc} (\partial_\mu G_\nu^a) G^{b\mu} G^{c\nu} \\ &\quad + g_s^2 f^{abc} f^{ade} G_\mu^b G_\nu^c G^{d\mu} G^{e\nu}] H \end{aligned}$$

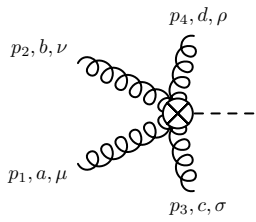
From this expression, it is then straight forward to find the Feynman rules corresponding to the four possible vertices:



$$= i \frac{C_1}{v} \delta^{ab} (g^{\mu\nu} p_1 p_2 - p_1^\nu p_2^\mu)$$



$$= \frac{C_1}{v} g_s f^{abc} [-g^{\mu\sigma} p_1^\nu + g^{\mu\nu} p_1^\sigma + g^{\nu\sigma} p_2^\mu - g^{\mu\nu} p_2^\sigma - g^{\nu\sigma} p_3^\mu + g^{\mu\sigma} p_3^\nu]$$



$$= i \frac{C_1}{v} g_s^2 \left[f^{abn} f^{cdn} (g^{\mu\rho} g^{\nu\sigma} - g^{\mu\sigma} g^{\nu\rho}) + f^{acn} f^{bdn} (g^{\mu\rho} g^{\nu\sigma} - g^{\mu\nu} g^{\sigma\rho}) \right. \\ \left. + f^{adn} f^{bcn} (g^{\mu\sigma} g^{\nu\rho} - g^{\mu\nu} g^{\sigma\rho}) \right]$$

of the computations for a physical observable, but it changes how the result is computed. One choice of gauge used for our computations corresponds to *Feynman-gauge*, defined by taking the R_ξ -gauge with $\xi = 1$. This gauge can be achieved by adding an additional term to the gauge Lagrangian:

$$\mathcal{L}_{\text{gauge}} = \frac{1}{4} G_{\mu\nu}^a G^{a\mu\nu} - \frac{1}{2\xi} (\partial^\mu G_\mu^a)^2$$

Then the gluon propagator takes the form:

$$iG_{R_\xi}^{\mu\nu ab} = \frac{-i\delta^{ab}}{p^2 + i\epsilon} \left(g^{\mu\nu} + (1 - \xi) \frac{p^\mu p^\nu}{p^2} \right)$$

$$\xrightarrow{\xi=1} \frac{-i\delta^{ab} g^{\mu\nu}}{p^2 + i\epsilon}.$$

The addition of this term into the Lagrangian requires to include diagrams containing ghosts in both internal propagators as well as in the external legs to remove the unphysical polarizations of the gluons. These ghost contributions are a direct consequence of the Faddeev-Popov procedure [212] for fixing the gauge, where they are obtained as extra terms in the path integral in the form of a determinant:

$$\det \left(\frac{\delta(\partial^\mu G_\mu^a)}{\delta\pi^c} \right), \quad G_\mu^a \xrightarrow{\text{gauge transf.}} G_\mu^a + \frac{1}{g_s} \partial_\mu \pi^a + f^{abc} G_\mu^b \pi^c, \quad (\text{A.3.2})$$

with $\pi = \pi(x)$ parametrizes the local transformation. This determinant can be written as a contribution to the Lagrangian by means of the identity [212]:

$$\left(\prod_i \int dc_i^* dc_i \right) e^{-c_i^* A_{ij} c_j} = \det(A) \quad (\text{A.3.3})$$

where A is a non-singular matrix, and c_i 's are Grassmann variables (anticommuting Lorentz scalars). Knowing the gauge transformation is possible to evaluate the expression inside the determinant in eq.(A.3.2):

$$\det \left(\frac{\delta(\partial_\nu G_\mu^a)}{\delta\pi^c} \right) = \det \left(\frac{1}{g_s} \delta^{ac} \partial^2 + f^{abc} \partial^\mu G_\mu^b \right).$$

This leads to the ghost Lagrangian:

$$\mathcal{L}_{\text{ghost}} = (\partial_\mu \bar{c}^a) (\delta^{ac} \partial^\mu + g_s f^{abc} \partial^\mu G_\mu^b) c^c,$$

where c and \bar{c} are ghosts fields, and the overall factor of $\frac{1}{g_s}$ has been reabsorbed into the ghost fields.

These results can then be summarized by the following Feynman rules:

$$a, \mu \text{ } \cdots \cdots \blacktriangleright \cdots \cdots b, \nu \quad = \quad i \delta^{ab} \frac{1}{p^2 + i0}$$

$$a, \mu \text{ } \underbrace{\quad \cdots \cdots \quad}_{\text{loop}} \quad b, \nu \quad = \quad -i \frac{g^{\mu\nu} \delta^{ab}}{p^2}$$

$$\begin{array}{l} p_3, c, \nu \\ \text{ } \searrow \text{ } \cdots \cdots \text{ } \underbrace{\quad \cdots \cdots \quad}_{\text{loop}} \quad p_1, a, \rho \\ p_2, b, \mu \nearrow \text{ } \cdots \cdots \text{ } \end{array} = g_s f^{abc} (p_3^\nu + p_1^\rho)$$

Checking that the final result of the computation is invariant under a gauge transformation represents an important check on the result. In general, this would require to keep the explicit ζ dependence of the R_ζ -gauge and check that it vanishes in the final expression for the cross-section. Alternatively, one can consider another gauge and checked whether or not the two results agree. As second choice we have considered the *Axial gauge*, defined by:

$$\mathcal{L}_{\text{gauge}} = \frac{1}{4} G_{\mu\nu}^a G^{a\mu\nu} - \frac{1}{2\zeta} (\eta^\mu G_\mu^a)^2, \quad \det \left(\frac{\delta(\eta_\nu G_\mu^a)}{\delta\pi^c} \right) = \det \left(\frac{1}{g_s} \delta^{ac} \eta^\nu \partial_\nu + f^{abc} \eta^\mu G_\mu^b \right) \quad (\text{A.3.4})$$

with $\eta^\mu \eta_\mu = 0$. We choose the physical gauge by taking the limit of $\zeta = 0$ in the expression of the gluon propagator:

$$iG_{\text{Axial}}^{\mu\nu ab} = \frac{i\delta^{ab}}{p^2 + i\epsilon} \left(-g^{\mu\nu} + \frac{\eta^\mu p^\nu + \eta^\nu p^\mu}{\eta p} - (\eta^2 + \zeta p^2) \frac{p^\mu p^\nu}{(\eta p)^2} \right) \quad (\text{A.3.5a})$$

$$\xrightarrow{\zeta=0} \frac{i\delta^{ab}}{p^2 + i\epsilon} \left(-g^{\mu\nu} + \frac{\eta^\mu p^\nu + \eta^\nu p^\mu}{\eta p} - \eta^2 \frac{p^\mu p^\nu}{(\eta p)^2} \right). \quad (\text{A.3.5b})$$

In the physical gauge, we have that $\eta_\mu G_{\text{Axial}}^{\mu\nu ab} = 0$. The ghost Lagrangian is computed gauge by means of eq.(A.3.3) from the second term in eq.(A.3.4) and comes with a factor η_μ . This factor ensures that the ghosts decouple from the physical particles (gluons) for this particular

choice of gauge [213]. Therefore, the only relevant Feynman rule in this gauge is the gluon propagator, given by:

$$\begin{array}{c} a, \mu \\ \text{-----} \\ b, \nu \end{array} \stackrel{\text{Axial}}{=} \frac{i\delta^{ab}}{p^2 + i\epsilon} \left(-g^{\mu\nu} + \frac{\eta^\mu p^\nu + \eta^\nu p^\mu}{\eta p} - \eta^2 \frac{p^\mu p^\nu}{(\eta p)^2} \right).$$

B

DIFFERENTIAL EQUATIONS

B.1 DIFFERENTIAL EQUATIONS

One key ingredient in the evaluation of cross-sections, and more precisely master integrals, is the use of differential equations as in refs. [51–70]. The differential equations are used to obtain the master integrals as an expansion in terms of the dimensional regulator or, as we did, for performing the threshold expansion using differential equations combined with the expansion by regions [128, 172].

B.1.1 *Differential equation in terms of external momenta*

The main idea behind the use of differential equations is that, despite our inability to solve the integrals exactly, we can still build for them a system of differential equations by looking at their integrands. Once we have a system of differential equations, we can use it to obtain an expression for the corresponding master integrals.

Let us consider a process with N external momenta p_i , then the final expression will be a function of the Lorentz invariant kinematics represented by s_{ij} . Notice that in the case of on-shell externals with $s_{ii} = p_i^2 = 0$ the number of such invariants is reduced. At the integrand level however, the scalar products can also involve the loop momenta. To extract the dependence on the external kinematics s_{ij} from the integrand, we need to take derivatives with respect to the external momenta p_i^μ .

Assuming all $s_{ij} \neq 0$, we can cast the problem as follows:

$$\frac{\partial}{\partial s_{ij}} = \sum_{(mn)} \alpha_{(ij),(mn)} p_m^\mu \frac{\partial}{\partial p_n^\mu}, \quad (\text{B.1.1})$$

$$(ij), (mn) \in \{11, 12, \dots, 1N, 22, 23, \dots, NN\},$$

The expression for the matrix $\alpha_{(ij),(mn)}$ can be derived by acting with both sides of eq.(B.1.1) on all the different s_{ij} . Then the problem of finding the matrix α reduces to computing the inverse:

$$\alpha = (\alpha^{-1})^{-1} = \left(\left[p_m^\mu \frac{\partial s_{ij}}{\partial p_n^\mu} \right]_{(ij),(mn)} \right)^{-1},$$

The problem simplifies when some of the external momenta are on-shell (massless). Because of the reduced number of external kinematics, we can also consider a smaller set of operators of the form $p_m \frac{\partial}{\partial p_n}$. When reducing the number of operators, one must be careful and ensure that the limit $s_{ii} = 0$ commutes with each derivative. For example, if $s_{11} = p_1^2 = 0$ we then require that its derivative vanishes in all kinematics, yielding:

$$\frac{\partial}{\partial s_{ij}} p_1^2 = 0, \quad (ij) \neq (11).$$

This means that every massless external momentum produces a set of constraints that, according to eq.(B.1.1), correspond to a series of relations among different $p_m \frac{\partial}{\partial p_n}$ operators.

EXAMPLE 1

Take $N = 3$ and $p_1^2 = p_2^2 = p_3^2 = 0$. Then the set of independent kinematics is represented by

$$s_{12}, \quad s_{13}, \quad s_{23}.$$

We can make an educated guess for the form of the solution by knowing that we need three different differential operators. One possibility is to pick:

$$\frac{\partial}{\partial s_{ij}} = \sum_{(ij),k} \alpha_{(ij),k} p_k \frac{\partial}{\partial p_k}, \quad (ij) \in \{12, 13, 23\}, \quad k \in \{1, 2, 3\}$$

Where now the matrix α is a 3×3 -dimensional matrix. This choice of differential operators fulfils both constraints: that the matrix $[p_k \frac{\partial s_{ij}}{\partial p_k}]$ must not be singular and that $\frac{\partial s_{kk}}{\partial s_{ij}} = 0$. With the aforementioned basis we can then write:

$$\begin{aligned}\frac{\partial}{\partial s_{12}} &= \frac{1}{2s_{12}} \left(+p_1^\mu \frac{\partial}{\partial p_1^\mu} + p_2^\mu \frac{\partial}{\partial p_2^\mu} - p_3^\mu \frac{\partial}{\partial p_3^\mu} \right), \\ \frac{\partial}{\partial s_{13}} &= \frac{1}{2s_{13}} \left(+p_1^\mu \frac{\partial}{\partial p_1^\mu} - p_2^\mu \frac{\partial}{\partial p_2^\mu} + p_3^\mu \frac{\partial}{\partial p_3^\mu} \right), \\ \frac{\partial}{\partial s_{23}} &= \frac{1}{2s_{23}} \left(-p_1^\mu \frac{\partial}{\partial p_1^\mu} + p_2^\mu \frac{\partial}{\partial p_2^\mu} + p_3^\mu \frac{\partial}{\partial p_3^\mu} \right).\end{aligned}$$

EXAMPLE 2

Let us consider a more interesting case, corresponding to the kinematic configurations of the Higgs-differential cross-section. All scalar products depend on three independent external momenta, those of the two massless incoming partons, and the massive Higgs. In this case we write $N = 3$ and $p_1^2 = p_2^2 = 0$ together with $p_3^2 \neq 0$. The set of independent kinematics is now extended to:

$$s_{12}, \quad s_{13}, \quad s_{23}, \quad s_{33}.$$

In this case, we use the same set of differential operators as for the previous example, and we choose the additional one to be $p_1 \frac{\partial}{\partial p_3}$. It is easy to prove that they are all elements of $\{p_i \frac{\partial}{\partial p_j} | p_i \frac{\partial s_{kk}}{\partial p_j} = 0, k = 1, 2\}$, then we get:

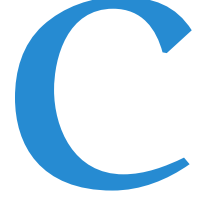
$$\alpha = \begin{pmatrix} \frac{s_{13}s_{23}}{4s_{12}s_{13}s_{23} - 2s_{12}^2s_{33}} & \frac{s_{13}s_{23} - s_{12}s_{33}}{4s_{12}s_{13}s_{23} - 2s_{12}^2s_{33}} & -\frac{s_{13}s_{23}}{4s_{12}s_{13}s_{23} - 2s_{12}^2s_{33}} & \frac{s_{23}s_{33}}{4s_{12}s_{13}s_{23} - 2s_{12}^2s_{33}} \\ \frac{s_{13}s_{23} - s_{12}s_{33}}{4s_{13}^2s_{23} - 2s_{12}s_{13}s_{33}} & -\frac{s_{13}s_{23} - s_{12}s_{33}}{4s_{13}^2s_{23} - 2s_{12}s_{13}s_{33}} & \frac{s_{23}}{4s_{13}s_{23} - 2s_{12}s_{33}} & -\frac{s_{23}s_{33}}{4s_{13}^2s_{23} - 2s_{12}s_{13}s_{33}} \\ \frac{s_{13}}{2s_{12}s_{33} - 4s_{13}s_{23}} & \frac{s_{13}}{4s_{13}s_{23} - 2s_{12}s_{33}} & \frac{s_{13}}{4s_{13}s_{23} - 2s_{12}s_{33}} & \frac{s_{33}}{2s_{12}s_{33} - 4s_{13}s_{23}} \\ \frac{s_{13}^2 + s_{12}s_{13} - s_{23}s_{13} + s_{12}s_{33}}{4s_{13}^2s_{23} - 2s_{12}s_{13}s_{33}} & -\frac{s_{13}(s_{13} - s_{23}) + s_{12}(s_{13} + s_{33})}{2s_{13}(2s_{13}s_{23} - s_{12}s_{33})} & \frac{s_{12} + s_{13} + s_{23}}{2s_{12}s_{33} - 4s_{13}s_{23}} & \frac{2s_{13}s_{23} + s_{33}s_{23} + s_{13}s_{33}}{4s_{13}^2s_{23} - 2s_{12}s_{13}s_{33}} \end{pmatrix}$$

$$\begin{pmatrix} \frac{\partial}{\partial s_{12}} \\ \frac{\partial}{\partial s_{13}} \\ \frac{\partial}{\partial s_{23}} \\ \frac{\partial}{\partial s_{33}} \end{pmatrix} = \alpha \begin{pmatrix} p_1^\mu \frac{\partial}{\partial p_1^\mu} \\ p_2^\mu \frac{\partial}{\partial p_2^\mu} \\ p_3^\mu \frac{\partial}{\partial p_3^\mu} \\ p_1^\mu \frac{\partial}{\partial p_3^\mu} \end{pmatrix}$$

For the computation of the Higgs-differential cross-section we use a different set of kinematics to describe our system, namely (x, λ, \bar{z}, s) . To obtain the representation of the corresponding differential operators $(\frac{\partial}{\partial x}, \frac{\partial}{\partial \lambda}, \frac{\partial}{\partial \bar{z}}, \frac{\partial}{\partial s})$, we can either rotate the differential matrix for s_{ij} or directly use the new basis to build the matrix α in terms of the same set of operator $p_i \frac{\partial}{\partial p_j}$ as before:

$$\alpha' = \begin{pmatrix} \frac{1-\lambda\bar{z}}{2(x-1)(\lambda x\bar{z}-1)} & \frac{\lambda\bar{z}-1}{2(x-1)(\lambda x\bar{z}-1)} & \frac{\lambda\bar{z}-1}{2(x-1)(\lambda x\bar{z}-1)} & \frac{\bar{z}-1}{(x-1)(\lambda x\bar{z}-1)} \\ \frac{\lambda^3 x\bar{z}^2 + \lambda^2 x(1-2\bar{z})\bar{z} + \lambda(\bar{z}-2)+1}{2(\lambda-1)\lambda(\lambda\bar{z}-1)(\lambda x\bar{z}-1)} & -\frac{\lambda^3 x\bar{z}^2 + \lambda^2 x(1-2\bar{z})\bar{z} + \lambda(\bar{z}-2)+1}{2(\lambda-1)\lambda(\lambda\bar{z}-1)(\lambda x\bar{z}-1)} & \frac{\lambda^2 x\bar{z} - 2\lambda + 1}{2(\lambda-1)\lambda(\lambda x\bar{z}-1)} & \frac{(\bar{z}-1)(\lambda^2 x\bar{z} - 2\lambda + 1)}{(\lambda-1)\lambda(\lambda\bar{z}-1)(\lambda x\bar{z}-1)} \\ \frac{\lambda^2 x\bar{z}^2 + \lambda x\bar{z} - 2}{2\bar{z}(\lambda\bar{z}-1)(\lambda x\bar{z}-1)} & -\frac{\lambda^2 x\bar{z}^2 + \lambda x\bar{z} - 2}{2\bar{z}(\lambda\bar{z}-1)(\lambda x\bar{z}-1)} & \frac{2-\lambda x\bar{z}}{2\bar{z}-2\lambda x\bar{z}^2} & \frac{2-\bar{z}(\lambda x+1)}{\bar{z}(\lambda\bar{z}-1)(\lambda x\bar{z}-1)} \\ \frac{1}{2s} & \frac{1}{2s} & \frac{1}{2s} & 0 \end{pmatrix} \tag{B.1.2a}$$

$$\begin{pmatrix} \frac{\partial}{\partial x} \\ \frac{\partial}{\partial \lambda} \\ \frac{\partial}{\partial \bar{z}} \\ \frac{\partial}{\partial s} \end{pmatrix} = \alpha' \begin{pmatrix} p_1^\mu \frac{\partial}{\partial p_1^\mu} \\ p_2^\mu \frac{\partial}{\partial p_2^\mu} \\ p_3^\mu \frac{\partial}{\partial p_3^\mu} \\ p_1^\mu \frac{\partial}{\partial p_3^\mu} \end{pmatrix} \tag{B.1.2b}$$



LTD TABLES AND PROPAGATOR DEFINITIONS

C.1 EXPRESSION FOR THE $q\bar{q} \rightarrow \gamma_1\gamma_2\gamma_3$ AMPLITUDE AND ITS COUNTERTERMS

In order to provide an explicit parametrisation of all the integrals that appear in the computation of the $q\bar{q} \rightarrow \gamma_1\gamma_2\gamma_3$, we give the expression for the diagrams and the counterterms. The individual diagrams can be written as explicit integrals using dimensional regularisation, since in general they contain singularities.

The integrals appearing in figure 4.6 are given by:

$$I_1 = C_1 \mu^{2\epsilon} (4\pi)^2 \int \frac{d^d k}{(2\pi)^d} \frac{\bar{v}_2 \hat{\epsilon}_1(-\not{p}_{23}) \gamma^\mu (-\not{k} - \not{p}_{23}) \hat{\epsilon}_2(-\not{k} + \not{p}_{15}) \hat{\epsilon}_3(-\not{k} + \not{p}_1) \gamma_\mu u_1}{s_{23} k^2 (k + p_{23})^2 (k - p_{15})^2 (k - p_1)^2} \quad (\text{C.1.1})$$

$$I_2 = C_1 \mu^{2\epsilon} (4\pi)^2 \int \frac{d^d k}{(2\pi)^d} \frac{\bar{v}_2 \gamma^\mu (-\not{k} - \not{p}_2) \hat{\epsilon}_1(-\not{k} - \not{p}_{23}) \hat{\epsilon}_2(-\not{k} + \not{p}_{15}) \gamma_\mu (\not{p}_{15}) \hat{\epsilon}_3 u_1}{s_{15} k^2 (k + p_2)^2 (k + p_{23})^2 (k - p_{15})^2} \quad (\text{C.1.2})$$

$$I_3 = C_1 \mu^{2\epsilon} (4\pi)^2 \int \frac{d^d k}{(2\pi)^d} \frac{\bar{v}_2 \gamma^\mu (-\not{k} - \not{p}_2) \hat{\epsilon}_1(-\not{k} - \not{p}_{23}) \hat{\epsilon}_2(-\not{k} + \not{p}_{15}) \hat{\epsilon}_3(-\not{k} + \not{p}_1) \gamma_\mu u_1}{k^2 (k + p_2)^2 (k + p_{23})^2 (k - p_{15})^2 (k - p_1)^2} \quad (\text{C.1.3})$$

$$I_4 = C_1 \mu^{2\epsilon} (4\pi)^2 \int \frac{d^d k}{(2\pi)^d} \frac{\bar{v}_2 \hat{\epsilon}_1(-\not{p}_{23}) \hat{\epsilon}_2(\not{p}_{15}) \gamma^\mu (-\not{k} + \not{p}_{15}) \gamma_\mu (\not{p}_{15}) \hat{\epsilon}_3 u_1}{s_{23} s_{15}^2 k^2 (k - p_{15})^2} \quad (\text{C.1.4})$$

$$I_5 = C_1 \mu^{2\epsilon} (4\pi)^2 \int \frac{d^d k}{(2\pi)^d} \frac{\bar{v}_2 \hat{\epsilon}_1(-\not{p}_{23}) \gamma^\mu (-\not{k} - \not{p}_{23}) \hat{\epsilon}_2(-\not{k} + \not{p}_{15}) \gamma_\mu (\not{p}_{15}) \hat{\epsilon}_3 u_1}{s_{23} s_{15} k^2 (k + p_{23})^2 (k - p_{15})^2} \quad (\text{C.1.5})$$

$$I_6 = C_1 \mu^{2\epsilon} (4\pi)^2 \int \frac{d^d k}{(2\pi)^d} \frac{\bar{v}_2 \hat{\epsilon}_1(-\not{p}_{23}) \gamma^\mu (-\not{k} - \not{p}_{23}) \gamma_\mu (-\not{p}_{23}) \hat{\epsilon}_2(\not{p}_{15}) \hat{\epsilon}_3 u_1}{s_{23}^2 s_{15} k^2 (k + p_{23})^2} \quad (\text{C.1.6})$$

$$I_7 = C_1 \mu^{2\epsilon} (4\pi)^2 \int \frac{d^d k}{(2\pi)^d} \frac{\bar{v}_2 \hat{\epsilon}_1(-\not{p}_{23}) \hat{\epsilon}_2(\not{p}_{15}) \gamma^\mu (-\not{k} + \not{p}_{15}) \hat{\epsilon}_3(-\not{k} + \not{p}_1) \gamma_\mu u_1}{s_{23} s_{15} k^2 (k - p_{15})^2 (k - p_1)^2} \quad (\text{C.1.7})$$

$$I_8 = C_1 \mu^{2\epsilon} (4\pi)^2 \int \frac{d^d k}{(2\pi)^d} \frac{\bar{v}_2 \gamma^\mu (-\not{k} - \not{p}_2) \hat{\epsilon}_1(-\not{p}_{23}) \gamma_\mu (-\not{p}_{23}) \hat{\epsilon}_2(\not{p}_{15}) \hat{\epsilon}_3 u_1}{s_{23} s_{15} k^2 (k + p_2)^2 (k + p_{23})^2} \quad (\text{C.1.8})$$

The IR counterterm reads:

$$I_{\text{IR}} = C_1 \mu^{2\epsilon} (4\pi)^2 \int \frac{d^d k}{(2\pi)^d} \frac{\bar{v}_2 \gamma^\mu (-\not{k} - \not{p}_2) \hat{\epsilon}_1(-\not{p}_{23}) \hat{\epsilon}_2(\not{p}_{15}) \hat{\epsilon}_3(-\not{k} + \not{p}_1) \gamma_\mu u_1}{s_{23} s_{15} k^2 (k + p_2)^2 (k - p_1)^2} \quad (\text{C.1.9})$$

The UV counterterms read:

$$I_{\text{UV}_4} = C_1 \mu^{2\epsilon} (4\pi)^2 \int \frac{d^d k}{(2\pi)^d} \frac{\bar{v}_2 \hat{\not{\epsilon}}_1(-\not{p}_{23}) \hat{\not{\epsilon}}_2(\not{p}_{15}) \gamma^\mu \left((-\not{k}) - \frac{(-\not{k})(\not{p}_{15})(-\not{k})}{k^2 - \mu_{uv}^2} \right) \gamma_\mu(\not{p}_{15}) \hat{\not{\epsilon}}_3 u_1}{s_{23} s_{15}^2 [k^2 - \mu_{uv}^2]^2} \quad (\text{C.1.10})$$

$$I_{\text{UV}_5} = C_1 \mu^{2\epsilon} (4\pi)^2 \int \frac{d^d k}{(2\pi)^d} \frac{\bar{v}_2 \hat{\not{\epsilon}}_1(-\not{p}_{23}) \gamma^\mu(-\not{k}) \hat{\not{\epsilon}}_2(-\not{k}) \gamma_\mu(\not{p}_{15}) \hat{\not{\epsilon}}_3 u_1}{s_{23} s_{15} [k^2 - \mu_{uv}^2]^3} \quad (\text{C.1.11})$$

$$I_{\text{UV}_6} = C_1 \mu^{2\epsilon} (4\pi)^2 \int \frac{d^d k}{(2\pi)^d} \frac{\bar{v}_2 \hat{\not{\epsilon}}_1(-\not{p}_{23}) \gamma_\mu \left((-\not{k}) - \frac{(-\not{k})(-\not{p}_{23})(-\not{k})}{k^2 - \mu_{uv}^2} \right) \gamma_\mu(-\not{p}_{23}) \hat{\not{\epsilon}}_2(\not{p}_{15}) \hat{\not{\epsilon}}_3 u_1}{s_{23}^2 s_{15} [k^2 - \mu_{uv}^2]^2} \quad (\text{C.1.12})$$

$$I_{\text{UV}_7} = C_1 \mu^{2\epsilon} (4\pi)^2 \int \frac{d^d k}{(2\pi)^d} \frac{\bar{v}_2 \hat{\not{\epsilon}}_1(-\not{p}_{23}) \hat{\not{\epsilon}}_2(\not{p}_{15}) \gamma^\mu(-\not{k}) \hat{\not{\epsilon}}_3(-\not{k}) \gamma_\mu u_1}{s_{23} s_{15} [k^2 - \mu_{uv}^2]^3} \quad (\text{C.1.13})$$

$$I_{\text{UV}_8} = C_1 \mu^{2\epsilon} (4\pi)^2 \int \frac{d^d k}{(2\pi)^d} \frac{\bar{v}_2 \gamma^\mu(-\not{k}) \hat{\not{\epsilon}}_1(-\not{k}) \gamma_\mu(-\not{p}_{23}) \hat{\not{\epsilon}}_2(\not{p}_{15}) \hat{\not{\epsilon}}_3 u_1}{s_{23} s_{15} [k^2 - \mu_{uv}^2]^3} \quad (\text{C.1.14})$$

$$I_{\text{UV}_{\text{IR}}} = C_1 \mu^{2\epsilon} (4\pi)^2 \int \frac{d^d k}{(2\pi)^d} \frac{\bar{v}_2 \gamma^\mu(-\not{k}) \hat{\not{\epsilon}}_1(-\not{p}_{23}) \hat{\not{\epsilon}}_2(\not{p}_{15}) \hat{\not{\epsilon}}_3(-\not{k}) \gamma_\mu u_1}{s_{23} s_{15} [k^2 - \mu_{uv}^2]^3} \quad (\text{C.1.15})$$

C.2 LOOP-TREE DUALITY WITH RAISED PROPAGATORS

When a diagram contains raised propagators, the Minkowski representation of the integrand features complex poles in the energy with order higher than one. Thus, in order to generalise the integration of the energy component of loop momenta carried out in sect. 4.1, it is necessary to use the definition of higher-order residues [214].

Raised propagators generally appear at higher loops when a diagram has a propagator insertion on a propagator. They also appear as a result of using Integration by Parts identities. The UV counterterm we constructed also features a raised propagator, since in the UV limit every propagator scales as $1/(k^2 - \mu_{\text{UV}}^2)$.

Applying residue theorem to a general integral with raised propagators we obtain:

$$\begin{aligned} \oint_{x_+} dk_0 \frac{F(k_0, \vec{k})}{(k_0 - x_+)^{1+n} (k_0 - x_-)^{1+n}} &= \frac{1}{n!} \frac{\partial^n}{\partial k_0^n} \frac{F(k_0, \vec{k})}{(k_0 - x_-)^{1+n}} \Bigg|_{k_0=x_+} \\ &= \frac{1}{n!} \sum_{m=0}^n (-1)^{n-m} \frac{(2n-m)!}{(n-m)! m!} \frac{\partial_k^m F(k_0, \vec{k})}{(x_+ - x_-)^{1+2n-m}} \Bigg|_{k_0=x_+}. \end{aligned} \quad (\text{C.2.1})$$

For the processes considered in chapter 4 that need UV regulation, namely the one-loop QCD corrections to the $d\bar{d}$ to photons, the numerator function F will consist of a spinor contraction

containing a product of order n in the loop momentum k and the other propagators excluded from this particular residue.

C.2.1 *LTD tables of scalar integrals*

In this appendix we present the numerical result of integrating different scalar integrals using the deformation. We scan different topologies free of pinch singularities by setting the external momenta off-shell (i.e. $p^2 \neq 0$) or the propagator to contain a regulating mass. The results of the integration are compared with the analytic results whenever possible.



Topology	Kin.	N_C	N_E	N_S	L_{\max}	N_p [10^9]	τ/p [s]	Phase	Exp.	Reference	Numerical LTD	Δ [e]	Δ [%]	Δ [‰]
	I	4	4	4	[2,2,2,2]	3	15	Re	-08	-6.57830	-6.57637 +/- 0.00122	1.590	0.029	0.022
								Im		-7.43707	-7.43805 +/- 0.00121	0.813	0.013	
Box4E	I	5	8	1	[8]	3	15	Re	-12	-3.44342	-3.44317 +/- 0.00045	0.564	0.007	0.007
								Im		-2.56487	-2.56505 +/- 0.00046	0.400	0.007	
	II	5	10	1	[10]	3	15	Re	-13	0	-0.00036 +/- 0.00029	1.266		0.006
								Im		5.97143	5.97143 +/- 0.00029	0.003	2e-05	
	III	5	8	2	[7,7]	3	16	Re	-12	-0.83905	-0.83888 +/- 0.00016	1.029	0.020	0.012
								Im		-1.71341	-1.71325 +/- 0.00017	0.937	0.009	
1L5P	IV	5	8	3	[7,7,7]	3	17	Re	-12	-3.48997	-3.49044 +/- 0.00054	0.870	0.013	0.013
								Im		-3.90013	-3.89965 +/- 0.00054	0.891	0.012	
	V	5	6	4	[2,2,3,4]	3	19	Re	-10	0.89920	0.90036 +/- 0.00076	1.519	0.129	0.027
								Im		4.17837	4.17823 +/- 0.00080	0.180	0.003	
	VI	5	8	5	[4,4,5,5,5]	3	19	Re	-13	0.04119	0.04227 +/- 0.00068	1.593	2.634	0.057
								Im		-2.18057	-2.18118 +/- 0.00068	0.891	0.028	
	I	6	12	1	[12]	3	20	Re	-13	0.03040	0.03046 +/- 0.00006	1.067	0.202	0.009
								Im		-1.17683	-1.17691 +/- 0.00008	1.057	0.007	
	II	6	6	2	[1,5]	3	21	Re	+01	-2.07014	-2.07392 +/- 0.00188	2.004	0.182	0.214
								Im		0.42343	0.42593 +/- 0.00161	1.551	0.590	
	III	6	12	2	[11,10]	3	20	Re	-15	1.36918	1.36950 +/- 0.00052	0.628	0.024	0.024
								Im		-2.25901	-2.25957 +/- 0.00053	1.054	0.025	
	IV	6	12	3	[9,10,10]	3	22	Re	-15	1.29770	1.29802 +/- 0.00038	0.847	0.025	0.019
								Im		-2.16590	-2.16555 +/- 0.00037	0.929	0.016	
	V	6	6	4	[2,3,3,3]	3	22	Re	-14	-0.27217	-0.27225 +/- 0.00010	0.839	0.032	0.007
								Im		-1.20896	-1.20895 +/- 0.00011	0.098	0.001	
	VI	6	9	4	[4,6,6,6]	3	23	Re	-17	2.83772	2.83777 +/- 0.00040	0.118	0.002	0.002
								Im		0.83142	0.83144 +/- 0.00040	0.059	0.003	
	VII	6	10	4	[7,7,8,8]	3	23	Re	-17	-3.01939	-3.01976 +/- 0.00040	0.917	0.012	0.008
								Im		-7.73337	-7.73280 +/- 0.00047	1.199	0.007	
	VIII	6	10	4	[3,5,6,7]	3	24	Re	-02	2.11928	2.13487 +/- 0.03230	0.483	0.736	1.055
								Im		0.64030	0.65770 +/- 0.03145	0.553	2.717	
	IX	6	12	4	[8,9,9,10]	3	22	Re	-14	0.00794	0.00804 +/- 0.00014	0.710	1.253	0.009
								Im		-1.15282	-1.15278 +/- 0.00014	0.290	0.004	
	X	6	10	5	[6,6,7,7,7]	3	24	Re	+00	-2.81475	-2.81583 +/- 0.00060	1.809	0.038	0.029
								Im		2.47327	2.47308 +/- 0.00061	0.313	0.008	

TABLE C.1: Results for one-loop four-point to six-point functions. Box4E has been used as an example topology throughout this work. See the main text for details.

Topology	Kin.	N_c	N_E	N_S	L_{\max}	N_p [10^9]	t/p [s]	Phase	Exp.	Reference	Numerical LTD	Δ [∅]	Δ [%]	$ \Delta $ [%]
	I	11	2	6	[2]	3	39	Re	-06	3.82891 [215]	3.82875 +/- 0.00015	1.107	0.004	0.003
								Im		-4.66840	-4.66843 +/- 0.00017	0.188	0.001	
2L4P.a	II	11	4	7	[4]	3	42	Re	-10	2.83647 [215]	2.83742 +/- 0.00072	1.312	0.033	0.032
								Im		3.38265	3.38163 +/- 0.00066	1.558	0.030	
	I	15	13	8	[13]	3	55	Re	-02	-5.89700 [216]	-5.89794 +/- 0.00099	0.956	0.016	0.025
								Im		0	0.00112 +/- 0.00095	1.171		
	I	20	20	14	[20]	3	88	Re	+01	-8.608 +/- 0.009 [73]	-8.64045 +/- 0.00392	0.045	0.064	
								Im		-8.66 +/- 0.08 [191]	-0.00220 +/- 0.00393			
2L6P.a	I	23	23	18	[21,22]	3	95	Re	+02	-1.1886 +/- 0.0005 [73]	-1.19040 +/- 0.00092	0.077	0.109	
								Im		-1.17 +/- 0.02 [191]	0.00147 +/- 0.00092			
	I	24	24	20	[19,22,22]	3	94	Re	+01	-7.607 +/- 0.006 [73]	-7.62856 +/- 0.00716	0.094	0.133	
								Im		-7.8 +/- 0.1 [191]	-0.00052 +/- 0.00724			
2L6P.c	I	24	23	15	[23]	3	91	Re	+01	-1.833 +/- 0.002 [73]	-1.83639 +/- 0.00075	0.041	0.058	
								Im		-1.91 +/- 0.02 [191]	-0.00042 +/- 0.00075			
	I	26	26	19	[25,25]	3	101	Re	+01	-4.597 +/- 0.004 [73]	-4.61094 +/- 0.00423	0.092	0.131	
								Im		-4.64 +/- 0.08 [191]	0.00404 +/- 0.00430			
2L6P.e	I	27	33	20	[29,32]	3	119	Re	+02	-1.0271 +/- 0.0003 [73]	-1.02723 +/- 0.00111	0.108	0.153	
								Im		-1.03 +/- 0.02 [191]	0.00165 +/- 0.00112			
2L6P.f	I	27	33	20	[29,32]	3	119	Re	+02	-1.0271 +/- 0.0003 [73]	-1.02723 +/- 0.00111	0.108	0.153	
								Im		-1.03 +/- 0.02 [191]	0.00165 +/- 0.00112			

TABLE C.2: Results for two-loop topologies with benchmark kinematics from the literature. See the main text for details.

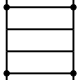
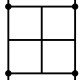
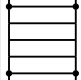
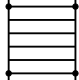
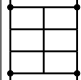
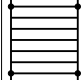
Topology	Kin.	N_c	N_E	N_S	L_{\max}	N_p	τ/p [-s]	Phase	Exp.	Reference	Numerical LTD	Δ [e]	Δ [%]	Δ [·]
	I	56	22	49	[22]	1	346	Re	-03	0	0.00796 +/- 0.00877	0.907		0.149
3L4P								Im		-6.74400	-6.73786 +/- 0.00856	0.717	0.091	
	I	192	44	280	[44]	0.7	0	Re	-05	8.41610	8.38828 +/- 0.07772	0.358	0.331	0.352
4L4P.a								Im		0	-0.01028 +/- 0.07754	0.133		
	I	209	33	270	[33]	0.5	2712	Re	-04	7.41128	7.96654 +/- 0.11281	4.922	7.492	7.562
4L4P.b								Im		0	0.07617 +/- 0.11858	0.642		
	I	780	0	0		1.8	255	Re	-16	0				0.843
5L4P								Im		3.31697	3.28900 +/- 0.01964	1.424	0.843	
	I	2415	0	0		14.5	1196	Re	-19	8.40449	8.36493 +/- 0.02167	1.825	0.471	0.471
6L4P.a								Im		0				
	I	2911	0	0		1	1200	Re	-18	0.90600	1.09968 +/- 0.41729	0.464	21.38	21.38
6L4P.b								Im		0				

TABLE C.3: Results for three- to six-loop ladder and fishnet integrals. The five- and six-loop configurations do not have any singular E-surfaces. See the main text for details.

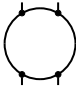
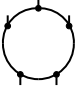
Topology	Kin.	N_C	N_E	N_S	L_{\max}	N_p	t/p [-s]	Phase	Exp.	Reference	Numerical LTD	Δ [°]	Δ [%]	Δ [·%]
	K1	4	5	1	[5]	3	14	Re	-03	1.13116	1.13123 +/- 0.00006	1.126	0.006	0.005
								Im		-0.55487	-0.55486 +/- 0.00005	0.163	0.002	
	K2	4	5	1	[5]	3	12	Re	-05	5.71928	5.71929 +/- 0.00055	0.003	3e-05	0.005
								Im		-7.24005	-7.24055 +/- 0.00053	0.952	0.007	
	K3	4	5	1	[5]	3	12	Re	-06	1.55382	1.55376 +/- 0.00012	0.545	0.004	0.005
								Im		-2.06994	-2.07005 +/- 0.00012	0.930	0.005	
K1*	4	5	3	[3,3,3]	3	16	Re	-03	1.85226	1.85214 +/- 0.00012	1.069	0.007	0.004	
							Im		-2.18400	-2.18397 +/- 0.00012	0.285	0.002		
K2*	4	5	2	[3,3]	3	14	Re	-04	0.30270	0.30272 +/- 0.00004	0.527	0.007	0.005	
							Im		-1.08125	-1.08130 +/- 0.00004	1.313	0.005		
K3*	4	3	1	[3]	3	12	Re	-06	-0.17986	-0.17991 +/- 0.00005	1.054	0.028	0.007	
							Im		-2.27578	-2.27593 +/- 0.00008	1.970	0.007		
	K1	5	8	2	[7,7]	3	18	Re	-05	-1.90847	-1.90856 +/- 0.00074	0.120	0.005	0.006
								Im		-6.45346	-6.45306 +/- 0.00077	0.515	0.006	
	K2	5	8	3	[5,5,7]	3	18	Re	-06	-0.15108	-0.15137 +/- 0.00032	0.937	0.197	0.017
								Im		-1.80679	-1.80672 +/- 0.00033	0.210	0.004	
	K3	5	8	3	[5,5,7]	3	20	Re	-09	-0.66240	-0.66271 +/- 0.00032	0.957	0.046	0.034
								Im		-1.23531	-1.23567 +/- 0.00032	1.102	0.029	
K1*	5	8	2	[6,6]	3	19	Re	-05	2.60399	2.60394 +/- 0.00072	0.060	0.002	0.012	
							Im		-7.94917	-7.95017 +/- 0.00076	1.320	0.013		
K2*	5	8	3	[4,5,5]	3	20	Re	-06	-0.48303	-0.48305 +/- 0.00059	0.034	0.004	0.009	
							Im		-3.27695	-3.27664 +/- 0.00061	0.509	0.009		
K3*	5	6	2	[5,5]	3	16	Re	-09	-1.21497	-1.21508 +/- 0.00020	0.560	0.009	0.006	
							Im		-1.53129	-1.53126 +/- 0.00020	0.188	0.002		

TABLE C-4: Results for one-loop four-point and five-point topologies for scattering kinematics ($2 \rightarrow N$) for massless and massive propagators (indicated by a *). See the main text for details.

Topology	Kin.	N_C	N_E	N_S	L_{\max}	N_p [10^9]	t/p [s]	Phase	Exp.	Reference	Numerical LTD	Δ [e]	Δ [%]	Δ [‰]
	K1	6	12	2	[11,9]	3	24	Re	-06	0.51025	0.51018 +/- 0.00031	0.224	0.014	0.009
								Im		-1.54756	-1.54768 +/- 0.00032	0.380	0.008	
	K2	6	12	5	[8,8,8,9,10]	3	27	Re	-08	0.60440	0.60407 +/- 0.00216	0.154	0.055	0.015
								Im		-6.96339	-6.96436 +/- 0.00213	0.457	0.014	
	K3	6	12	3	[8,9,10]	3	25	Re	-12	0.40660	0.40655 +/- 0.00152	0.028	0.010	0.144
								Im		-2.51956	-2.51588 +/- 0.00157	2.343	0.146	
	K1*	6	12	4	[8,9,9,9]	3	27	Re	-06	1.30210	1.30529 +/- 0.00289	1.107	0.245	0.192
								Im		-2.27354	-2.27744 +/- 0.00284	1.374	0.171	
	K2*	6	12	4	[8,8,8,9]	3	27	Re	-08	-2.19936	-2.20131 +/- 0.00241	0.809	0.089	0.032
								Im		-6.37931	-6.37841 +/- 0.00254	0.354	0.014	
	K3*	6	10	3	[7,8,8]	3	22	Re	-12	-1.27979	-1.28057 +/- 0.00088	0.884	0.061	0.486
								Im		-2.22849	-2.21602 +/- 0.00088	14.09	0.559	
K1	8	23	2	[22,18]	3	37	Re	-10	5.09917	5.10300 +/- 0.00400	0.958	0.075	0.086	
							Im		-1.62799	-1.62544 +/- 0.00373	0.685	0.157		
K2	8	23	9	[14,15,16,15,14,16,19,19,18]	3	47	Re	-12	4.20915	4.21309 +/- 0.00421	0.934	0.093	0.134	
							Im		-1.95289	-1.95771 +/- 0.00394	1.223	0.247		
K3	8	23	12	[15,15,15,14,16,18,14,18,18,16,18,18]	3	52	Re	-19	1.27379	1.26931 +/- 0.00486	0.923	0.352	1.004	
							Im		-0.82567	-0.84023 +/- 0.00503	2.898	1.764		
K1*	8	23	4	[20,19,19,18]	3	37	Re	-09	-0.35693	-0.35626 +/- 0.00057	1.168	0.187	0.082	
							Im		-1.46806	-1.46911 +/- 0.00058	1.822	0.072		
K2*	8	23	7	[14,14,16,17,18,17,18]	3	45	Re	-12	-1.14718	-1.16905 +/- 0.00794	2.754	1.906	1.004	
							Im		-2.70587	-2.72569 +/- 0.00967	2.050	0.732		
K3*	8	21	6	[17,17,16,15,14,14]	3	37	Re	-08	-0.57515	-0.57605 +/- 0.00196	0.459	0.156	0.048	
							Im		-4.04221	-4.04047 +/- 0.00202	0.858	0.043		

TABLE C.5: Results for one-loop six-point and eight-point topologies for scattering kinematics ($2 \rightarrow N$) for massless and massive propagators (indicated by a *). See the main text for details.

Topology	Kin.	N_c	N_E	N_S	L_{\max}	N_p	10^9	t/p	$[-s]$	Phase	Exp.	Reference	Numerical LTD	Δ	$[\text{ae}]$	Δ	$[\%]$	$ \cdot $		
K1	15 12 8	[12]	3	53	Re	-06	-1.08406	[216]	-1.0856	+/-	0.00127	1.971	0.230	0.090	Im	2.86702	+/-	0.00125	0.951	0.041
K2	15 10 8	[10]	3	55	Re	-08	3.11053	[216]	3.0946	+/-	0.00696	2.021	0.452	0.140	Im	9.53885	+/-	0.00706	0.094	0.007
K3	15 10 8	[10]	3	56	Re	-10	1.70372	[216]	1.70253	+/-	0.00285	0.419	0.070	0.025	Im	4.56497	+/-	0.00291	0.031	0.002
K1*	15 9 11	[7,8]	3	62	Re	-06	2.802	+/- 0.008	[73]	2.80094	+/-	0.00023	0.008	0.008	Im	3.34866	+/-	0.00025	0.007	
																				Im
K2*	15 6 13	[4,4]	3	77	Re	-08	7.9	+/- 0.7	[73]	8.15559	+/-	0.00123	0.015	0.017	Im	6.10277	+/-	0.00124	0.020	
																				Im
K3*	15 7 8	[7]	3	55	Re	-10	3.1	+/- 0.1	[73]	3.10306	+/-	0.00021	0.007	0.009	Im	0.1	+/- 0.1	0.00020	0.212	
																				Im
K1	19 17 14	[16,16]	3	80	Re	-07	n/a	n/a	n/a	0.27368	+/-	0.00131	0.479	0.125	Im	1.44760	+/-	0.00129	0.089	
																				Im
K2	19 13 19	[8,8,12]	3	86	Re	-09	n/a	n/a	n/a	1.08568	+/-	0.00342	0.315	0.230	Im	1.78725	+/-	0.00339	0.190	
																				Im
K3	19 13 19	[8,8,12]	3	86	Re	-13	n/a	n/a	n/a	2.09848	+/-	0.00648	0.309	0.313	Im	2.04022	+/-	0.00648	0.318	
																				Im
K1*	19 14 16	[13,12]	3	80	Re	-07	n/a	n/a	n/a	1.51586	+/-	0.00027	0.018	0.019	Im	1.31451	+/-	0.00027	0.021	
																				Im
K2*	19 10 20	[8,9]	3	97	Re	-09	n/a	n/a	n/a	1.97798	+/-	0.01394	0.705	0.799	Im	1.13209	+/-	0.01173	1.036	
																				Im
K3*	19 12 18	[10,10,10]	3	84	Re	-13	n/a	n/a	n/a	2.00638	+/-	0.00061	0.030	0.043	Im	-0.08277	+/-	0.00060	0.730	
																				Im



2L4P.b



2L5P

TABLE C.6: Results for two-loop topologies for scattering kinematics ($2 \rightarrow N$) for massless and massive propagators (indicated by a *). When there is no reference result, $\Delta[\%]$ and $\Delta[\%] \cdot |\cdot|$ refer to the Monte-Carlo accuracy relative to the central value. See the main text for details.

Topology	Kin.	N_C	N_E	N_S	L_{\max}	N_p [10^9]	τ/p [s]	Phase	Exp.	Reference	Numerical LTD	Δ [°]	Δ [%]	Δ [‰]
	K1	20	20	15	[19, 14]	3	100	Re	-09	n/a	4.58688 +/- 0.05132	1.119	1.119	1.059
								Im		n/a	5.04144 +/- 0.05075	1.007		
2L6P.a	K1*	20	17	24	[12, 13, 13, 13, 13]	3	116	Re	-09	n/a	-1.04316 +/- 0.35247	33.79	33.79	10.99
								Im		n/a	-4.42468 +/- 0.35421	8.005		
	K1	23	23	15	[22, 19]	3	91	Re	-09	n/a	1.17336 +/- 0.00888	0.757	0.757	0.303
								Im		n/a	3.99809 +/- 0.00896	0.224		
2L6P.b	K1*	23	20	20	[18, 17, 18]	3	103	Re	-09	n/a	5.35217 +/- 0.00153	0.029	0.029	0.033
								Im		n/a	3.81579 +/- 0.00150	0.039		
	K1	24	22	16	[20, 21]	3	89	Re	-09	n/a	4.90974 +/- 0.01407	0.286	0.286	0.375
								Im		n/a	-2.13974 +/- 0.01434	0.670		
2L6P.c	K1*	24	20	22	[17, 17, 17, 17]	3	108	Re	-08	n/a	1.05934 +/- 0.15850	14.96	14.96	14.87
								Im		n/a	1.03698 +/- 0.15312	14.77		
	K1	24	20	26	[16, 7, 14, 14, 4]	3	136	Re	-08	n/a	1.90487 +/- 0.05753	3.020	3.020	2.017
								Im		n/a	-3.55267 +/- 0.05746	1.617		
2L6P.d	K1*	24	17	30	[13, 12, 12, 12, 2]	3	144	Re	-08	n/a	-2.97419 +/- 0.00961	0.323	0.323	0.367
								Im		n/a	-2.18847 +/- 0.00957	0.437		
	K1	26	21	34	[16, 9, 9, 14, 15, 9, 7]	3	163	Re	-07	n/a	2.87833 +/- 0.00951	0.330	0.330	0.386
								Im		n/a	1.99937 +/- 0.00961	0.481		
2L6P.e	K1*	26	18	43	[13, 12, 7, 7, 12, 12, 12, 12, 7, 5]	3	172	Re	-07	n/a	1.67332 +/- 0.00578	0.346	0.346	0.482
								Im		n/a	-0.21788 +/- 0.00571	2.620		
	K1	27	27	22	[24, 21, 24]	3	121	Re	-08	n/a	-0.95486 +/- 0.00890	0.932	0.932	0.368
								Im		n/a	3.28530 +/- 0.00889	0.271		
2L6P.f	K1*	27	24	34	[19, 20, 20, 20, 20]	3	152	Re	-08	n/a	2.55104 +/- 0.00208	0.082	0.082	0.097
								Im		n/a	-1.63019 +/- 0.00205	0.126		
	K1	39	46	40	[37, 42, 41, 40]	3	237	Re	-12	n/a	-5.15438 +/- 0.03310	0.642	0.642	0.544
2L8P								Im		n/a	6.78546 +/- 0.03243	0.478		

TABLE C.7: Results for two-loop topologies for scattering kinematics ($2 \rightarrow N$) for massless and massive propagators (indicated by a *). When there is no reference result, Δ [%] and Δ [‰] refer to the Monte-Carlo accuracy relative to the central value. See the main text for details.

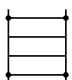
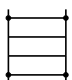
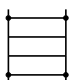



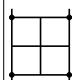
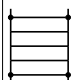
Topology	Kin.	N_C	N_E	N_S	L_{\max}	N_p [10^9]	t/p [-s]	Phase	Exp.	Reference	Numerical LTD	Δ [e]	Δ [%]	Δ [%]
	K1	56	17	49	[17]	1	357	Re	-09	-2.42423 [216]	-2.43299 +/- 0.03927	0.223	0.361	0.471
								Im		-3.40035	-3.41797 +/- 0.03956	0.445	0.518	
	K2	56	17	49	[17]	1	366	Re	-11	-5.30309 [216]	-5.36759 +/- 0.14110	0.457	1.216	1.246
	K3	56	17	49	[17]	1	378	Re	-14	-4.47047 [216]	-4.46226 +/- 0.10022	0.082	0.184	1.462
								Im		-0.66383	-0.72941 +/- 0.09918	0.661	9.879	
	K1*	56	7	55	[7]	1	379	Re	-09	n/a	-3.89588 +/- 0.00173		0.044	0.043
							Im		n/a	3.89127 +/- 0.00165		0.043		
	K2*	56	7	61	[5,5]	1	454	Re	-11	n/a	-3.15581 +/- 0.00639		0.203	0.208
								Im		n/a	2.97368 +/- 0.00633		0.213	
	K3*	56	12	49	[12]	1	364	Re	-14	n/a	-0.10876 +/- 0.00096		0.883	0.072
							Im		n/a	1.86939 +/- 0.00095		0.051		
	K1	71	24	80	[23,23]	1	490	Re	-10	n/a	-1.06298 +/- 0.02843		2.675	2.922
								Im		n/a	-0.88557 +/- 0.02875		3.246	
	K2	71	20	80	[14,19]	1	503	Re	-06	n/a	-3.28794 +/- 0.07308		2.223	3.202
							Im		n/a	-0.29022 +/- 0.07635		26.31		
	K3	71	20	103	[13,13,19]	1	589	Re	-17	n/a	-1.61475 +/- 0.14277		8.841	12.07
								Im		n/a	0.25654 +/- 0.13621		53.10	
	K1*	71	17	99	[15,14]	1	563	Re	-10	n/a	-1.26220 +/- 0.00124		0.098	0.106
							Im		n/a	1.06124 +/- 0.00123		0.116		
	K2*	71	3	57	[3]	1	427	Re	-07	n/a	4.58640 +/- 0.00609		0.133	0.180
								Im		n/a	1.80523 +/- 0.00645		0.357	
	K3*	71	20	102	[17,17,18]	1	572	Re	-18	n/a	-1.05359 +/- 0.01706		1.619	0.396
							Im		n/a	5.92117 +/- 0.01660		0.280		
	K1*	192	14	408	[13,13]	0.5	3602	Re	-09	n/a	1.28725 +/- 0.00637		0.495	0.281
								Im		n/a	2.95568 +/- 0.00642		0.217	
		K1*	209	13	292	[9,10,10]	0.5	3140	Re	-12	n/a	-4.34119 +/- 0.01166		0.269
								Im		n/a	-2.77244 +/- 0.01160		0.419	

TABLE C.8: Results for three- and four-loop topologies for scattering kinematics ($2 \rightarrow N$) for massless and massive propagators (indicated by a *). When there is no reference result, Δ [%] and Δ [%] refer to the Monte-Carlo accuracy relative to the central value. See the main text for details.

D

RECURSIVE CANCELLATION OF SPURIOUS SINGULARITIES

D.1 EXPLICIT REMOVAL OF SPURIOUS SINGULARITIES

In what follows we derive the recursion relation presented in eq. (5.6) that allows to remove in a systematic way all the spurious singularities from our starting expression in eq.(5.5) with $n > 0$. Remember that if $n = 1$ it is already free of spurious singularities. We start by selecting an (arbitrary) order in $\mathbf{x} = (x_1, \dots, x_n)$, pick its first variable x_1 and work towards the intermediate goal of deriving an expression where all spurious singularities at $x_1 = x_j$ for $1 < j \leq \dim(\mathbf{x})$ are explicitly removed. As we will see, this result can in turn be expressed as a recursive formula of terms similar to the starting expression, which are now manifestly free of singularities in x_1 . The application of this recursive formula is described in section 5.1, where we apply this relation recursively to our starting expression in eq. (5.5) to render it manifestly free of all spurious singularities, resulting in eq. (5.7).

More explicitly, we consider our starting expression in eq. (5.5) and split off the first summand, as

$$F \left(\begin{matrix} \mathbf{x} \\ \bar{\mathbf{x}} \end{matrix}; \mathcal{N} \right) = \frac{\mathcal{N}_{\mathcal{N}}([x_1])E(x_1|\bar{\mathbf{x}})}{\prod_{j \neq 1}(x_1 - x_j)} + \sum_{i=2}^n \frac{\mathcal{N}_{\mathcal{N}}([x_i])E(x_i|\bar{\mathbf{x}})}{\prod_{j \neq i}(x_i - x_j)}. \quad (\text{D.1.1})$$

We then use the identity

$$\sum_{i=1}^n \frac{1}{\prod_{j \neq i}(x_i - x_j)} = 0 \quad (\text{D.1.2})$$

and apply it to the first summand in eq. (D.1.1) and obtain

$$\frac{\mathcal{N}_{\mathcal{N}}([x_1])E(x_1|\bar{\mathbf{x}})}{\prod_{j \neq 1}(x_1 - x_j)} = -\mathcal{N}_{\mathcal{N}}([x_1]) \sum_{i=2}^n \frac{E(x_1|\bar{\mathbf{x}})}{\prod_{j \neq i}(x_i - x_j)}. \quad (\text{D.1.3})$$

Note that the identity in eq. (D.1.2) allowed us to move each of the poles $x_1 = x_j$ for $1 < j \leq n$ in the product on the left-hand side in eq. (D.1.3) into a separate summand on the right-hand side. As a next step, we want to remove this pole from each of the summands. This we will do

through an iteration over $\bar{\mathbf{x}}$. Therefore, we first pick an (arbitrary) order in $\bar{\mathbf{x}} = (\bar{x}_1, \dots, \bar{x}_{\bar{n}})$. We observe that using the relation

$$E(x_1|\bar{x}_1) - E(x_i|\bar{x}_1) = (x_i - x_1)E(x_1|\bar{x}_1)E(x_i|\bar{x}_1), \tag{D.1.4}$$

we can write

$$\frac{E(x_1|\bar{x}_1)}{\prod_{j \neq i}(x_i - x_j)} = \frac{E(x_1|\bar{x}_1)}{\prod_{j \neq i}(x_i - x_j)} - \frac{E(x_i|\bar{x}_1)}{\prod_{j \neq i}(x_i - x_j)} + \frac{E(x_i|\bar{x}_1)}{\prod_{j \neq i}(x_i - x_j)} \tag{D.1.5}$$

$$= \frac{E(x_1|\bar{x}_1)E(x_i|\bar{x}_1)}{\prod_{j \neq i,1}(x_i - x_j)} + \frac{E(x_i|\bar{x}_1)}{\prod_{j \neq i}(x_i - x_j)}, \tag{D.1.6}$$

such that the pole at $x_i = x_1$ has been regulated in the first summand while remaining present in the second term with the numerator now evaluated at x_i instead of x_1 .

Using this result and combining factors as $E(x_1|\bar{\mathbf{x}}) = E(x_1|\bar{x}_1)E(x_1|\bar{\mathbf{x}}_{(2)})$ we can express each summand on the right-hand side of eq. (D.1.3) as

$$\frac{E(x_1|\bar{\mathbf{x}})}{\prod_{j \neq i}(x_i - x_j)} = \frac{E(x_1|\bar{\mathbf{x}})E(x_i|\bar{x}_1)}{\prod_{j \neq i,1}(x_i - x_j)} + \frac{E(x_1|\bar{\mathbf{x}}_{(2)})E(x_i|\bar{x}_1)}{\prod_{j \neq i}(x_i - x_j)}. \tag{D.1.7}$$

Analogously, we apply the relation in eq. (D.1.5) with $\bar{x}_1 \leftrightarrow \bar{x}_2$ to the second summand in eq. (D.1.7). This step is performed for all \bar{x}_r with $1 \leq r \leq \bar{n}$ such that we arrive at

$$\frac{E(x_1|\bar{\mathbf{x}})}{\prod_{j \neq i}(x_i - x_j)} = \sum_{r=1}^{\bar{n}} \frac{E(x_1|\bar{\mathbf{x}}_{(r)})E(x_i|\bar{\mathbf{x}}_{(1,r)})}{\prod_{j \neq i,1}(x_i - x_j)} + \frac{E(x_i|\bar{\mathbf{x}})}{\prod_{j \neq i}(x_i - x_j)}. \tag{D.1.8}$$

Before we now use this result from eq. (D.1.8), we first note that eq. (D.1.1) and eq. (D.1.3) can be combined into a single sum as

$$F \left(\begin{matrix} \mathbf{x} \\ \bar{\mathbf{x}} \end{matrix}; \mathcal{N} \right) = \sum_{i=2}^n \left(\frac{N_{\mathcal{N}}([x_i])E(x_i|\bar{\mathbf{x}})}{\prod_{j \neq i}(x_i - x_j)} - \frac{N_{\mathcal{N}}([x_1])E(x_1|\bar{\mathbf{x}})}{\prod_{j \neq i}(x_i - x_j)} \right), \tag{D.1.9}$$

such that plugging in the relation in eq. (D.1.8) yields

$$F \left(\begin{matrix} \mathbf{x} \\ \bar{\mathbf{x}} \end{matrix}; \mathcal{N} \right) = - \sum_{i=2}^n \sum_{r=1}^{\bar{n}} \frac{N_{\mathcal{N}}([x_1])E(x_1|\bar{\mathbf{x}}_{(r)})E(x_i|\bar{\mathbf{x}}_{(1,r)})}{\prod_{j \neq i,1}(x_i - x_j)} + \sum_{i=2}^n \frac{N_{\mathcal{N}}([x_1, x_i])E(x_i|\bar{\mathbf{x}})}{\prod_{j \neq i,1}(x_i - x_j)}, \tag{D.1.10}$$

Note that all of the expressions on the right-hand side are manifestly free of singularities in x_1 , as no explicit denominators $(x_1 - x_j)$ with $1 < j \leq n$ appear. Of course, there is a hidden dependence on the denominator $(x_i - x_1)$ in the divide difference $N_{\mathcal{N}}([x_1, x_i])$ for $1 < i \leq n$,

which however is regular as we discussed in sect. 5.1.2. This observation now reveals that the singularities in x_1 of the left-hand side, as they appear in each summand in eq. (D.1.1) are indeed spurious. Furthermore, the arbitrary order in \mathbf{x} , respectively the choice of x_1 at the beginning of this section makes it clear that the recursion can be used to explicitly remove spurious singularities in any variable x_i for $1 \leq i \leq n$. We now observe that eq. (D.1.10) takes the implicit form of a recursion that we can make explicit by writing

$$F \left(\begin{array}{c} \mathbf{x} \\ \bar{\mathbf{x}} \end{array}; \mathcal{N}(\cdot) \right) = -\mathcal{N}_{\mathcal{N}}([x_1]) \sum_{r=1}^{\bar{n}} E(x_1 | \bar{\mathbf{x}}_{(r)}) F \left(\begin{array}{c} \mathbf{x}^{(2,')} \\ \bar{\mathbf{x}}_{(1,r)} \end{array}; 1 \right) + F \left(\begin{array}{c} \mathbf{x}^{(2,')} \\ \bar{\mathbf{x}} \end{array}; \mathcal{N}_{\mathcal{N}}([x_1, \cdot]) \right). \quad (\text{D.1.11})$$

It is straight-forward to make this recursion generic for an intermediate step with an arbitrary numerator \mathcal{F} and vectors $\mathbf{y} \in (\mathbb{H}^*)^{\dim(\mathbf{y})}$ and $\bar{\mathbf{y}} \in (\mathbb{H}^*)^{\dim(\bar{\mathbf{y}})}$. One then recovers precisely the recursion in eq. (5.6), which concludes its derivation.

Part V

REFERENCES

BIBLIOGRAPHY

1. F. Dulat, S. Lionetti, B. Mistlberger, A. Pelloni, C. Specchia, Higgs-differential cross section at NNLO in dimensional regularisation. *JHEP* **07**, 017, arXiv: 1704.08220 [hep-ph] (2017).
2. F. Dulat, B. Mistlberger, A. Pelloni, Differential Higgs production at N³LO beyond threshold. *JHEP* **01**, 145, arXiv: 1710.03016 [hep-ph] (2018).
3. F. Dulat, B. Mistlberger, A. Pelloni, Precision predictions at N³LO for the Higgs boson rapidity distribution at the LHC. *Phys. Rev.* **D99**, 034004, arXiv: 1810.09462 [hep-ph] (2019).
4. Z. Capatti, V. Hirschi, D. Kermanschah, A. Pelloni, B. Ruijl, Numerical Loop-Tree Duality: contour deformation and subtraction. *JHEP* **04**, 096, arXiv: 1912.09291 [hep-ph] (2020).
5. Z. Capatti, V. Hirschi, D. Kermanschah, A. Pelloni, B. Ruijl, Manifestly Causal Loop-Tree Duality. arXiv: 2009.05509 [hep-ph] (2020).
6. Z. Capatti, V. Hirschi, A. Pelloni, B. Ruijl, Local Unitarity: a representation of differential cross-sections that is locally free of infrared singularities at any order. arXiv: 2010.01068 [hep-ph] (2020).
7. J. Thomson, Cathode rays. *Phil. Mag. Ser. 5* **44**, 293–316 (1897).
8. G. Arnison *et al.*, Experimental Observation of Isolated Large Transverse Energy Electrons with Associated Missing Energy at $s^{1/2} = 540$ -GeV. *Phys. Lett. B* **122**, 103–116 (1983).
9. G. Arnison *et al.*, Experimental Observation of Lepton Pairs of Invariant Mass Around 95-GeV/ c^2 at the CERN SPS Collider. *Phys. Lett. B* **126**, 398–410 (1983).
10. G. Guralnik, C. Hagen, T. Kibble, Global Conservation Laws and Massless Particles. *Phys. Rev. Lett.* **13**, ed. by J. Taylor, 585–587 (1964).
11. P. W. Higgs, Broken Symmetries and the Masses of Gauge Bosons. *Phys. Rev. Lett.* **13**, ed. by J. Taylor, 508–509 (1964).
12. F. Englert, R. Brout, Broken Symmetry and the Mass of Gauge Vector Mesons. *Phys. Rev. Lett.* **13**, ed. by J. Taylor, 321–323 (1964).
13. Observation of a new particle in the search for the Standard Model Higgs boson with the ATLAS detector at the LHC. *Physics Letters B* **716**, 1–29, ISSN: 0370-2693, (<http://www.sciencedirect.com/science/article/pii/S037026931200857X>) (2012).

14. S. Chatrchyan *et al.*, Observation of a new boson at a mass of 125 GeV with the CMS experiment at the LHC. *Phys. Lett.* **B716**, 30–61, arXiv: 1207.7235 [hep-ex] (2012).
15. M. Aaboud *et al.*, Observation of Higgs boson production in association with a top quark pair at the LHC with the ATLAS detector. *Phys. Lett. B* **784**, 173–191, arXiv: 1806.00425 [hep-ex] (2018).
16. M. Tanabashi *et al.*, Review of Particle Physics. *Phys. Rev. D* **98**, 030001 (2018).
17. M. Cepeda *et al.*, in *Report on the Physics at the HL-LHC, and Perspectives for the HE-LHC*, ed. by A. Dainese, M. Mangano, A. B. Meyer, A. Nisati, G. Salam, M. A. Vesterinen, vol. 7, 221, arXiv: 1902.00134 [hep-ph].
18. S. Amoroso *et al.*, presented at the 11th Les Houches Workshop on Physics at TeV Colliders: PhysTeV Les Houches, arXiv: 2003.01700 [hep-ph].
19. K. G. Chetyrkin, B. A. Kniehl, M. Steinhauser, Hadronic Higgs decay to order α_s^4 . *Phys. Rev. Lett.* **79**, 353–356, arXiv: hep-ph/9705240 [hep-ph] (1997).
20. K. G. Chetyrkin, J. H. Kuhn, C. Sturm, QCD decoupling at four loops. *Nucl. Phys.* **B744**, 121–135, arXiv: hep-ph/0512060 [hep-ph] (2006).
21. M. Kramer, E. Laenen, M. Spira, Soft gluon radiation in Higgs boson production at the LHC. *Nucl. Phys. B* **511**, 523–549, arXiv: hep-ph/9611272 (1998).
22. Y. Schroder, M. Steinhauser, Four-loop decoupling relations for the strong coupling. *JHEP* **01**, 051, arXiv: hep-ph/0512058 [hep-ph] (2006).
23. A. Djouadi, M. Spira, P. M. Zerwas, Production of Higgs bosons in proton colliders: QCD corrections. *Phys. Lett.* **B264**, 440–446 (1991).
24. J. Grigo, K. Melnikov, M. Steinhauser, Virtual corrections to Higgs boson pair production in the large top quark mass limit. *Nucl. Phys. B* **888**, 17–29, arXiv: 1408.2422 [hep-ph] (2014).
25. M. Spira, Effective Multi-Higgs Couplings to Gluons. *JHEP* **10**, 026, arXiv: 1607.05548 [hep-ph] (2016).
26. C. Anastasiou, C. Duhr, F. Dulat, F. Herzog, B. Mistlberger, Higgs Boson Gluon-Fusion Production in QCD at Three Loops. *Phys. Rev. Lett.* **114**, 212001, arXiv: 1503.06056 [hep-ph] (2015).
27. B. Mistlberger, Higgs Boson Production at Hadron Colliders at N_3 LO in QCD. arXiv: 1802.00833v1 [hep-ph] (2018).
28. D. de Florian *et al.*, Handbook of LHC Higgs Cross Sections: 4. Deciphering the Nature of the Higgs Sector. arXiv: 1610.07922v2 [hep-ph] (2016).

29. F. Tkachov, A Theorem on Analytical Calculability of Four Loop Renormalization Group Functions. *Phys. Lett. B* **100**, 65–68 (1981).
30. K. Chetyrkin, F. Tkachov, Integration by Parts: The Algorithm to Calculate beta Functions in 4 Loops. *Nucl. Phys. B* **192**, 159–204 (1981).
31. P. Baikov, Explicit solutions of the multiloop integral recurrence relations and its application. *Nucl. Instrum. Meth. A* **389**, ed. by M. Werlen, D. Perret-Gallix, 347–349, arXiv: hep-ph/9611449 (1997).
32. V. A. Smirnov, O. Veretin, Analytical results for dimensionally regularized massless on-shell double boxes with arbitrary indices and numerators. *Nucl. Phys. B* **566**, 469–485, arXiv: hep-ph/9907385 (2000).
33. C. Anastasiou, T. Gehrmann, C. Oleari, E. Remiddi, J. Tausk, The Tensor reduction and master integrals of the two loop massless crossed box with lightlike legs. *Nucl. Phys. B* **580**, 577–601, arXiv: hep-ph/0003261 (2000).
34. S. Laporta, High precision calculation of multiloop Feynman integrals by difference equations. *Int. J. Mod. Phys. A* **15**, 5087–5159, arXiv: hep-ph/0102033 [hep-ph] (2000).
35. C. Anastasiou, A. Lazopoulos, Automatic integral reduction for higher order perturbative calculations. *JHEP* **07**, 046, arXiv: hep-ph/0404258 (2004).
36. A. Smirnov, V. A. Smirnov, Applying Grobner bases to solve reduction problems for Feynman integrals. *JHEP* **01**, 001, arXiv: hep-lat/0509187 (2006).
37. R. N. Lee, Group structure of the integration-by-part identities and its application to the reduction of multiloop integrals. *JHEP0807:031,2008*, arXiv: 0804.3008v2 [hep-ph] (2008).
38. P. Kant, Finding Linear Dependencies in Integration-By-Parts Equations: A Monte Carlo Approach. *Comput. Phys. Commun.* **185**, 1473–1476, arXiv: 1309.7287 [hep-ph] (2014).
39. A. von Manteuffel, R. M. Schabinger, A novel approach to integration by parts reduction. arXiv: 1406.4513v2 [hep-ph] (2014).
40. A. V. Smirnov, FIRE5: a C++ implementation of Feynman Integral REduction. *Comput. Phys. Commun.* **189**, 182–191, arXiv: 1408.2372 [hep-ph] (2015).
41. B. Ruijl, T. Ueda, J. Vermaseren, Forcer, a FORM program for the parametric reduction of four-loop massless propagator diagrams. *Comput. Phys. Commun.* **253**, 107198, arXiv: 1704.06650 [hep-ph] (2020).
42. P. Maierhöfer, J. Usovitsch, P. Uwer, Kira—A Feynman integral reduction program. *Comput. Phys. Commun.* **230**, 99–112, arXiv: 1705.05610 [hep-ph] (2018).

43. A. Smirnov, F. Chuharev, FIRE6: Feynman Integral REduction with Modular Arithmetic. arXiv: 1901.07808 [hep-ph] (2019).
44. T. Peraro, FiniteFlow: multivariate functional reconstruction using finite fields and dataflow graphs. *JHEP* **07**, 031, arXiv: 1905.08019 [hep-ph] (2019).
45. H. Frellesvig, F. Gasparotto, M. K. Mandal, P. Mastrolia, L. Mattiazzi, S. Mizera, Vector Space of Feynman Integrals and Multivariate Intersection Numbers. *Phys. Rev. Lett.* **123**, 201602, arXiv: 1907.02000 [hep-th] (2019).
46. J. Böhm, A. Georgoudis, K. J. Larsen, M. Schulze, Y. Zhang, Complete sets of logarithmic vector fields for integration-by-parts identities of Feynman integrals. *Phys. Rev. D* **98**, 025023, arXiv: 1712.09737 [hep-th] (2018).
47. D. A. Kosower, Direct Solution of Integration-by-Parts Systems. *Phys. Rev. D* **98**, 025008, arXiv: 1804.00131 [hep-ph] (2018).
48. A. von Manteuffel, C. Studerus, Reduze 2 - Distributed Feynman Integral Reduction. arXiv: 1201.4330 [hep-ph] (2012).
49. R. N. Lee, LiteRed 1.4: a powerful tool for reduction of multiloop integrals. *J. Phys. Conf. Ser.* **523**, ed. by J. Wang, 012059, arXiv: 1310.1145 [hep-ph] (2014).
50. H. Ita, Two-loop Integrand Decomposition into Master Integrals and Surface Terms. *Phys. Rev. D* **94**, 116015, arXiv: 1510.05626 [hep-th] (2016).
51. A. Kotikov, Differential equations method: New technique for massive Feynman diagrams calculation. *Phys. Lett. B* **254**, 158–164 (1991).
52. T. Gehrmann, E. Remiddi, Differential equations for two loop four point functions. *Nucl. Phys.* **B580**, 485–518, arXiv: hep-ph/9912329 [hep-ph] (2000).
53. E. Remiddi, J. Vermaseren, Harmonic polylogarithms. *Int. J. Mod. Phys. A* **15**, 725–754, arXiv: hep-ph/9905237 (2000).
54. A. B. Goncharov, Multiple polylogarithms, cyclotomy and modular complexes. *Math. Res. Lett.* **5**, 497–516, arXiv: 1105.2076 [math.AG] (1998).
55. F. C. Brown, Polylogarithmes multiples uniformes en une variable. *Compt. Rend. Math.* **338**, 527–532 (2004).
56. J. M. Henn, Multiloop integrals in dimensional regularization made simple. *Phys. Rev. Lett.* **110**, 251601, arXiv: 1304.1806 [hep-th] (2013).
57. R. N. Lee, Reducing differential equations for multiloop master integrals. *JHEP* **04**, 108, arXiv: 1411.0911 [hep-ph] (2015).

58. R. N. Lee, A. A. Pomeransky, Normalized Fuchsian form on Riemann sphere and differential equations for multiloop integrals. arXiv: 1707.07856 [hep-th] (2017).
59. A. Primo, L. Tancredi, On the maximal cut of Feynman integrals and the solution of their differential equations. *Nucl. Phys. B* **916**, 94–116, arXiv: 1610.08397 [hep-ph] (2017).
60. C. G. Papadopoulos, D. Tommasini, C. Wever, Two-loop Master Integrals with the Simplified Differential Equations approach. *JHEP* **01**, 072, arXiv: 1409.6114 [hep-ph] (2015).
61. C. Duhr, Hopf algebras, coproducts and symbols: an application to Higgs boson amplitudes. *JHEP* **08**, 043, arXiv: 1203.0454 [hep-ph] (2012).
62. T. Peraro, Scattering amplitudes over finite fields and multivariate functional reconstruction. *JHEP* **12**, 030, arXiv: 1608.01902 [hep-ph] (2016).
63. P. Mastrolia, T. Peraro, A. Primo, Adaptive Integrand Decomposition in parallel and orthogonal space. *JHEP* **08**, 164, arXiv: 1605.03157 [hep-ph] (2016).
64. J. Ablinger, J. Blümlein, A. De Freitas, M. van Hoeij, E. Imamoglu, C. Raab, C. Radu, C. Schneider, Iterated Elliptic and Hypergeometric Integrals for Feynman Diagrams. *J. Math. Phys.* **59**, 062305, arXiv: 1706.01299 [hep-th] (2018).
65. E. Remiddi, L. Tancredi, An Elliptic Generalization of Multiple Polylogarithms. *Nucl. Phys. B* **925**, 212–251, arXiv: 1709.03622 [hep-ph] (2017).
66. R. Bonciani, V. Del Duca, H. Frellesvig, J. Henn, M. Hidding, L. Maestri, F. Moriello, G. Salvatori, V. Smirnov, Evaluating a family of two-loop non-planar master integrals for Higgs + jet production with full heavy-quark mass dependence. *JHEP* **01**, 132, arXiv: 1907.13156 [hep-ph] (2020).
67. F. Moriello, Generalised power series expansions for the elliptic planar families of Higgs + jet production at two loops. *JHEP* **01**, 150, arXiv: 1907.13234 [hep-ph] (2020).
68. G. Passarino, Elliptic Polylogarithms and Basic Hypergeometric Functions. *Eur. Phys. J. C* **77**, 77, arXiv: 1610.06207 [math-ph] (2017).
69. J. Broedel, C. Duhr, F. Dulat, L. Tancredi, Elliptic polylogarithms and iterated integrals on elliptic curves II: an application to the sunrise integral. *Phys. Rev. D* **97**, 116009, arXiv: 1712.07095 [hep-ph] (2018).
70. J. Broedel, C. Duhr, F. Dulat, B. Penante, L. Tancredi, Elliptic polylogarithms and Feynman parameter integrals. *JHEP* **05**, 120, arXiv: 1902.09971 [hep-ph] (2019).
71. L. Adams, C. Bogner, S. Weinzierl, The two-loop sunrise integral around four space-time dimensions and generalisations of the Clausen and Glaisher functions towards the elliptic case. *J. Math. Phys.* **56**, 072303, arXiv: 1504.03255 [hep-ph] (2015).

72. J. Broedel, C. Duhr, F. Dulat, L. Tancredi, Elliptic polylogarithms and iterated integrals on elliptic curves. Part I: general formalism. *JHEP* **05**, 093, arXiv: 1712.07089 [hep-th] (2018).
73. S. Borowka, G. Heinrich, S. Jahn, S. Jones, M. Kerner, J. Schlenk, T. Zirke, pySecDec: a toolbox for the numerical evaluation of multi-scale integrals. *Comput. Phys. Commun.* **222**, 313–326, arXiv: 1703.09692 [hep-ph] (2018).
74. A. Smirnov, M. Tentyukov, Feynman Integral Evaluation by a Sector decomposition Approach (FIESTA). *Comput. Phys. Commun.* **180**, 735–746, arXiv: 0807.4129 [hep-ph] (2009).
75. W. Gong, Z. Nagy, D. E. Soper, Direct numerical integration of one-loop Feynman diagrams for N-photon amplitudes. *Phys. Rev. D* **79**, 033005, arXiv: 0812.3686 [hep-ph] (2009).
76. S. Becker, D. Goetz, C. Reuschle, C. Schwan, S. Weinzierl, NLO results for five, six and seven jets in electron-positron annihilation. *Phys. Rev. Lett.* **108**, 032005, arXiv: 1111.1733 [hep-ph] (2012).
77. S. Becker, S. Weinzierl, Direct numerical integration for multi-loop integrals. *Eur. Phys. J. C* **73**, 2321, arXiv: 1211.0509 [hep-ph] (2013).
78. D. E. Soper, Techniques for QCD calculations by numerical integration. *Phys. Rev. D* **62**, 014009, arXiv: hep-ph/9910292 (2000).
79. S. Catani, T. Gleisberg, F. Krauss, G. Rodrigo, J.-C. Winter, From loops to trees by-passing Feynman’s theorem. *JHEP* **09**, 065, arXiv: 0804.3170 [hep-ph] (2008).
80. I. Bierenbaum, S. Catani, P. Draggiotis, G. Rodrigo, A Tree-Loop Duality Relation at Two Loops and Beyond. *JHEP* **10**, 073, arXiv: 1007.0194 [hep-ph] (2010).
81. Z. Capatti, V. Hirschi, D. Kermanschah, B. Ruijl, Loop-Tree Duality for Multiloop Numerical Integration. *Phys. Rev. Lett.* **123**, 151602, arXiv: 1906.06138 [hep-ph] (2019).
82. R. Runkel, Z. Szőr, J. P. Vesga, S. Weinzierl, Causality and loop-tree duality at higher loops. *Phys. Rev. Lett.* **122**, [Erratum: *Phys.Rev.Lett.* **123**, 059902 (2019)], 111603, arXiv: 1902.02135 [hep-ph] (2019).
83. C. Anastasiou, R. Haindl, G. Sterman, Z. Yang, M. Zeng, Locally finite two-loop amplitudes for off-shell multi-photon production in electron-positron annihilation. arXiv: 2008.12293 [hep-ph] (2020).
84. D. E. Soper, QCD calculations by numerical integration. *Phys. Rev. Lett.* **81**, 2638–2641, arXiv: hep-ph/9804454 (1998).

85. S. Catani, M. Grazzini, An NNLO subtraction formalism in hadron collisions and its application to Higgs boson production at the LHC. *Phys. Rev. Lett.* **98**, 222002, arXiv: hep-ph/0703012 (2007).
86. C. Anastasiou, K. Melnikov, F. Petriello, Higgs boson production at hadron colliders: Differential cross sections through next-to-next-to-leading order. *Phys. Rev. Lett.* **93**, 262002, arXiv: hep-ph/0409088 (2004).
87. C. Anastasiou, K. Melnikov, F. Petriello, Fully differential Higgs boson production and the di-photon signal through next-to-next-to-leading order. *Nucl. Phys. B* **724**, 197–246, arXiv: hep-ph/0501130 (2005).
88. M. Grazzini, NNLO predictions for the Higgs boson signal in the $H \rightarrow WW \rightarrow l\nu l\nu$ and $H \rightarrow ZZ \rightarrow 4l$ decay channels. *JHEP* **02**, 043, arXiv: 0801.3232 [hep-ph] (2008).
89. X. Chen, J. Cruz-Martinez, T. Gehrmann, E. Glover, M. Jaquier, NNLO QCD corrections to Higgs boson production at large transverse momentum. *JHEP* **10**, 066, arXiv: 1607.08817 [hep-ph] (2016).
90. R. Boughezal, C. Focke, W. Giele, X. Liu, F. Petriello, Higgs boson production in association with a jet at NNLO using jetiness subtraction. *Phys. Lett. B* **748**, 5–8, arXiv: 1505.03893 [hep-ph] (2015).
91. R. Boughezal, F. Caola, K. Melnikov, F. Petriello, M. Schulze, Higgs boson production in association with a jet at next-to-next-to-leading order. *Phys. Rev. Lett.* **115**, 082003, arXiv: 1504.07922 [hep-ph] (2015).
92. F. Caola, K. Melnikov, M. Schulze, Fiducial cross sections for Higgs boson production in association with a jet at next-to-next-to-leading order in QCD. *Phys. Rev. D* **92**, 074032, arXiv: 1508.02684 [hep-ph] (2015).
93. X. Chen, T. Gehrmann, E. Glover, M. Jaquier, Precise QCD predictions for the production of Higgs + jet final states. *Phys. Lett. B* **740**, 147–150, arXiv: 1408.5325 [hep-ph] (2015).
94. A. Banfi, F. Caola, F. A. Dreyer, P. F. Monni, G. P. Salam, G. Zanderighi, F. Dulat, Jet-vetoed Higgs cross section in gluon fusion at $N^3\text{LO}+\text{NNLL}$ with small- R resummation. *JHEP* **04**, 049, arXiv: 1511.02886 [hep-ph] (2016).
95. C. Anastasiou, A. Daleo, Numerical evaluation of loop integrals. *JHEP* **10**, 031, arXiv: hep-ph/0511176 (2006).
96. T. Binoth, G. Heinrich, An automatized algorithm to compute infrared divergent multi-loop integrals. *Nucl. Phys. B* **585**, 741–759, arXiv: hep-ph/0004013 (2000).

97. K. Hepp, Proof of the Bogolyubov-Parasiuk theorem on renormalization. *Commun. Math. Phys.* **2**, 301–326 (1966).
98. M. Roth, A. Denner, High-energy approximation of one loop Feynman integrals. *Nucl. Phys. B* **479**, 495–514, arXiv: hep-ph/9605420 (1996).
99. R. Boughezal, K. Melnikov, F. Petriello, A subtraction scheme for NNLO computations. *Phys. Rev. D* **85**, 034025, arXiv: 1111.7041 [hep-ph] (2012).
100. R. Boughezal, X. Liu, F. Petriello, N -jettiness soft function at next-to-next-to-leading order. *Phys. Rev. D* **91**, 094035, arXiv: 1504.02540 [hep-ph] (2015).
101. J. Gaunt, M. Stahlhofen, F. J. Tackmann, J. R. Walsh, N -jettiness Subtractions for NNLO QCD Calculations. *JHEP* **09**, 058, arXiv: 1505.04794 [hep-ph] (2015).
102. P. Bärnreuther, M. Czakon, A. Mitov, Percent Level Precision Physics at the Tevatron: First Genuine NNLO QCD Corrections to $q\bar{q} \rightarrow t\bar{t} + X$. *Phys. Rev. Lett.* **109**, 132001, arXiv: 1204.5201 [hep-ph] (2012).
103. F. Caola, K. Melnikov, R. Röntsch, Nested soft-collinear subtractions in NNLO QCD computations. *Eur. Phys. J. C* **77**, 248, arXiv: 1702.01352 [hep-ph] (2017).
104. G. Somogyi, Z. Trocsanyi, V. Del Duca, A Subtraction scheme for computing QCD jet cross sections at NNLO: Regularization of doubly-real emissions. *JHEP* **01**, 070, arXiv: hep-ph/0609042 (2007).
105. A. Gehrmann-De Ridder, T. Gehrmann, E. Glover, Antenna subtraction at NNLO. *JHEP* **09**, 056, arXiv: hep-ph/0505111 (2005).
106. M. Cacciari, F. A. Dreyer, A. Karlberg, G. P. Salam, G. Zanderighi, Fully Differential Vector-Boson-Fusion Higgs Production at Next-to-Next-to-Leading Order. *Phys. Rev. Lett.* **115**, [Erratum: *Phys.Rev.Lett.* 120, 139901 (2018)], 082002, arXiv: 1506.02660 [hep-ph] (2015).
107. C. Anastasiou, F. Herzog, A. Lazopoulos, On the factorization of overlapping singularities at NNLO. *JHEP* **03**, 038, arXiv: 1011.4867 [hep-ph] (2011).
108. G. Altarelli, Partons in Quantum Chromodynamics. *Phys. Rept.* **81**, 1 (1982).
109. Y. L. Dokshitzer, Calculation of the Structure Functions for Deep Inelastic Scattering and e^+e^- Annihilation by Perturbation Theory in Quantum Chromodynamics. *Sov. Phys. JETP* **46**, [*Zh. Eksp. Teor. Fiz.* 73,1216(1977)], 641–653 (1977).
110. V. N. Gribov, L. N. Lipatov, Deep inelastic $e p$ scattering in perturbation theory. *Sov. J. Nucl. Phys.* **15**, [*Yad. Fiz.* 15,781(1972)], 438–450 (1972).
111. G. Altarelli, G. Parisi, Asymptotic Freedom in Parton Language. *Nucl. Phys.* **B126**, 298–318 (1977).

112. J. C. Collins, D. E. Soper, G. F. Sterman, Factorization of Hard Processes in QCD. *Adv. Ser. Direct. High Energy Phys.* **5**, 1–91, arXiv: hep-ph/0409313 [hep-ph] (1989).
113. W. A. Bardeen, A. J. Buras, D. W. Duke, T. Muta, Deep-inelastic scattering beyond the leading order in asymptotically free gauge theories. *Phys. Rev. D* **18**, 3998–4017, (<https://link.aps.org/doi/10.1103/PhysRevD.18.3998>) (11 1978).
114. D. J. Gross, F. Wilczek, Ultraviolet Behavior of Nonabelian Gauge Theories. *Phys. Rev. Lett.* **30**, 1343–1346 (1973).
115. G. 't. Hooft, M. Veltman, Regularization and renormalization of gauge fields. *Nuclear Physics B* **44**, 189–213, ISSN: 0550-3213, (<http://www.sciencedirect.com/science/article/pii/0550321372902799>) (1972).
116. J. C. Collins, *Renormalization*, Cambridge Books Online (Cambridge University Press, 1984), ISBN: 9780511622656, (<http://dx.doi.org/10.1017/CB09780511622656>).
117. L. H. C. S. W. Group *et al.*, Handbook of LHC Higgs Cross Sections: 1. Inclusive Observables. arXiv: 1101.0593v3 [hep-ph] (2011).
118. L. H. C. S. W. Group *et al.*, Handbook of LHC Higgs Cross Sections: 2. Differential Distributions. arXiv: 1201.3084v1 [hep-ph] (2012).
119. T. L. H. C. S. W. Group *et al.*, Handbook of LHC Higgs Cross Sections: 3. Higgs Properties. arXiv: 1307.1347v2 [hep-ph] (2013).
120. L. A. Harland-Lang, A. D. Martin, P. Motylinski, R. S. Thorne, Parton distributions in the LHC era: MMHT 2014 PDFs. *Eur. Phys. J.* **C75**, 204, arXiv: 1412.3989 [hep-ph] (2015).
121. A. Buckley, J. Ferrando, S. Lloyd, K. Nordström, B. Page, M. Rüfenacht, M. Schönherr, G. Watt, LHAPDF6: parton density access in the LHC precision era. *Eur. Phys. J.* **C75**, 132, arXiv: 1412.7420 [hep-ph] (2015).
122. S. Dawson, Radiative corrections to Higgs boson production. *Nucl. Phys. B* **359**, 283–300 (1991).
123. M. Spira, A. Djouadi, D. Graudenz, P. M. Zerwas, Higgs boson production at the LHC. *Nucl. Phys.* **B453**, 17–82, arXiv: hep-ph/9504378 [hep-ph] (1995).
124. D. Graudenz, M. Spira, P. M. Zerwas, QCD corrections to Higgs boson production at proton proton colliders. *Phys. Rev. Lett.* **70**, 1372–1375 (1993).
125. R. V. Harlander, W. B. Kilgore, Next-to-next-to-leading order Higgs production at hadron colliders. *Phys. Rev. Lett.* **88**, 201801, arXiv: hep-ph/0201206 [hep-ph] (2002).
126. C. Anastasiou, K. Melnikov, Higgs boson production at hadron colliders in NNLO QCD. *Nucl. Phys.* **B646**, 220–256, arXiv: hep-ph/0207004 [hep-ph] (2002).

127. V. Ravindran, J. Smith, W. L. van Neerven, NNLO corrections to the total cross-section for Higgs boson production in hadron hadron collisions. *Nucl. Phys.* **B665**, 325–366, arXiv: hep-ph/0302135 [hep-ph] (2003).
128. C. Anastasiou, C. Duhr, F. Dulat, E. Furlan, F. Herzog, B. Mistlberger, Soft expansion of double-real-virtual corrections to Higgs production at N³LO. *JHEP* **08**, 051, arXiv: 1505.04110 [hep-ph] (2015).
129. R. V. Harlander, K. J. Ozeren, Finite top mass effects for hadronic Higgs production at next-to-next-to-leading order. *JHEP* **11**, 088, arXiv: 0909.3420 [hep-ph] (2009).
130. A. Pak, M. Rogal, M. Steinhauser, Finite top quark mass effects in NNLO Higgs boson production at LHC. *JHEP* **02**, 025, arXiv: 0911.4662 [hep-ph] (2010).
131. J. Davies, R. Groeber, A. Maier, T. Rauh, M. Steinhauser, Top quark mass dependence of the Higgs-gluon form factor at three loops. *Phys. Rev. D* **100**, 034017 (2019), arXiv: 1906.00982v1 [hep-ph] (2019).
132. K. Chetyrkin, B. A. Kniehl, M. Steinhauser, Decoupling relations to O(α_s^3) and their connection to low-energy theorems. *Nucl. Phys. B* **510**, 61–87, arXiv: hep-ph/9708255 (1998).
133. M. Spira, QCD effects in Higgs physics. *Fortsch. Phys.* **46**, 203–284, arXiv: hep-ph/9705337 [hep-ph] (1998).
134. P. Nogueira, Automatic Feynman graph generation. *J. Comput. Phys.* **105**, 279–289 (1993).
135. J. Kuipers, T. Ueda, J. A. M. Vermaseren, J. Vollinga, FORM version 4.0. arXiv: 1203.6543v1 [cs.SC] (2012).
136. S. Laporta, Calculation of master integrals by difference equations. *Phys. Lett.* **B504**, 188–194, arXiv: hep-ph/0102032 [hep-ph] (2001).
137. C. Anastasiou, K. Melnikov, Pseudoscalar Higgs boson production at hadron colliders in NNLO QCD. *Phys. Rev. D* **67**, 037501, arXiv: hep-ph/0208115 (2003).
138. C. Anastasiou, L. J. Dixon, K. Melnikov, F. Petriello, Dilepton rapidity distribution in the Drell-Yan process at NNLO in QCD. *Phys. Rev. Lett.* **91**, 182002, arXiv: hep-ph/0306192 (2003).
139. C. Anastasiou, L. J. Dixon, K. Melnikov, F. Petriello, High precision QCD at hadron colliders: Electroweak gauge boson rapidity distributions at NNLO. *Phys. Rev. D* **69**, 094008, arXiv: hep-ph/0312266 (2004).
140. C. Anastasiou, C. Duhr, F. Dulat, B. Mistlberger, Soft triple-real radiation for Higgs production at N₃LO. *JHEP* **07**, 003, arXiv: 1302.4379 [hep-ph] (2013).

141. C. Anastasiou, C. Duhr, F. Dulat, F. Herzog, B. Mistlberger, Real-virtual contributions to the inclusive Higgs cross-section at N^3LO . *JHEP* **12**, 088, arXiv: 1311.1425 [hep-ph] (2013).
142. C. Anastasiou, C. Duhr, F. Dulat, E. Furlan, T. Gehrmann, F. Herzog, B. Mistlberger, Higgs Boson Gluon Fusion Production Beyond Threshold in N^3LO QCD. *JHEP* **03**, 091, arXiv: 1411.3584 [hep-ph] (2015).
143. F. Dulat, B. Mistlberger, Real-Virtual-Virtual contributions to the inclusive Higgs cross section at N^3LO . arXiv: 1411.3586 [hep-ph] (2014).
144. C. Duhr, T. Gehrmann, The two-loop soft current in dimensional regularization. *Phys. Lett. B* **727**, 452–455, arXiv: 1309.4393 [hep-ph] (2013).
145. C. Duhr, T. Gehrmann, M. Jaquier, Two-loop splitting amplitudes and the single-real contribution to inclusive Higgs production at N^3LO . *JHEP* **02**, 077, arXiv: 1411.3587 [hep-ph] (2015).
146. R. E. Cutkosky, Singularities and discontinuities of Feynman amplitudes. *Journal of Mathematical Physics* **1**, 429–433 (1960).
147. W. B. Kilgore, Regularization schemes and higher order corrections. *Phys. Rev. D* **83**, 114005, (<http://link.aps.org/doi/10.1103/PhysRevD.83.114005>) (11 2011).
148. R. V. Harlander, Virtual corrections to $g g \rightarrow H$ to two loops in the heavy top limit. *Phys. Lett. B* **492**, 74–80, arXiv: hep-ph/0007289 (2000).
149. T. Gehrmann, T. Huber, D. Maitre, Two-loop quark and gluon form-factors in dimensional regularisation. *Phys. Lett. B* **622**, 295–302, arXiv: hep-ph/0507061 (2005).
150. G. Somogyi, Angular integrals in d dimensions. *J. Math. Phys.* **52**, 083501, arXiv: 1101.3557 [hep-ph] (2011).
151. C. Anastasiou, E. Glover, C. Oleari, Application of the negative dimension approach to massless scalar box integrals. *Nucl. Phys. B* **565**, 445–467, arXiv: hep-ph/9907523 (2000).
152. T. Huber, D. Maitre, HypExp: A Mathematica package for expanding hypergeometric functions around integer-valued parameters. *Comput. Phys. Commun.* **175**, 122–144, arXiv: hep-ph/0507094 (2006).
153. T. Huber, D. Maitre, HypExp 2, Expanding Hypergeometric Functions about Half-Integer Parameters. *Comput. Phys. Commun.* **178**, 755–776, arXiv: 0708.2443 [hep-ph] (2008).
154. S. Buehler, C. Duhr, CHAPLIN - Complex Harmonic Polylogarithms in Fortran. *Comput. Phys. Commun.* **185**, 2703–2713, arXiv: 1106.5739 [hep-ph] (2014).

155. R. Boughezal, J. M. Campbell, R. K. Ellis, C. Focke, W. Giele, X. Liu, F. Petriello, C. Williams, Color singlet production at NNLO in MCFM. *Eur. Phys. J. C* **77**, 7, arXiv: 1605.08011 [hep-ph] (2017).
156. V. R. Tavolaro, Measurements of Higgs boson production and properties in the diphoton decay channel using the CMS detector Higgs boson to two photons using the CMS detector. (<http://pos.sissa.it/>).
157. G. Aad *et al.*, Measurements of the Total and Differential Higgs Boson Production Cross Sections Combining the $H \rightarrow \gamma\gamma$ and $H \rightarrow ZZ^* \rightarrow 4\ell$ Decay Channels at $\sqrt{s}=8$ TeV with the ATLAS Detector. *Phys. Rev. Lett.* **115**, 091801, arXiv: 1504.05833 [hep-ex] (2015).
158. G. Aad *et al.*, Measurements of fiducial and differential cross sections for Higgs boson production in the diphoton decay channel at $\sqrt{s} = 8$ TeV with ATLAS. *JHEP* **09**, 112, arXiv: 1407.4222 [hep-ex] (2014).
159. G. Aad *et al.*, Measurement of Higgs boson production in the diphoton decay channel in pp collisions at center-of-mass energies of 7 and 8 TeV with the ATLAS detector. *Phys. Rev. D* **90**, 112015, arXiv: 1408.7084 [hep-ex] (2014).
160. V. Khachatryan *et al.*, Precise determination of the mass of the Higgs boson and tests of compatibility of its couplings with the standard model predictions using proton collisions at 7 and 8 TeV. *Eur. Phys. J. C* **75**, 212, arXiv: 1412.8662 [hep-ex] (2015).
161. G. Aad *et al.*, Evidence for the spin-0 nature of the Higgs boson using ATLAS data. *Phys. Lett. B* **726**, 120–144, arXiv: 1307.1432 [hep-ex] (2013).
162. M. Aaboud *et al.*, Measurements of Higgs boson properties in the diphoton decay channel with 36 fb^{-1} of pp collision data at $\sqrt{s} = 13$ TeV with the ATLAS detector. *Phys. Rev. D* **98**, 052005, arXiv: 1802.04146 [hep-ex] (2018).
163. S. Catani, B. Webber, Infrared safe but infinite: Soft gluon divergences inside the physical region. *JHEP* **10**, 005, arXiv: hep-ph/9710333 (1997).
164. A. von Manteuffel, R. M. Schabinger, Quark and gluon form factors to four-loop order in QCD: the N_f^3 contributions. *Phys. Rev. D* **95**, 034030, arXiv: 1611.00795 [hep-ph] (2017).
165. S. Badger, C. Brønnum-Hansen, H. B. Hartanto, T. Peraro, Analytic helicity amplitudes for two-loop five-gluon scattering: the single-minus case. *JHEP* **01**, 186, arXiv: 1811.11699 [hep-ph] (2019).
166. S. Abreu, J. Dormans, F. Febres Cordero, H. Ita, B. Page, Analytic Form of Planar Two-Loop Five-Gluon Scattering Amplitudes in QCD. *Phys. Rev. Lett.* **122**, 082002, arXiv: 1812.04586 [hep-ph] (2019).

167. R. N. Lee, A. V. Smirnov, V. A. Smirnov, M. Steinhauser, Four-loop quark form factor with quartic fundamental colour factor. *JHEP* **02**, 172, arXiv: 1901.02898 [hep-ph] (2019).
168. J. Henn, T. Peraro, M. Stahlhofen, P. Wasser, Matter dependence of the four-loop cusp anomalous dimension. *Phys. Rev. Lett.* **122**, 201602, arXiv: 1901.03693 [hep-ph] (2019).
169. A. von Manteuffel, R. M. Schabinger, Quark and gluon form factors in four loop QCD: The N_f^2 and $N_{q\gamma}N_f$ contributions. *Phys. Rev. D* **99**, 094014, arXiv: 1902.08208 [hep-ph] (2019).
170. R. H. Lewis, *Computer Algebra System Fermat*, <http://www.bway.net/lewis>, Accessed: 2010-09-30.
171. P. S. Wang, M. J. T. Guy, J. H. Davenport, P-Adic Reconstruction of Rational Numbers. *SIGSAM Bull.* **16**, 2–3, ISSN: 0163-5824, (<https://doi.org/10.1145/1089292.1089293>) (1982).
172. M. Beneke, V. A. Smirnov, Asymptotic expansion of Feynman integrals near threshold. *Nucl. Phys. B* **522**, 321–344, arXiv: hep-ph/9711391 (1998).
173. C. W. Bauer, A. Frink, R. Kreckel, Introduction to the GiNaC framework for symbolic computation within the C++ programming language. *J. Symb. Comput.* **33**, 1, arXiv: cs/0004015 [cs-sc] (2000).
174. T. Gehrmann, E. W. N. Glover, T. Huber, N. Ikizlerli, C. Studerus, Calculation of the quark and gluon form factors to three loops in QCD. *JHEP* **06**, 094, arXiv: 1004.3653 [hep-ph] (2010).
175. Y. Li, A. von Manteuffel, R. M. Schabinger, H. X. Zhu, N³LO Higgs and Drell-Yan production at threshold: the one-loop two-emission contribution. *Phys. Rev. D* **90**, 053006 (2014), arXiv: 1404.5839v2 [hep-ph] (2014).
176. C. Anastasiou, L. J. Dixon, K. Melnikov, NLO Higgs boson rapidity distributions at hadron colliders. *Nucl. Phys. B Proc. Suppl.* **116**, ed. by J. Blumlein, F. Jegerlehner, T. Riemann, W. Hollik, J. H. Kuhn, 193–197, arXiv: hep-ph/0211141 (2003).
177. F. Herzog, B. Mistlberger, The Soft-Virtual Higgs Cross-section at N₃LO and the Convergence of the Threshold Expansion. arXiv: 1405.5685v1 [hep-ph] (2014).
178. C. Anastasiou, C. Duhr, F. Dulat, E. Furlan, T. Gehrmann, F. Herzog, A. Lazopoulos, B. Mistlberger, High precision determination of the gluon fusion Higgs boson cross-section at the LHC. *JHEP* **05**, 058, arXiv: 1602.00695 [hep-ph] (2016).
179. R. Bonciani, S. Catani, M. Grazzini, H. Sargsyan, A. Torre, The q_T subtraction method for top quark production at hadron colliders. *Eur.Phys.J. C* **75** (2015) *12*, 581, arXiv: 1508.03585v2 [hep-ph] (2015).

180. G. Bozzi, S. Catani, D. de Florian, M. Grazzini, Transverse-momentum resummation and the spectrum of the Higgs boson at the LHC. *Nucl.Phys.B* **737**:73-120,2006, arXiv: hep-ph/0508068v1 [hep-ph] (2005).
181. L. Cieri, X. Chen, T. Gehrmann, E. N. Glover, A. Huss, Higgs boson production at the LHC using the q_T subtraction formalism at N³LO QCD. *JHEP* **02**, 096, arXiv: 1807.11501 [hep-ph] (2019).
182. M. Aaboud *et al.*, Combined measurement of differential and total cross sections in the $H \rightarrow \gamma\gamma$ and the $H \rightarrow ZZ^* \rightarrow 4\ell$ decay channels at $\sqrt{s} = 13$ TeV with the ATLAS detector. *Phys. Lett. B* **786**, 114–133, arXiv: 1805.10197 [hep-ex] (2018).
183. A. M. Sirunyan *et al.*, Combined measurements of Higgs boson couplings in proton–proton collisions at $\sqrt{s} = 13$ TeV. *Eur. Phys. J. C* **79**, 421, arXiv: 1809.10733 [hep-ex] (2019).
184. F. Dulat, A. Lazopoulos, B. Mistlberger, iHixs 2 — Inclusive Higgs cross sections. *Comput. Phys. Commun.* **233**, 243–260, arXiv: 1802.00827 [hep-ph] (2018).
185. T. Ahmed, M. K. Mandal, N. Rana, V. Ravindran, Rapidity Distributions in Drell-Yan and Higgs Productions at Threshold to Third Order in QCD. *Phys. Rev. Lett.* **113**, 212003 (2014), arXiv: 1404.6504v2 [hep-ph] (2014).
186. R. Thorne, L. Harland-Lang, A. Martin, P. Motylinski, MMHT 2014 Parton Distributions Functions. *PoS DIS2015*, 056 (2015).
187. T. Hahn, CUBA: A Library for multidimensional numerical integration. *Comput. Phys. Commun.* **168**, 78–95, arXiv: hep-ph/0404043 (2005).
188. S. Buchta, G. Chachamis, P. Draggiotis, G. Rodrigo, Numerical implementation of the loop–tree duality method. *Eur. Phys. J. C* **77**, 274, arXiv: 1510.00187 [hep-ph] (2017).
189. J. J. Aguilera-Verdugo, F. Driencourt-Mangin, J. Plenter, S. Ramírez-Uribe, G. Rodrigo, G. F. Sborlini, W. J. Torres Bobadilla, S. Tracz, Causality, unitarity thresholds, anomalous thresholds and infrared singularities from the loop-tree duality at higher orders. *JHEP* **12**, 163, arXiv: 1904.08389 [hep-ph] (2019).
190. S. Becker, C. Reuschle, S. Weinzierl, Numerical NLO QCD calculations. *JHEP* **12**, 013, arXiv: 1010.4187 [hep-ph] (2010).
191. S. Becker, C. Reuschle, S. Weinzierl, Efficiency Improvements for the Numerical Computation of NLO Corrections. *JHEP* **07**, 090, arXiv: 1205.2096 [hep-ph] (2012).
192. S. Becker, S. Weinzierl, Direct contour deformation with arbitrary masses in the loop. *Phys. Rev. D* **86**, 074009, arXiv: 1208.4088 [hep-ph] (2012).

193. R. J. Hernandez-Pinto, G. F. R. Sborlini, G. Rodrigo, Towards gauge theories in four dimensions. *JHEP* **02**, 044, arXiv: 1506.04617 [hep-ph] (2016).
194. F. Driencourt-Mangin, G. Rodrigo, G. F. Sborlini, W. J. Torres Bobadilla, On the interplay between the loop-tree duality and helicity amplitudes. arXiv: 1911.11125 [hep-ph] (2019).
195. M. Gell-Mann, F. Low, Bound states in quantum field theory. *Phys. Rev.* **84**, 350–354 (1951).
196. C. Anastasiou, G. Sterman, Removing infrared divergences from two-loop integrals. *JHEP* **07**, 056, arXiv: 1812.03753 [hep-ph] (2019).
197. F. Driencourt-Mangin, G. Rodrigo, G. F. Sborlini, W. J. Torres Bobadilla, Universal four-dimensional representation of $H \rightarrow \gamma\gamma$ at two loops through the Loop-Tree Duality. *JHEP* **02**, 143, arXiv: 1901.09853 [hep-ph] (2019).
198. V. Hirschi, R. Frederix, S. Frixione, M. V. Garzelli, F. Maltoni, R. Pittau, Automation of one-loop QCD corrections. *JHEP* **05**, 044, arXiv: 1103.0621 [hep-ph] (2011).
199. J. Alwall, R. Frederix, S. Frixione, V. Hirschi, F. Maltoni, O. Mattelaer, H. -S. Shao, T. Stelzer, P. Torrielli, M. Zaro, The automated computation of tree-level and next-to-leading order differential cross sections, and their matching to parton shower simulations. *JHEP* **07**, 079, arXiv: 1405.0301 [hep-ph] (2014).
200. S. Carrazza, R. K. Ellis, G. Zanderighi, QCDLoop: a comprehensive framework for one-loop scalar integrals. *Comput. Phys. Commun.* **209**, 134–143, arXiv: 1605.03181 [hep-ph] (2016).
201. H. Murayama, I. Watanabe, K. Hagiwara, HELAS: HELicity amplitude subroutines for Feynman diagram evaluations. (1992).
202. W. Kilian, T. Kleinschmidt, *Numerical Evaluation of Feynman Loop Integrals by Reduction to Tree Graphs*, 2009, arXiv: 0912.3495 [hep-ph].
203. Z. Nagy, D. E. Soper, General subtraction method for numerical calculation of one loop QCD matrix elements. *JHEP* **09**, 055, arXiv: hep-ph/0308127 (2003).
204. M. Assadsolimani, S. Becker, S. Weinzierl, A Simple formula for the infrared singular part of the integrand of one-loop QCD amplitudes. *Phys. Rev. D* **81**, 094002, arXiv: 0912.1680 [hep-ph] (2010).
205. S. Seth, S. Weinzierl, Numerical integration of subtraction terms. *Phys. Rev. D* **93**, 114031, arXiv: 1605.06646 [hep-ph] (2016).

206. G. F. R. Sborlini, F. Driencourt-Mangin, R. Hernandez-Pinto, G. Rodrigo, Four-dimensional unsubtraction from the loop-tree duality. *JHEP* **08**, 160, arXiv: 1604.06699 [hep-ph] (2016).
207. Y. Ma, A Forest Formula to Subtract Infrared Singularities in Amplitudes for Wide-angle Scattering. *JHEP* **05**, 012, arXiv: 1910.11304 [hep-ph] (2020).
208. J. J. Aguilera-Verdugo, F. Driencourt-Mangin, R. J. Hernandez Pinto, J. Plenter, S. Ramirez-Uribe, A. E. Renteria Olivo, G. Rodrigo, G. F. Sborlini, W. J. Torres Bobadilla, S. Tracz, Open loop amplitudes and causality to all orders and powers from the loop-tree duality. *Phys. Rev. Lett.* **124**, 211602, arXiv: 2001.03564 [hep-ph] (2020).
209. J. J. Aguilera-Verdugo, R. J. Hernandez-Pinto, G. Rodrigo, G. F. Sborlini, W. J. Torres Bobadilla, Causal representation of multi-loop amplitudes within the loop-tree duality. arXiv: 2006.11217 [hep-ph] (2020).
210. S. Ramírez-Uribe, R. J. Hernández-Pinto, G. Rodrigo, G. F. Sborlini, W. J. Torres Bobadilla, Universal opening of four-loop scattering amplitudes to trees. arXiv: 2006.13818 [hep-ph] (2020).
211. J. Campbell, J. Huston, F. Krauss, *The Black Book of Quantum Chromodynamics: A Primer for the LHC Era* (Oxford University Press, 2017), ISBN: 978-0-19-965274-7.
212. M. Peskin, D. Schroeder, *An Introduction to Quantum Field Theory* (Addison-Wesley Publishing Company, 1995), ISBN: 9780201503975, (<https://books.google.ch/books?id=i35LALN0GosC>).
213. F. J. Ynduráin, in (Springer Berlin Heidelberg, Berlin, Heidelberg, 2006), chap. QCD as a Field Theory, 19, ISBN: 978-3-540-33210-7, (http://dx.doi.org/10.1007/3-540-33210-3_2).
214. I. Bierenbaum, S. Buchta, P. Draggiotis, I. Malamos, G. Rodrigo, Tree-Loop Duality Relation beyond simple poles. *JHEP* **03**, 025, arXiv: 1211.5048 [hep-ph] (2013).
215. H. Frellesvig, M. Hidding, L. Maestri, F. Moriello, G. Salvatori, The complete set of two-loop master integrals for Higgs + jet production in QCD. *JHEP* **06**, 093, arXiv: 1911.06308 [hep-ph] (2020).
216. N. Usyukina, A. I. Davydychev, An Approach to the evaluation of three and four point ladder diagrams. *Phys. Lett. B* **298**, 363–370 (1993).
217. B. Basso, L. J. Dixon, Gluing Ladder Feynman Diagrams into Fishnets. *Phys. Rev. Lett.* **119**, 071601, arXiv: 1705.03545 [hep-th] (2017).